41st ISYA Lecturer: *Gustavo Bruzual, IRyA, UNAM; Campus Morelia, México*

Topic: *GALAXIES (6 lectures)*

Description: An overview of the basic properties of galaxies due to the distribution, kinematics, dynamics, relevance, and evolution of their different stellar populations. A view of the basic properties and processes in the distant universe as revealed by galaxies of all types discovered so far.

Syllabus:

Lecture 1: The Milky Way as a galaxy
- The structure of the Galaxy
- The galactic disk
- The galactic bulge
- The galactic halo
- The galactic center
- Velocity of the sun
- Rotation curve of the Galaxy
- Stellar populations in the Galaxy

Lecture 2: The world of galaxies (1)
- Morphological classification. The Hubble Sequence
- Other types of galaxies
- Elliptical galaxies
- Spiral galaxies
- Galaxies in the local group
- Scaling relations

Lecture 3: The world of galaxies (2)
- The extragalactic distance scale
- The luminosity function of galaxies
- Black holes in the centers of galaxies
- Galaxies as gravitational lenses
- Stellar population synthesis
- Spectral evolution of galaxies
- Chemical evolution of galaxies

Lecture 4: Clusters and groups of galaxies
- The local group
- Galaxies in clusters and groups
- Morphological classification of clusters
- Spatial distribution of galaxies in clusters
- Luminosity function of cluster galaxies
- Clusters of galaxies as gravitational lenses
- Evolution of clusters

Lecture 5: Galaxies at high redshift (1)
- Lyman-break galaxies
- Starburst galaxies
- Extremely red objects
- Sub-millimeter sources
- Damped Lyman-alpha systems
- Lyman-alpha blobs
- Gamma-ray bursts

Lecture 6: Galaxies at high redshift (2)
- Background radiation
- Re-ionization of the universe
- Cosmic star formation history
- Galaxy formation and evolution

Requirements: Video projector in the class room

Bibliography:
- Schneider, *Extragalactic astronomy and cosmology*
- Sparke & Gallager, *Galaxies in the Universe*
- Mo, van den Bosch & White, Galaxy formation and evolution (selected chapters)

3.4 Scaling Relations

The kinematic properties of spirals and ellipticals are closely related to their luminosity. As we shall discuss below, spirals follow the *Tully–Fisher relation* (Sect. 3.4.1), whereas elliptical galaxies obey the *Faber–Jackson relation* (Sect. 3.4.2) and are located in the *fundamental plane* (Sect. 3.4.3). These scaling relations are a very important tool for distance estimations, as will be discussed in Sect. 3.6. Furthermore, these scaling relations express relations between galaxy properties which any successful model of galaxy evolution must be able to explain. Here we will describe these scaling relations and discuss their physical origin.

3.4.1 The Tully–Fisher Relation

Using 21-cm observations of spiral galaxies, in 1977 R. Brent Tully and J. Richard Fisher found that the maximum rotation velocity of spirals is closely related to their luminosity, following the relation

$$\boxed{L \propto v_{\max}^{\alpha}}\,, \tag{3.14}$$

where the slope of the Tully–Fisher relation is about $\alpha \sim 4$. The larger the wavelength of the filter in which the luminosity is measured, the smaller the dispersion of the Tully–Fisher relation (see Fig. 3.19). This is to be expected because radiation at larger wavelengths is less affected by dust absorption and by the current star-formation rate, which may vary to some extent between individual spirals. Furthermore, it is found that the value of α increases with the wavelength of the filter; the Tully–Fisher relation is steeper in the red. The dispersion of galaxies around the relation (3.14) in the near infrared (e.g., in the H-band) is about 10%.

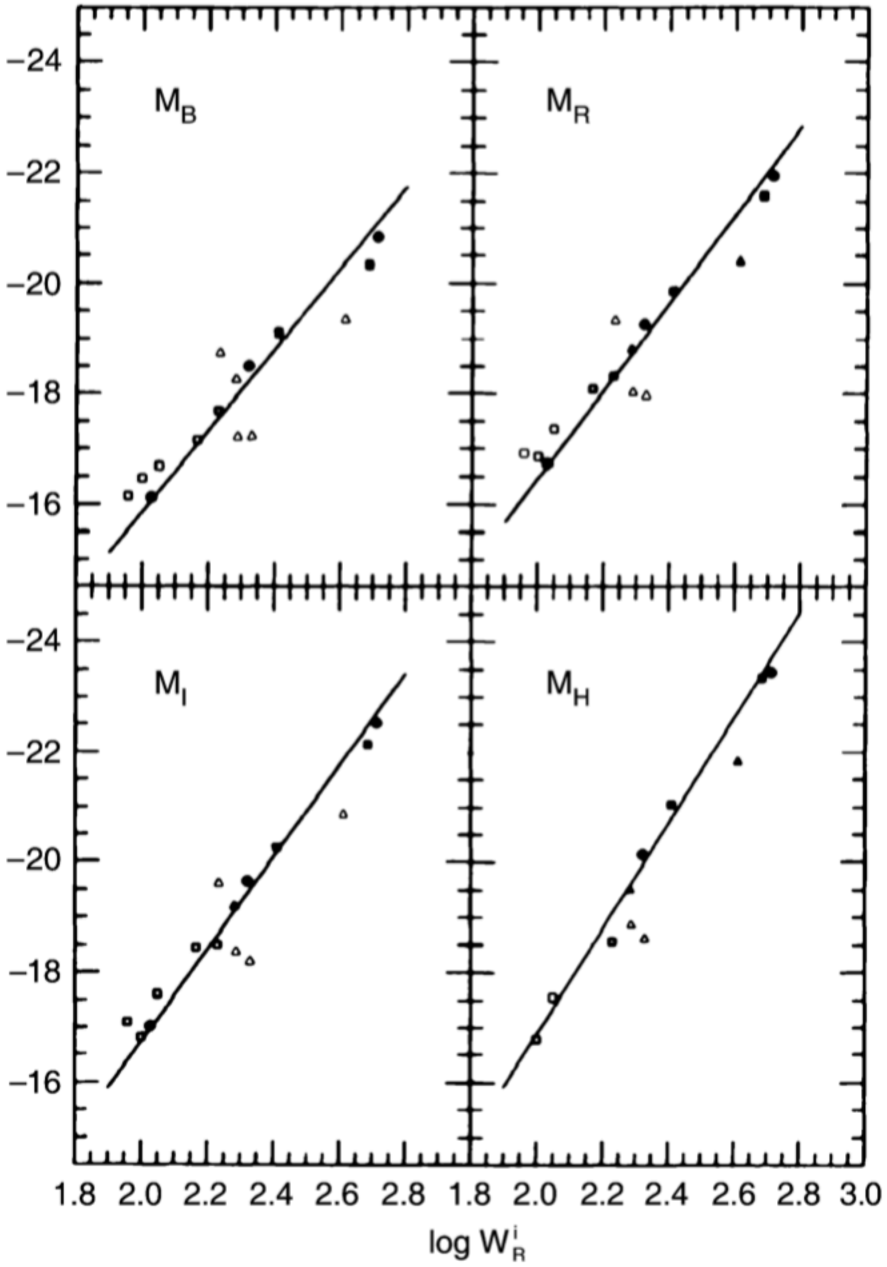

Fig. 3.19. The Tully–Fisher relation for galaxies in the Local Group (dots), in the Sculptor group (triangles), and in the M81 group (squares). The absolute magnitude is plotted as a function of the width of the 21-cm profile which indicates the maximum rotation velocity (see Fig. 3.20). Filled symbols represent galaxies for which independent distance estimates were obtained, either from RR Lyrae stars, Cepheids, or planetary nebulae. For galaxies represented by open symbols, the average distance of the respective group is used. The solid line is a fit to similar data for the Ursa-Major cluster, together with data of those galaxies for which individual distance estimates are available (filled symbols). The larger dispersion around the mean relation for the Sculptor group galaxies is due to the group's extent along the line-of-sight

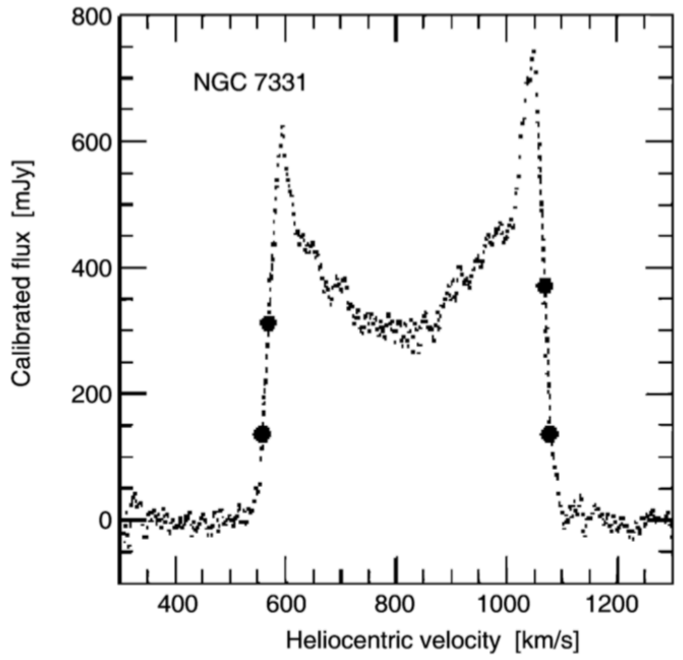

Fig. 3.20. 21 cm profile of the galaxy NGC 7331. The bold dots indicate 20% and 50% of the maximum flux; these are of relevance for the determination of the line width from which the rotational velocity is derived

Because of this close correlation, the luminosity of spirals can be estimated quite precisely by measuring the rotational velocity. The determination of the (maximum) rotational velocity is independent of the galaxy's distance. By comparing the luminosity, as determined from the Tully–Fisher relation, with the measured flux one can then estimate the distance of the galaxy – without utilizing the Hubble relation!

The measurement of $v_{\max}$ is obtained either from a spatially resolved rotation curve, by measuring $v_{\rm rot}(\theta)$, which is possible for relatively nearby galaxies, or by observing an integrated spectrum of the 21-cm line of HI that has a Doppler width corresponding to about $2v_{\max}$ (see Fig. 3.20). The Tully–Fisher relation shown in Fig. 3.19 was determined by measuring the width of the 21-cm line.

Explaining the Tully–Fisher Relation. The shapes of the rotation curves of spirals are very similar to each other, in particular with regard to their flat behavior in the outer part. The flat rotation curve implies

$$\boxed{M = \frac{v_{\rm max}^2 R}{G}} \,, \tag{3.15}$$

where the distance R from the center of the galaxy refers to the flat part of the rotation curve. The exact value is not important, though, if only $v(R) \approx$ const. By re-writing (3.15),

$$L = \left(\frac{M}{L}\right)^{-1} \frac{v_{\rm max}^2 R}{G} \,, \tag{3.16}$$

and replacing R by the mean surface brightness $\langle I \rangle = L/R^2$, we obtain

$$L = \left(\frac{M}{L}\right)^{-2} \left(\frac{1}{G^2 \langle I \rangle}\right) v_{\rm max}^4 \,. \tag{3.17}$$

This is the Tully–Fisher relation *if* M/L and $\langle I \rangle$ are the same for all spirals. The latter is in fact suggested by Freeman's law (Sect. 3.3.2). Since the shapes of rotation curves for spirals seem to be very similar, the radial dependence of the ratio of luminous to dark matter may also be quite similar among spirals. Furthermore, since the red or infrared mass-to-light ratios of a stellar population do not depend strongly on its age, the constancy of M/L could also be valid if dark matter is included.

Although the line of argument presented above is far from a proper derivation of the Tully–Fisher-relation, it nevertheless makes the existence of such a scaling relation plausible.

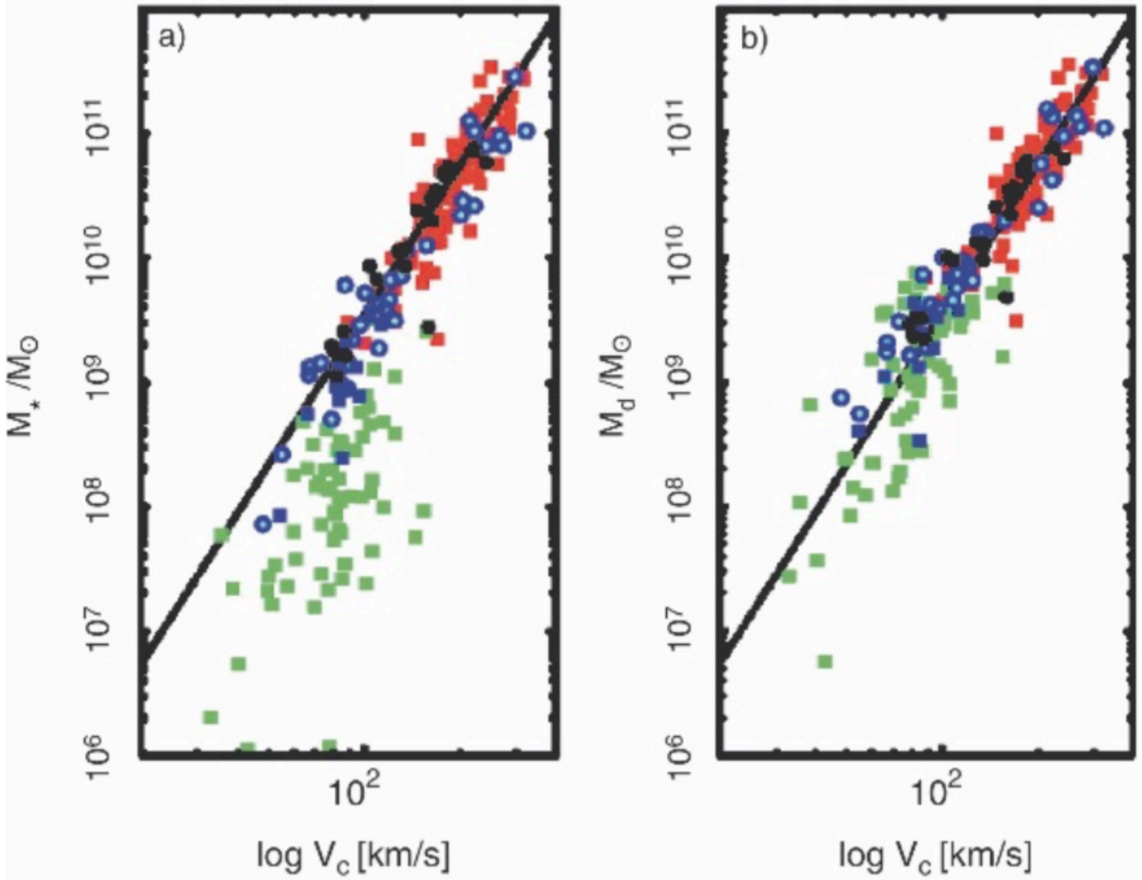

Fig. 3.21. Left panel: the mass contained in stars as a function of the rotational velocity V_c for spirals. This stellar mass is computed from the luminosity by multiplying it with a suitable stellar mass-to-light ratio which depends on the chosen filter and which can be calculated from stellar population models. This is the "classical" Tully–Fisher relation. Squares and circles denote galaxies for which V_c was determined from the 21-cm line width or from a spatially resolved rotation curve, respectively. The colors of the symbols indicate the filter band in which the luminosity was measured: H (red), K′ (black), I (green), B (blue). Right panel: instead of the stellar mass, here the sum of the stellar and gaseous mass is plotted. The gas mass was derived from the flux in the 21-cm line, $M_{\rm gas} = 1.4 M_{\rm HI}$, corrected for helium and metals. Molecular gas has no significant contribution to the baryonic mass. The line in both plots is the Tully–Fisher relation with a slope of $\alpha = 4$

3.4.2 The Faber–Jackson Relation

A relation for elliptical galaxies, analogous to the Tully–Fisher relation, was found by Sandra Faber and Roger Jackson. They discovered that the velocity dispersion in the center of ellipticals, σ_0, scales with luminosity (see Fig. 3.22),

$$\boxed{L \propto \sigma_0^4} \; ,$$

or

$$\boxed{\log(\sigma_0) = -0.1 M_B + \text{const}} \; . \tag{3.20}$$

"Deriving" the Faber–Jackson scaling relation is possible under the same assumptions as the Tully–Fisher relation. However, the dispersion of ellipticals about this relation is larger than that of spirals about the Tully–Fisher relation.

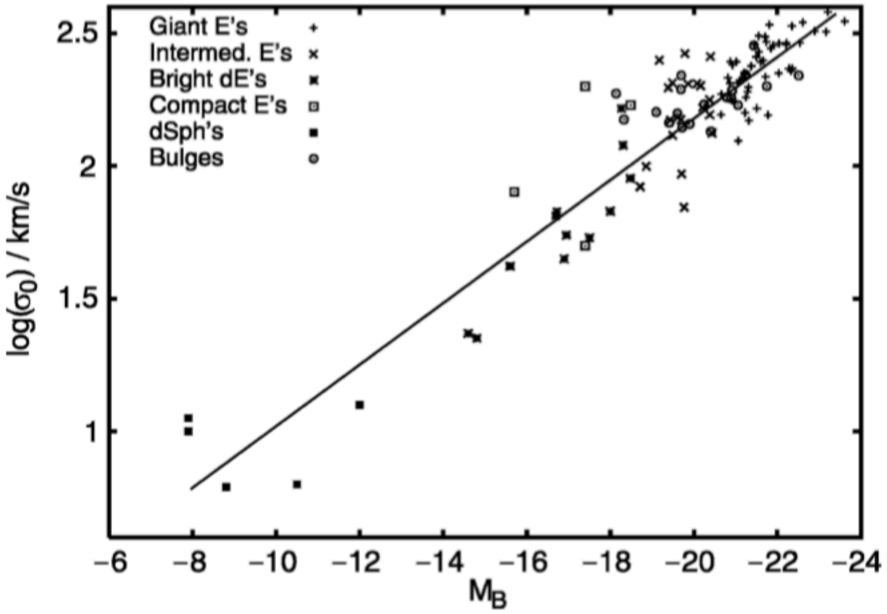

Fig. 3.22. The Faber–Jackson relation expresses a relation between the velocity dispersion and the luminosity of elliptical galaxies. It can be derived from the virial theorem

3.4.3 The Fundamental Plane

The Tully–Fisher and Faber–Jackson relations specify a connection between the luminosity and a kinematic property of galaxies. As we discussed previously, various relations exist between the parameters of elliptical galaxies. Thus one might wonder whether a relation exists between observables of elliptical galaxies for which the dispersion is smaller than that of the Faber–Jackson relation. Such a relation was indeed found and is known as the *fundamental plane*.

To explain this relation, we will consider the various relations between the parameters of ellipticals. In Sect. 3.2.2 we saw that the effective radius of normal ellipticals is related to the luminosity (see Fig. 3.7). This implies a relation between the surface brightness and the effective radius,

$$\boxed{R_e \propto \langle I \rangle_e^{-0.83}} , \qquad (3.21)$$

where $\langle I \rangle_e$ is the average surface brightness within the effective radius, so that

$$\boxed{L = 2\pi R_e^2 \langle I \rangle_e} . \qquad (3.22)$$

From this, a relation between the luminosity and $\langle I \rangle_e$ results,

$$L \propto R_e^2 \langle I \rangle_e \propto \langle I \rangle_e^{-0.66}$$

or

$$\boxed{\langle I \rangle_e \propto L^{-1.5}} . \qquad (3.23)$$

Hence, more luminous ellipticals have smaller surface brightnesses, as is also shown in Fig. 3.7. By means of the Faber–Jackson relation, L is related to σ_0, the central velocity dispersion, and therefore, σ_0, $\langle I \rangle_e$, and R_e are related to each other. The distribution of elliptical galaxies in the three-dimensional parameter space (R_e, $\langle I \rangle_e$, σ_0) is located close to a plane defined by

$$\boxed{R_e \propto \sigma_0^{1.4} \langle I \rangle_e^{-0.85}} . \qquad (3.24)$$

Writing this relation in logarithmic form, we obtain

$$\boxed{\log R_e = 0.34 \langle \mu \rangle_e + 1.4 \log \sigma_0 + \mathrm{const}} , \qquad (3.25)$$

where $\langle \mu \rangle_e$ is the average surface brightness within R_e, measured in mag/arcsec^2. Equation (3.25) defines a plane in this three-dimensional parameter space that is known as the *fundamental plane* (*FP*). Different projections of the fundamental plane are displayed in Fig. 3.23.

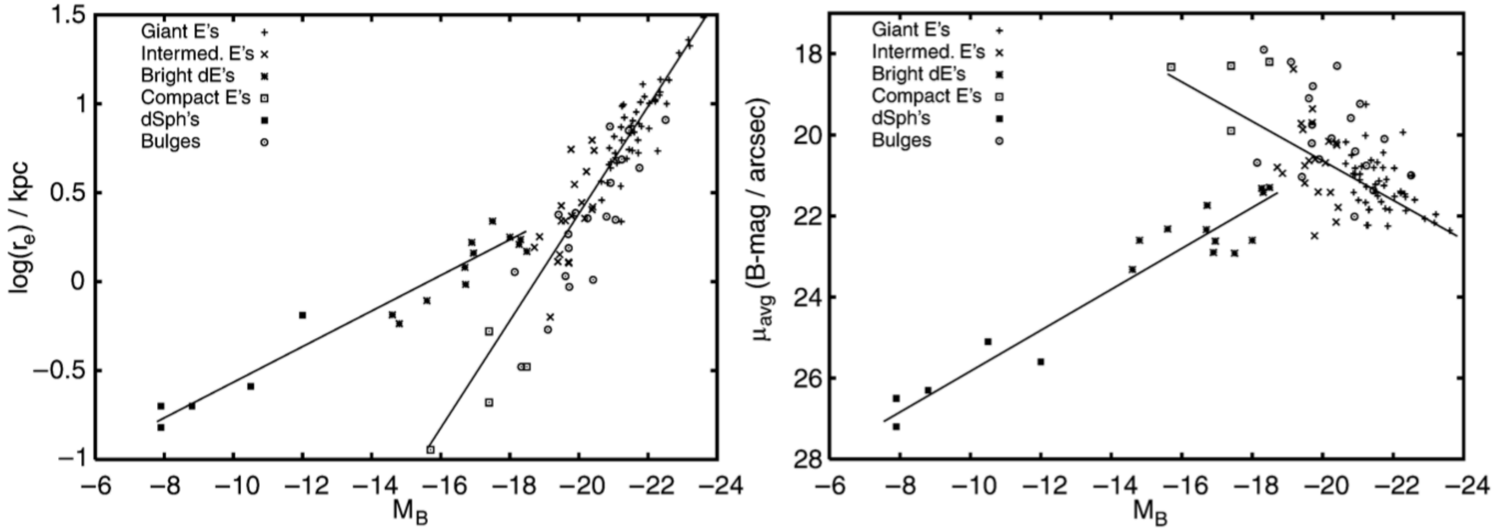

Fig. 3.7. Left panel: effective radius R_e versus absolute magnitude M_B; the correlation for normal ellipticals is different from that of dwarfs. Right panel: average surface brightness μ_{ave} versus M_B; for normal ellipticals, the surface brightness decreases with increasing luminosity while for dwarfs it increases

Projections of the Fundamental Plane

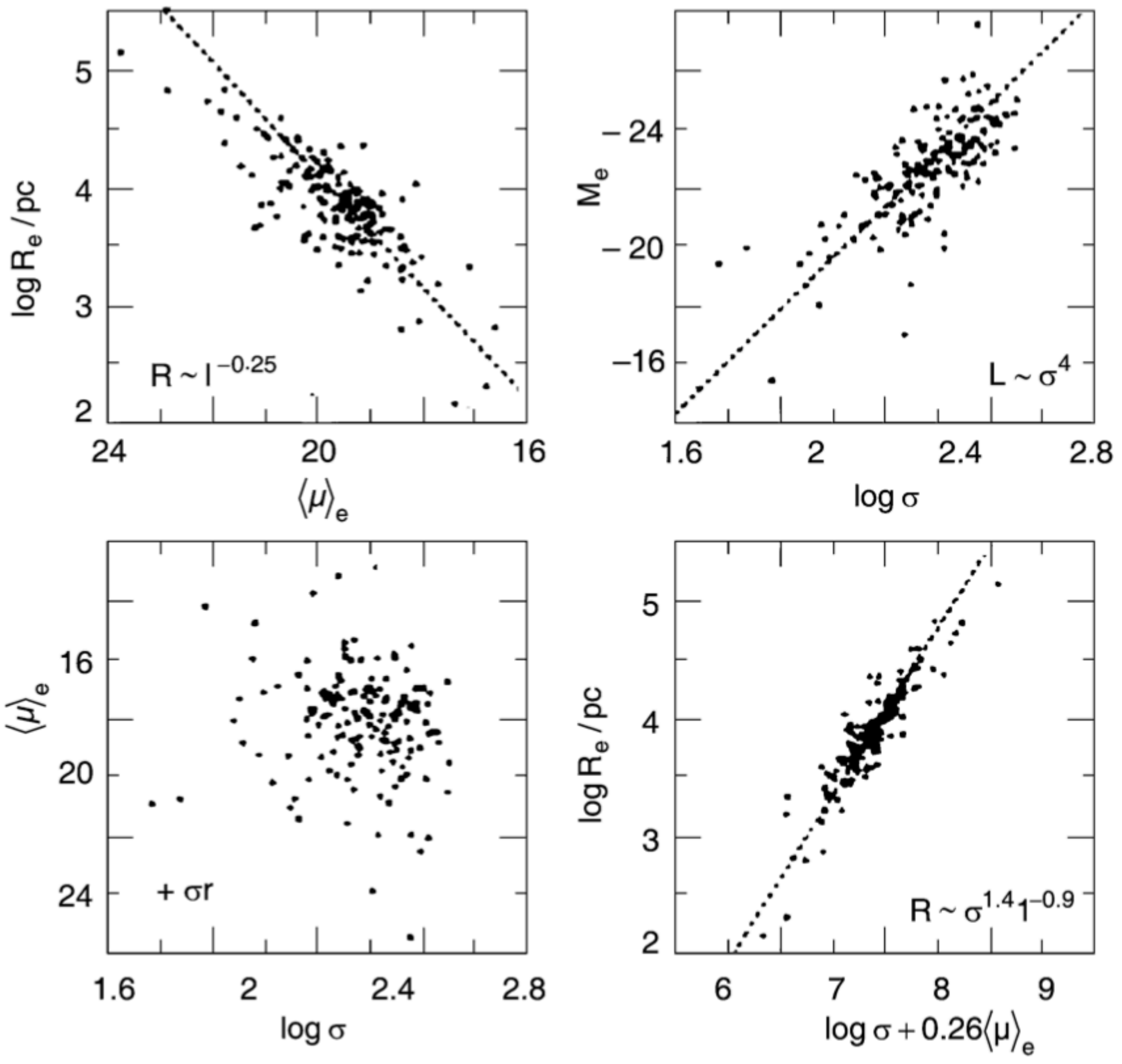

$$\log R_e = 0.34\,\langle\mu\rangle_e + 1.4\log\sigma_0 + \mathrm{const}$$

Fig. 3.23. Projections of the fundamental plane onto different two-parameter planes. Upper left: the relation between radius and mean surface brightness within the effective radius. Upper right: Faber–Jackson relation. Lower left: the relation between mean surface brightness and velocity dispersion shows the fundamental plane viewed from above. Lower right: the fundamental plane viewed from the side – the linear relation between radius and a combination of surface brightness and velocity dispersion

The Fundamental Plane

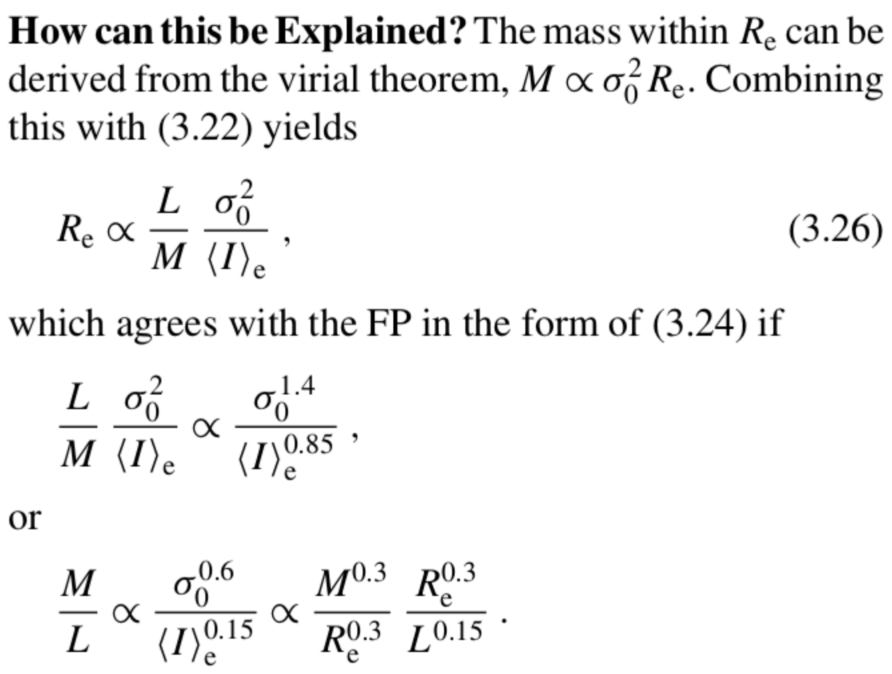

How can this be Explained? The mass within R_e can be derived from the virial theorem, $M \propto \sigma_0^2 R_\mathrm{e}$. Combining this with (3.22) yields

$$R_\mathrm{e} \propto \frac{L}{M} \frac{\sigma_0^2}{\langle I \rangle_\mathrm{e}} , \tag{3.26}$$

which agrees with the FP in the form of (3.24) if

$$\frac{L}{M} \frac{\sigma_0^2}{\langle I \rangle_\mathrm{e}} \propto \frac{\sigma_0^{1.4}}{\langle I \rangle_\mathrm{e}^{0.85}} ,$$

or

$$\frac{M}{L} \propto \frac{\sigma_0^{0.6}}{\langle I \rangle_\mathrm{e}^{0.15}} \propto \frac{M^{0.3}}{R_\mathrm{e}^{0.3}} \frac{R_\mathrm{e}^{0.3}}{L^{0.15}} .$$

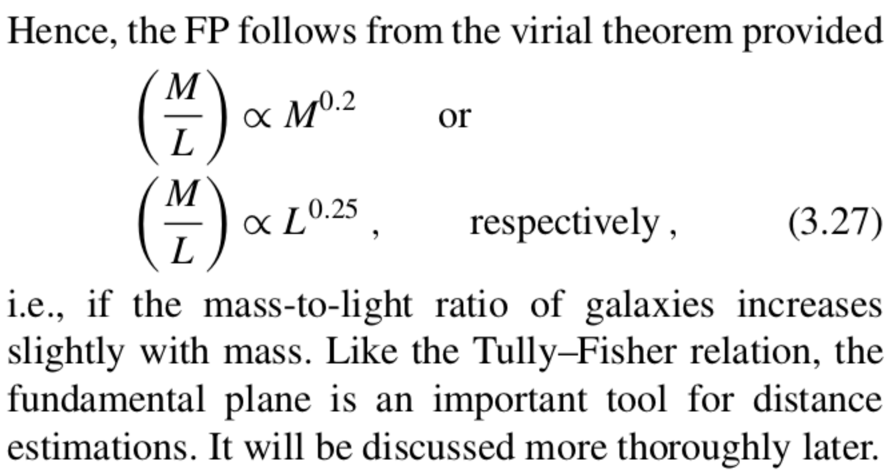

Hence, the FP follows from the virial theorem provided

$$\left(\frac{M}{L}\right) \propto M^{0.2} \qquad \text{or}$$
$$\left(\frac{M}{L}\right) \propto L^{0.25} , \qquad \text{respectively} , \tag{3.27}$$

i.e., if the mass-to-light ratio of galaxies increases slightly with mass. Like the Tully–Fisher relation, the fundamental plane is an important tool for distance estimations. It will be discussed more thoroughly later.

3.4.4 The D_n–σ Relation

Another scaling relation for ellipticals which is of substantial importance in practical applications is the D_n–σ relation. D_n is defined as that diameter of an ellipse within which the average surface brightness I_n corresponds to a value of 20.75 mag/arcsec^2 in the B-band. If we now assume that all ellipticals have a self-similar brightness profile, $I(R) = I_\mathrm{e}\, f(R/R_\mathrm{e})$, with $f(1) = 1$, then the luminosity within D_n can be written as

$$
\begin{aligned}
I_n \left(\frac{D_n}{2}\right)^2 \pi &= 2\pi I_\mathrm{e} \int_0^{D_n/2} \mathrm{d}R\; R\; f(R/R_\mathrm{e}) \\
&= 2\pi I_\mathrm{e} R_\mathrm{e}^2 \int_0^{D_n/(2R_\mathrm{e})} \mathrm{d}x\; x\; f(x)\,.
\end{aligned}
$$

For a de Vaucouleurs profile we have approximately $f(x) \propto x^{-1.2}$ in the relevant range of radius. Computing the integral with this expression, we obtain

$$D_n \propto R_\mathrm{e}\, I_\mathrm{e}^{0.8}\,. \tag{3.28}$$

Replacing R_e by the fundamental plane (3.24) then results in

$$D_n \propto \sigma_0^{1.4}\, \langle I \rangle_\mathrm{e}^{-0.85}\, I_\mathrm{e}^{0.8}\,.$$

Since $\langle I \rangle_\mathrm{e} \propto I_\mathrm{e}$ due to the assumed self-similar brightness profile, we finally find

$$\boxed{D_n \propto \sigma_0^{1.4}\, I_\mathrm{e}^{0.05}}\,. \tag{3.29}$$

This implies that D_n is nearly independent of I_e and only depends on σ_0. The D_n–σ relation (3.29) describes the properties of ellipticals considerably better than the Faber–Jackson relation and, in contrast to the fundamental plane, it is a relation between only two observables. Empirically, we find that ellipticals follow the normalized D_n–σ relation

$$\frac{D_n}{\mathrm{kpc}} = 2.05 \left(\frac{\sigma_0}{100\,\mathrm{km/s}}\right)^{1.33}\,, \tag{3.30}$$

and they scatter around this relation with a relative width of about 15%.

The World of Galaxies (2)

3.6 Extragalactic Distance Determination

In Sect. 2.2 we discussed methods for distance determination within our own Galaxy. We will now proceed with the determination of distances to other galaxies. It should be noted that the Hubble law (1.2) specifies a relation between the redshift of an extragalactic object and its distance. The redshift z is easily measured from the shift in spectral lines. For this reason, the Hubble law (and its generalization – see Sect. 4.3.3) provides a simple method for determining distance. However, to apply this law, the Hubble constant H_0 must first be known, i.e., the Hubble law must be calibrated. Therefore, in order to determine the Hubble constant, distances have to be measured independently from redshift.

Furthermore, it has to be kept in mind that besides the general cosmic expansion, which is expressed in the Hubble law, objects also show *peculiar motion*, like the velocities of galaxies in clusters of galaxies or the motion of the Magellanic Clouds around our Milky Way. These peculiar velocities are induced by gravitational acceleration resulting from the locally inhomogeneous mass distribution in the Universe. For instance, our Galaxy is moving towards the Virgo Cluster of galaxies, a dense accumulation of galaxies, due to the gravitational attraction caused by the cluster mass. The measured redshift, and therefore the Doppler shift, is always a superposition of the cosmic expansion velocity and peculiar velocities.

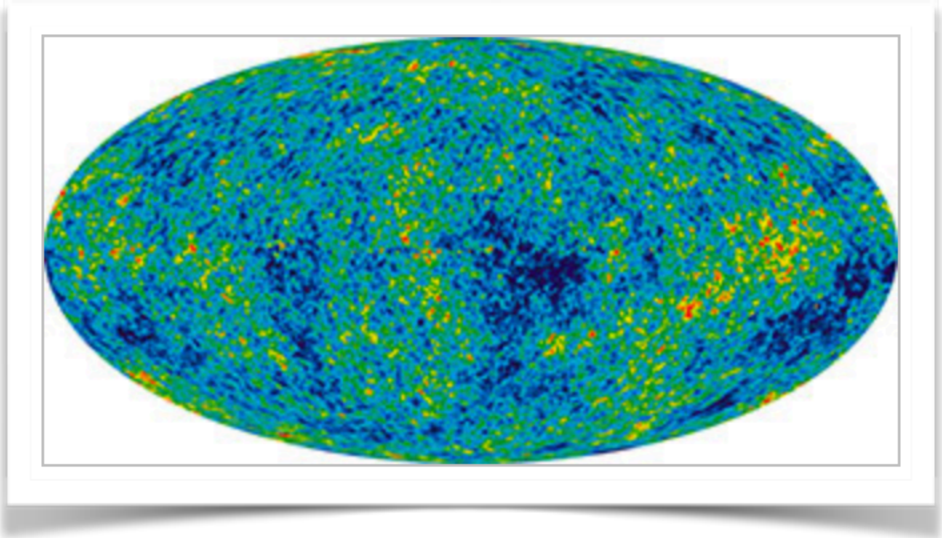

CMB Dipole Anisotropy. The peculiar velocity of the Galaxy is very precisely known. The radiation of the cosmic microwave background is not completely isotropic but instead shows a dipole component. This component originates in the velocity of the Solar System relative to the rest-frame in which the CMB appears isotropic (see Fig. 1.17). Due to the Doppler effect, the CMB appears hotter than average in the direction of our motion and cooler in the opposite direction. Analyzing this CMB dipole allows us to determine our peculiar velocity, which yields the result that the Sun moves at a velocity of $(368 \pm 2)\,\mathrm{km/s}$ relative to the CMB rest-frame. Furthermore, the Local Group of galaxies (see Sect. 6.1) is moving at $v_{\mathrm{LG}} \approx 600\,\mathrm{km/s}$ relative to the CMB rest-frame.

Hubble's law = Hubble expansion

$$\boxed{v = cz = H_0 D}$$

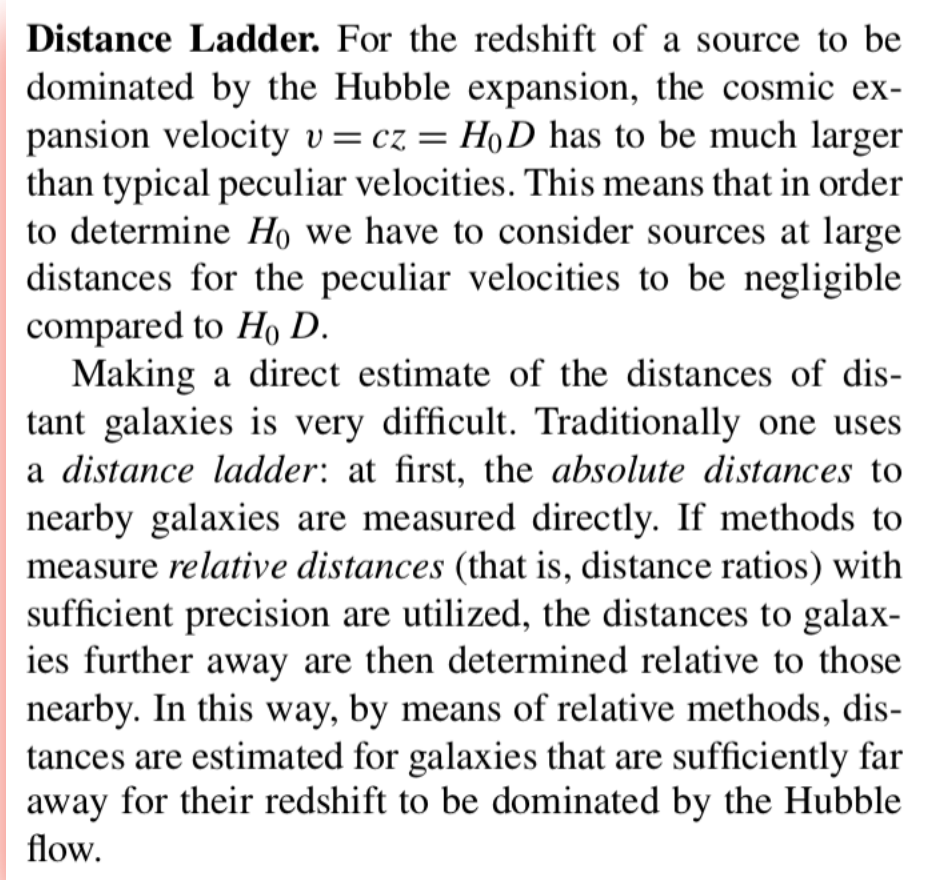

Distance Ladder. For the redshift of a source to be dominated by the Hubble expansion, the cosmic expansion velocity $v = cz = H_0 D$ has to be much larger than typical peculiar velocities. This means that in order to determine H_0 we have to consider sources at large distances for the peculiar velocities to be negligible compared to $H_0\,D$.

Making a direct estimate of the distances of distant galaxies is very difficult. Traditionally one uses a *distance ladder*: at first, the *absolute distances* to nearby galaxies are measured directly. If methods to measure *relative distances* (that is, distance ratios) with sufficient precision are utilized, the distances to galaxies further away are then determined relative to those nearby. In this way, by means of relative methods, distances are estimated for galaxies that are sufficiently far away for their redshift to be dominated by the Hubble flow.

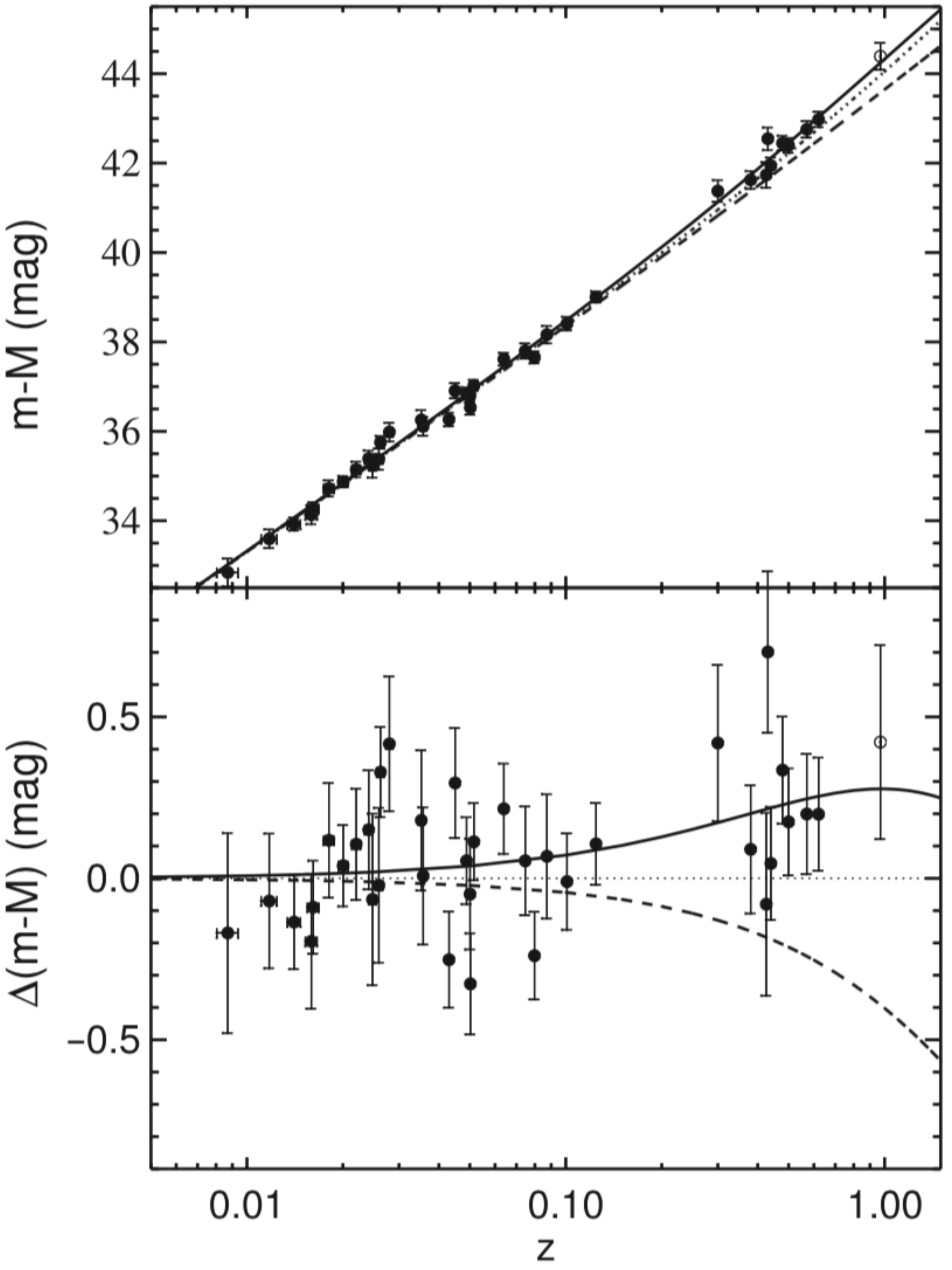

Fig. 3.3. The upper panel shows distance modulus, $(m - \mathscr{M}) = 5\log(d_\mathrm{L}/10\,\mathrm{pc})$, against redshift for Type Ia supernovae for which the light curve shape has been used to estimate their absolute magnitudes (data points). The predicted relations for three cosmological models are indicated by dashed ($\Omega_{\mathrm{m},0} = 1$, $\Omega_{\Lambda,0} = 0$), dotted ($\Omega_{\mathrm{m},0} = 0.2$, $\Omega_{\Lambda,0} = 0$) and solid ($\Omega_{\mathrm{m},0} = 0.28$, $\Omega_{\Lambda,0} = 0.72$) curves. The lower panel shows the difference between the distance modulus and the prediction for the ($\Omega_{\mathrm{m},0} = 0.2$, $\Omega_{\Lambda,0} = 0$) model. [Adapted from Riess et al. (1998) by permission of AAS]

3.6.1 Distance of the LMC

The distance of the Large Magellanic Cloud (LMC) can be estimated using various methods. For example, we can resolve and observe individual stars in the LMC, which forms the basis of the MACHO experiments (see Sect. 2.5.2). Because the metallicity of the LMC is significantly lower than that of the Milky Way, some of the methods discussed in Sect. 2.2 are only applicable after correcting for metallicity effects, e.g., the photometric distance determination or the period–luminosity relation for pulsating stars.

Perhaps the most precise method of determining the distance to the LMC is a purely geometrical one. The supernova SN 1987A that exploded in 1987 in the LMC illuminates a nearly perfectly elliptical ring (see Fig. 3.29). This ring consists of material that was once ejected by the stellar winds of the progenitor star of the supernova and that is now radiatively excited by energetic photons from the supernova explosion. The corresponding recombination radiation is thus emitted only when photons from the SN hit this gas. Because the observed ring is almost certainly intrinsically circular and the observed ellipticity is caused only by its inclination with respect to the line-of-sight, the distance to SN 1987A can be derived from observations of the ring. First, the inclination angle is determined from its observed ellipticity. The gas in the ring is excited by photons from the SN a time R/c after the original explosion, where R is the radius of the ring. We do not observe the illumination of the ring instantaneously because light from the section of the ring closer to us reaches us earlier than light from the more distant part. Thus, its illumination was seen sequentially along the ring. Combining the time delay in the illumination between the nearest and farthest part of the ring with its inclination angle, we then obtain the physical diameter of the ring. When this is compared to the measured angular diameter of $\sim 1''\!.7$, the ratio yields the distance to SN 1987A,

$$\boxed{D_{\rm SN1987A} \approx 51.8\,{\rm kpc} \pm 6\%}$$

If we now assume the extent of the LMC along the line-of-sight to be small, this distance can be identified with the distance to the LMC. The value is also compatible with other distance estimates (e.g., as derived by using photometric methods based on the properties of main-sequence stars – see Sect. 2.2.4).

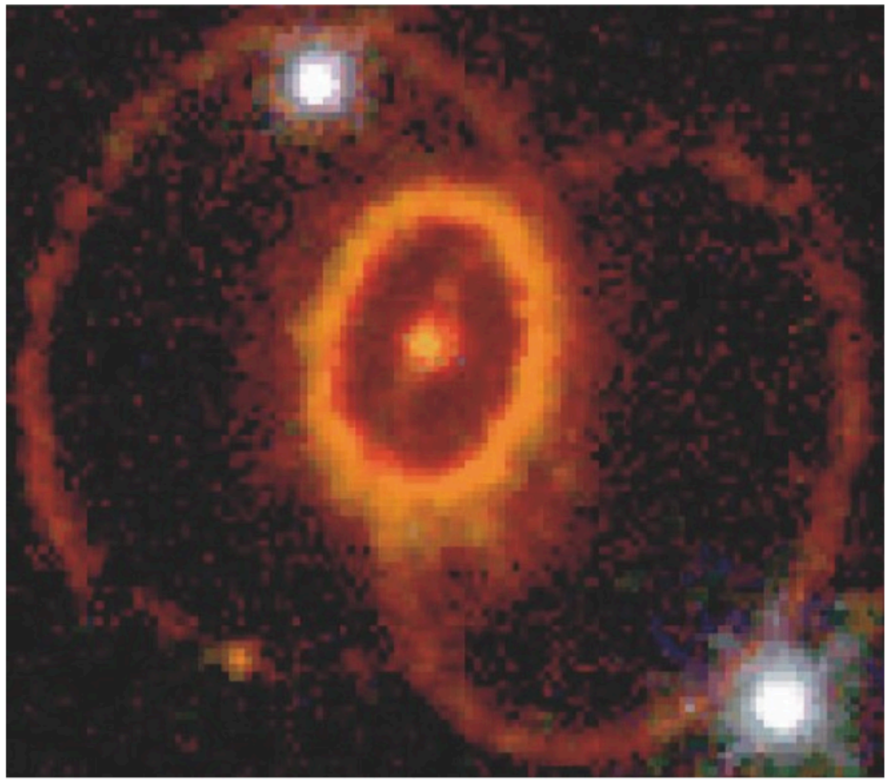

Fig. 3.29. The ring around supernova 1987A in the LMC is illuminated by photons from the explosion which induce the radiation from the gas in the ring. It is inclined towards the line-of-sight; thus it appears to be elliptical. Lighting up of the ring was not instantaneous, due to the finite speed of light: those sections of the ring closer to us lit up earlier than the more distant parts. From the time shift in the onset of radiation across the ring, its diameter can be derived. Combining this with the measured angular diameter of the ring, the distance to SN 1987A – and thus the distance to the LMC – can be determined

3.6.2 The Cepheid Distance

In Sect. 2.2.7, we discussed the period–luminosity relation of pulsating stars. Due to their high luminosity, Cepheids turn out to be particularly useful since they can be observed out to large distances.

For the period–luminosity relation of the Cepheids to be a good distance measure, it must first be calibrated. This calibration has to be done with as large a sample of Cepheids as possible at a known distance. Cepheids in the LMC are well-suited for this purpose because we believe we know the distance to the LMC quite precisely, see above. Also, due to the relatively small extent of the LMC along the line-of-sight, all Cepheids in the LMC should be located at approximately the same distance. For this reason, the period–luminosity relation is calibrated in the LMC. Due to the large number of Cepheids available for this purpose (many of them have been found in the microlensing surveys), the resulting statistical errors are small. Uncertainties remain in the form of systematic errors related to the metallicity dependence of the period–luminosity relation; however, these can be corrected for since the color of Cepheids depends on the metallicity as well.

With the high angular resolution of the HST, individual Cepheids in galaxies are visible at distances up to that of the Virgo cluster of galaxies. In fact, determining the distance to Virgo as a central step in the determination of the Hubble constant was one of the major scientific aims of the HST. In the *Hubble Key Project*, the distances to numerous spiral galaxies in the Virgo Cluster were determined by identifying Cepheids and measuring their periods.

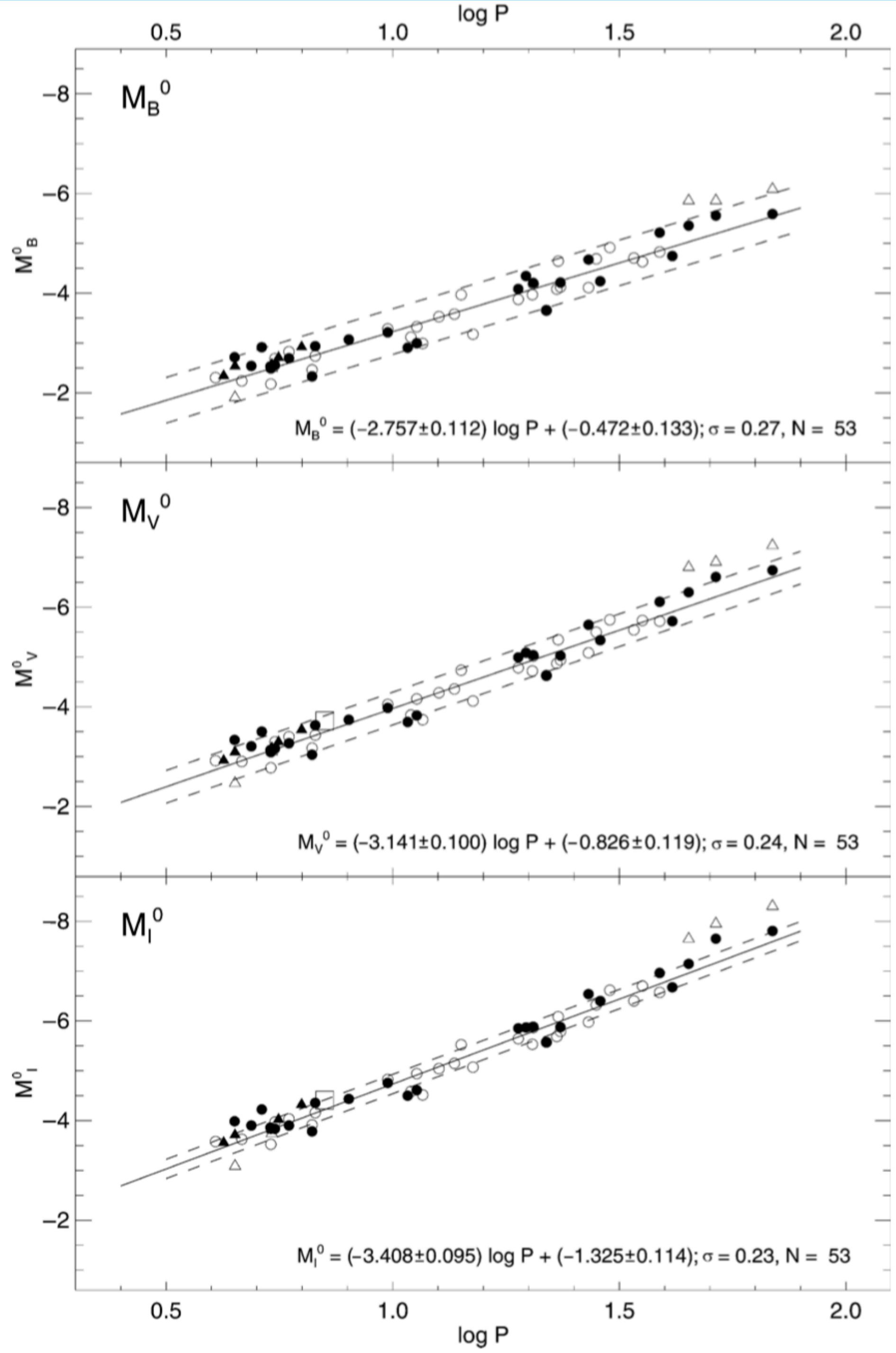

Fig. 2.9. Period–luminosity relation for Galactic Cepheids, measured in three different filters bands (B, V, and I, from top to bottom). The absolute magnitudes were corrected for extinction by using colors. The period is given in days. Open and solid circles denote data for those Cepheids for which distances were estimated using different methods; the three objects marked by triangles have a variable period and are discarded in the derivation of the period–luminosity relation. The latter is indicated by the solid line, with its parametrisation specified in the plots. The broken lines indicate the uncertainty range of the period–luminosity relation. The slope of the period–luminosity relation increases if one moves to redder filters

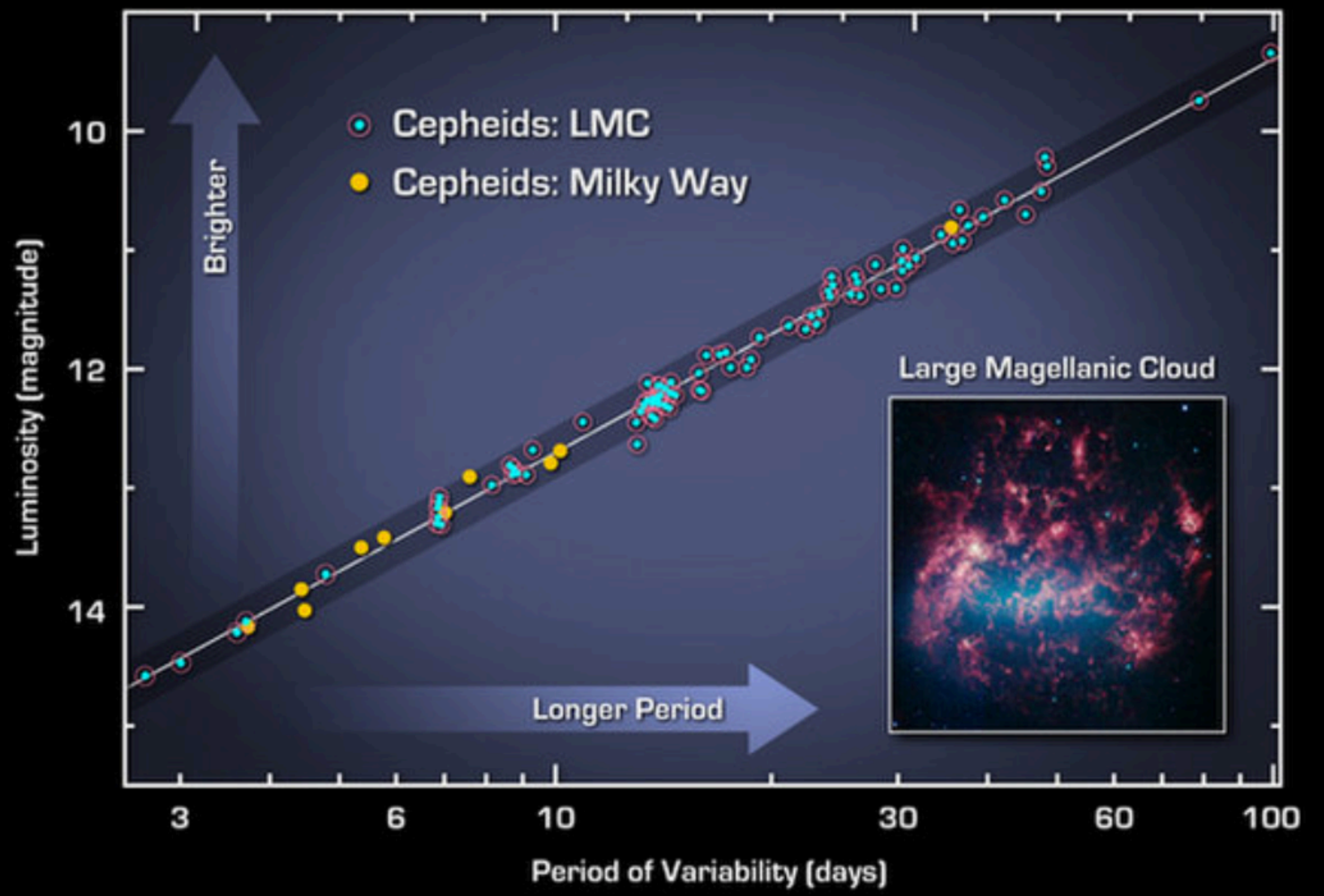

Calibrated Period-luminosity Relationship for Cepheids

Spitzer Space Telescope • IRAC

NASA / JPL-Caltech / W. Freedman (Carnegie)

ssc2012-13a

This graph illustrates the cepheid period-luminosity relationship, which establishes that if you know the period, or timing, of a cepheid star's pulses, you can determine its intrinsic brightness. By comparing intrinsic brightness to observed brightness, you can determine the star's distance, because it dims as it moves farther away. These distance measurements were used by the Spitzer telescope to measure the expansion rate of the universe more precisely than ever.

Credit: NASA/JPL-Caltech/Carnegie

3.6.3 Secondary Distance Indicators

The Virgo Cluster, at a measured distance of about 16 Mpc, is not sufficiently far away from us to directly determine the Hubble constant from its distance and redshift, because peculiar velocities still contribute considerably to the measured redshift at this distance. To get to larger distances, a number of relative distance indicators are used. They are all based on measuring the distance *ratio* of galaxies. If the distance to one of the two is known, the distance to the other is then obtained from the ratio. By this procedure, distances to more remote galaxies can be measured. Below, we will review some of the most important secondary distance indicators.

SN Ia. Supernovae of Type Ia are to good approximation standard candles, as will be discussed more thoroughly in Sect. 8.3.1. This means that the absolute magnitudes of SNe Ia are all within a very narrow range. To measure the value of this absolute magnitude, distances must be known for galaxies in which SN Ia explosions have been observed and accurately measured. Therefore, the Cepheid method was applied especially to such galaxies, in this way calibrating the brightness of SNe Ia. SNe Ia are visible over very large distances, so that they also permit distance estimates at such large redshifts that the simple Hubble law (1.6) is no longer valid, but needs to be generalized based on a cosmological model (Sect. 4.3.3). As we will see later, these measurements belong to the most important pillars on which our standard model of cosmology rests.

Surface Brightness Fluctuations of Galaxies. Another method of estimating distance ratios is surface brightness fluctuations. It is based on the fact that the number of bright stars per area element in a galaxy fluctuates – purely by Poisson noise: If N stars are expected in an area element, relative fluctuations of $\sqrt{N}/N = 1/\sqrt{N}$ of the number of stars will occur. These are observed in fluctuations of the local surface brightness. To demonstrate that this effect can be used to estimate distances, we consider a solid angle $\mathrm{d}\omega$. The corresponding area element $\mathrm{d}A = D^2\,\mathrm{d}\omega$ depends quadratically on the distance D of the galaxy; the larger the distance, the larger the number of stars N in this solid angle, and the smaller the relative fluctuations of the surface brightness. By comparing the surface brightness fluctuations of different galaxies, one can then estimate relative distances. This method also has to be calibrated on the galaxies for which Cepheid distances are available.

Scaling Relations. The scaling relations for galaxies – fundamental plane for ellipticals, Tully–Fisher relation for spirals (see Sect. 3.4) – can be calibrated on local groups of galaxies or on the Virgo Cluster, the distances of which have been determined from Cepheids. Although the scatter of these scaling relations can be 15% for individual galaxies, the statistical fluctuations are reduced when observing several galaxies at about the same distance (such as in clusters and groups). This enables us to estimate the distance ratio of two clusters of galaxies.

Planetary Nebulae. The brightness distribution of planetary nebulae in a galaxy seems to have an upper limit which is the nearly the same for each galaxy (see Fig. 3.30). If a sufficient number of planetary nebulae are observed and their brightnesses measured, it enables us to determine their luminosity function from which the maximum apparent magnitude is then derived. By calibration on galaxies of known Cepheid distance, the corresponding maximum absolute magnitude can be determined, which then allows the determination of the distance modulus for other galaxies, thus their distances.

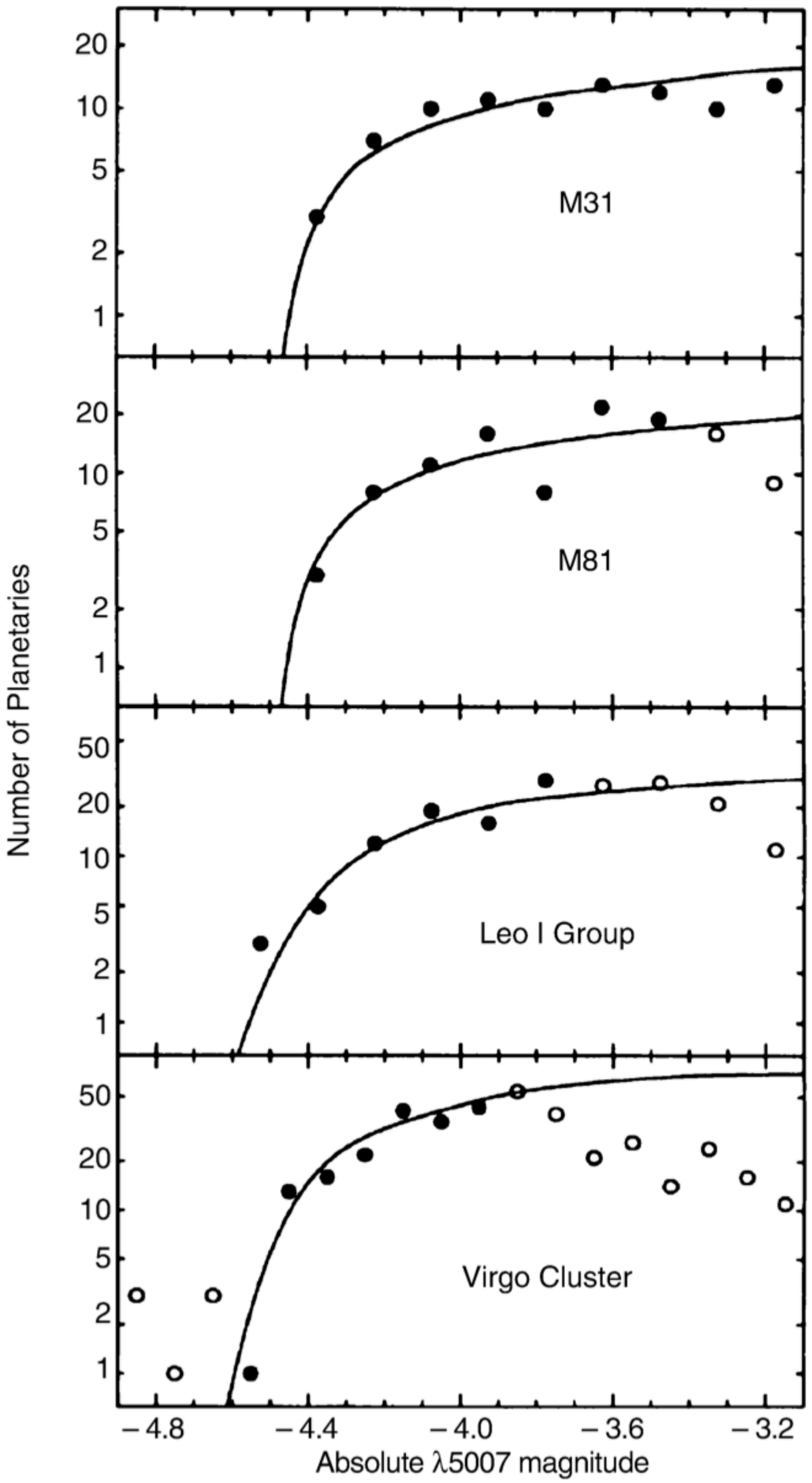

Fig. 3.30. Brightness distribution of planetary nebulae in Andromeda (M31), M81, three galaxies in the Leo I group, and six galaxies in the Virgo Cluster. The plotted absolute magnitude was measured in the emission line of double-ionized oxygen at $\lambda = 5007$ Å in which a large fraction of the luminosity of a planetary nebula is emitted. This characteristic property is also used in the identification of such objects in other galaxies. In all cases, the distribution is described by a nearly identical luminosity function; it seems to be a universal function in galaxies. Therefore, the brightness distribution of planetary nebulae can be used to estimate the distance of a galaxy. In the fits shown, the data points marked by open symbols were disregarded: at these magnitudes, the distribution function is probably not complete

The Hubble Constant. In particular, the ratio of distances to the Virgo and the Coma clusters of galaxies is estimated by means of these various secondary distance measures. Together with the distance to the Virgo Cluster as determined from Cepheids, we can then derive the distance to Coma. Its redshift ($z \approx 0.023$) is large enough for its peculiar velocity to make no significant contribution to its redshift, so that it is dominated by the Hubble expansion. By combining the various methods we obtain a distance to the Coma cluster of about 90 Mpc, resulting in a Hubble constant of

$$\boxed{H_0 = 72 \pm 8\,\mathrm{km/s/Mpc}}\,. \tag{3.36}$$

The error given here denotes the statistical uncertainty in the determination of H_0. Besides this uncertainty, possible systematic errors of the same order of magnitude may exist. In particular, the distance to the LMC plays a crucial role. As the lowest rung in the distance latter, it has an effect on all further distance estimates. We will see later (Sect. 8.7.1) that the Hubble constant can also be measured by a completely different method, based on tiny small-scale anisotropies of the cosmic microwave background, and that this method results in a value which is in impressively good agreement with the one in (3.36).

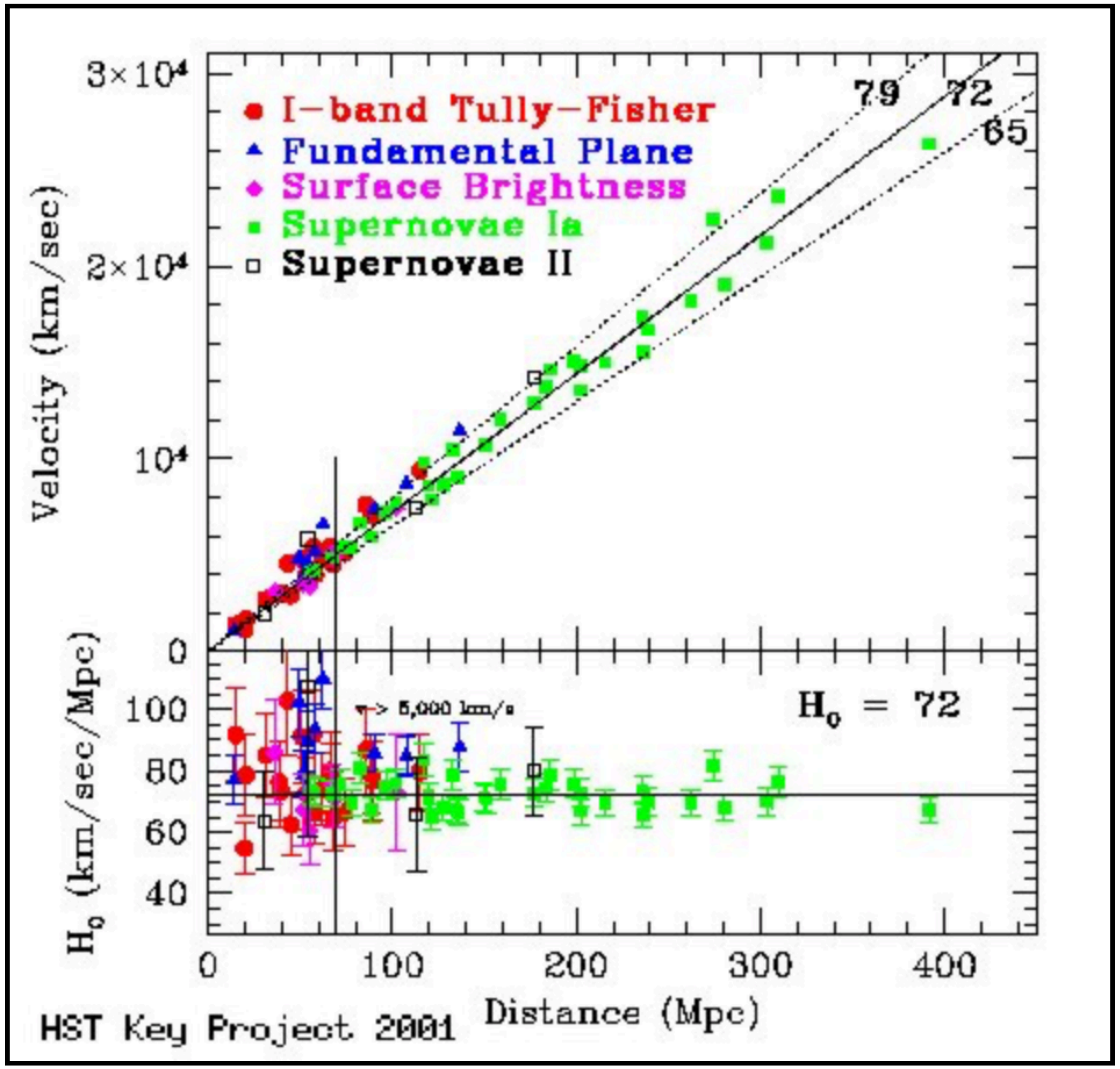

3.7 Luminosity Function of Galaxies

Definition of the Luminosity Function. The luminosity function specifies the way in which the members of a class of objects are distributed with respect to their luminosity. More precisely, the luminosity function is the number density of objects (here galaxies) of a specific luminosity. $\Phi(M)\,\mathrm{d}M$ is defined as the number density of galaxies with absolute magnitude in the interval $[M, M+\mathrm{d}M]$. The total density of galaxies is then

$$\nu = \int_{-\infty}^{\infty} \mathrm{d}M\ \Phi(M)\ . \tag{3.37}$$

Accordingly, $\Phi(L)\,\mathrm{d}L$ is defined as the number density of galaxies with a luminosity between L and $L+\mathrm{d}L$. It should be noted here explicitly that both definitions of the luminosity function are denoted by the same symbol, although they represent different mathematical functions, i.e., they describe different functional relations. It is therefore important (and in most cases not difficult) to deduce from the context which of these two functions is being referred to.

Problems in Determining the Luminosity Function. At first sight, the task of determining the luminosity function of galaxies does not seem very difficult. The history of this topic shows, however, that we encounter a number of problems in practice. As a first step, the determination of galaxy luminosities is required, for which, besides measuring the flux, distance estimates are also necessary. For very distant galaxies redshift is a sufficiently reliable measure of distance, whereas for nearby galaxies the methods discussed in Sect. 3.6 have to be applied.

Another problem occurs for nearby galaxies, namely the large-scale structure of the galaxy distribution. To obtain a representative sample of galaxies, a sufficiently large volume has to be surveyed because the galaxy distribution is heavily structured on scales of $\sim 100\,h^{-1}$ Mpc. On the other hand, galaxies of particularly low luminosity can only be observed locally, so the determination of $\Phi(L)$ for small L always needs to refer to local galaxies. Finally, one has to deal with the so-called *Malmquist bias*; in a flux-limited sample luminous galaxies will always be overrepresented because they are visible at larger distances (and therefore are selected from a larger volume). A correction for this effect is always necessary.

3.7.1 The Schechter Luminosity Function

The global galaxy distribution is well approximated by the *Schechter luminosity function*

$$\boxed{\Phi(L) = \left(\frac{\Phi^*}{L^*}\right)\left(\frac{L}{L^*}\right)^{\alpha} \exp\left(-L/L^*\right)} , \qquad (3.38)$$

where L^* is a characteristic luminosity above which the distribution decreases exponentially, α is the slope of the luminosity function for small L, and Φ^* specifies the normalization of the distribution. A schematic plot of this function is shown in Fig. 3.31.

Expressed in magnitudes, this function appears much more complicated. Considering that an interval $\mathrm{d}L$ in luminosity corresponds to an interval $\mathrm{d}M$ in absolute magnitude, with $\mathrm{d}L/L = -0.4 \ln 10\,\mathrm{d}M$, and using $\Phi(L)\,\mathrm{d}L = \Phi(M)\,\mathrm{d}M$, i.e., the number of sources in these intervals are of course the same, we obtain

$$\Phi(M) = \Phi(L)\left|\frac{\mathrm{d}L}{\mathrm{d}M}\right| = \Phi(L)\,0.4 \ln 10\, L \qquad (3.39)$$

$$= (0.4 \ln 10)\Phi^* 10^{0.4(\alpha+1)(M^*-M)} \times \exp\left(-10^{0.4(M^*-M)}\right) . \qquad (3.40)$$

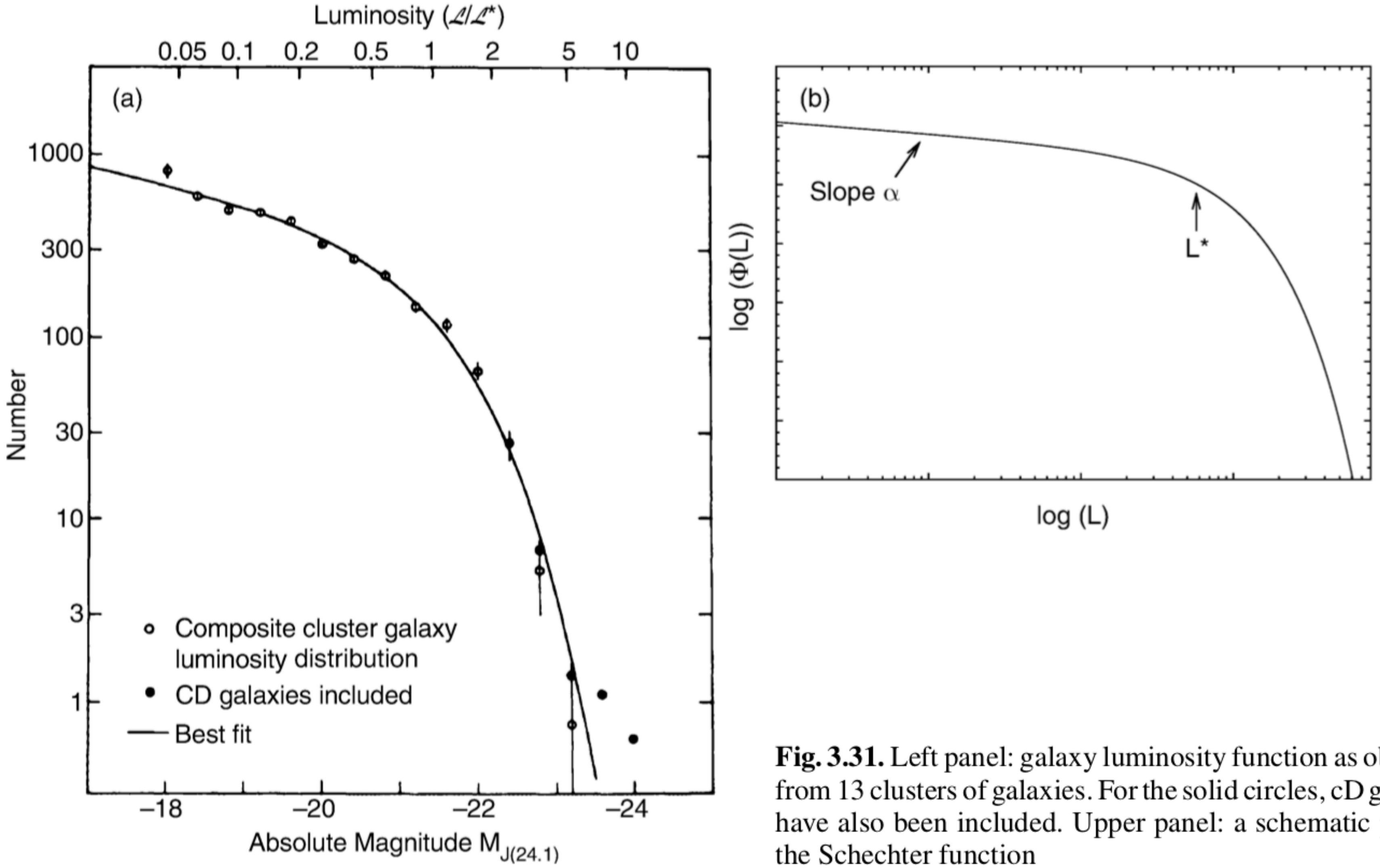

Fig. 3.31. Left panel: galaxy luminosity function as obtained from 13 clusters of galaxies. For the solid circles, cD galaxies have also been included. Upper panel: a schematic plot of the Schechter function

As mentioned above, the determination of the parameters entering the Schechter function is difficult; a set of parameters in the blue band is

$$\begin{aligned} \Phi^* &= 1.6 \times 10^{-2}\, h^3\, \mathrm{Mpc}^{-3}\,, \\ M_B^* &= -19.7 + 5 \log h\,, \qquad \text{or} \\ L_B^* &= 1.2 \times 10^{10}\, h^{-2}\, L_\odot\,, \\ \alpha &= -1.07\,. \end{aligned} \tag{3.41}$$

While the blue light of galaxies is strongly affected by star formation, the luminosity function in the red bands measures the typical stellar distribution. In the K-band, we have

$$\begin{aligned} \Phi^* &= 1.6 \times 10^{-2}\, h^3\, \mathrm{Mpc}^{-3}\,, \\ M_K^* &= -23.1 + 5 \log h\,, \\ \alpha &= -0.9\,. \end{aligned} \tag{3.42}$$

The total number density of galaxies is formally infinite if $\alpha \leq -1$, but the validity of the Schechter function does of course not extend to arbitrarily small L. The luminosity density

$$l_{\mathrm{tot}} = \int_0^\infty \mathrm{d}L\; L\, \Phi(L) = \Phi^*\, L^*\, \Gamma(2+\alpha) \tag{3.43}$$

is finite for $\alpha \geq -2$.[6] The integral in (3.43), for $\alpha \sim -1$, is dominated by $L \sim L^*$, and $n = \Phi^*$ is thus a good estimate for the mean density of L^*-galaxies.

---

[6] $\Gamma(x)$ is the Gamma function, defined by

$$\Gamma(x) = \int_0^\infty \mathrm{d}y\; y^{(x-1)}\, \mathrm{e}^{-y}\,. \tag{3.44}$$

For positive integers, $\Gamma(n+1) = n!$. We have $\Gamma(0.7) \approx 1.30$, $\Gamma(1) = 1$, $\Gamma(1.3) \approx 0.90$. Since these values are all close to unity, $l_{\mathrm{tot}} \sim \Phi^* L^*$ is a good approximation for the luminosity density.

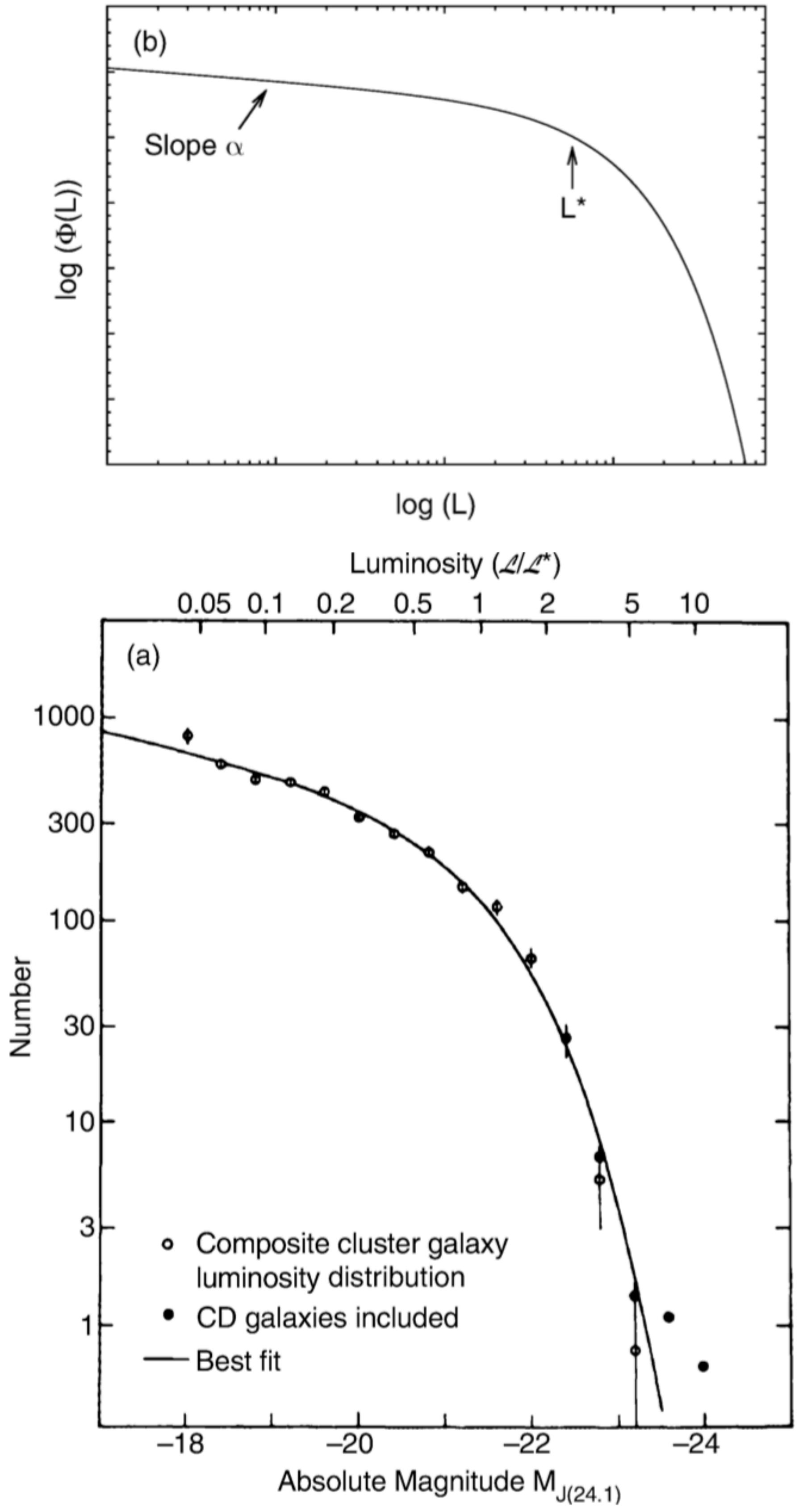

Fig. 3.31. Left panel: galaxy luminosity function as obtained from 13 clusters of galaxies. For the solid circles, cD galaxies have also been included. Upper panel: a schematic plot of the Schechter function

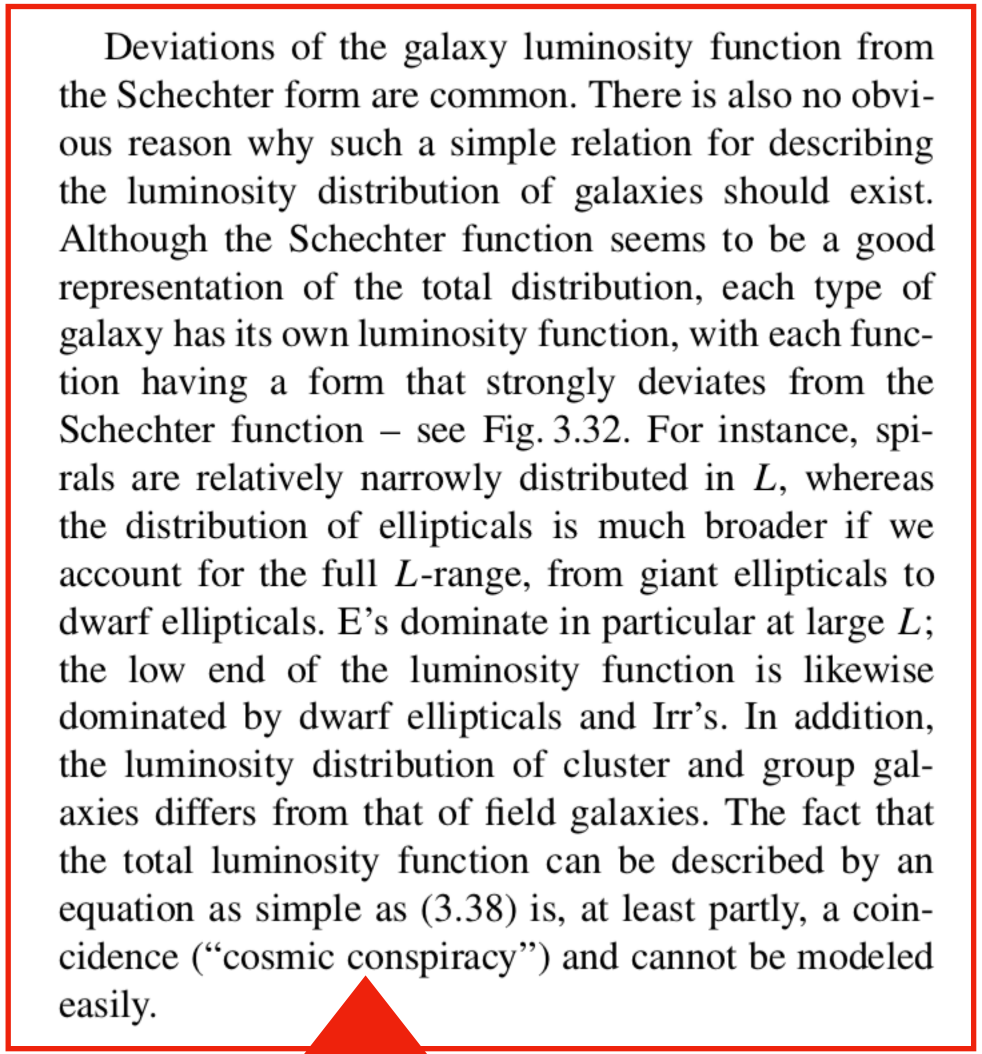

Deviations of the galaxy luminosity function from the Schechter form are common. There is also no obvious reason why such a simple relation for describing the luminosity distribution of galaxies should exist. Although the Schechter function seems to be a good representation of the total distribution, each type of galaxy has its own luminosity function, with each function having a form that strongly deviates from the Schechter function – see Fig. 3.32. For instance, spirals are relatively narrowly distributed in L, whereas the distribution of ellipticals is much broader if we account for the full L-range, from giant ellipticals to dwarf ellipticals. E's dominate in particular at large L; the low end of the luminosity function is likewise dominated by dwarf ellipticals and Irr's. In addition, the luminosity distribution of cluster and group galaxies differs from that of field galaxies. The fact that the total luminosity function can be described by an equation as simple as (3.38) is, at least partly, a coincidence ("cosmic conspiracy") and cannot be modeled easily.

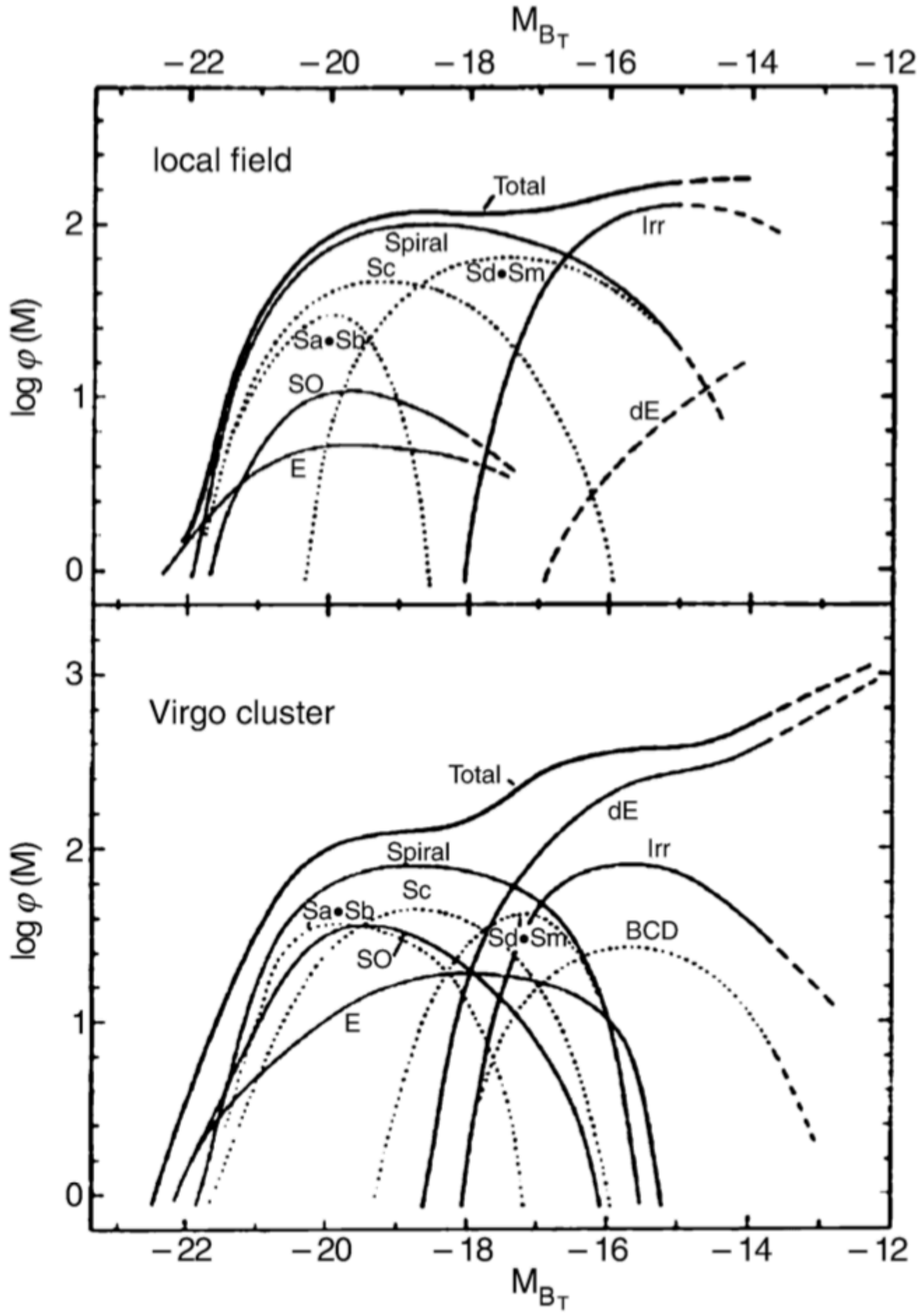

Fig. 3.32. The luminosity function for different Hubble types of field galaxies (top) and galaxies in the Virgo Cluster of galaxies (bottom). Dashed curves denote extrapolations. In contrast to Fig. 3.31, the more luminous galaxies are plotted towards the left. The Schechter luminosity function of the total galaxy distribution is compiled from the sum of the luminosity distributions of individual galaxy types that all deviate significantly from the Schechter function. One can see that in clusters the major contribution at faint magnitudes comes from the dwarf ellipticals (dEs), and that at the bright end ellipticals and S0's contribute much more strongly to the luminosity function than they do in the field. This trend is even more prominent in regular clusters of galaxies

3.7.2 The Bimodal Color Distribution of Galaxies

The classification of galaxies by morphology, given by the Hubble classification scheme (Fig. 3.2), has the disadvantage that morphologies of galaxies are not easy to quantify. Traditionally, this was done by visual inspection but of course this method bears some subjectivity of the researcher doing it. Furthermore, this visual inspection is time consuming and cannot be performed on large samples of galaxies. Various techniques were developed to perform such a classification automatically, including brightness profile fitting – a de Vaucouleurs profile indicates an elliptical galaxy whereas an exponential brightness profile corresponds to a spiral.

Even these methods cannot be applied to galaxy samples for which the angular resolution of the imaging is not much better than the angular size of galaxies – since then, no brightness profiles can be fitted. An alternative to classify galaxies is provided by their color. We expect that early-type galaxies are red, whereas late-type galaxies are considerably bluer. Colors are much easier to measure than morphology, in particular for very small galaxies. Therefore, one can study the luminosity function of galaxies, classifying them by their color.

Using photometric measurements and spectroscopy from the Sloan Digital Sky Survey (see Sect. 8.1.2), the colors and absolute magnitudes of $\sim 70\,000$ low-redshift galaxies has been studied; their density distribution in a color–magnitude diagram are plotted in the left-hand side of Fig. 3.33. From this figure we see immediately that there are two density peaks of the galaxy distribution in this diagram: one at high luminosities and red color, the other at significantly fainter absolute magnitudes and much bluer color. It appears that the galaxies are distributed at and around these two density peaks, hence galaxies tend to be either luminous and red, or less luminous and blue. We can also easily see from this diagram that the luminosity function of red galaxies is quite different from that of blue galaxies, which is another indication for the fact that the simple Schechter luminosity function (3.38) for the whole galaxy population most likely is a coincidence.

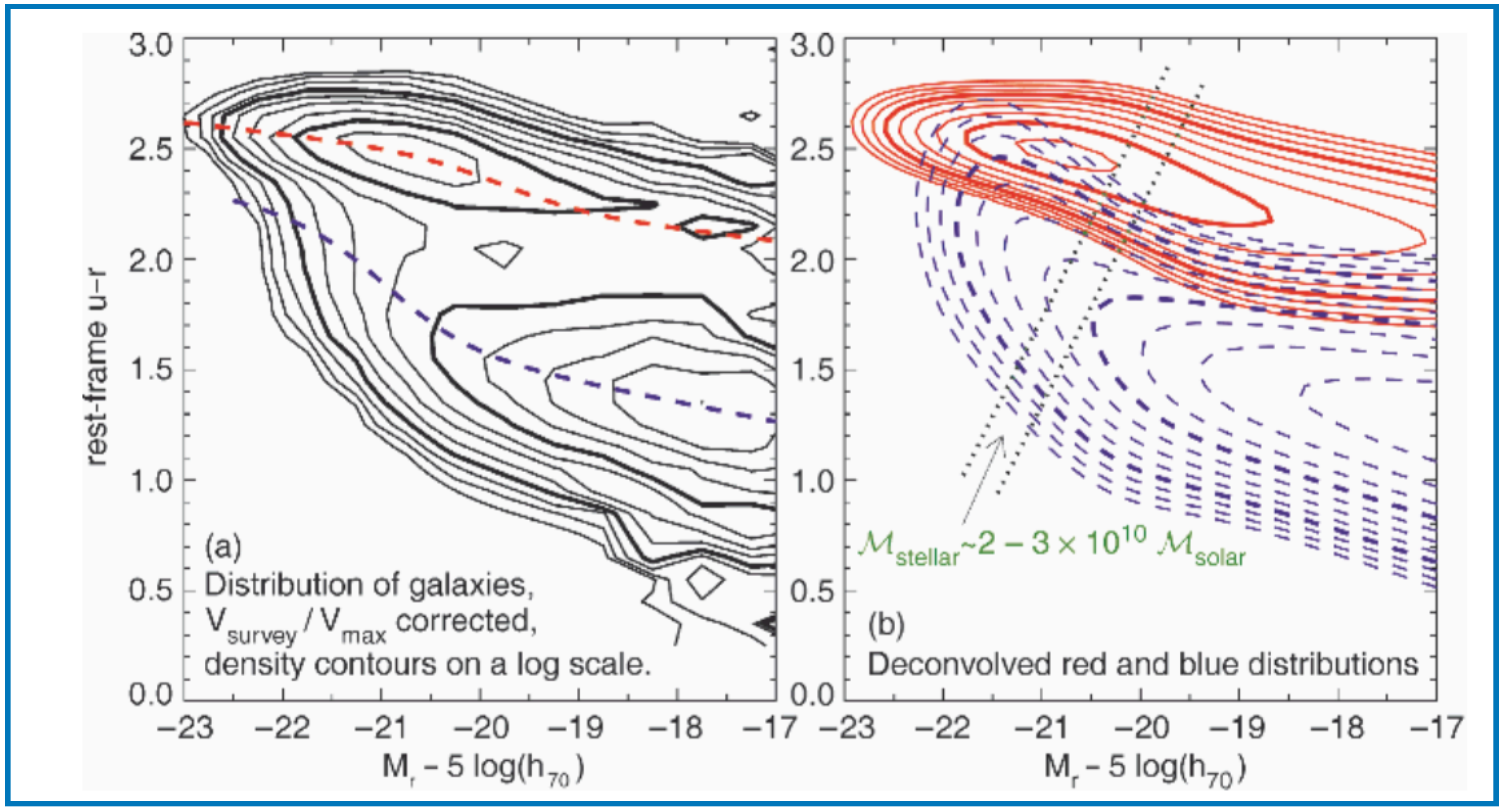

Fig. 3.33. The density of galaxies in color–magnitude space. The color of $\sim 70\,000$ galaxies with redshifts $0.01 \leq z \leq 0.08$ from the Sloan Digital Sky Survey is measured by the rest-frame $u-r$, i.e., after a (small) correction for their redshift was applied. The density contours, which were corrected for selection effects like the Malmquist bias, are logarithmically spaced, with a factor of $\sqrt{2}$ between consecutive contours. In the left-hand panel, the measured distribution is shown. Obviously, two peaks of the galaxy density are clearly visible, one at a red color of $u-r \sim 2.5$ and an absolute magnitude of $M_r \sim -21$, the other at a bluer color of $u-r \sim 1.3$ and significantly fainter magnitudes. The right-hand panel corresponds to the modeled galaxy density, as is described in the text

We can next consider the color distribution of galaxies at a fixed absolute magnitude M_r. This is obtained by plotting the galaxy number density along vertical cuts through the left-hand side of Fig. 3.33. When this is done for different M_r, it turns out that the color distribution of galaxies is bimodal: over a broad range in absolute magnitude, the color distribution has two peaks, one at red, the other at blue $u-r$. Again, this fact can be seen directly from Fig. 3.33. For each value of M_r, the color distribution of galaxies can be very well fitted by the sum of two Gaussian functions. The central colors of the two Gaussians is shown by the two dashed curves in the left panel of Fig. 3.33. They become redder the more luminous the galaxies are. This luminosity-dependent reddening is considerably more pronounced for the blue population than for the red galaxies.

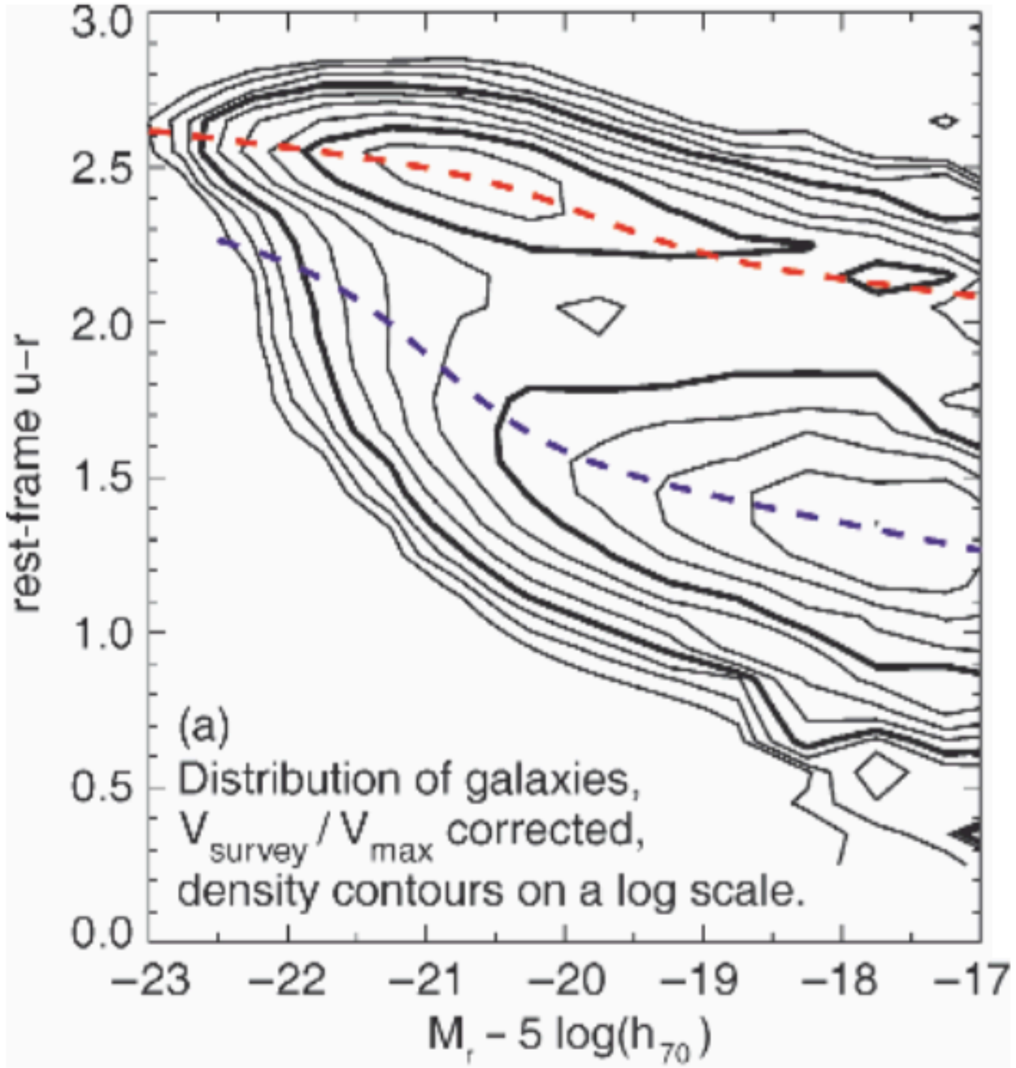

To see how good this fit indeed is, the right-hand side of Fig. 3.33 shows the galaxy density as obtained from the two-Gaussian fits, with solid contours corresponding to the red galaxies and dashed contours to the blue ones. We thus conclude that the local galaxy population can be described as a bimodal distribution in $u-r$ color, where the characteristic color depends slightly on absolute magnitude. The galaxy distribution at bright absolute magnitudes is dominated by red galaxies, whereas for less luminous galaxies the blue population dominates. The luminosity function of both populations can be described by Schechter functions; however these two are quite different. The characteristic luminosity is about one magnitude brighter for the red galaxies than for the blue ones, whereas the faint-end slope α is significantly steeper for the blue galaxies. This again is in agreement of what we just learned: for high luminosities, the red galaxies clearly dominate, whereas at small luminosities, the blue galaxies are much more abundant.

The mass-to-light ratio of a red stellar population is larger than that of a blue population, since the former no longer contains massive luminous stars. The difference in the peak absolute magnitude between the red and blue galaxies therefore corresponds to an even larger difference in the stellar mass of these two populations. Red galaxies in the local Universe have on average a much higher stellar mass than blue galaxies. This fact is illustrated by the two dotted lines in the right-hand panel of Fig. 3.33 which correspond to lines of constant stellar mass of ~ 2–$3 \times 10^{10}\,M_\odot$. This seems to indicate a very characteristic mass scale for the galaxy distribution: most galaxies with a stellar mass larger than this characteristic mass scale are red, whereas most of those with a lower stellar mass are blue.

Obviously, these statistical properties of the galaxy distribution must have an explanation in terms of the evolution of galaxies; we will come back to this issue in Chap. 9.

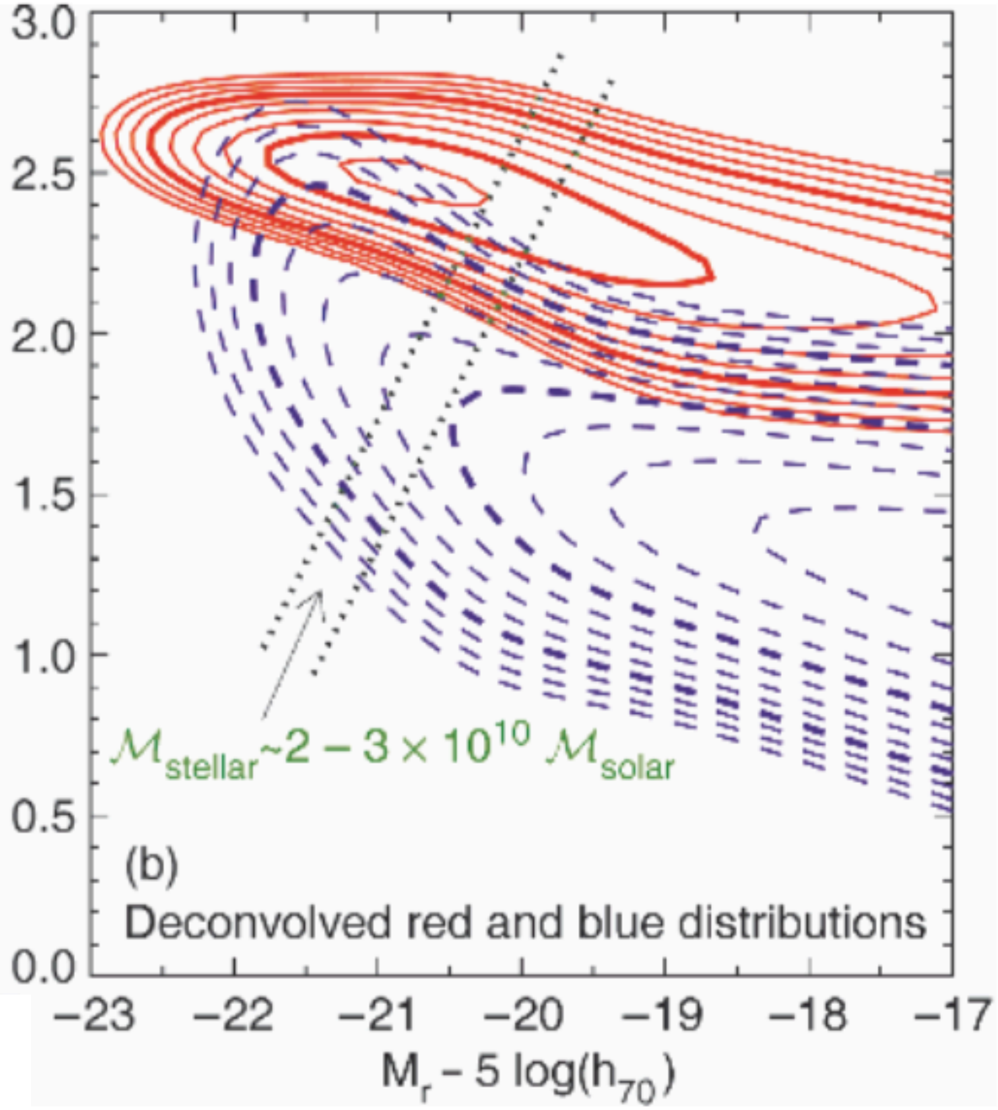

Stellar Population Synthesis

What is stellar population synthesis?

How does it work?

How do we use it?

The visible universe

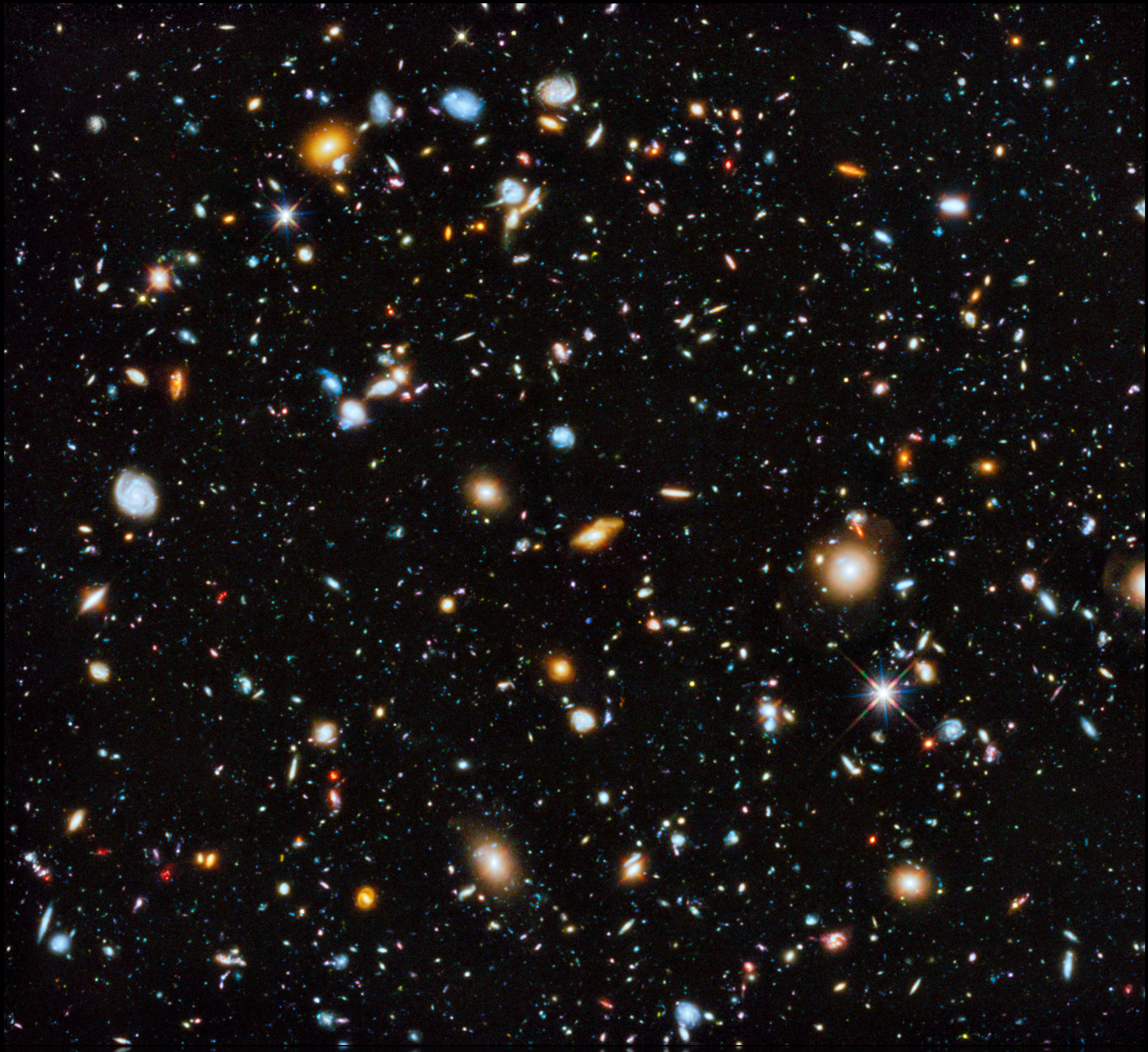

Stellar population synthesis (SPS) is a tool to interpret the visible universe

HST

How does SPS work?

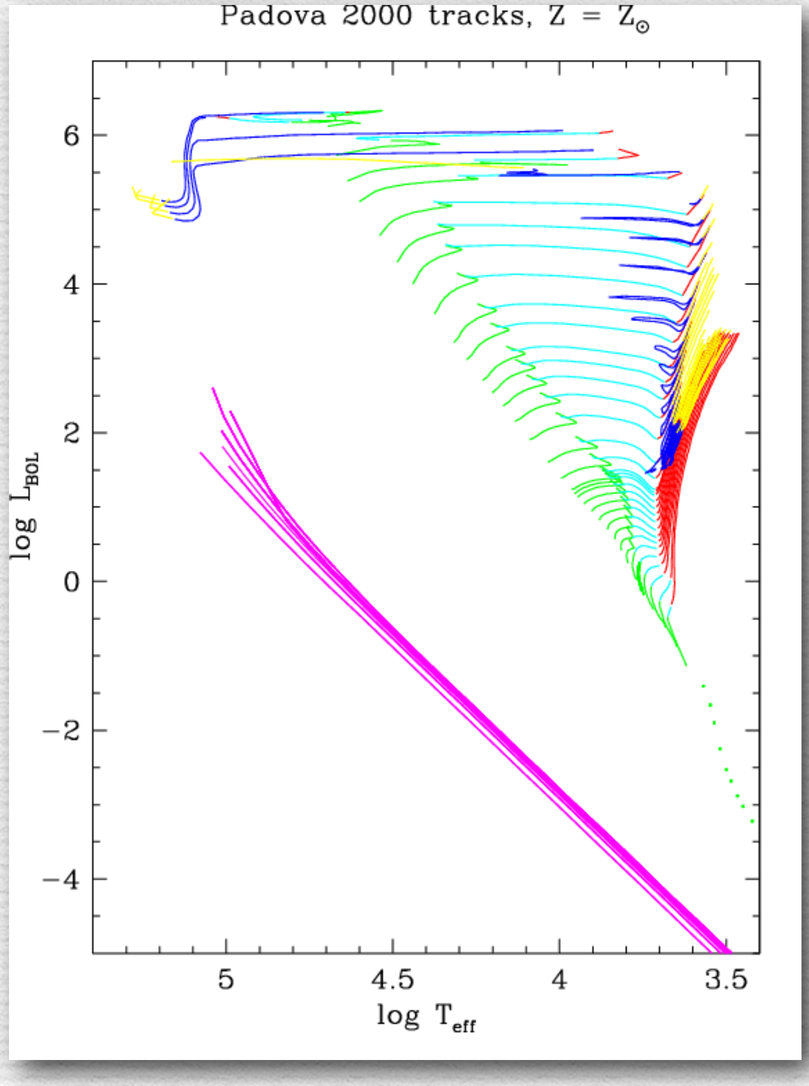

+

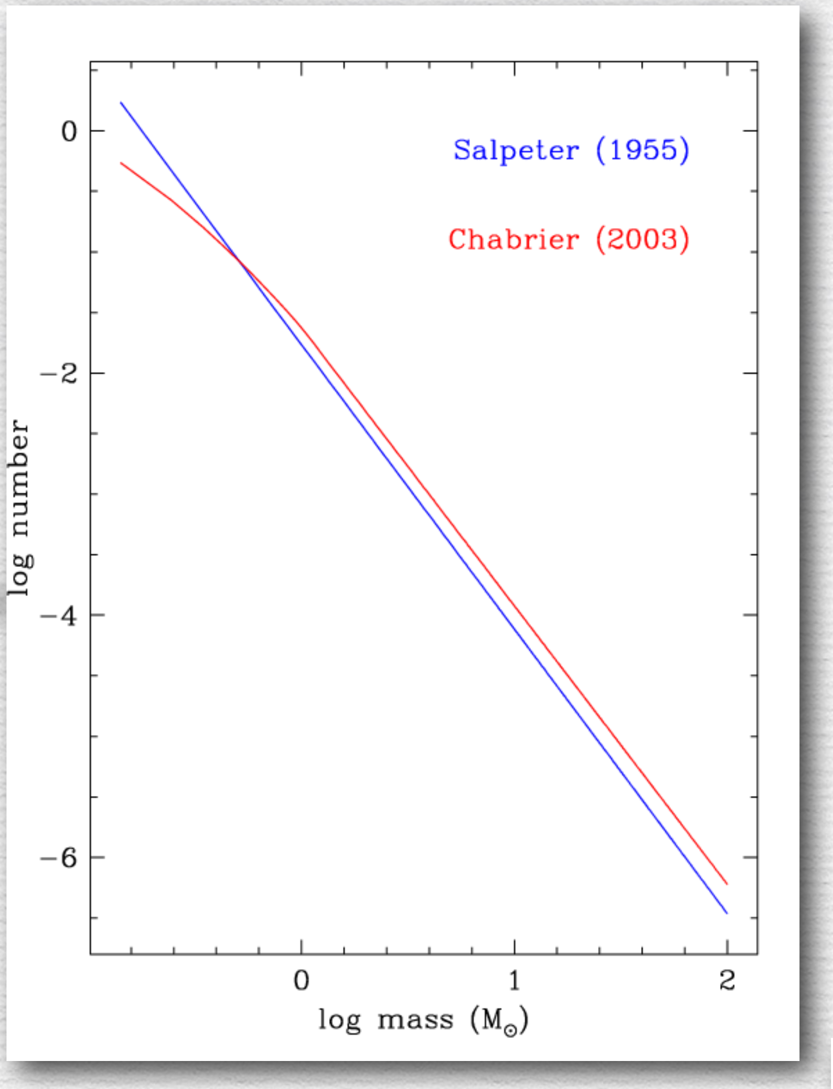

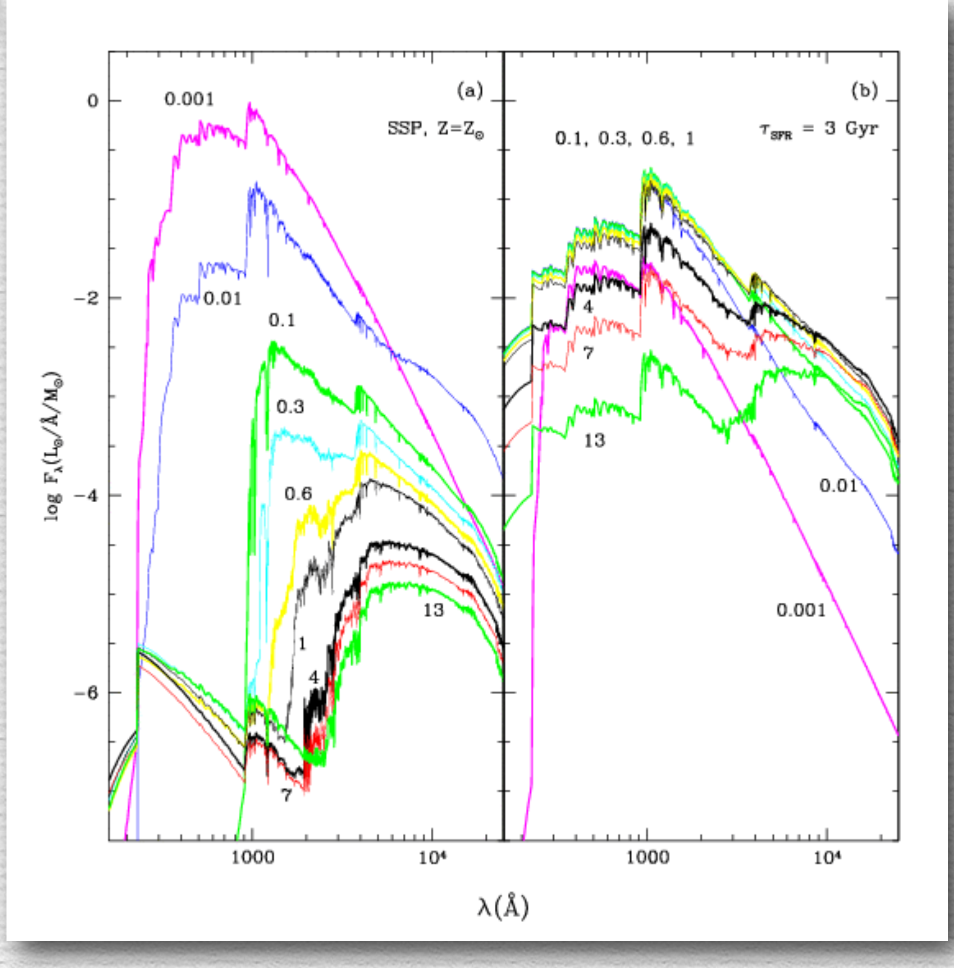

Algebra of stellar population synthesis

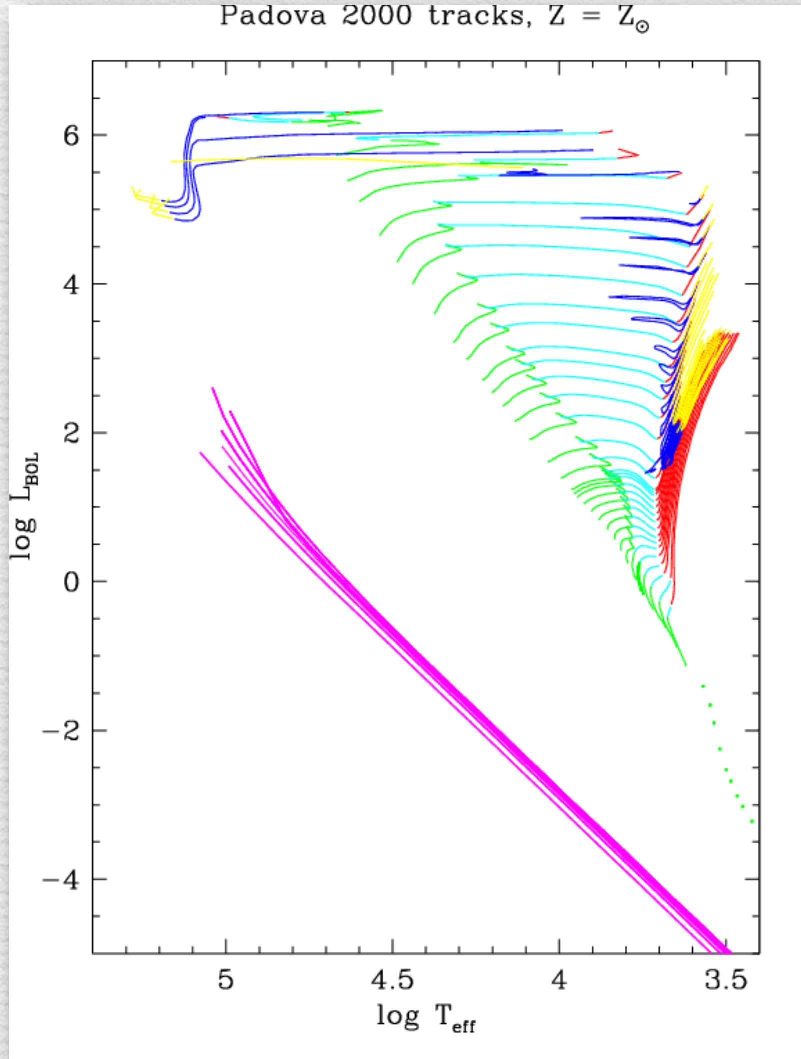

+

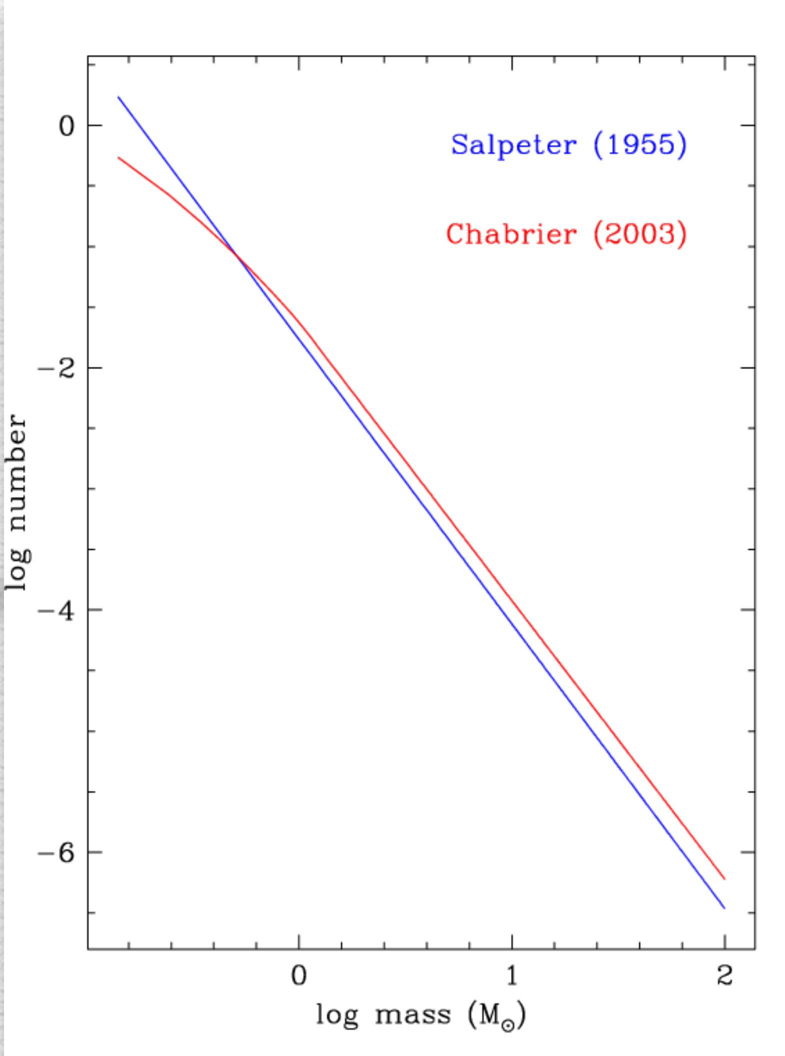

+ spectral atlas =

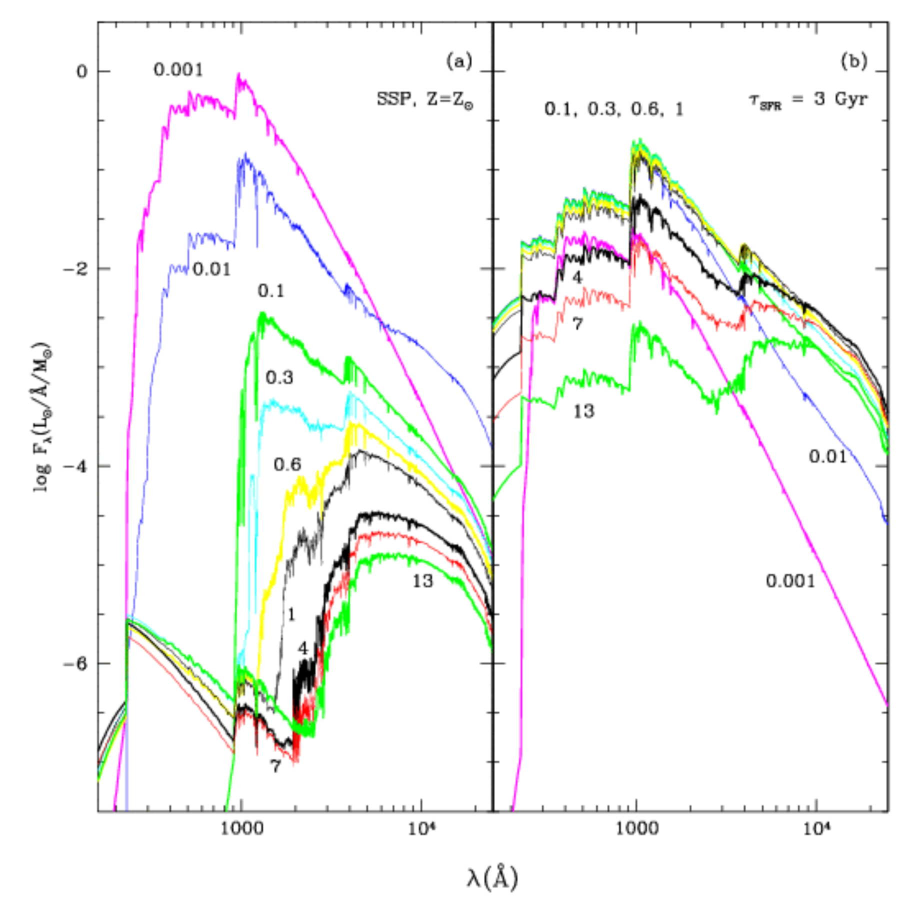

Stellar Evolutionary Tracks

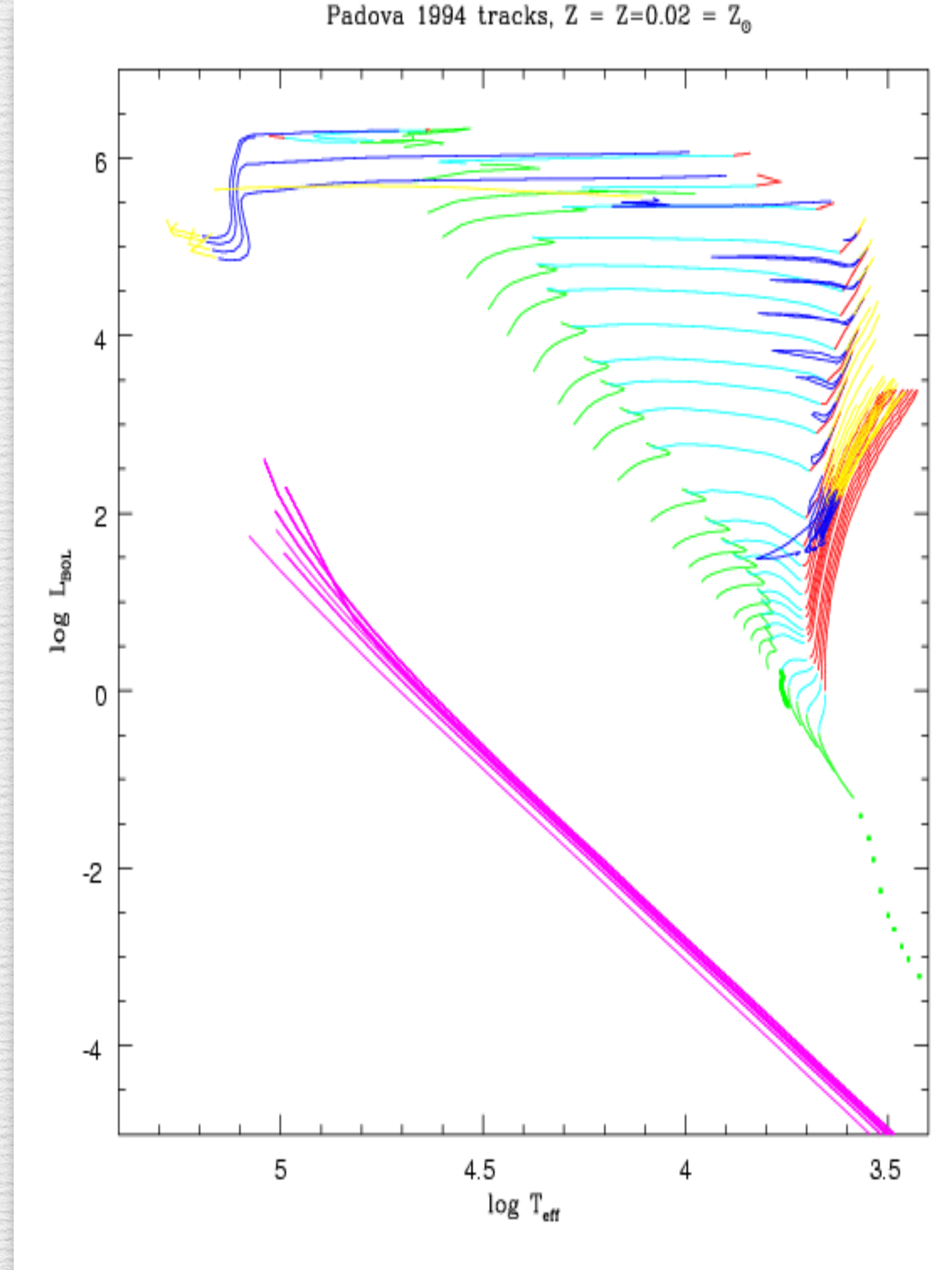

Evolutionary phases:

MS
SGB
RGB
HB
AGB
REST

Evolutionary Tracks

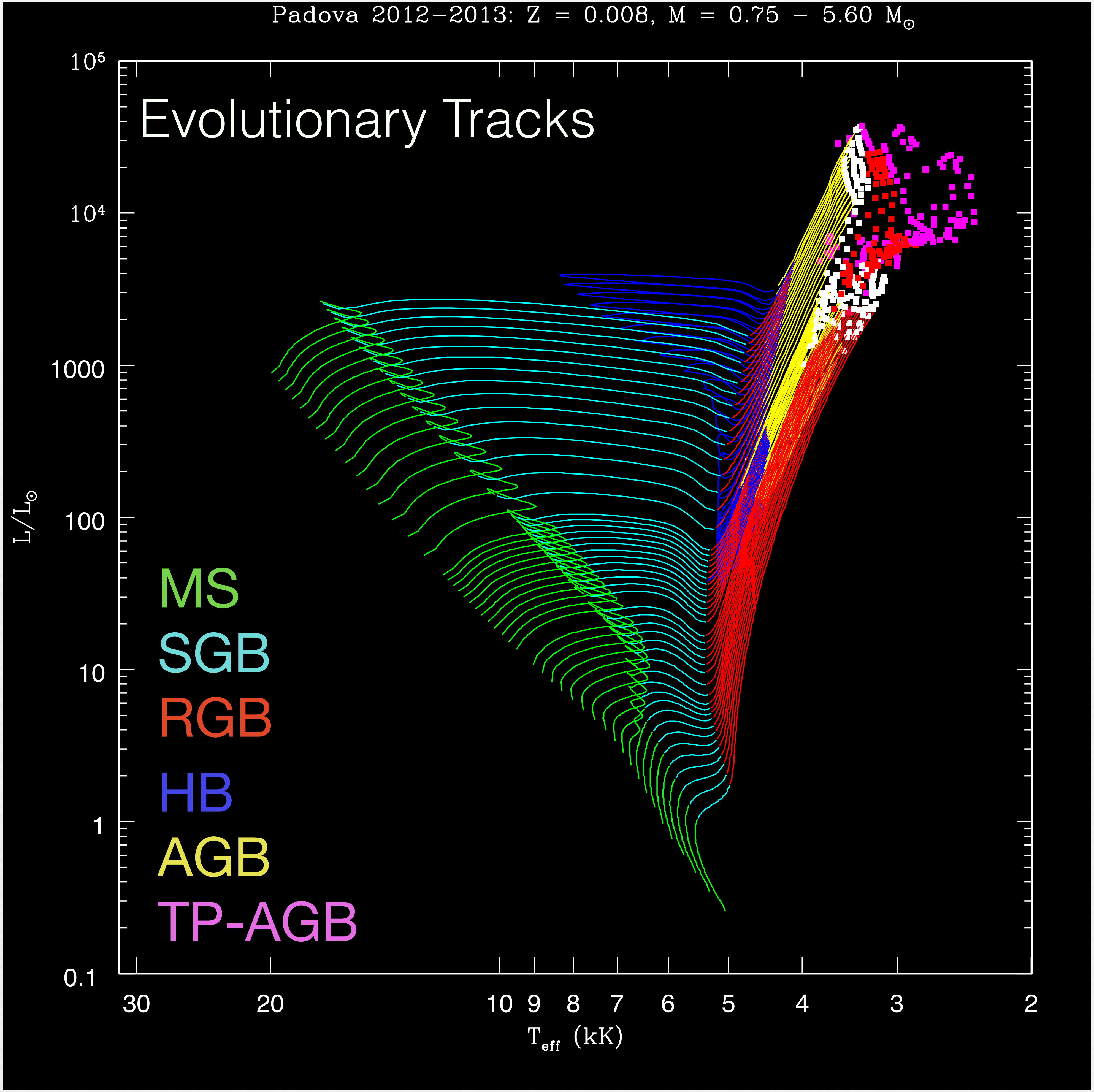

Isochrones

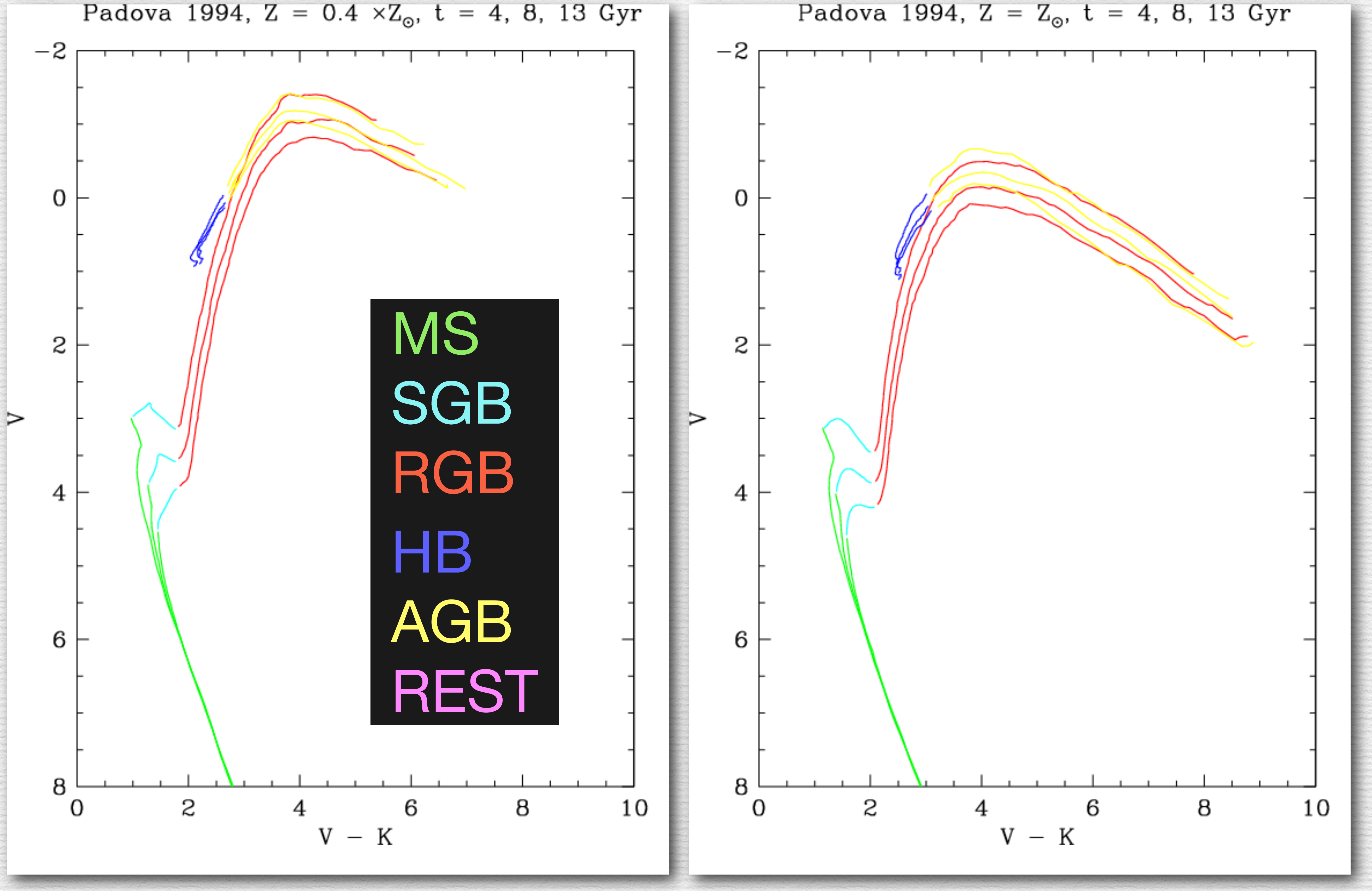
Padova 1994, Z = 0.4 ×Z$_\odot$, t = 4, 8, 13 Gyr
Padova 1994, Z = Z$_\odot$, t = 4, 8, 13 Gyr
V
V − K
−2
0
2
4
6
8
0
2
4
6
8
10
MS
SGB
RGB
HB
AGB
REST

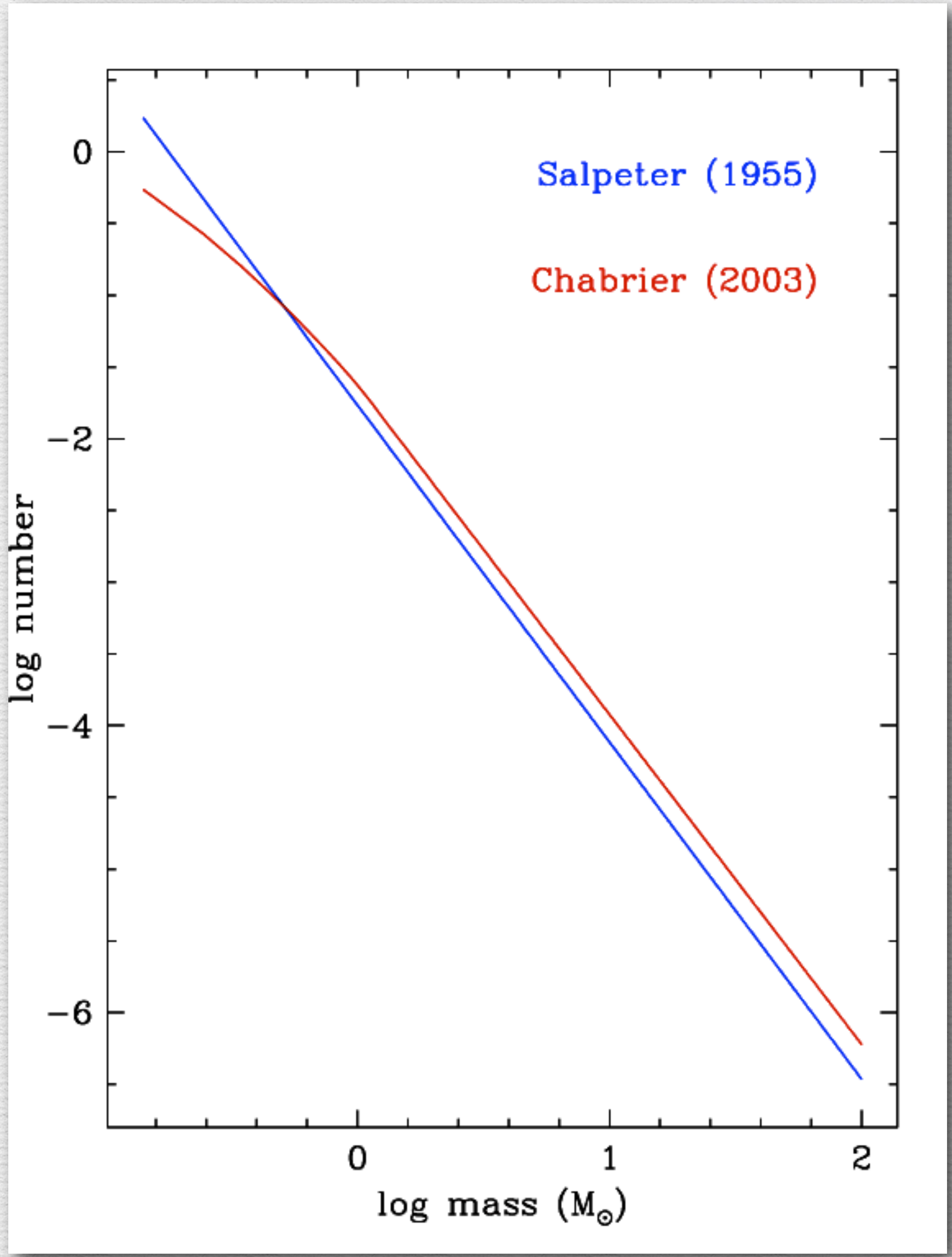

Initial mass function (IMF)

- Quite similar for M > 1 Mo
- Chabrier's IMF implies a lower number of stars below 1 Mo than Salpeter's
- Both IMF's are normalized to same total mass

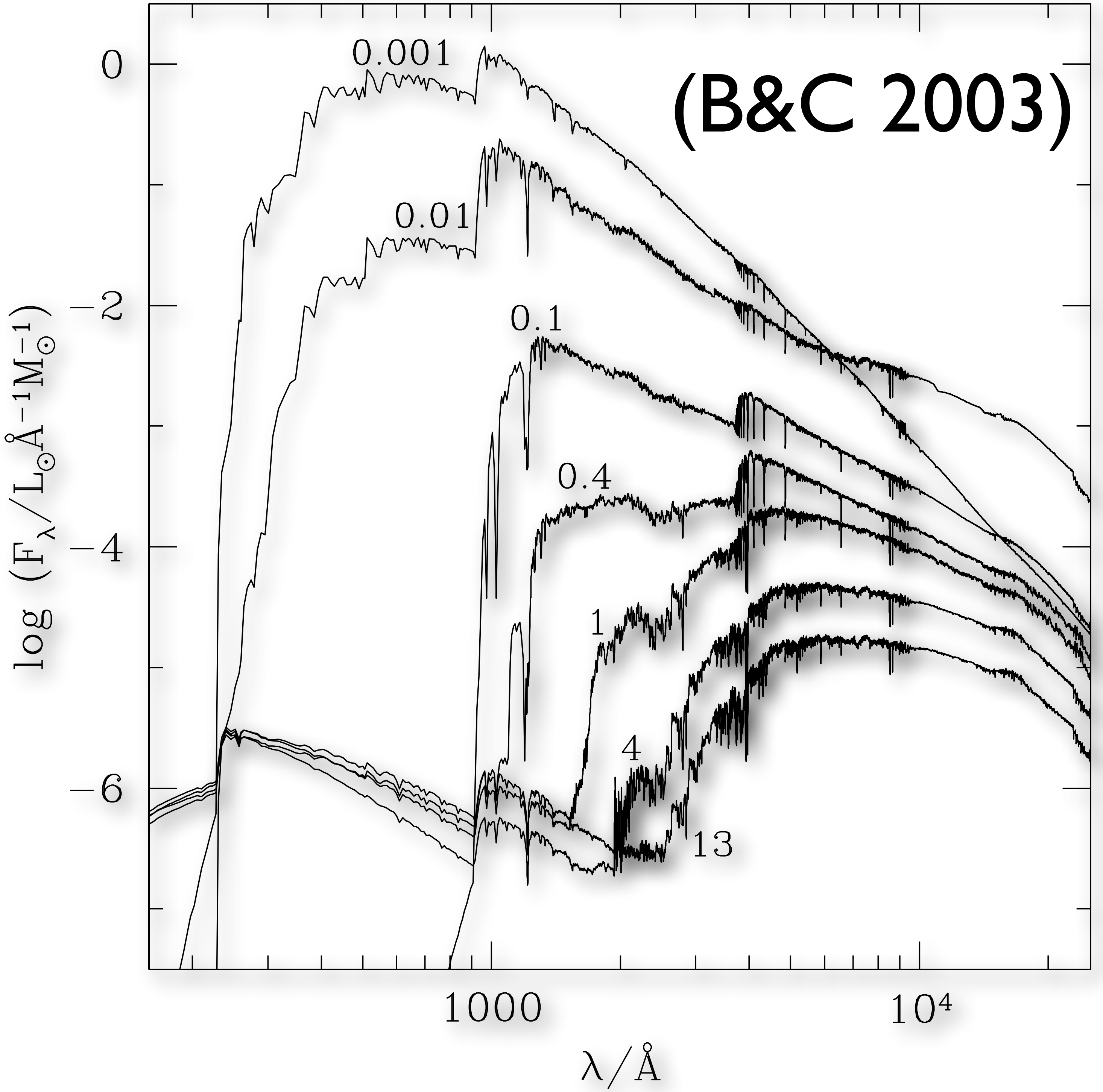

(B&C 2003)

SPS models:

Provide the time evolution of the spectral energy distribution (SED) of a stellar population (star cluster or galaxy) whose stars were born in an instantaneous burst at t = 0.

For stellar populations with a complex star formation history, SFH = Ψ(t), the SED can be computed from:

$$F_\lambda(t) = \int_0^t \psi(t-t')\, S_\lambda\left[t', \zeta(t-t')\right]\, dt'$$

Most basic applications of SPS:

Dating SP (how old are they)

Discovering distant galaxies

$t = 0$

HR diagram

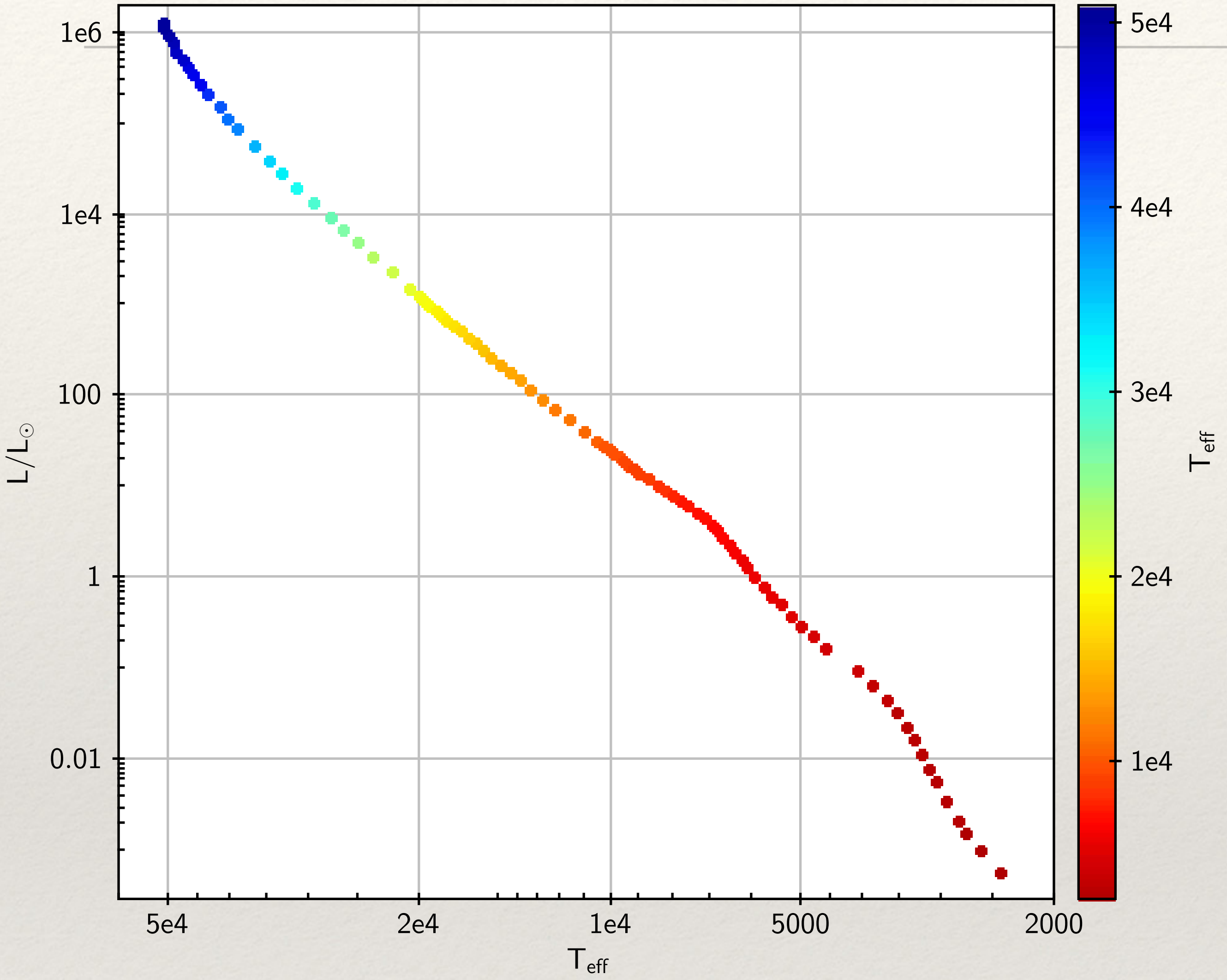

Spectral energy distribution

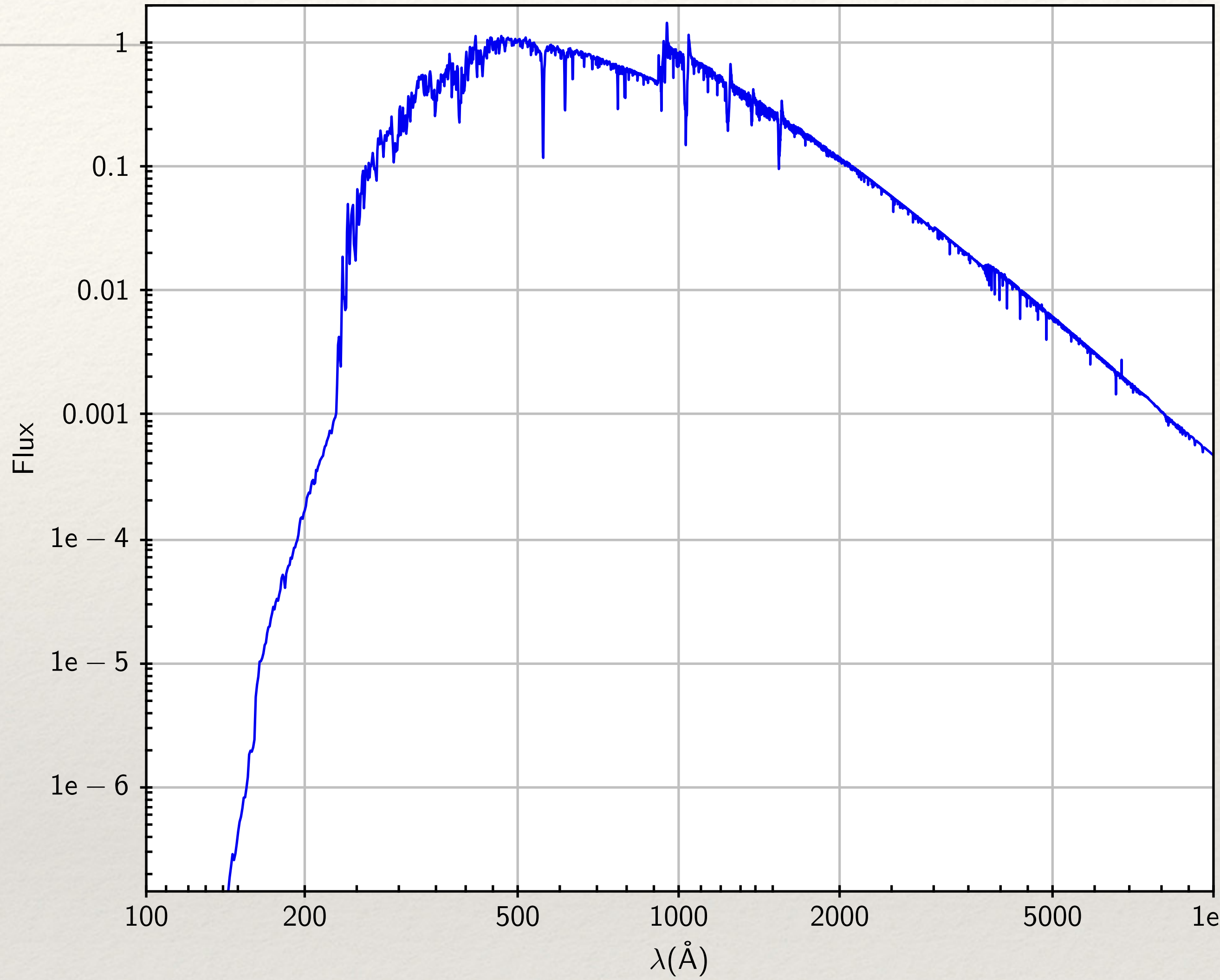

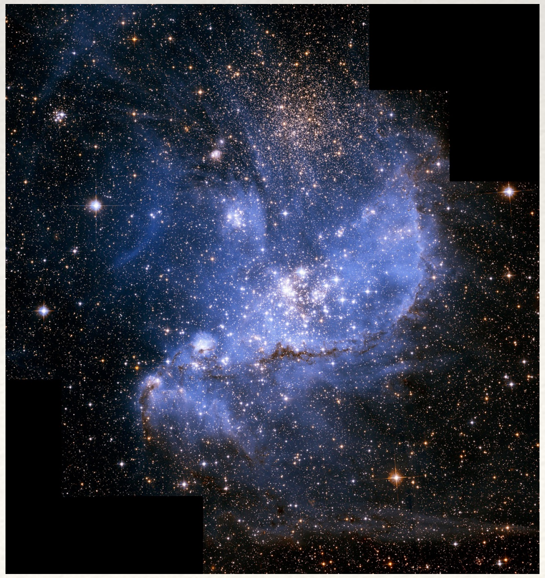

time

t = 2 Myr

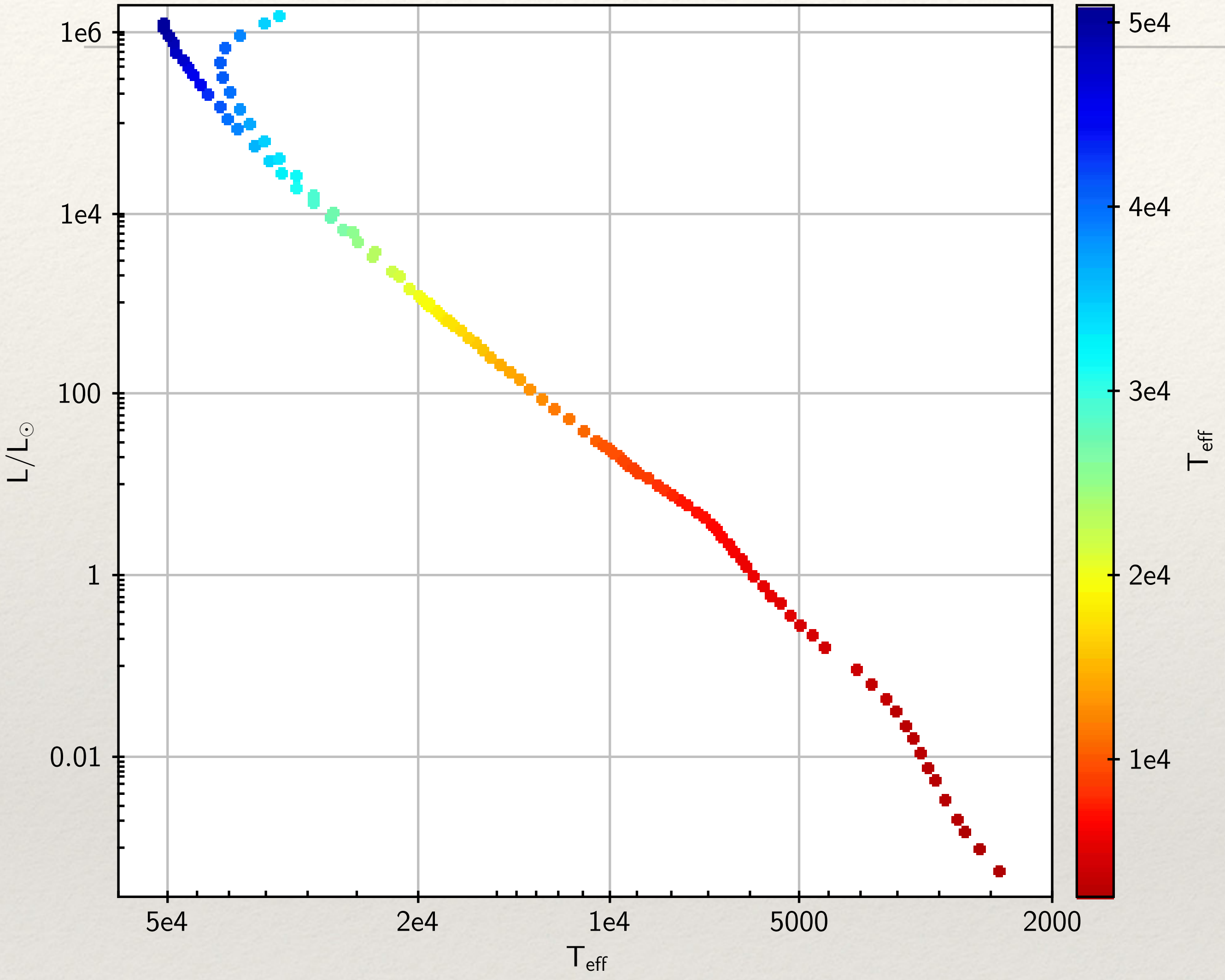
L/L$_\odot$
1e6
1e4
100
1
0.01
T$_{\mathrm{eff}}$
5e4
2e4
1e4
5000
2000
T$_{\mathrm{eff}}$
5e4
4e4
3e4
2e4
1e4

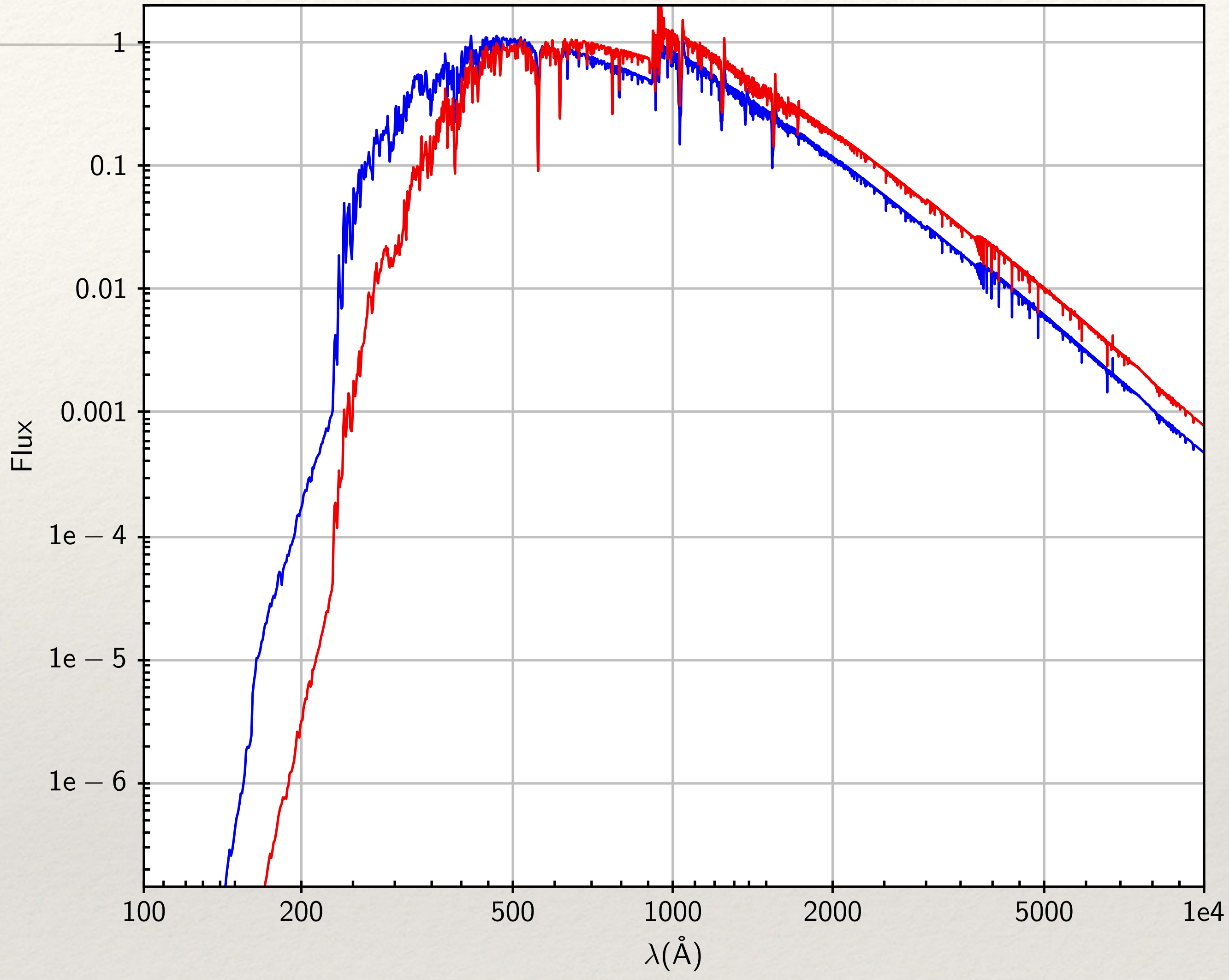
Flux
1
0.1
0.01
0.001
1e − 4
1e − 5
1e − 6
λ(Å)
100
200
500
1000
2000
5000
1e4

time

t = 5 Myr

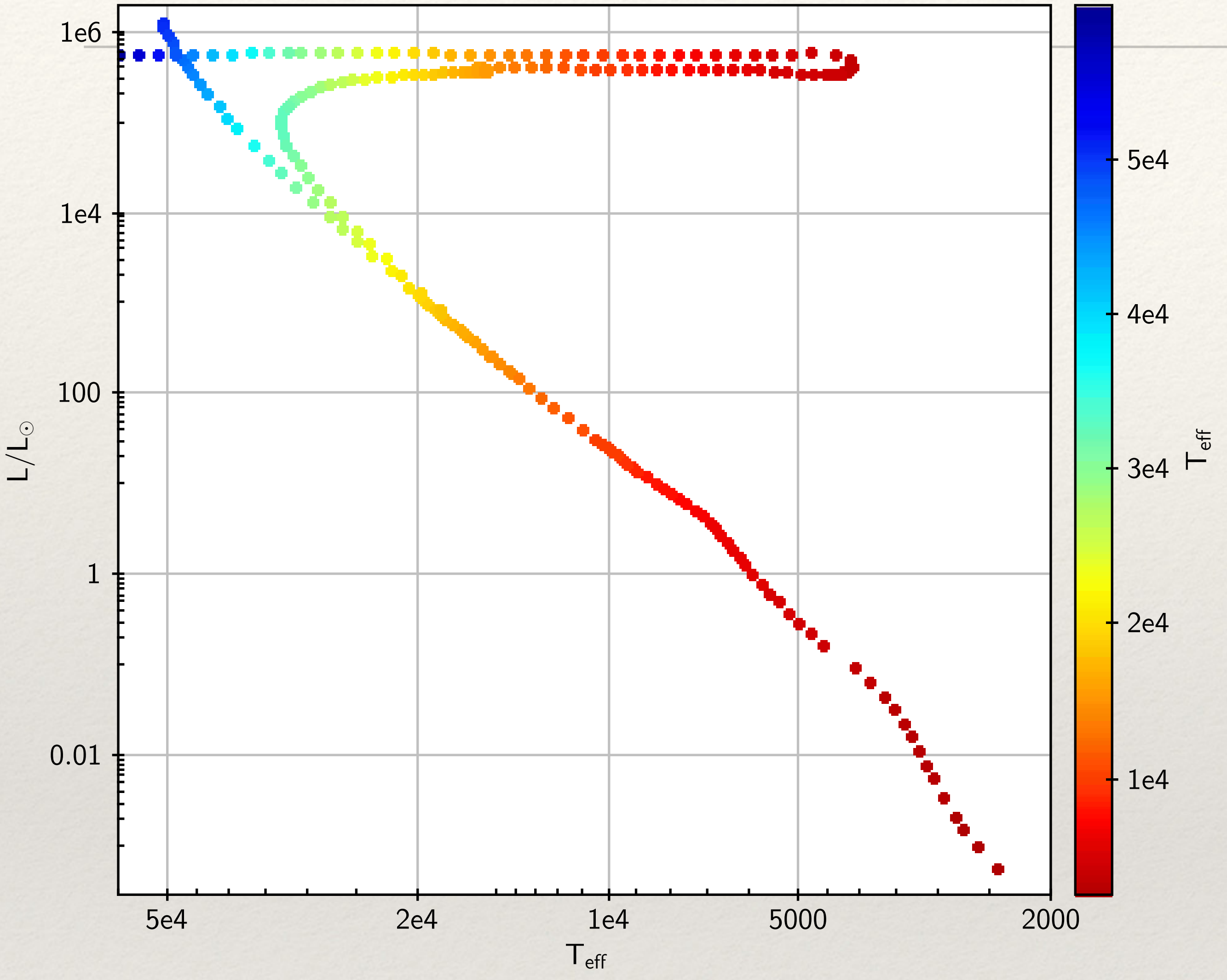
1e6
1e4
100
1
0.01
L/L$_\odot$
5e4
2e4
1e4
5000
2000
T$_{\rm eff}$
5e4
4e4
3e4
2e4
1e4
T$_{\rm eff}$

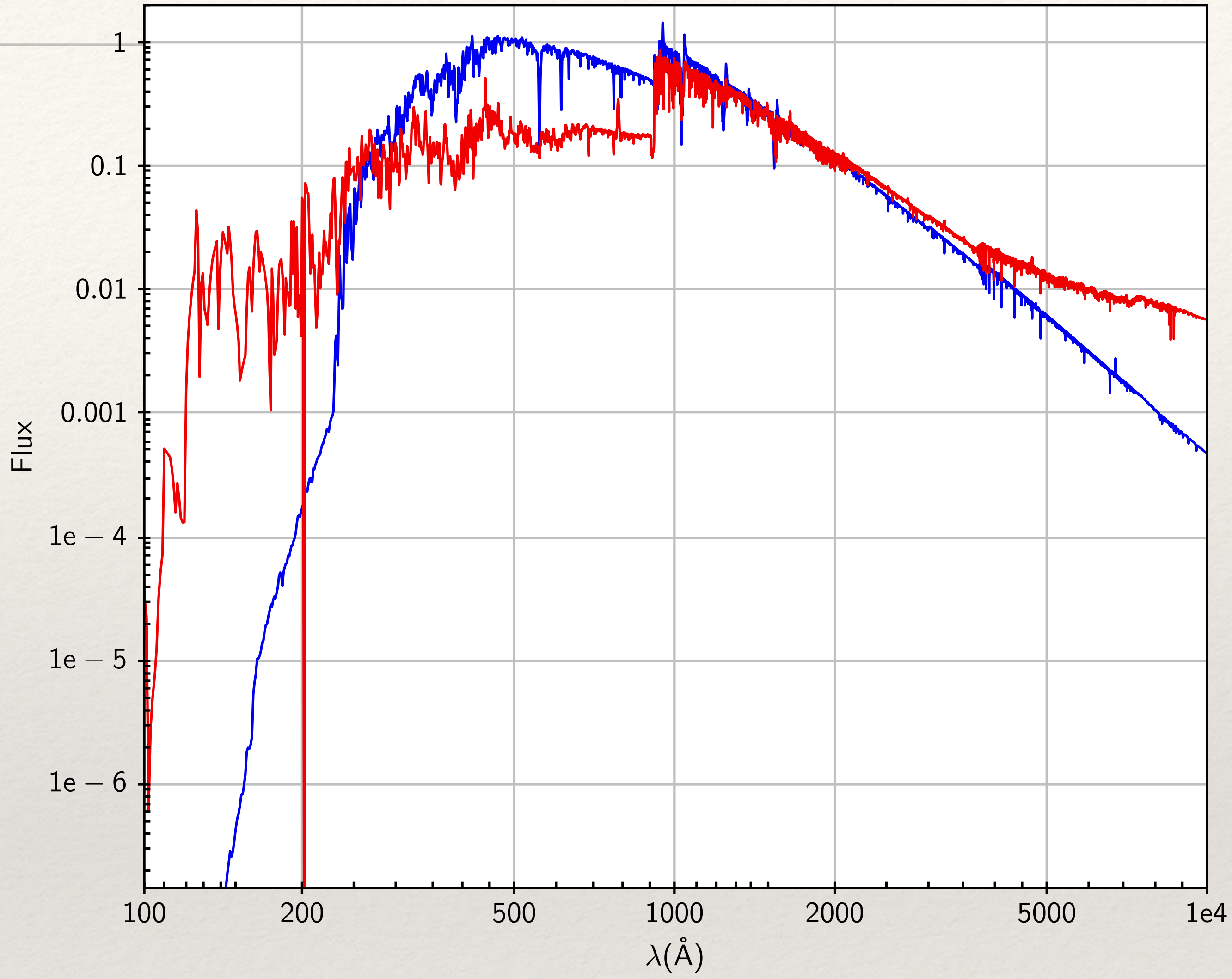
1
0.1
0.01
0.001
1e − 4
1e − 5
1e − 6
Flux
100
200
500
1000
2000
5000
1e4
λ(Å)

time

t = 10 Myr

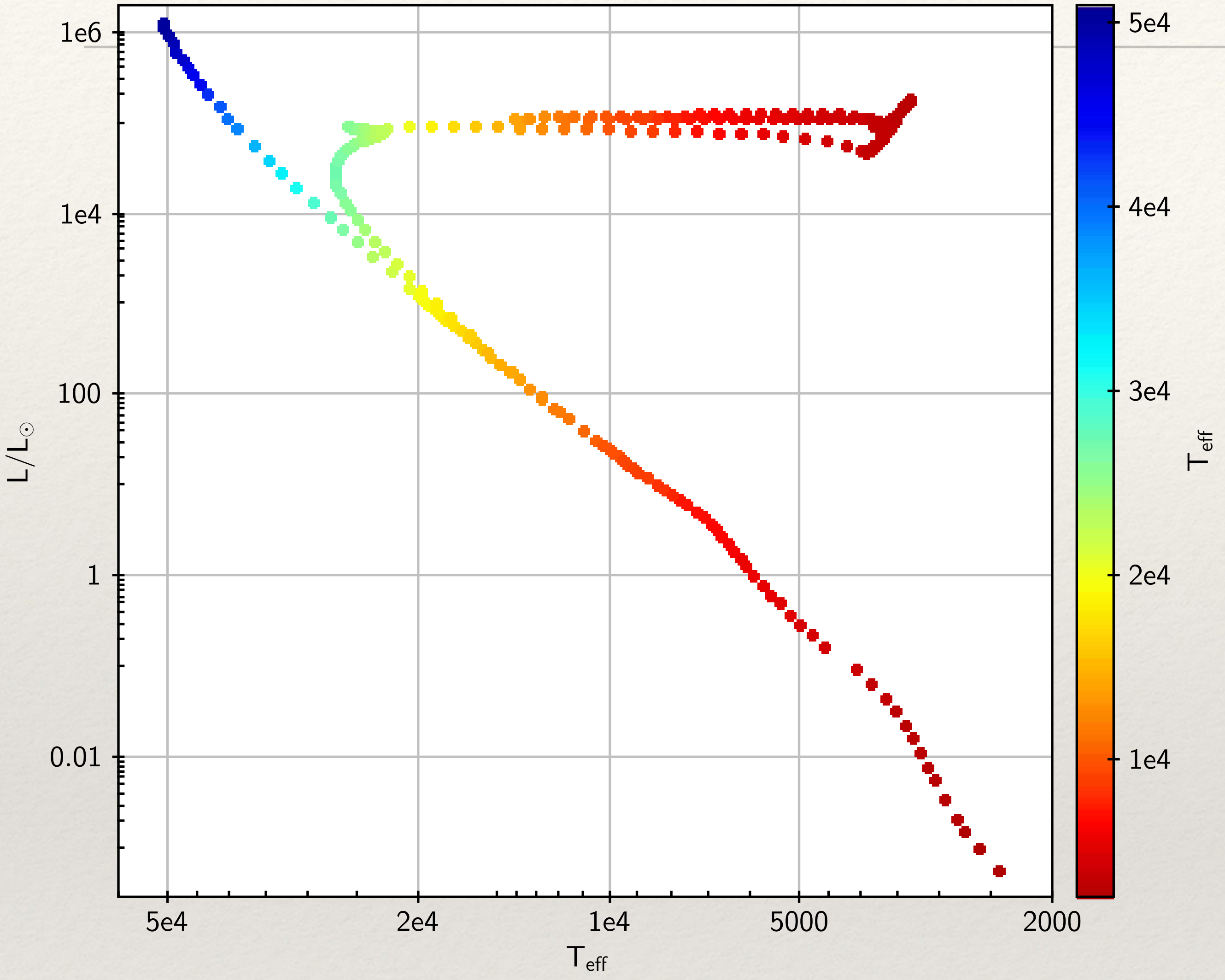

1e6
1e4
100
1
0.01
L/L$_\odot$
5e4
2e4
1e4
5000
2000
T$_{eff}$
5e4
4e4
3e4
2e4
1e4
T$_{eff}$

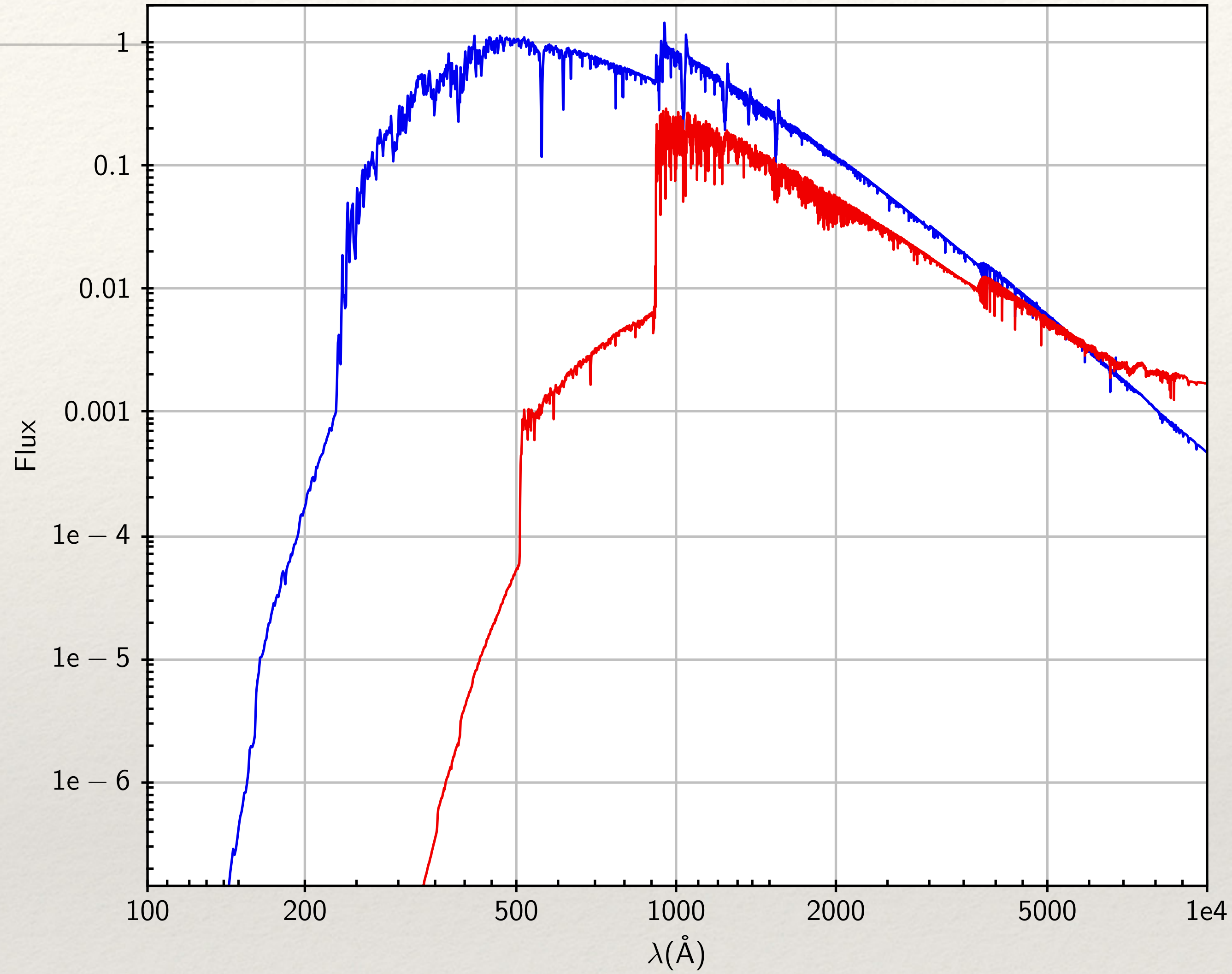

1
0.1
0.01
0.001
1e − 4
1e − 5
1e − 6
Flux
100
200
500
1000
2000
5000
1e4
λ(Å)

time

t = 20 Myr

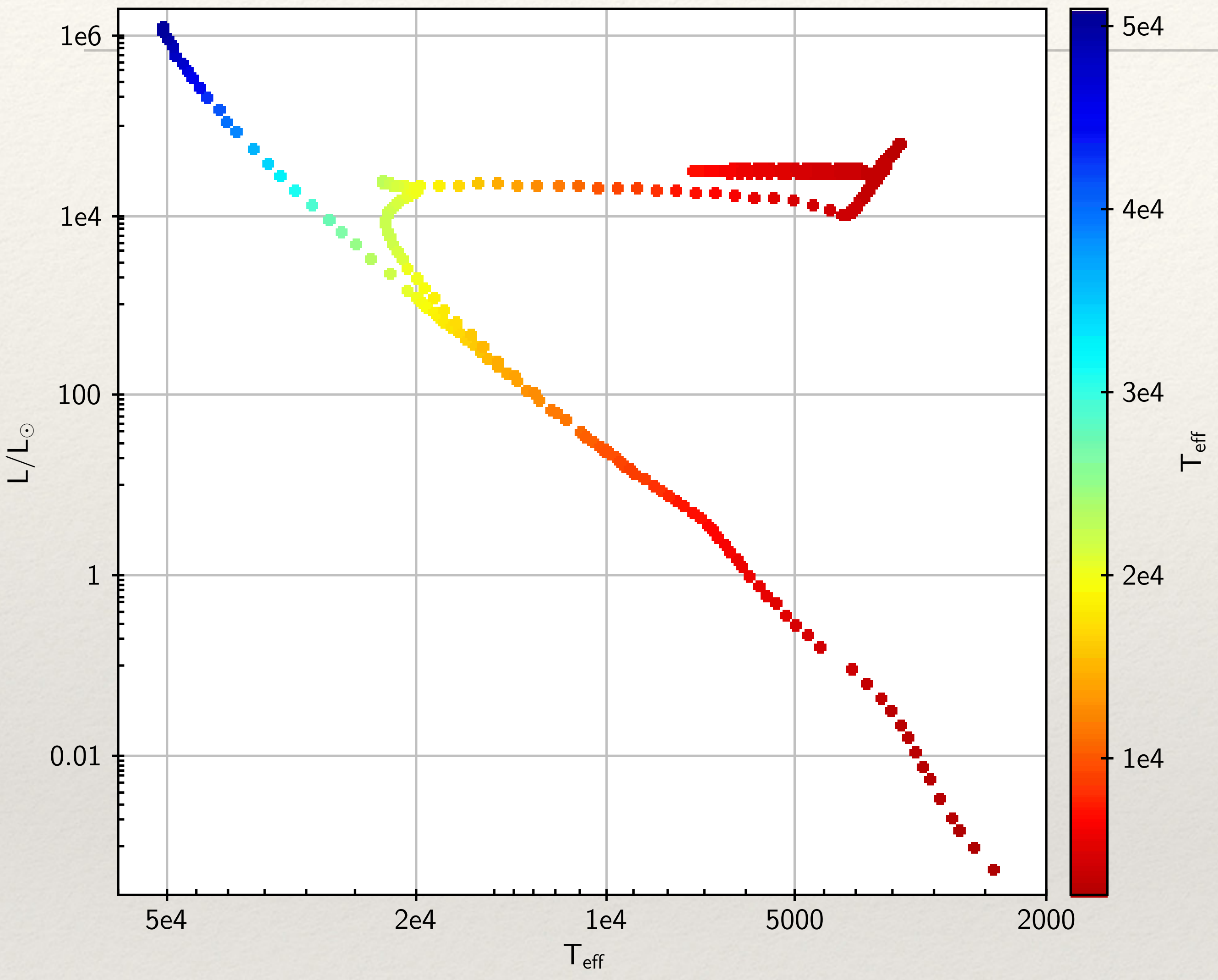
1e6
1e4
100
1
0.01
L/L$_\odot$
5e4
2e4
1e4
5000
2000
T$_{\rm eff}$
5e4
4e4
3e4
2e4
1e4
T$_{\rm eff}$

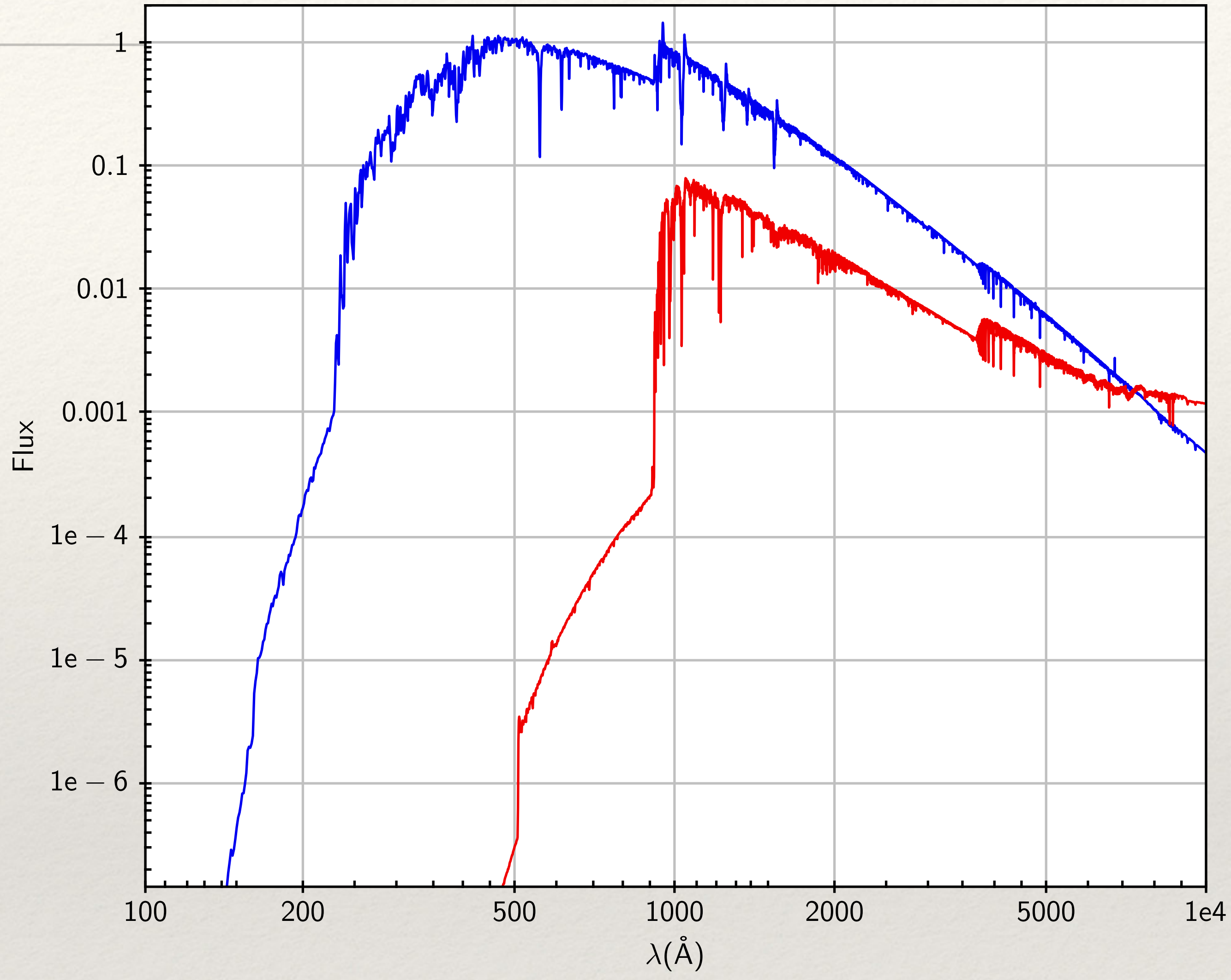
1
0.1
0.01
0.001
1e − 4
1e − 5
1e − 6
Flux
100
200
500
1000
2000
5000
1e4
λ(Å)

time

t = 50 Myr

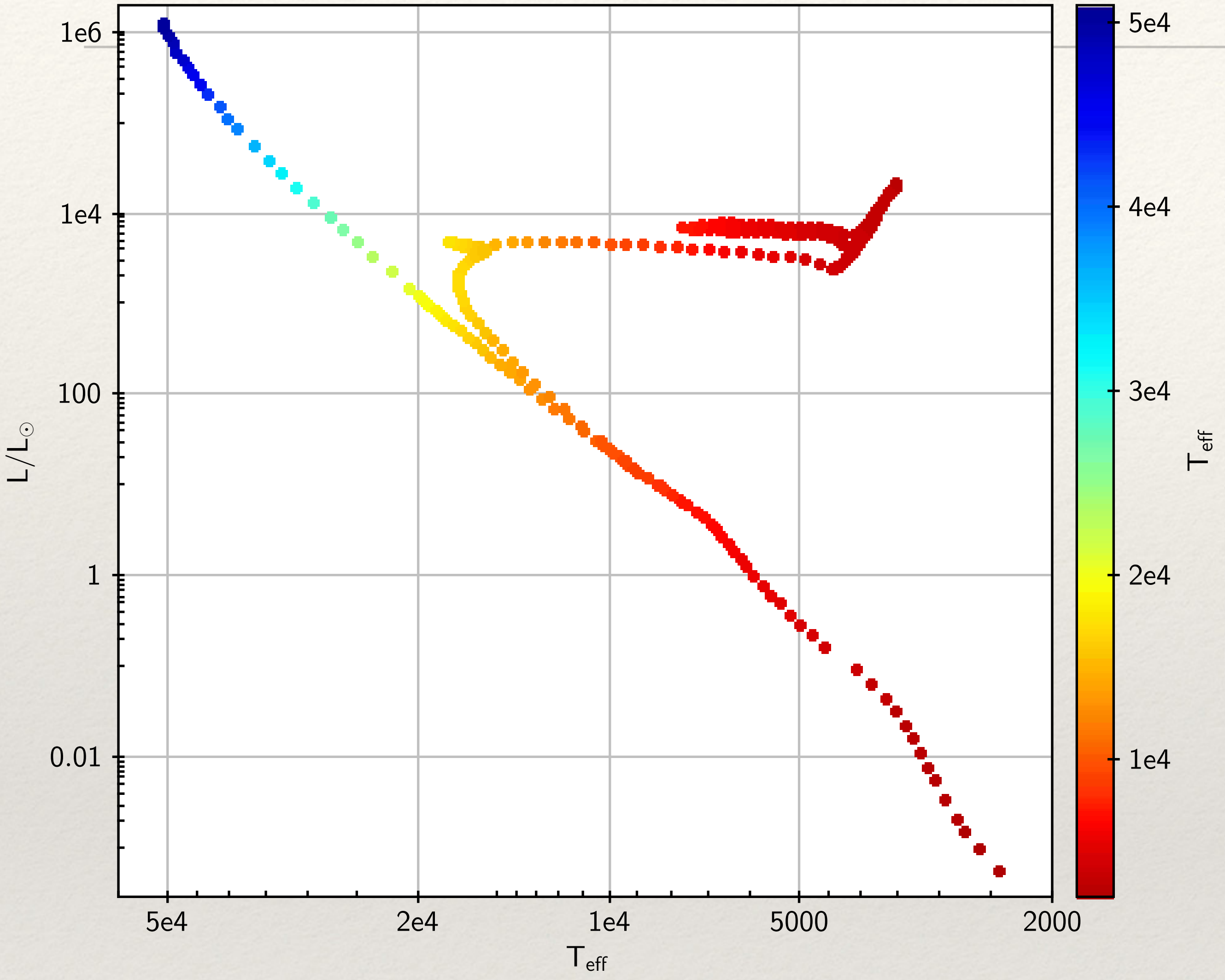
1e6
1e4
100
1
0.01
L/L$_\odot$
5e4
2e4
1e4
5000
2000
T$_{\mathrm{eff}}$
5e4
4e4
3e4
2e4
1e4
T$_{\mathrm{eff}}$

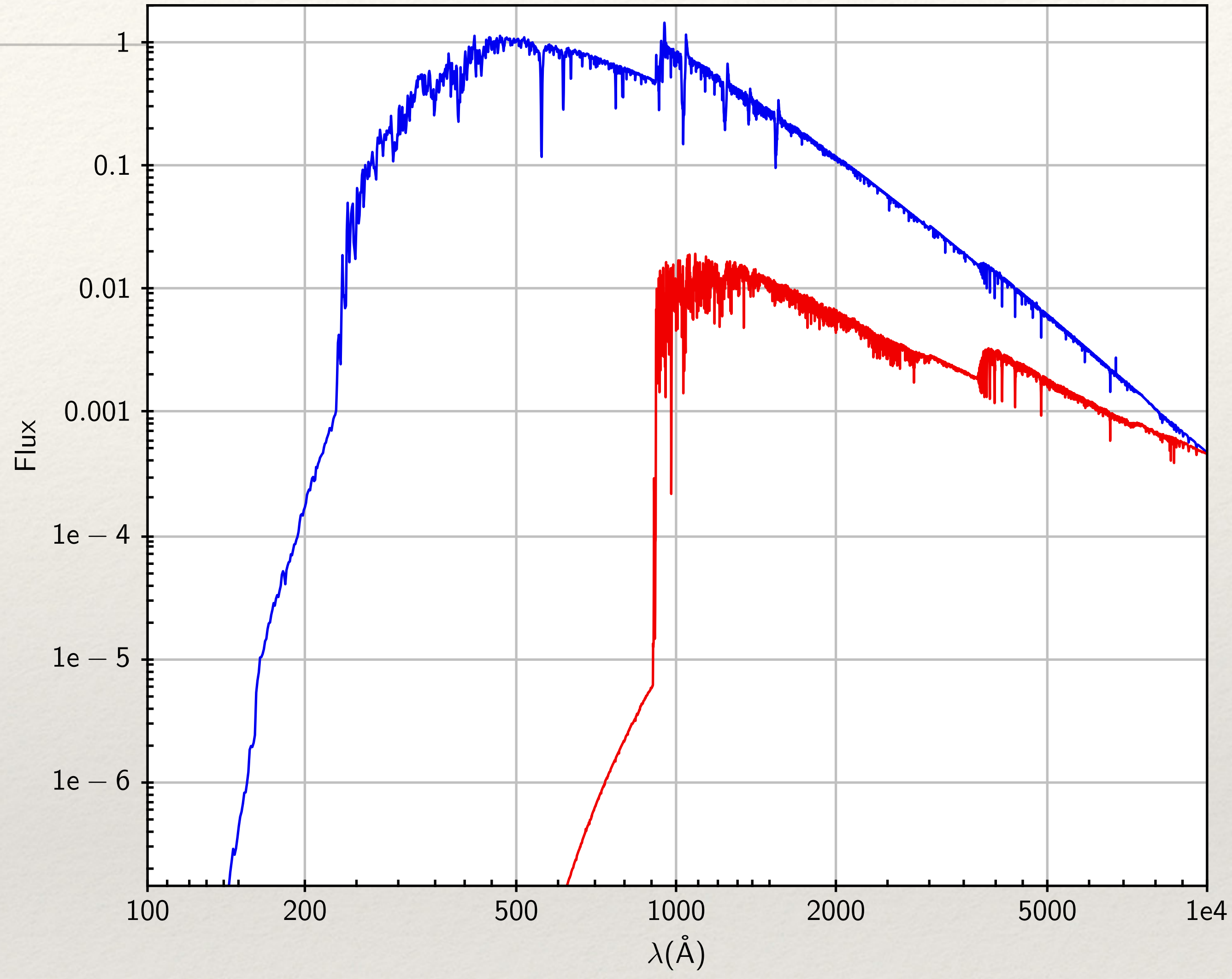
1
0.1
0.01
0.001
1e − 4
1e − 5
1e − 6
Flux
100
200
500
1000
2000
5000
1e4
λ(Å)

time →

t = 100 Myr

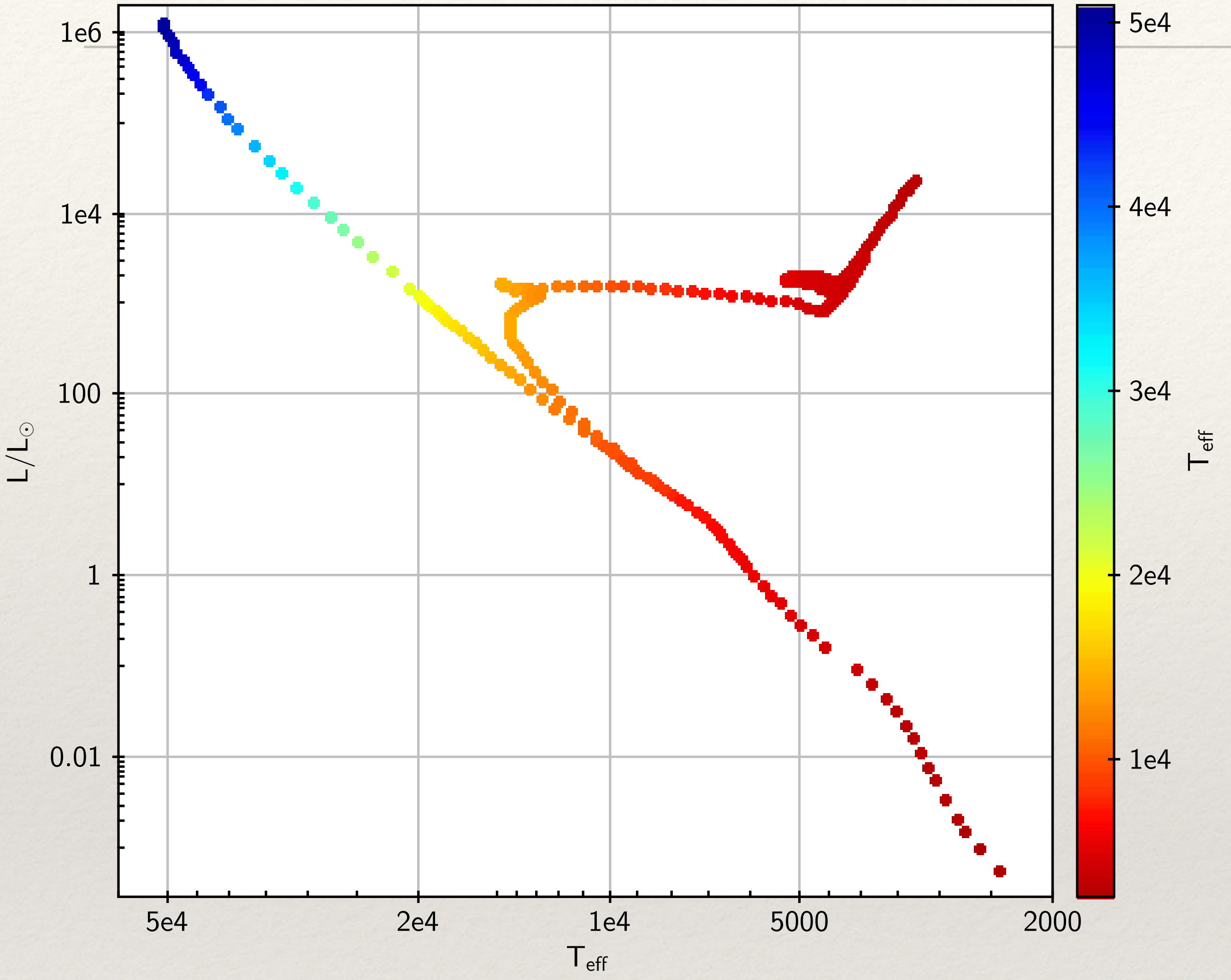

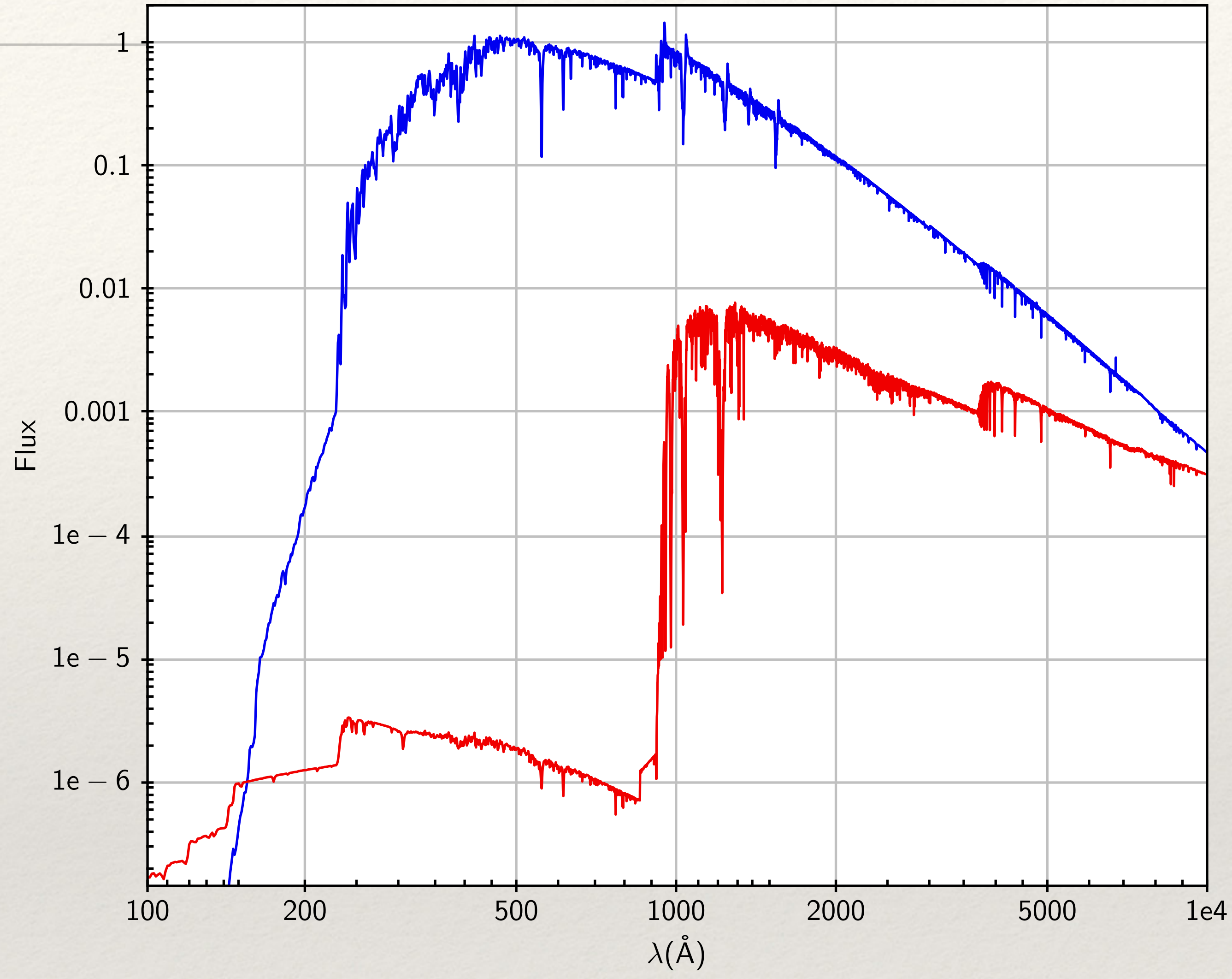

time

t = 200 Myr

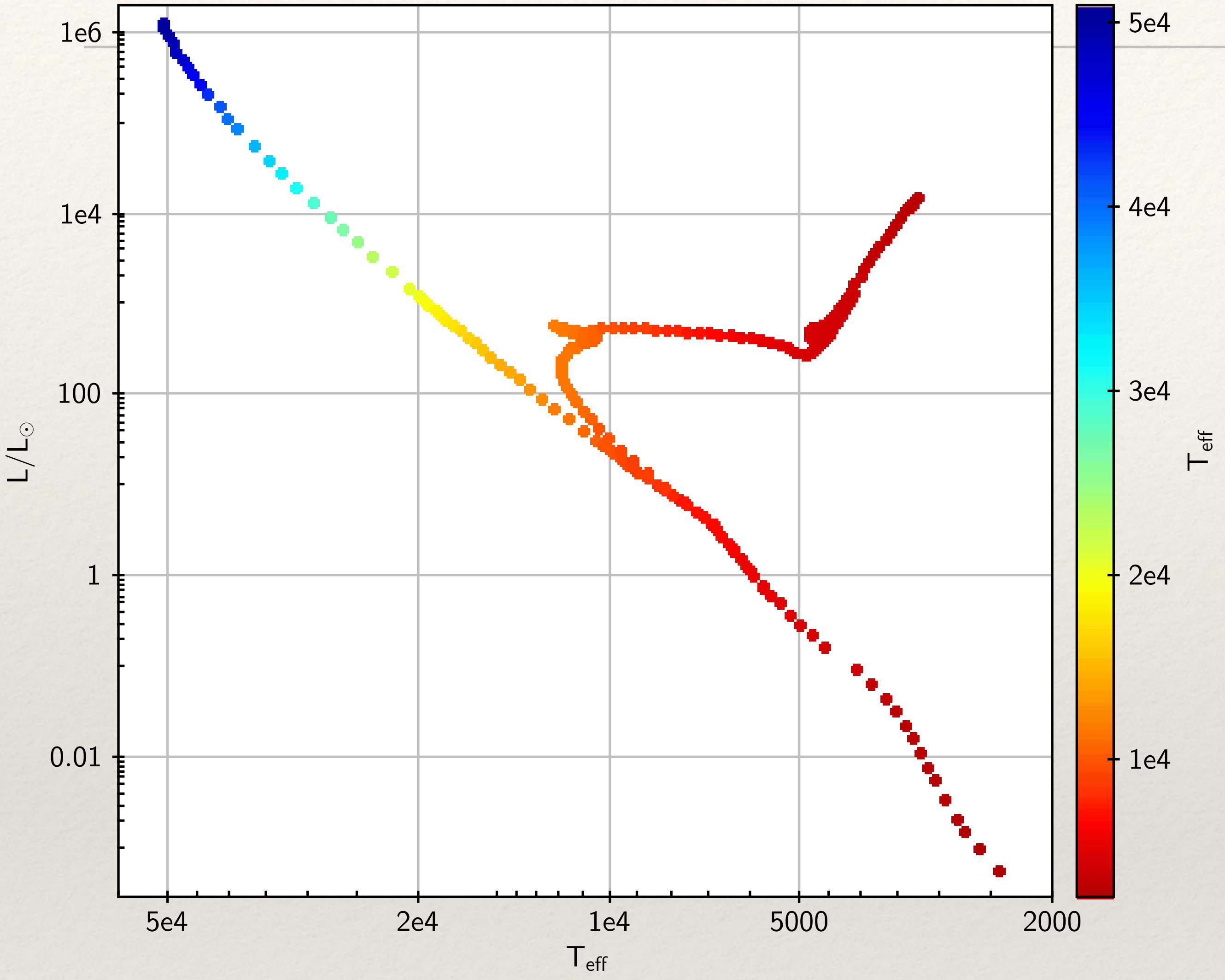

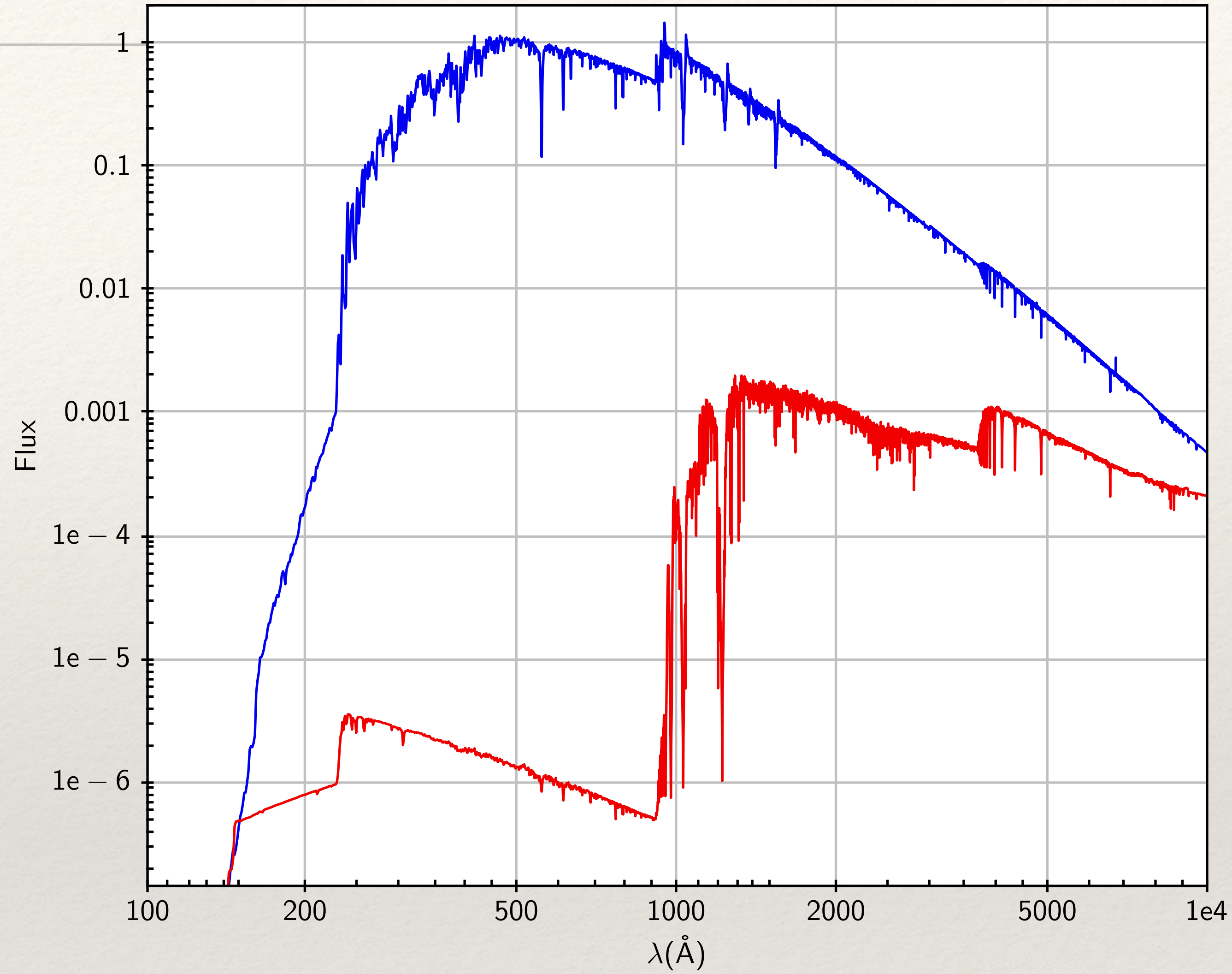

time

t = 300 Myr

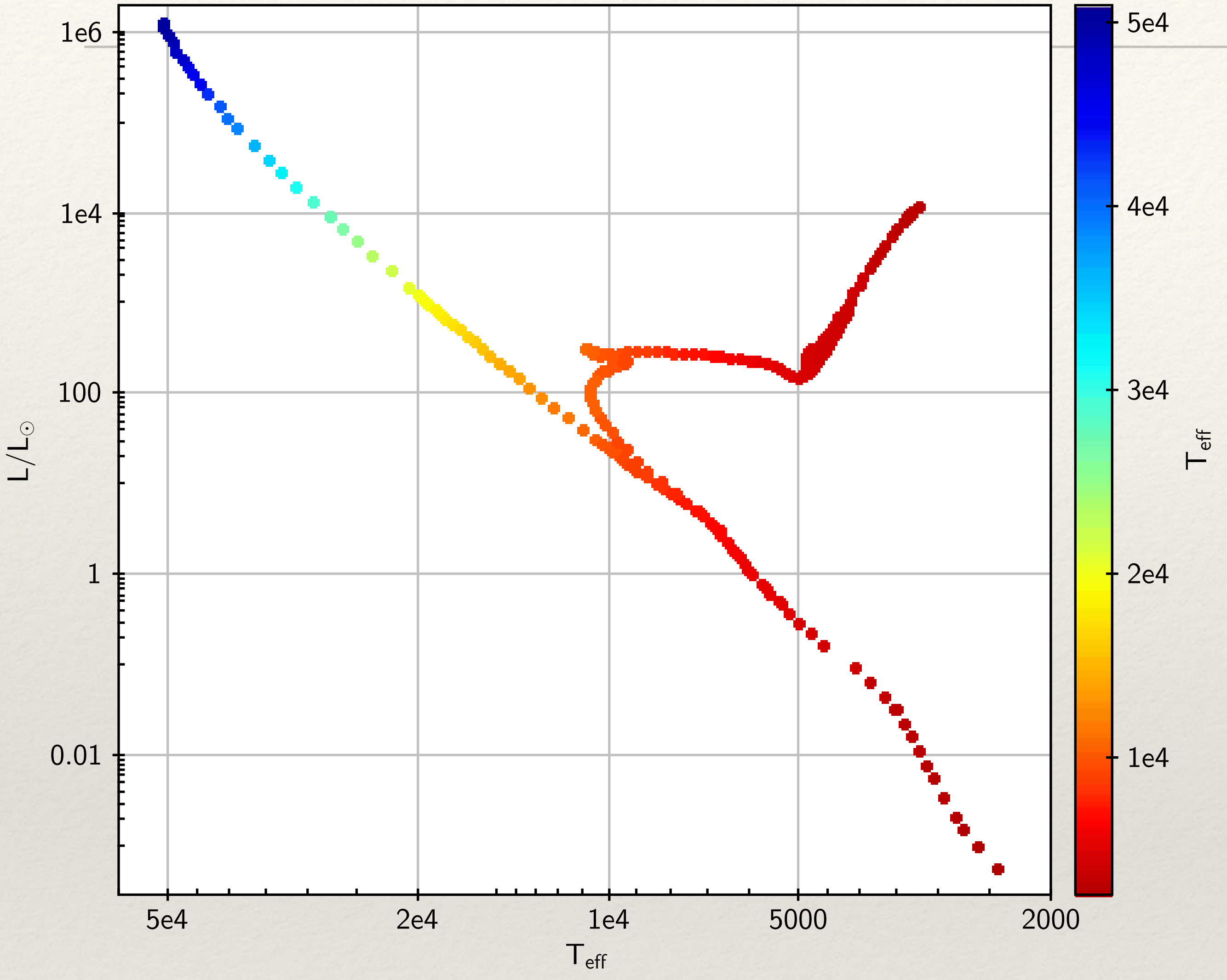

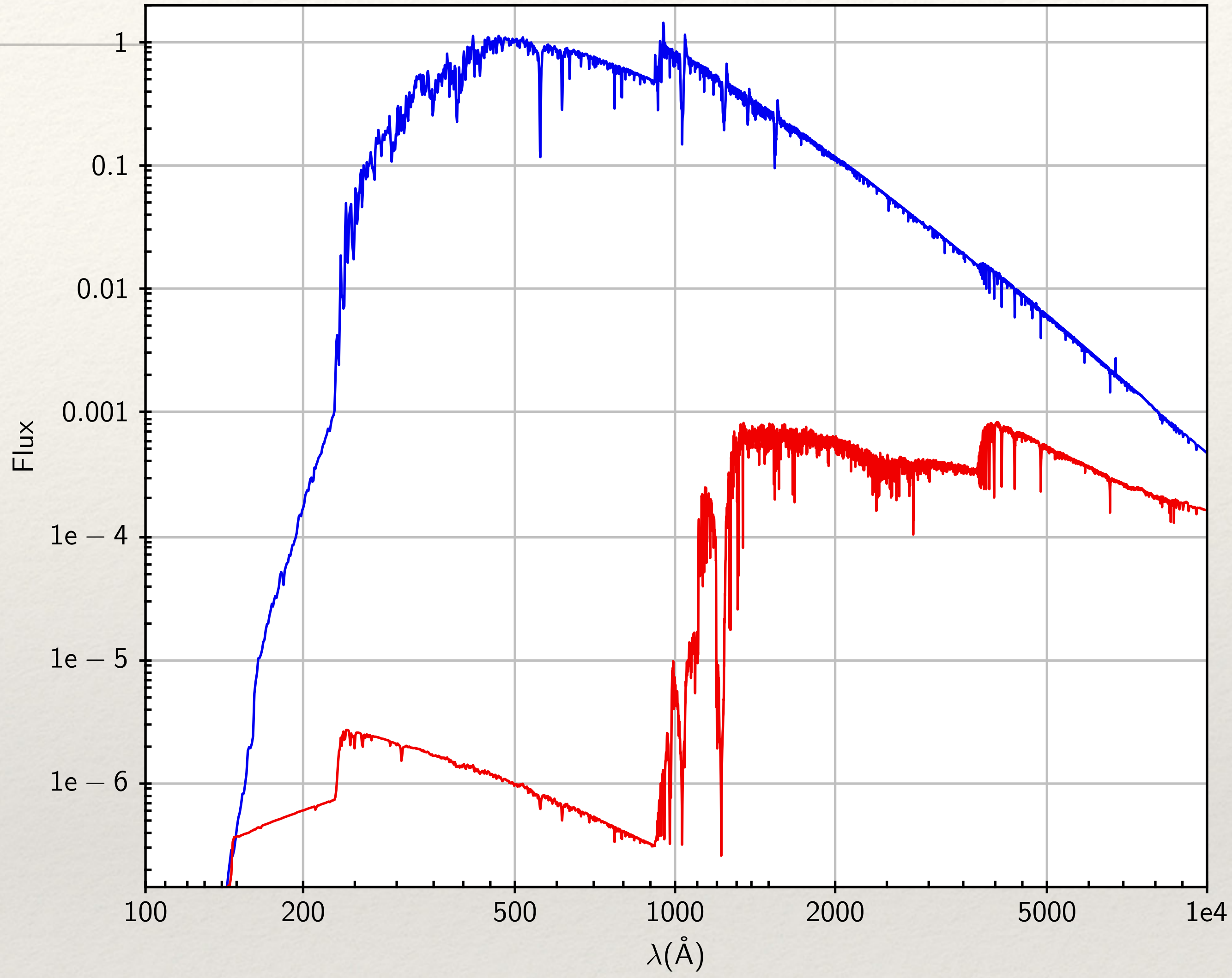

time

t = 400 Myr

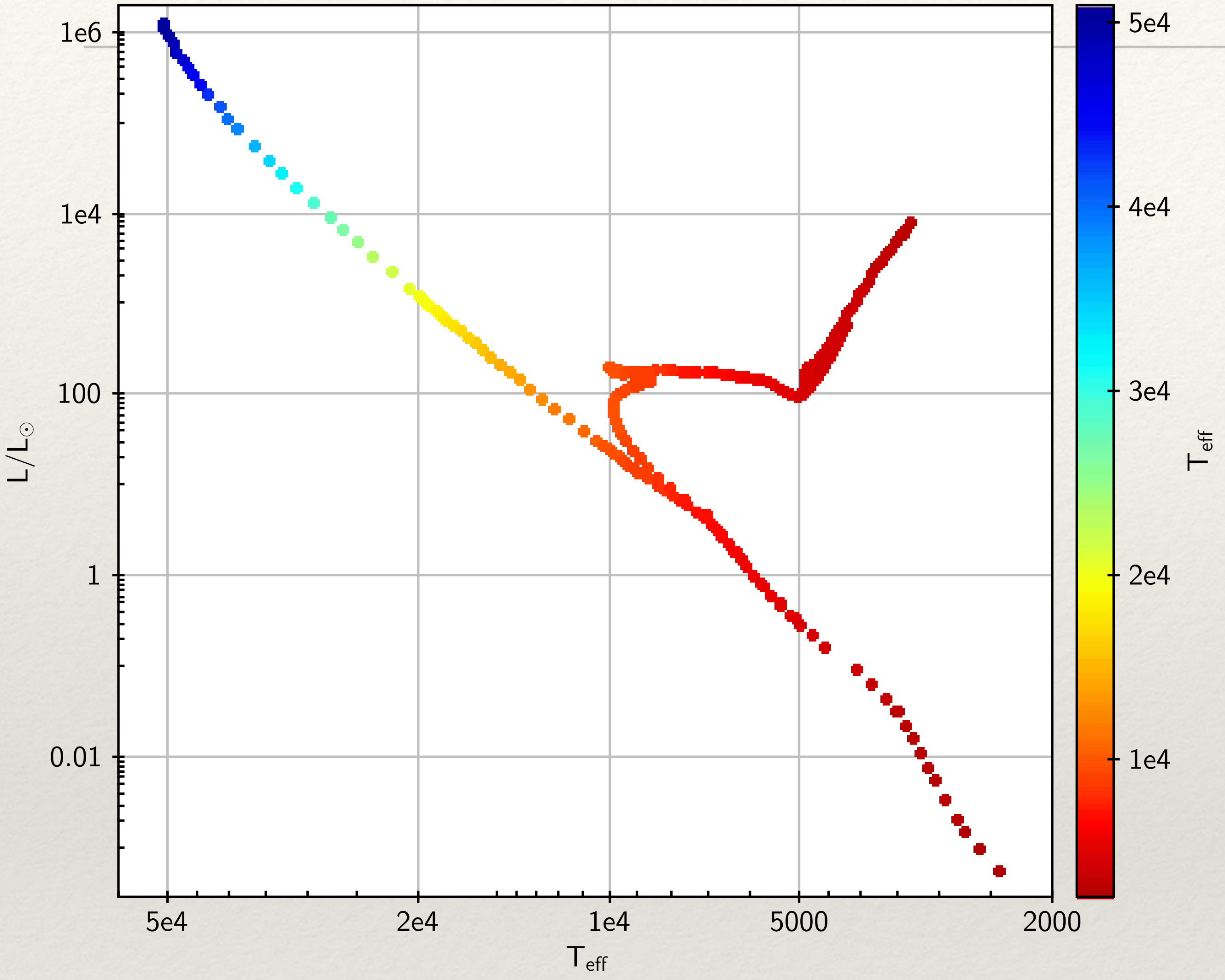

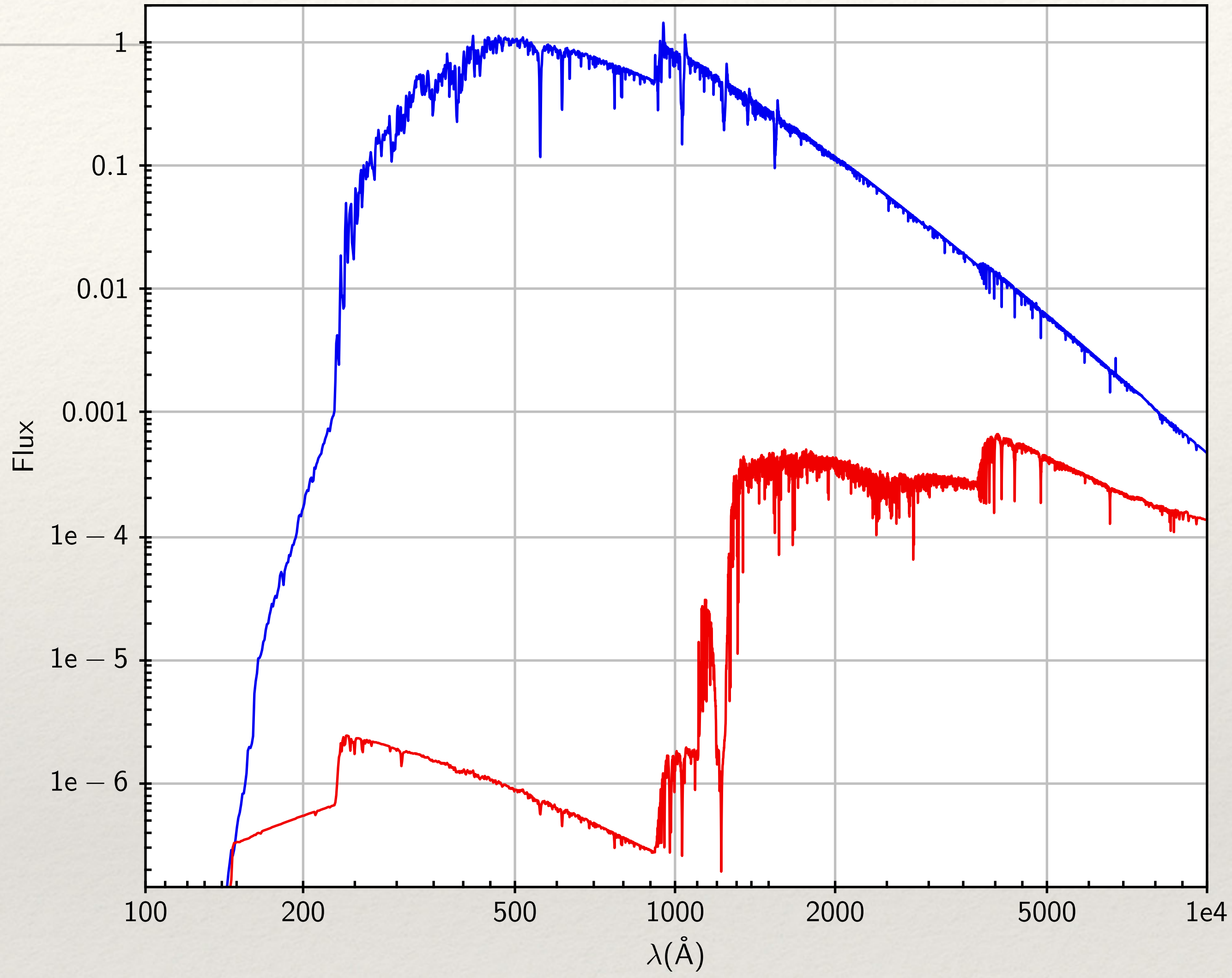

time

t = 500 Myr

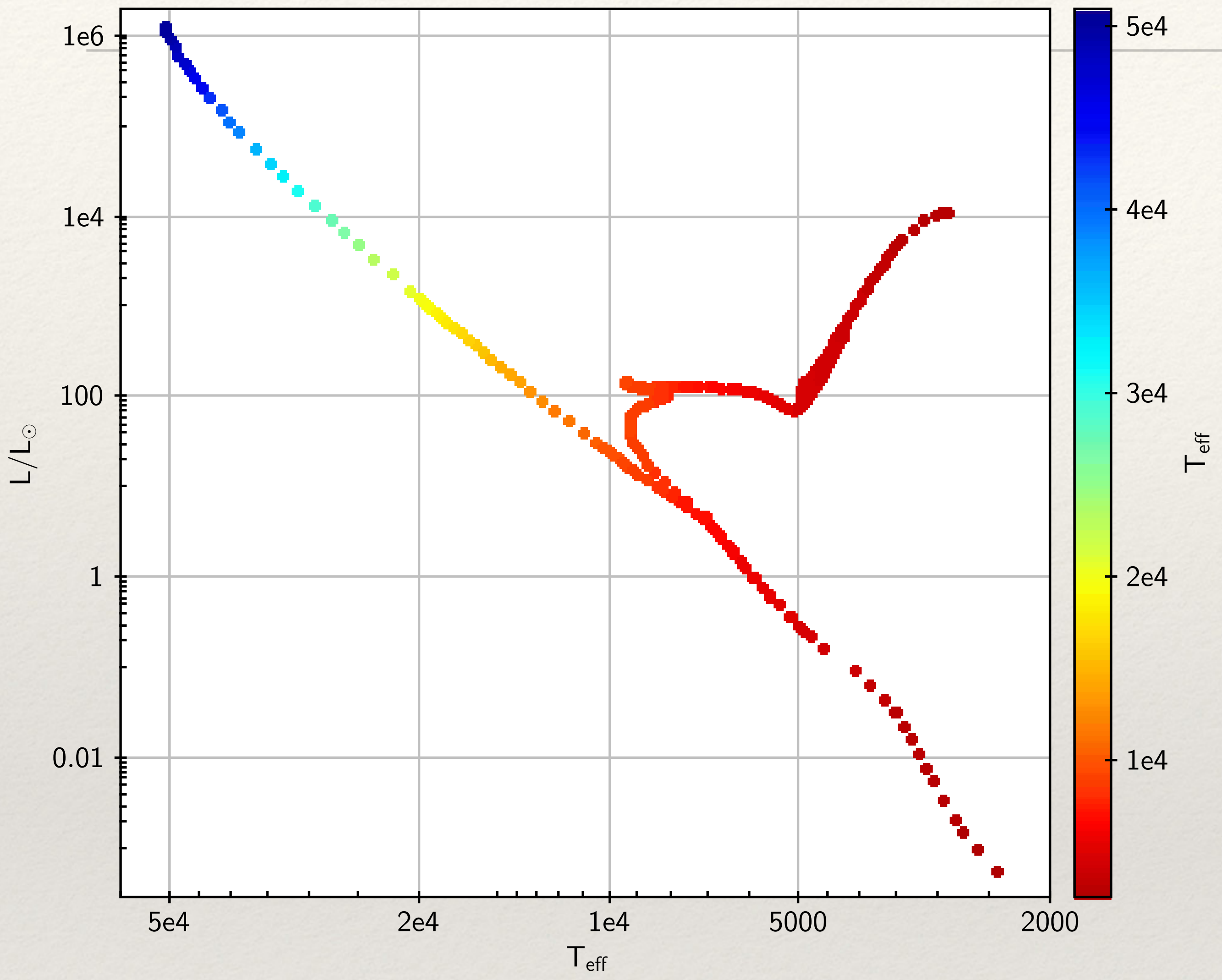

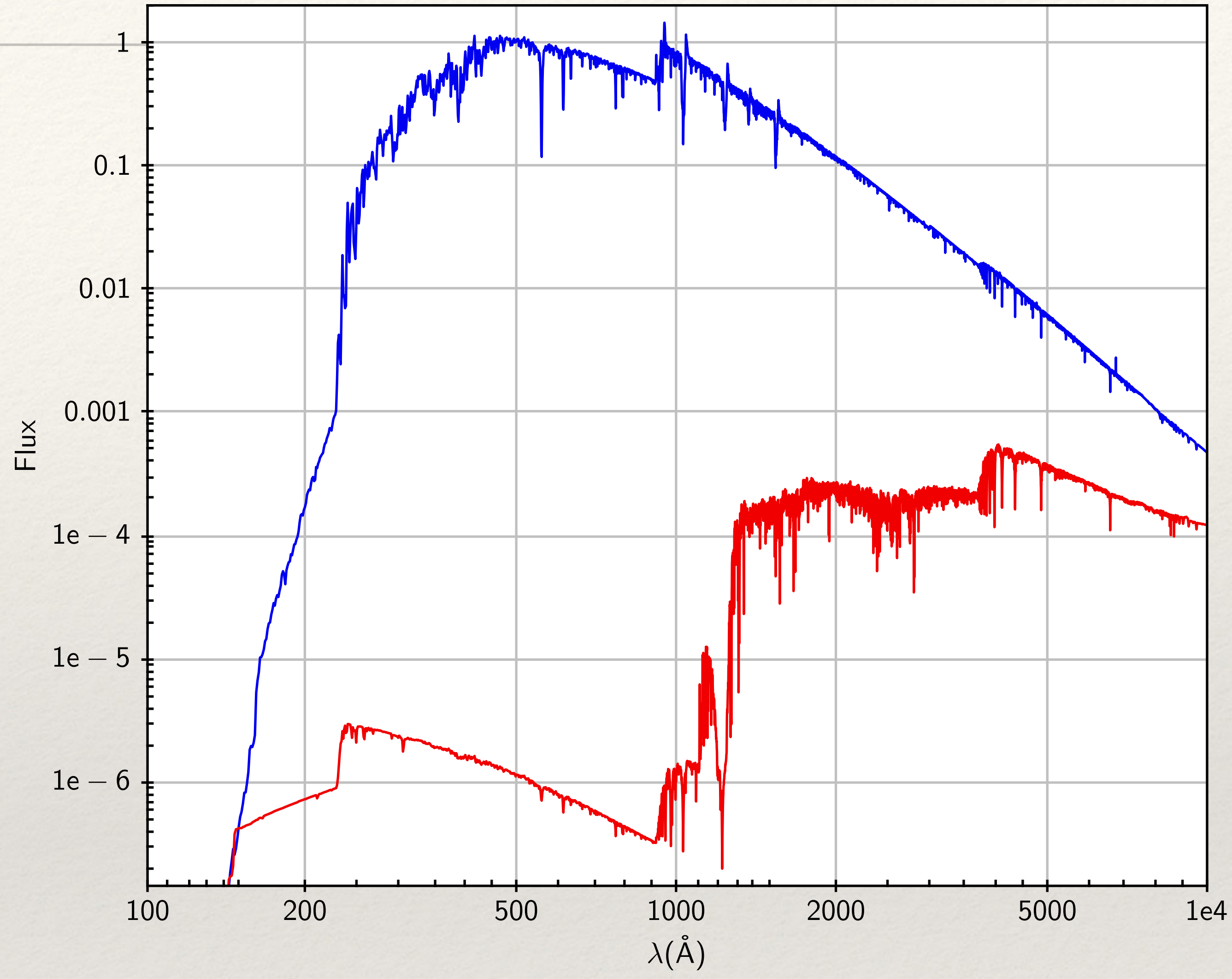

time

t = 1,000 Myr

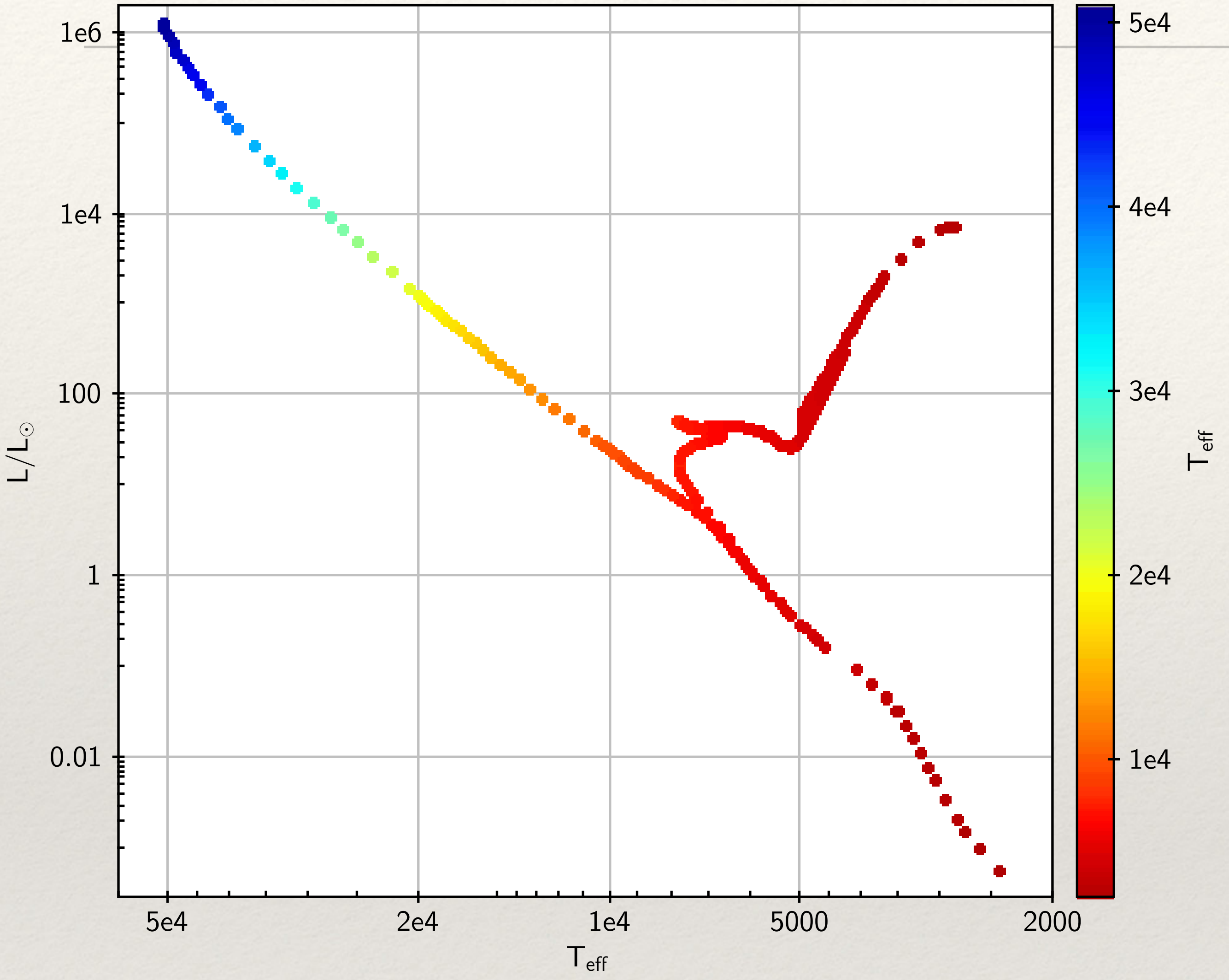

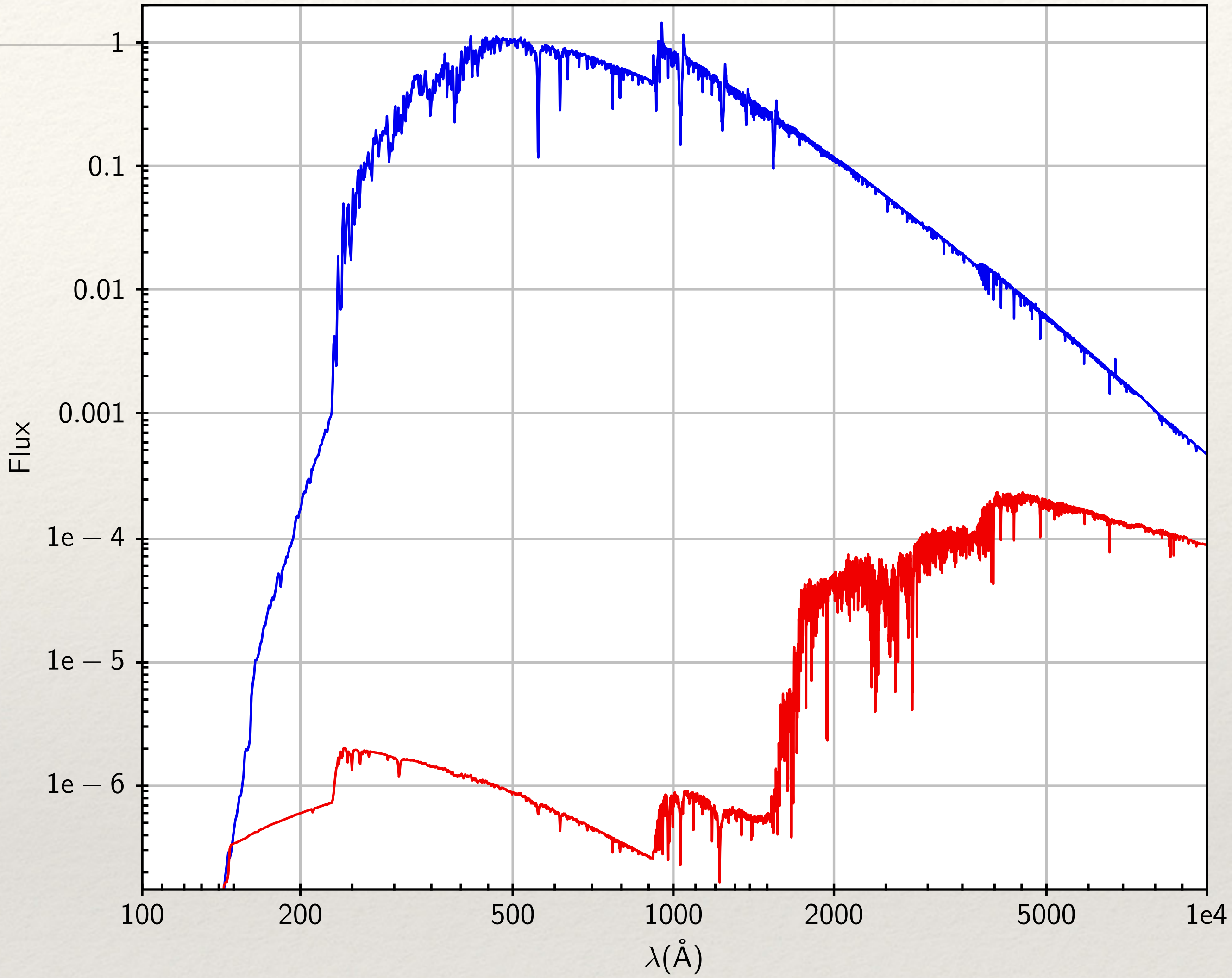

time

t = 2,000 Myr

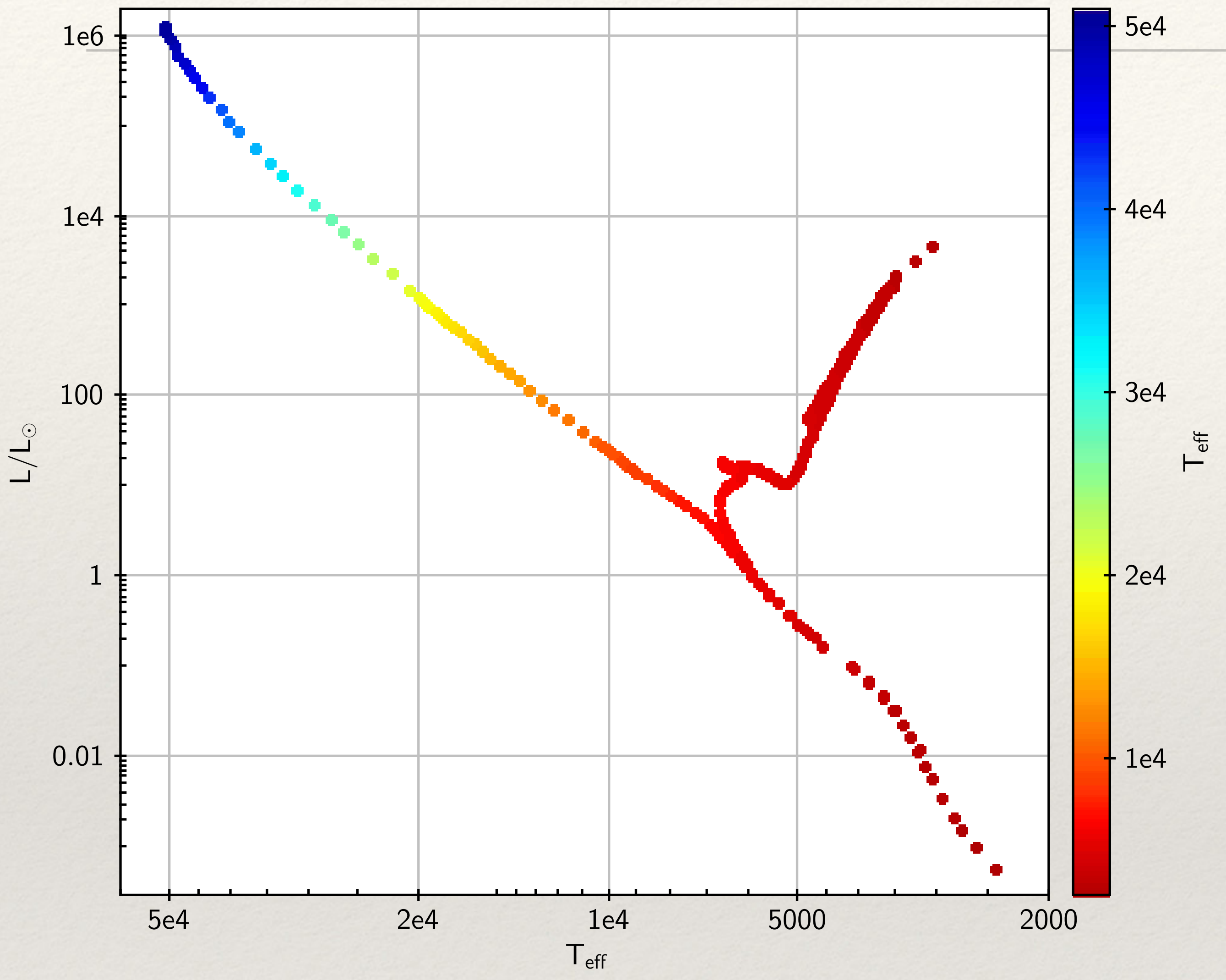

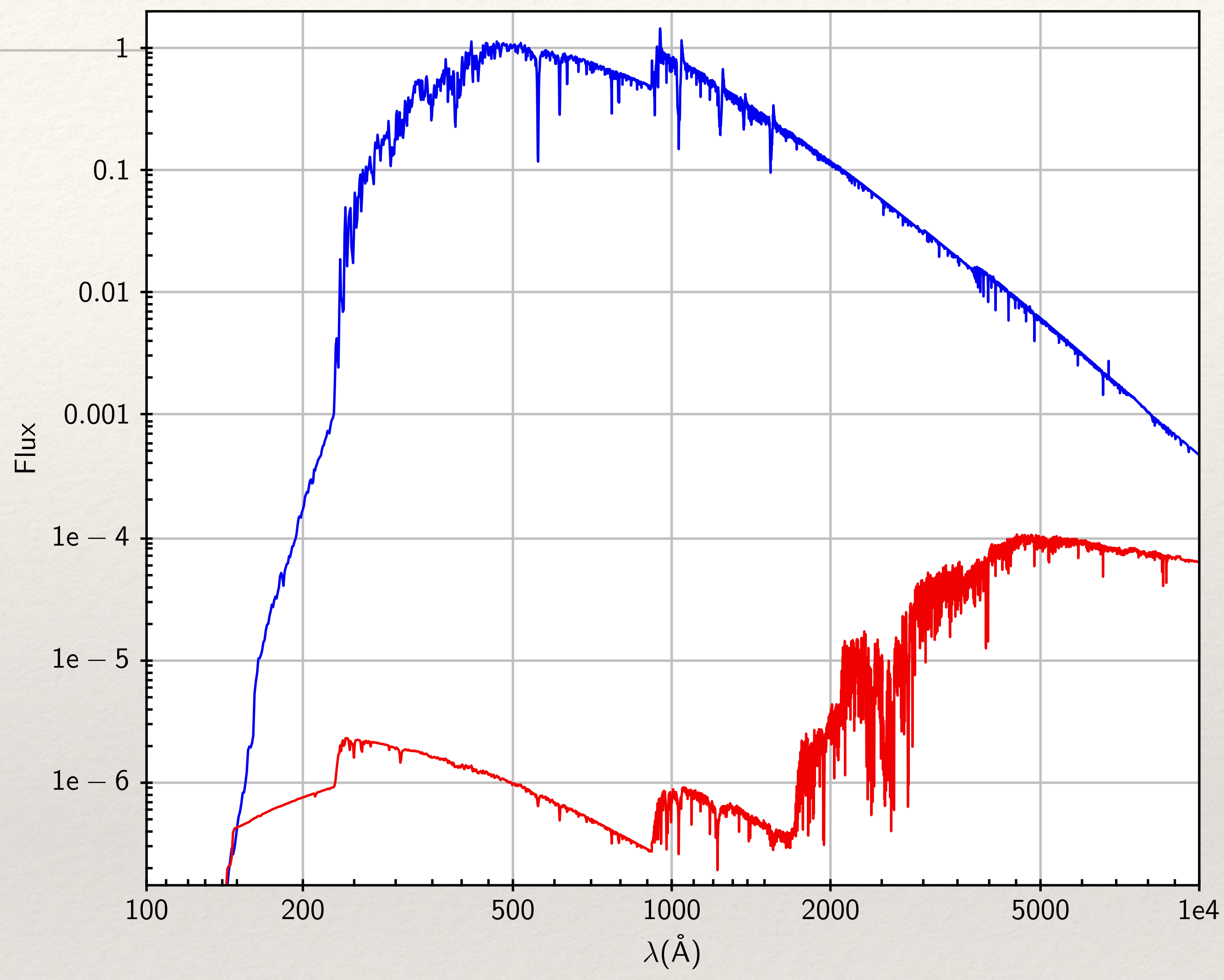

time

t = 5,000 Myr

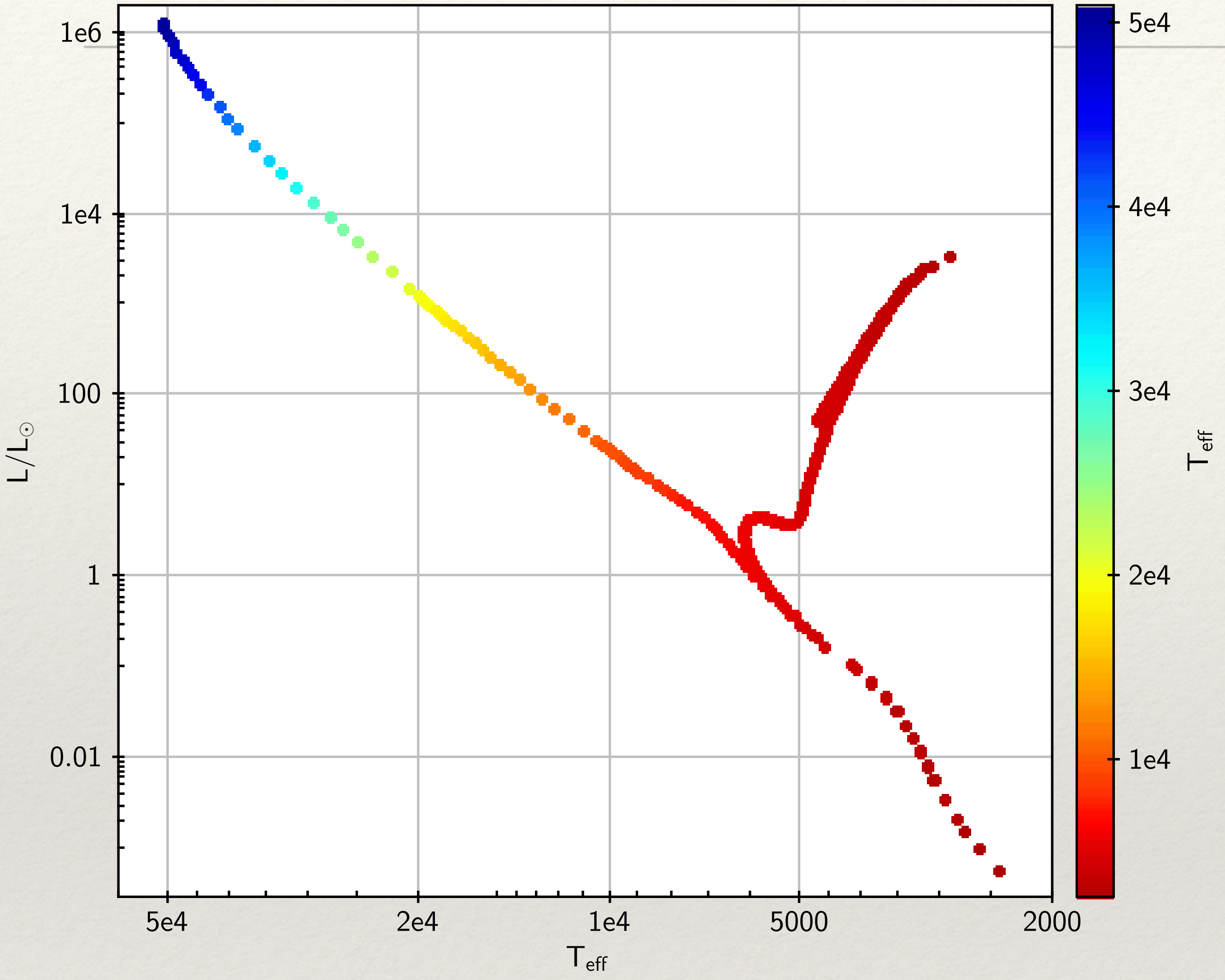

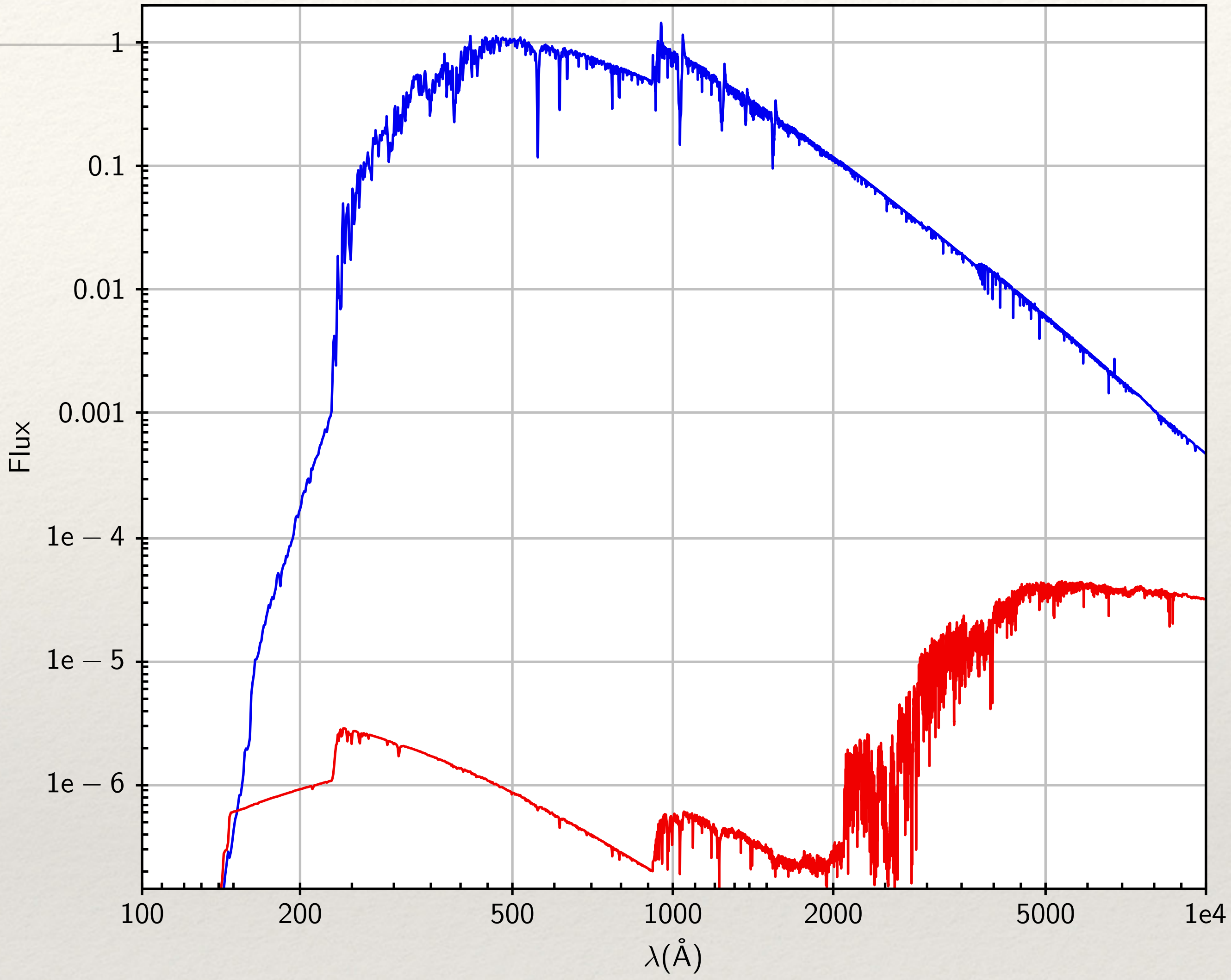

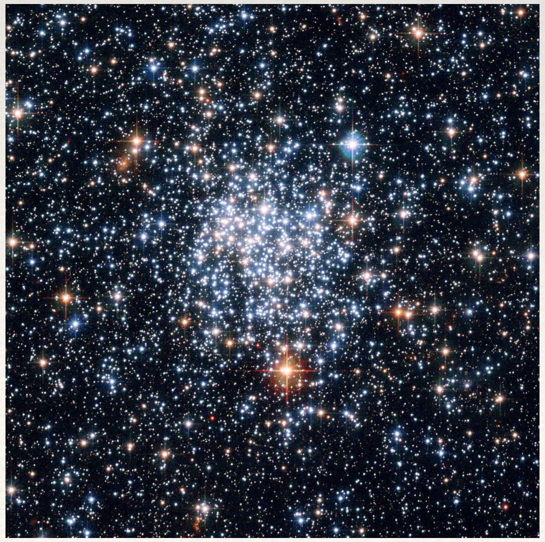

time

t = 10,000 Myr

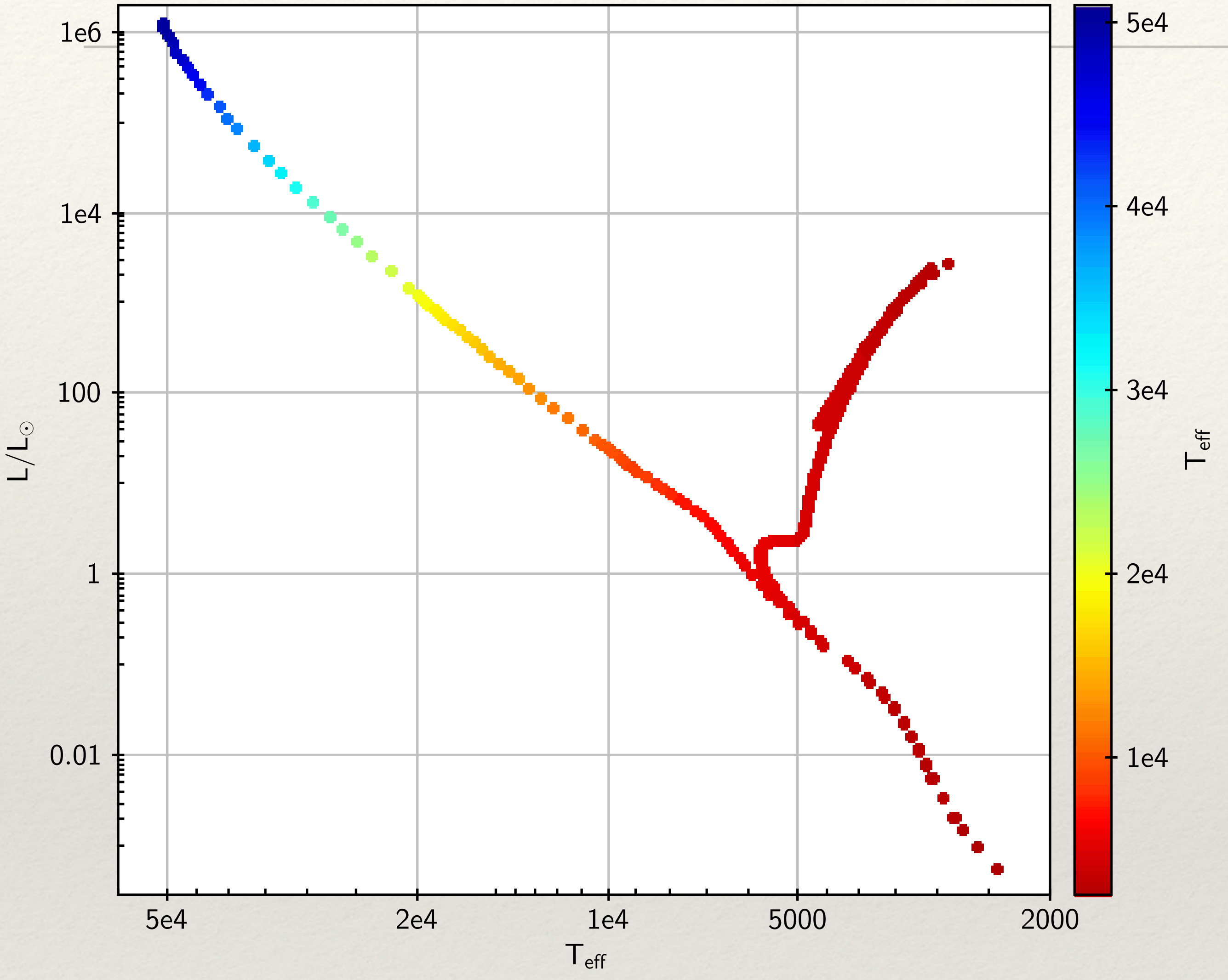

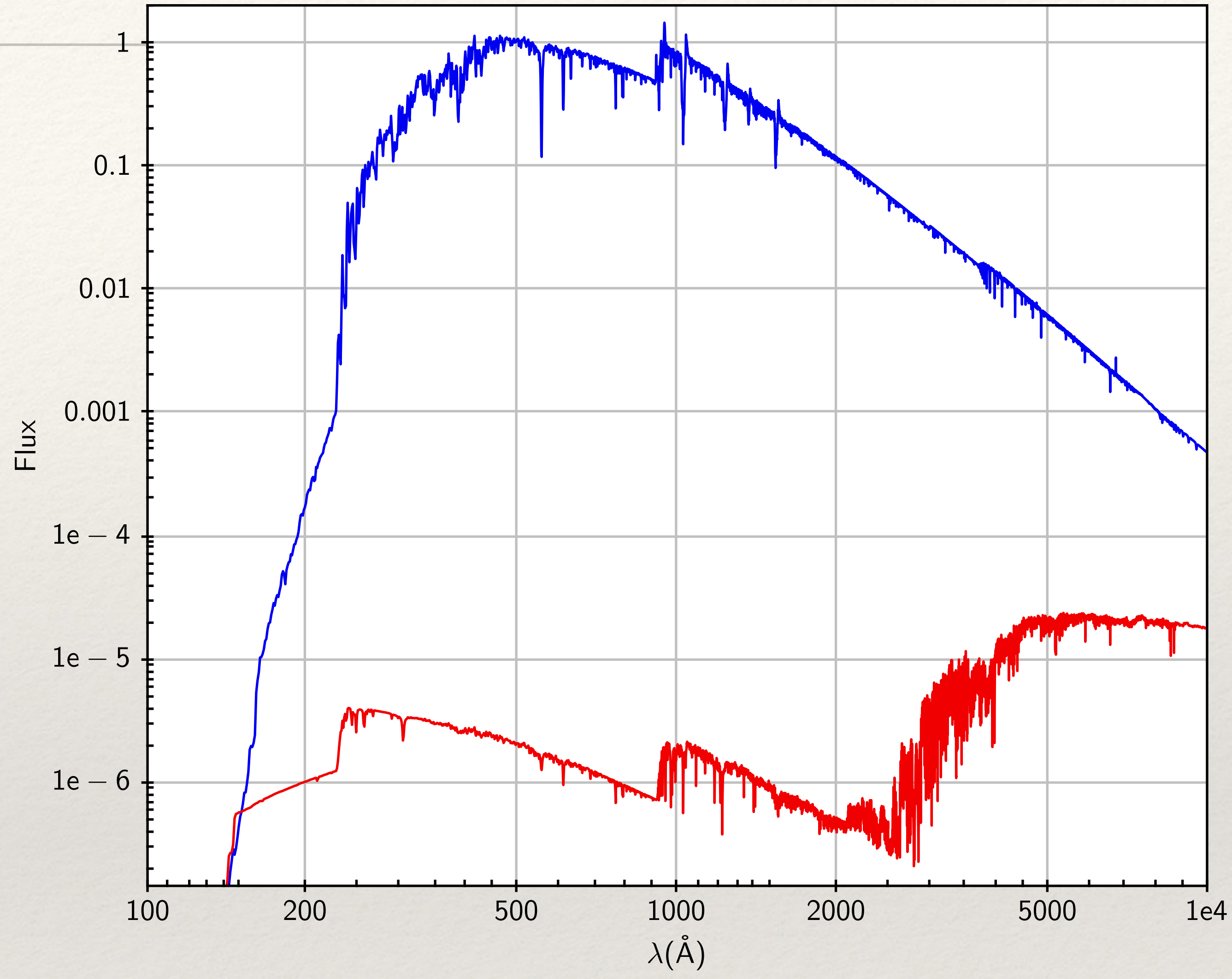

time

t = 13,600 Myr

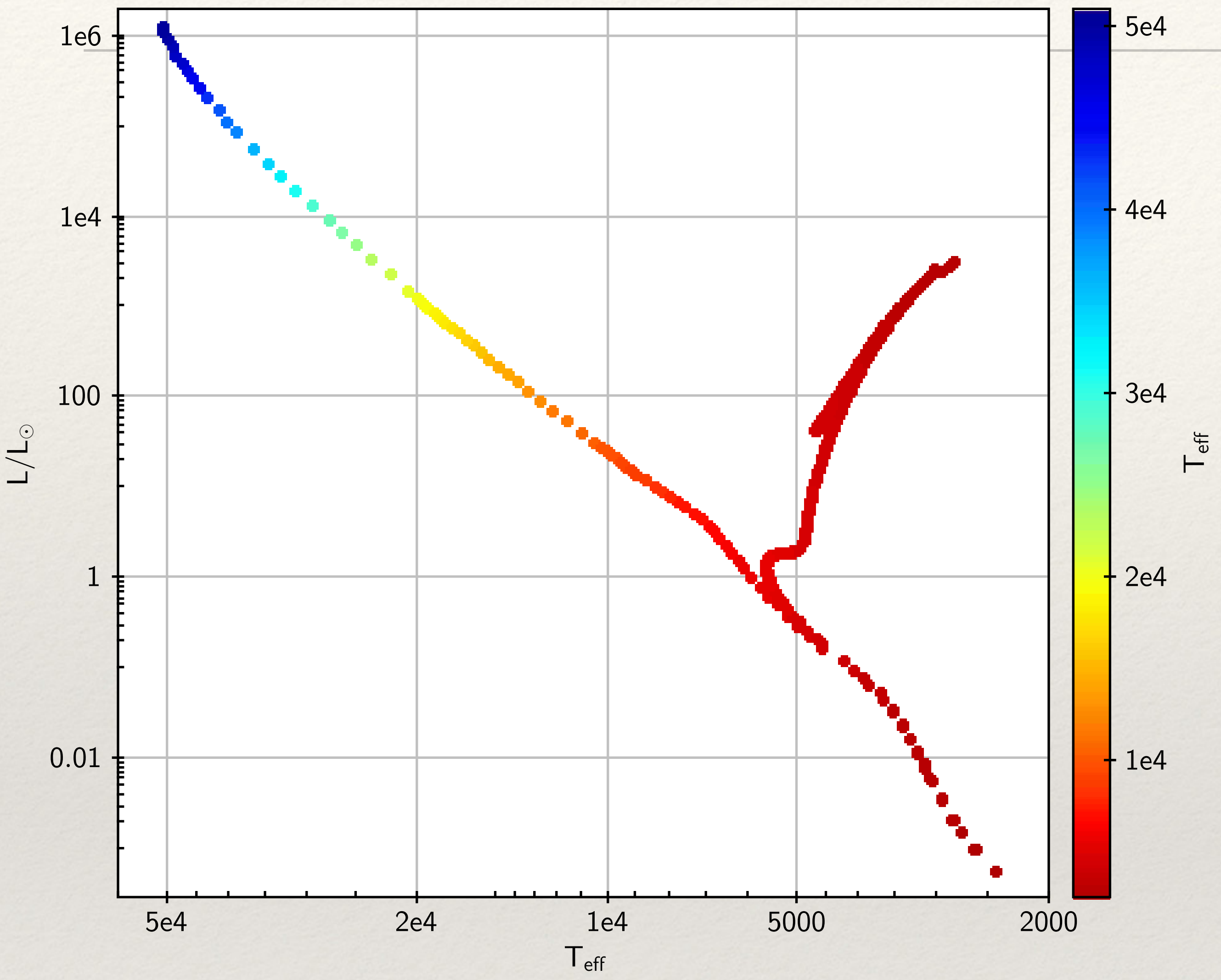

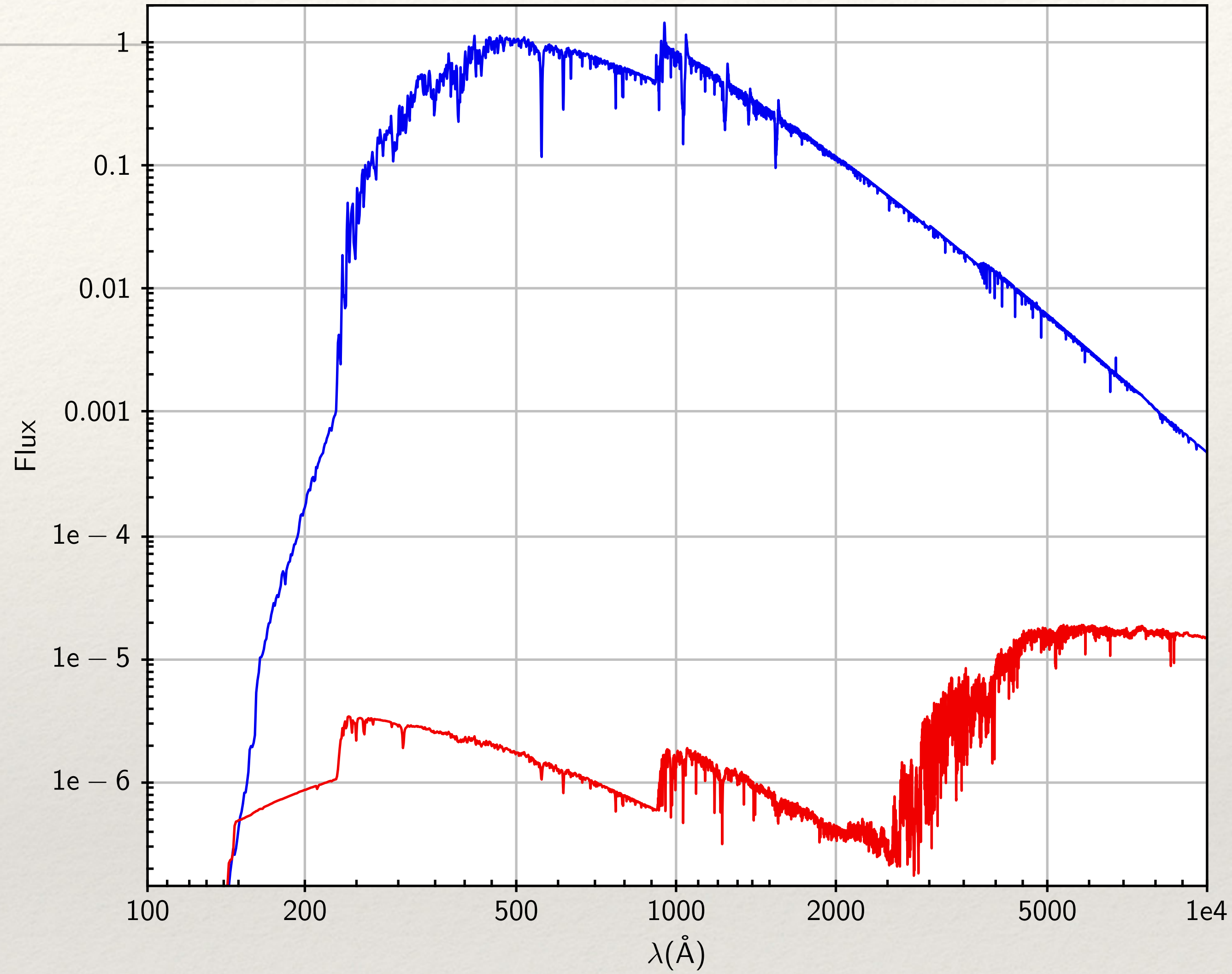

time

Measuring photometric colors

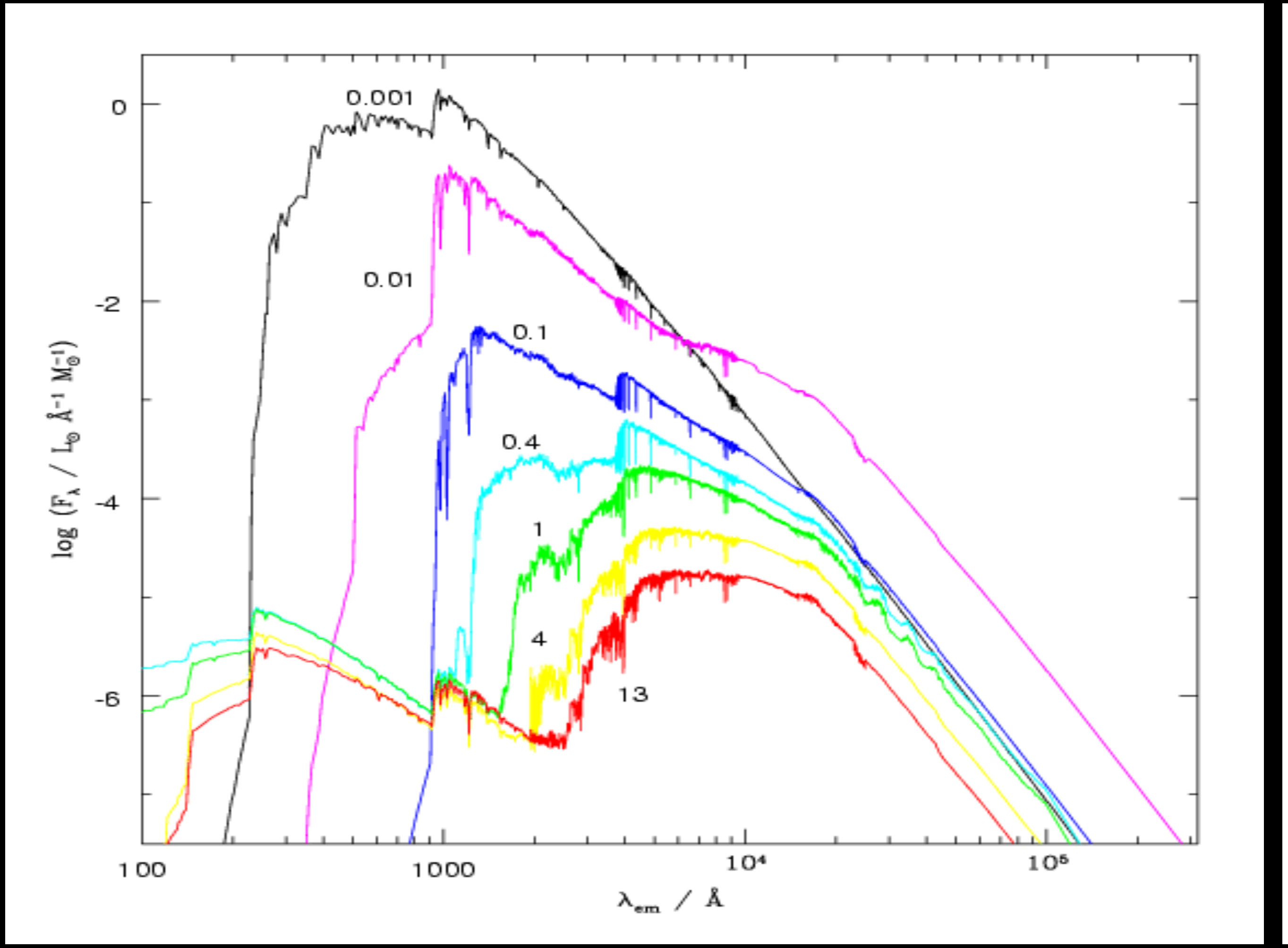

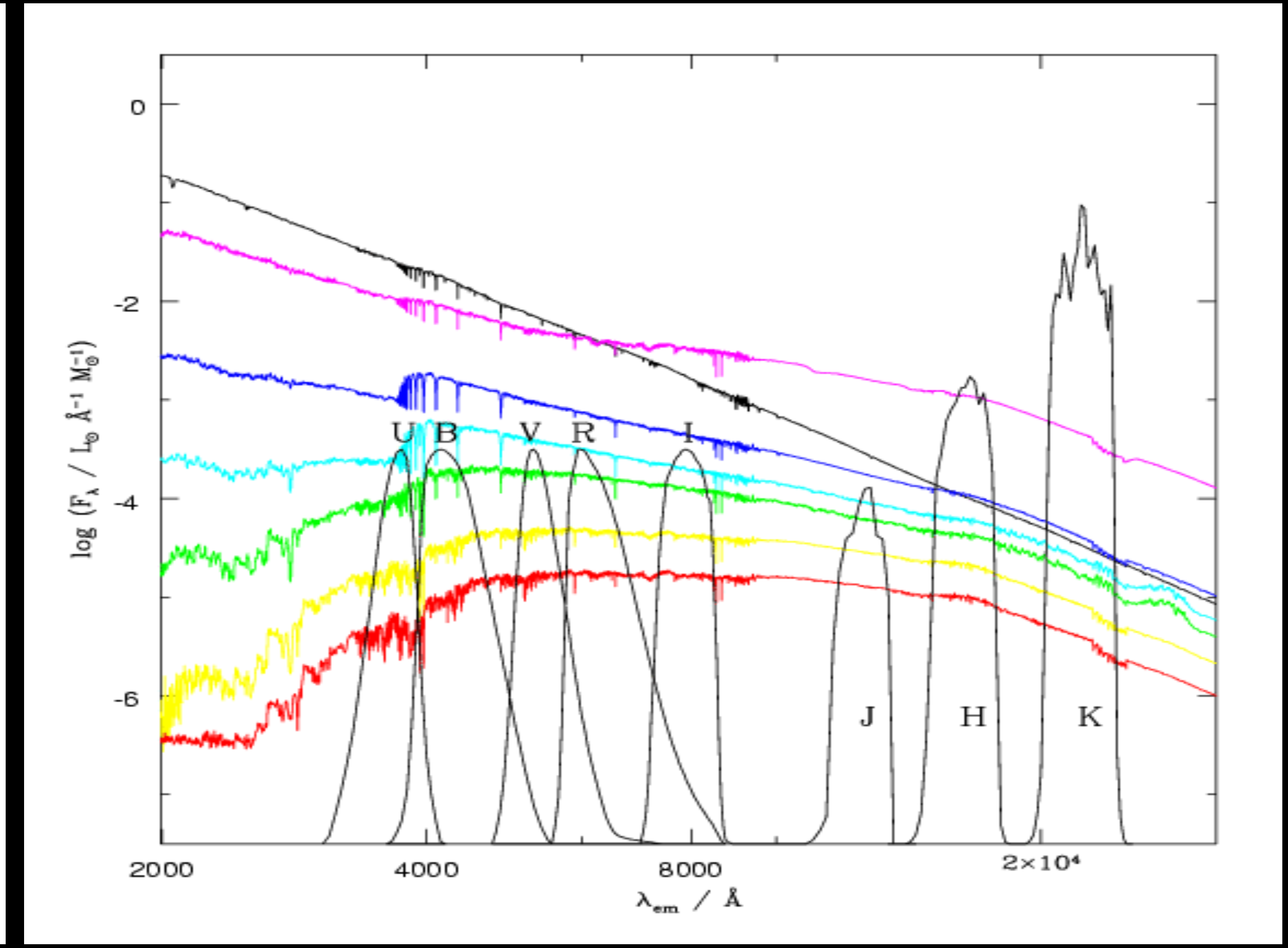

Spectral evolution

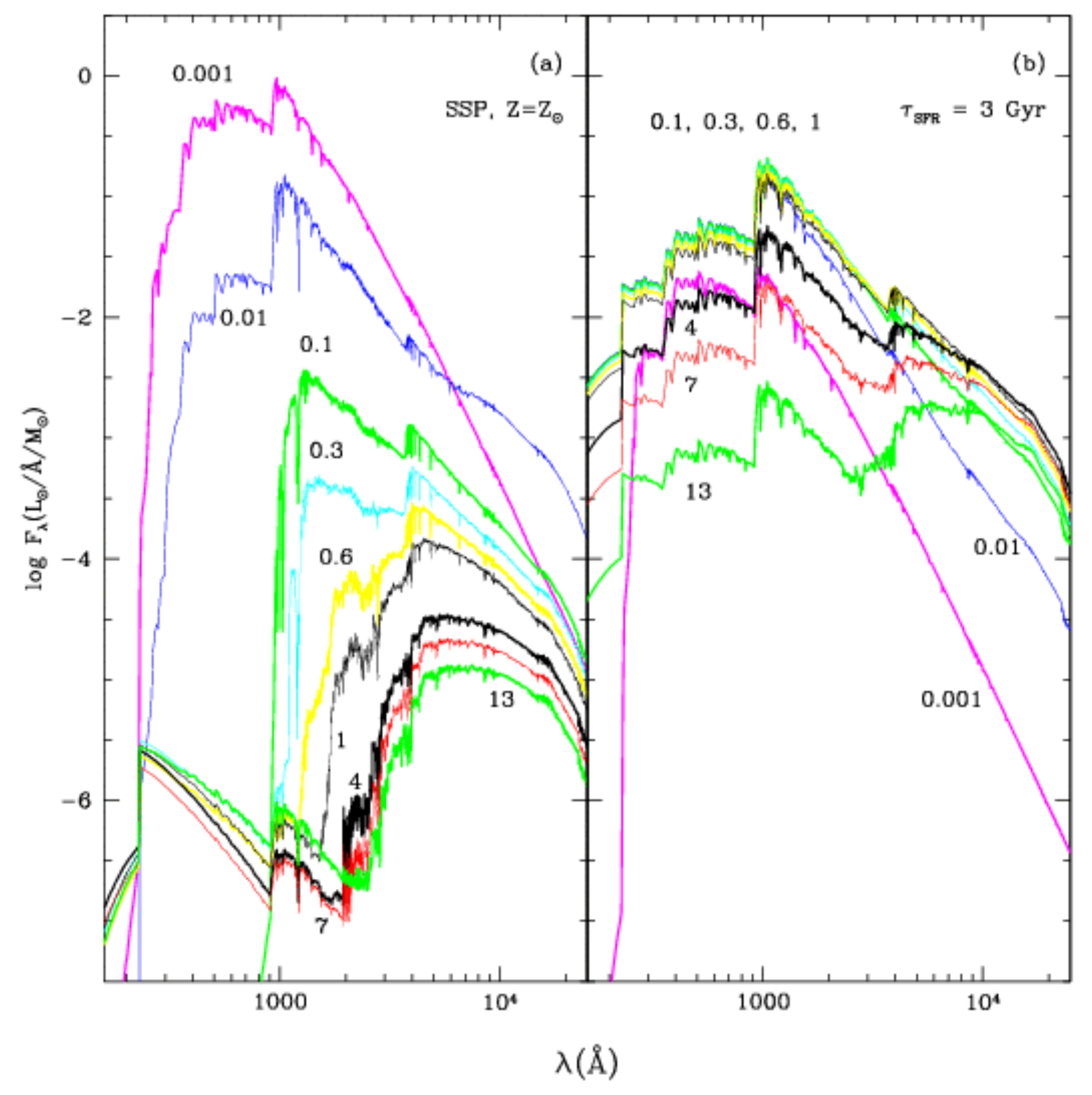

SIMPLE
vs.
COMPOSITE
stellar
populations

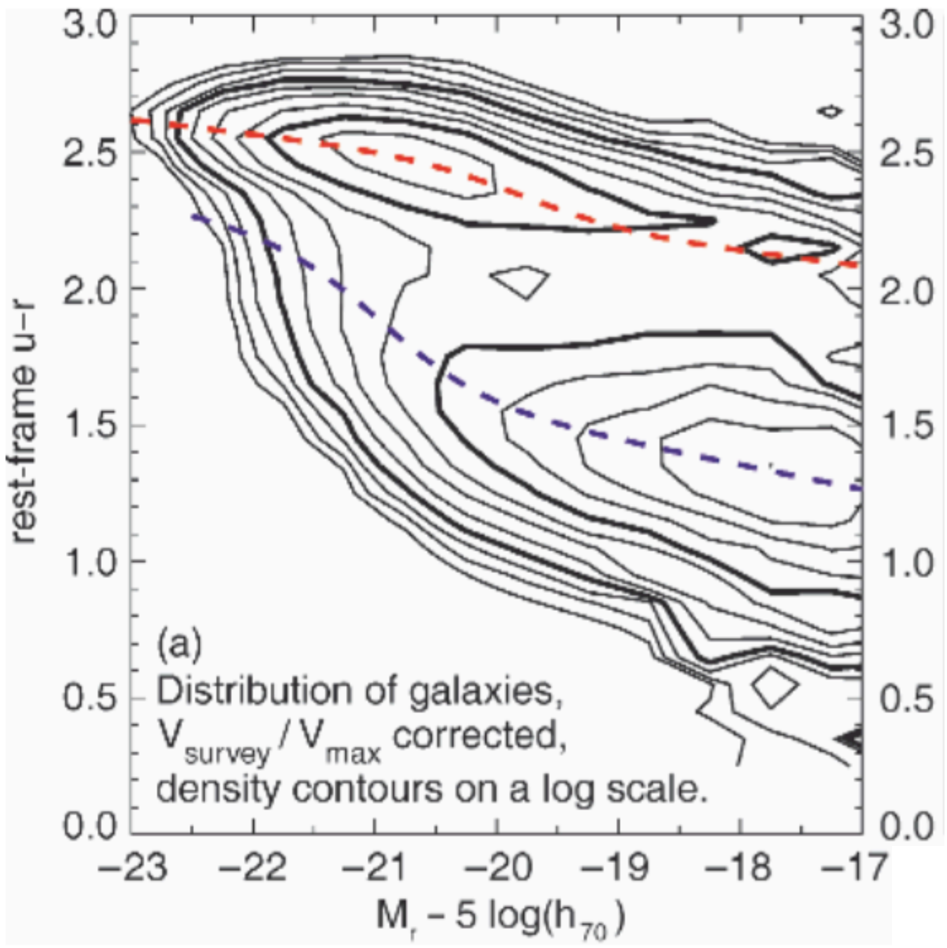

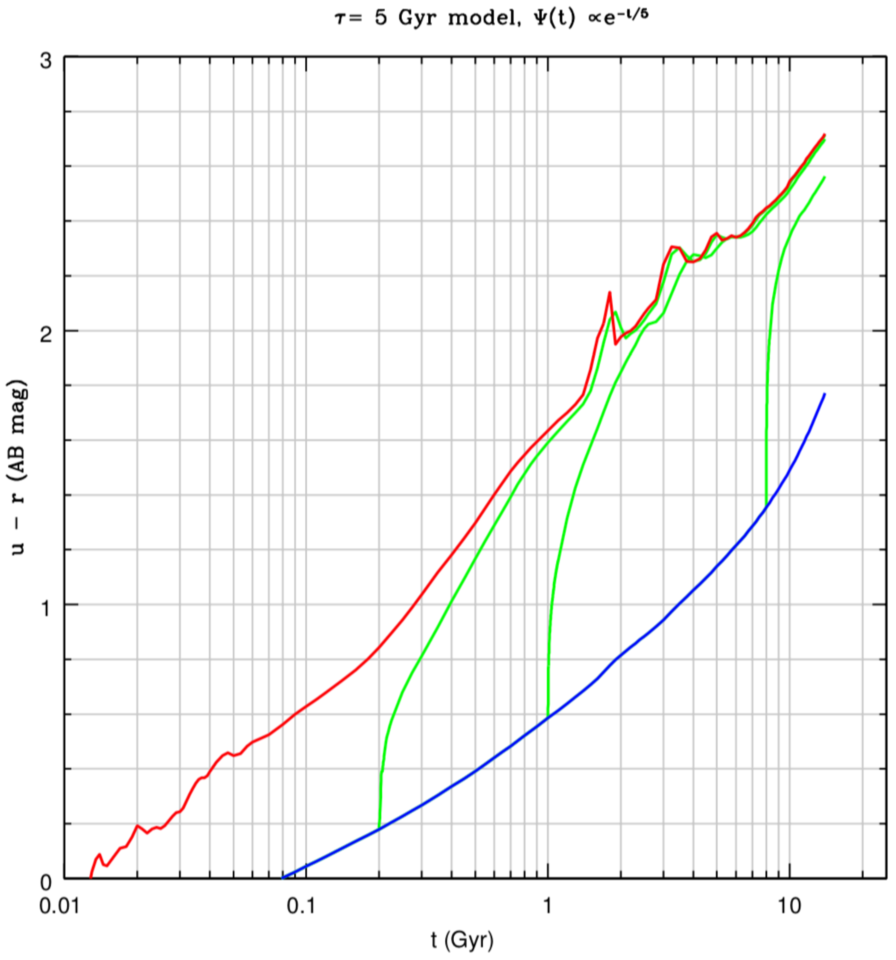

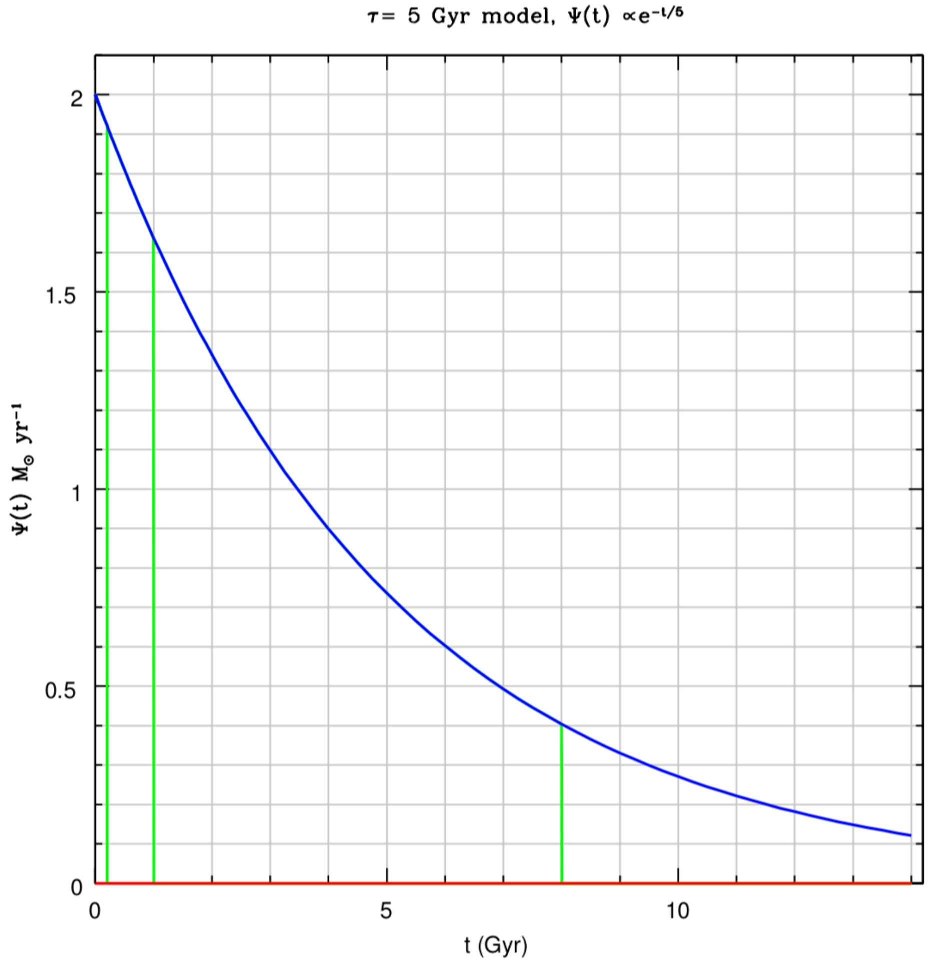

SFR:

$$\Psi(t) \propto e^{-t/5} \quad \text{(t in Gyr)}$$

Quenching at:

0.2, 1, and 8 Gyr

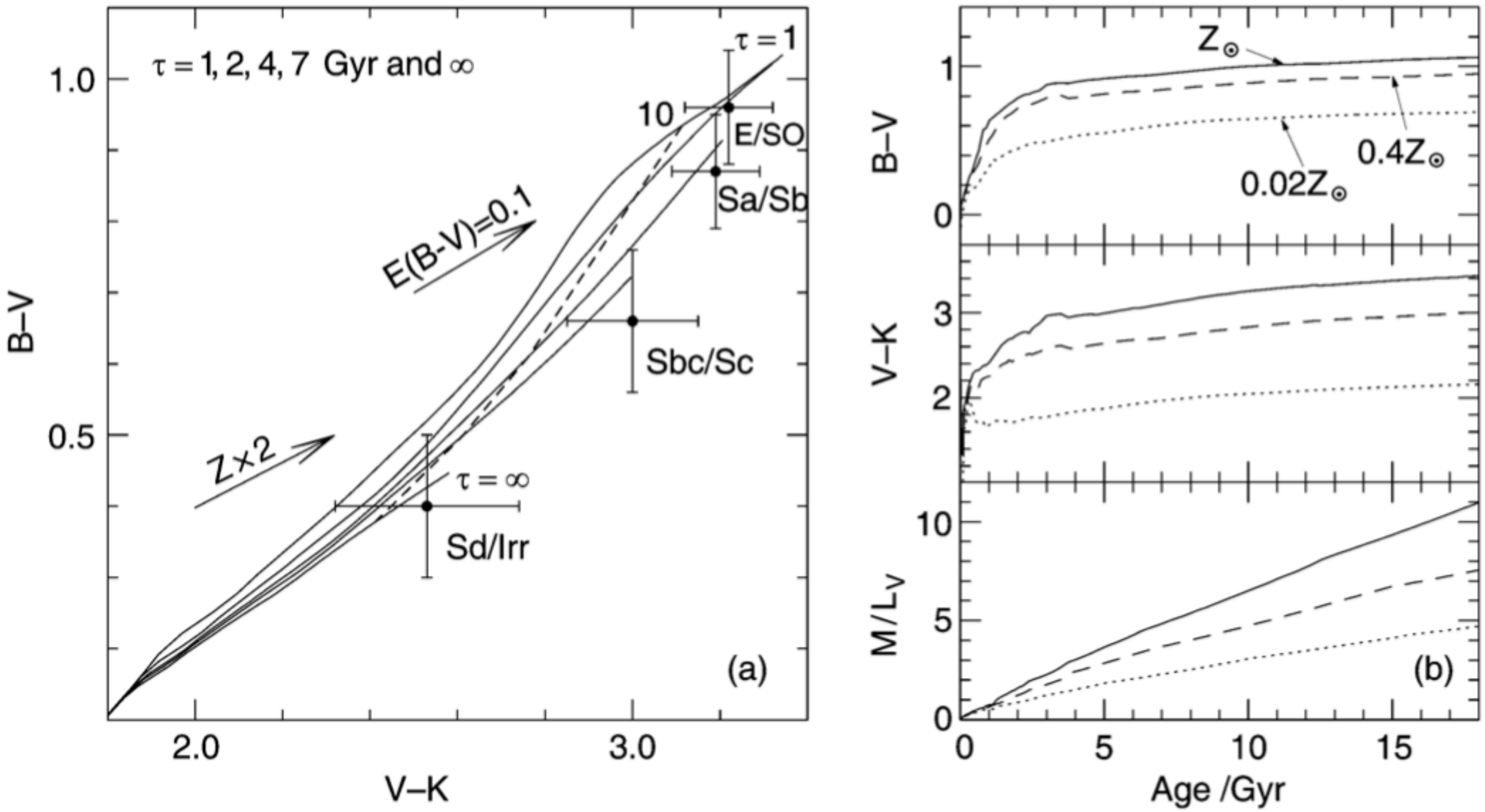

Fig. 3.49. a) Evolution of colors between $0 \leq t \leq 17 \times 10^9$ yr for a stellar population with star-formation rate given by (3.69), for five different values of the characteristic time-scale τ ($\tau = \infty$ is the limiting case for a constant star-formation rate) –Galactic center see solid curves. The typical colors for four different morphological types of galaxies are plotted. For each τ, the evolution begins at the lower left, i.e., as a blue population in both color indices. In the case of constant star formation, the population never becomes redder than Irr's; to achieve redder colors, τ has to be smaller. The dashed line connects points of $t = 10^{10}$ yr on the different curves. Here, a Salpeter IMF and Solar metallicity was assumed. The shift in color obtained by doubling the metallicity is indicated by an arrow, as well as that due to an extinction coefficient of $E(B-V) = 0.1$; both effects will make galaxies appear redder. **b**) The dependence of colors and M/L on the metallicity of the population

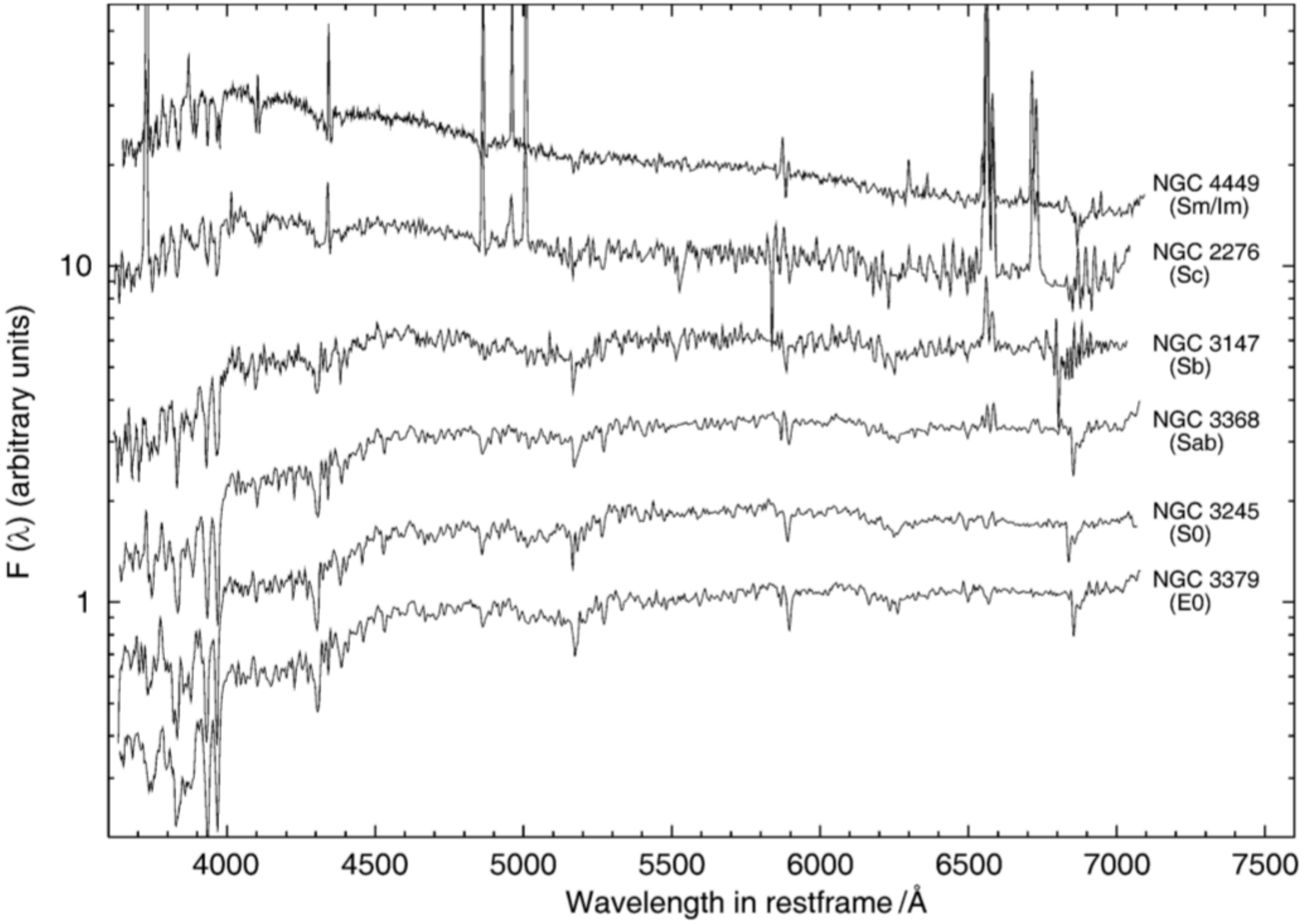

Fig. 3.50. Spectra of galaxies of different types, where the spectral flux is plotted logarithmically in arbitrary units. The spectra are ordered according to the Hubble sequence, with early types at the bottom and late-type spectra at the top

but …

In reality we observe this evolution in reverse, from the present to the past

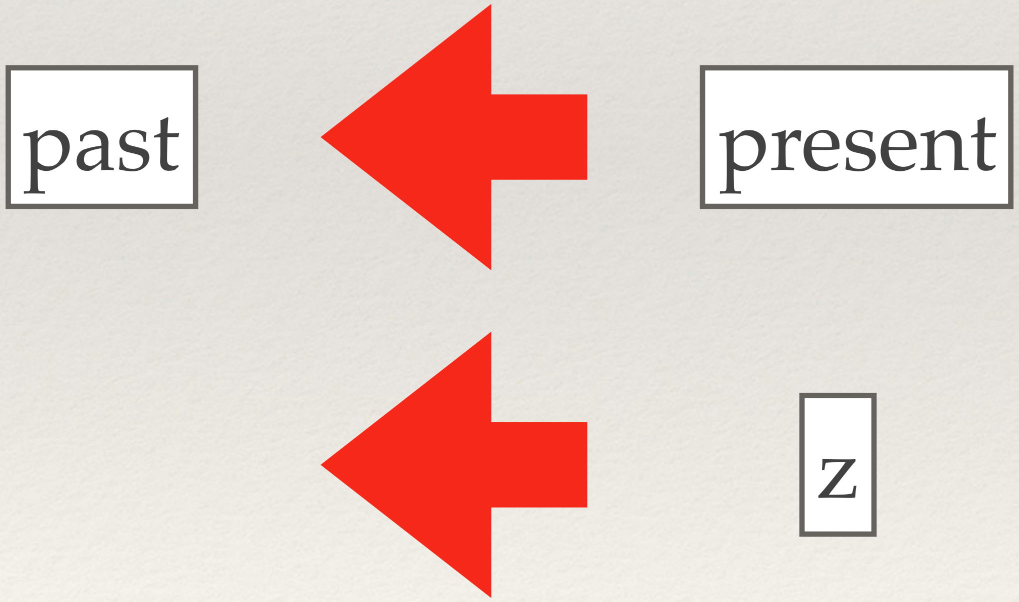

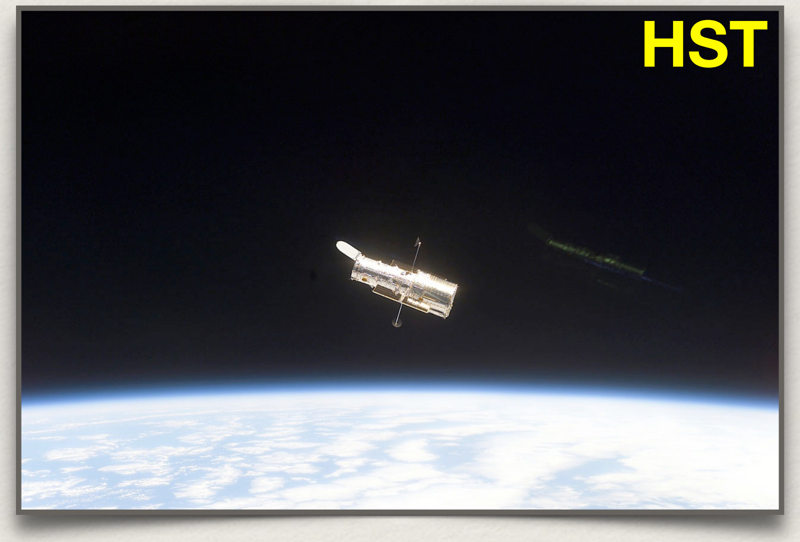

Age of the universe vs. redshift (z)

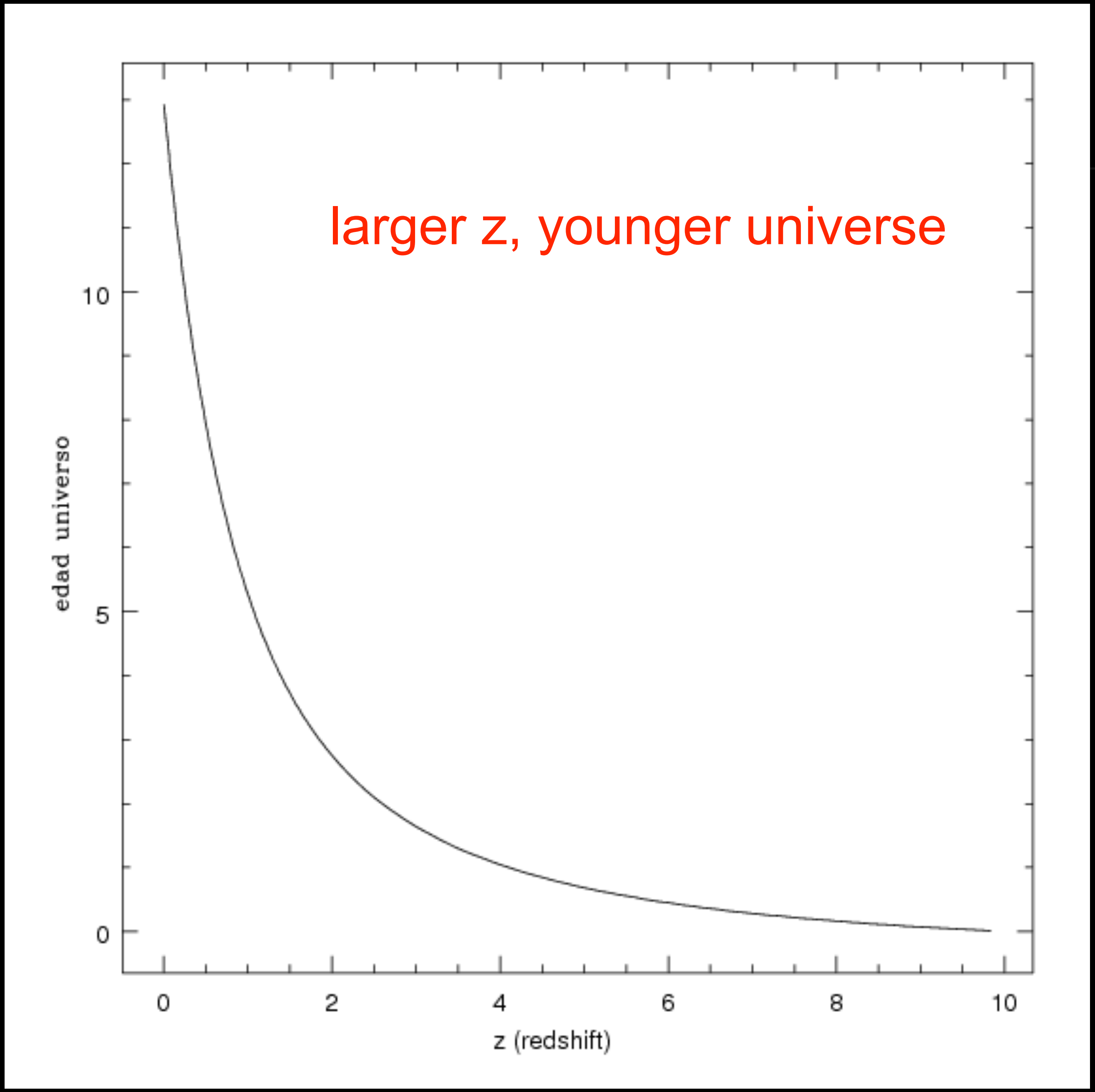

% of age at given z

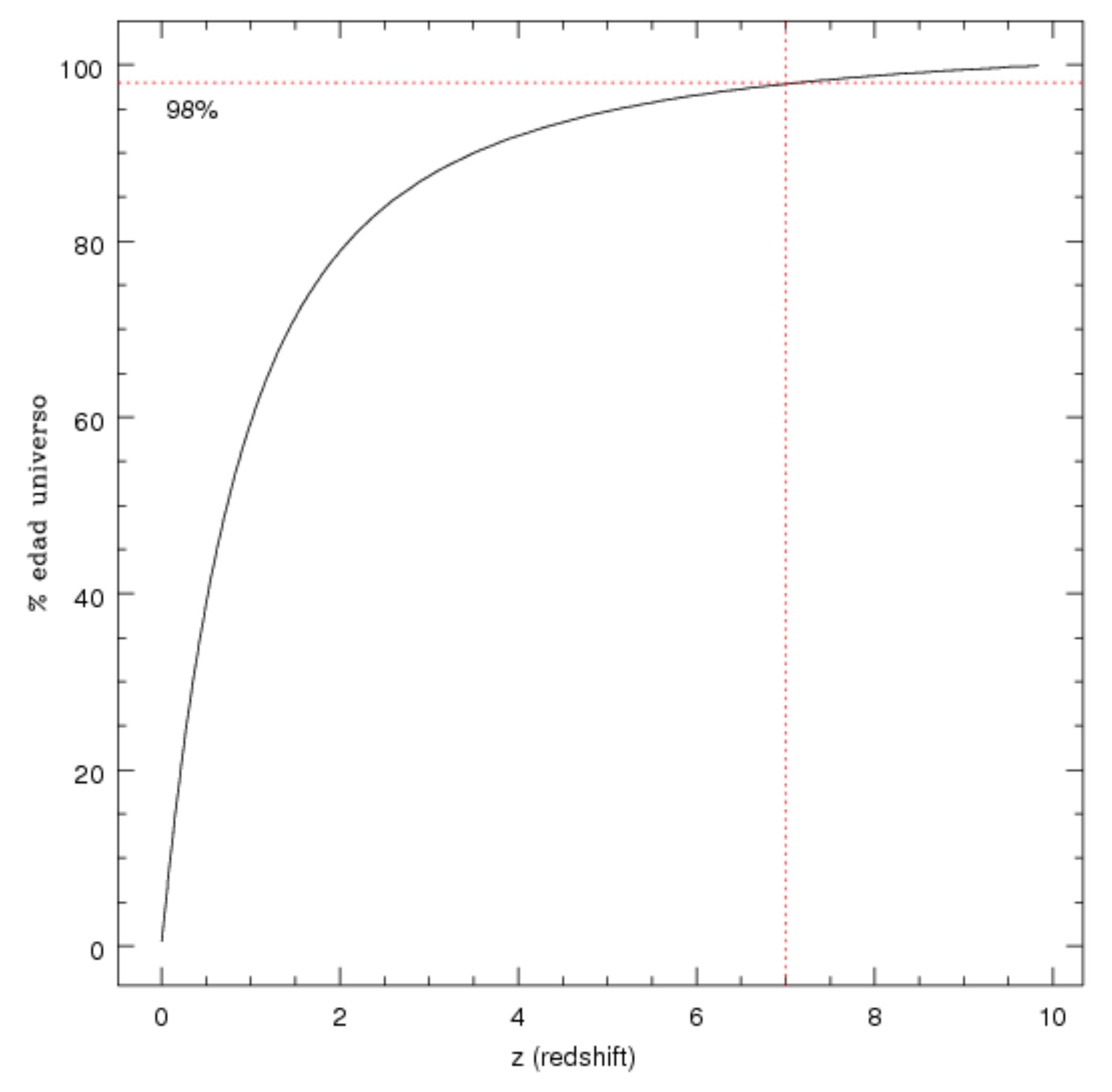

Objects at z = 7 have been there for 98% of the age of the universe

t = 13,600 Myr

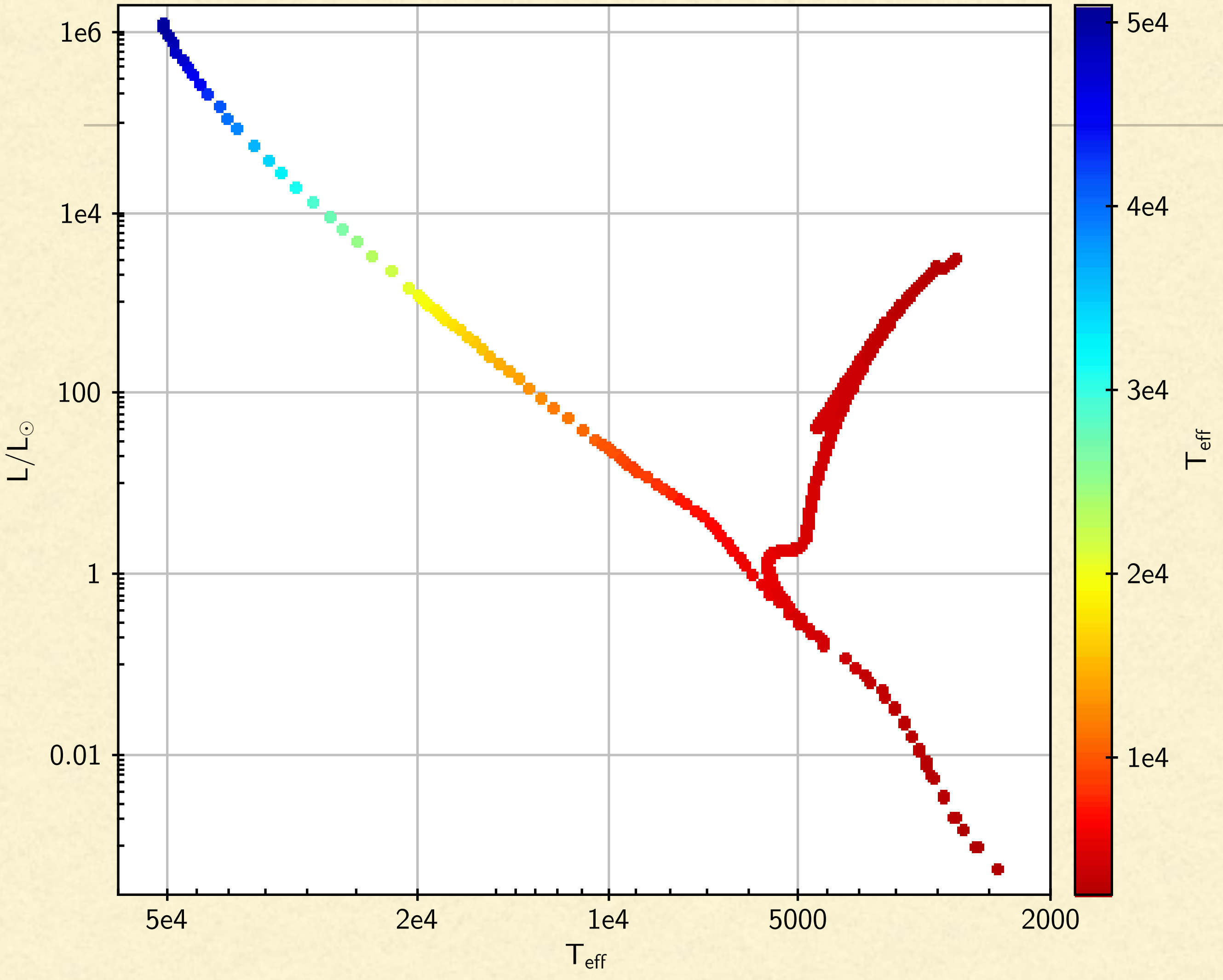

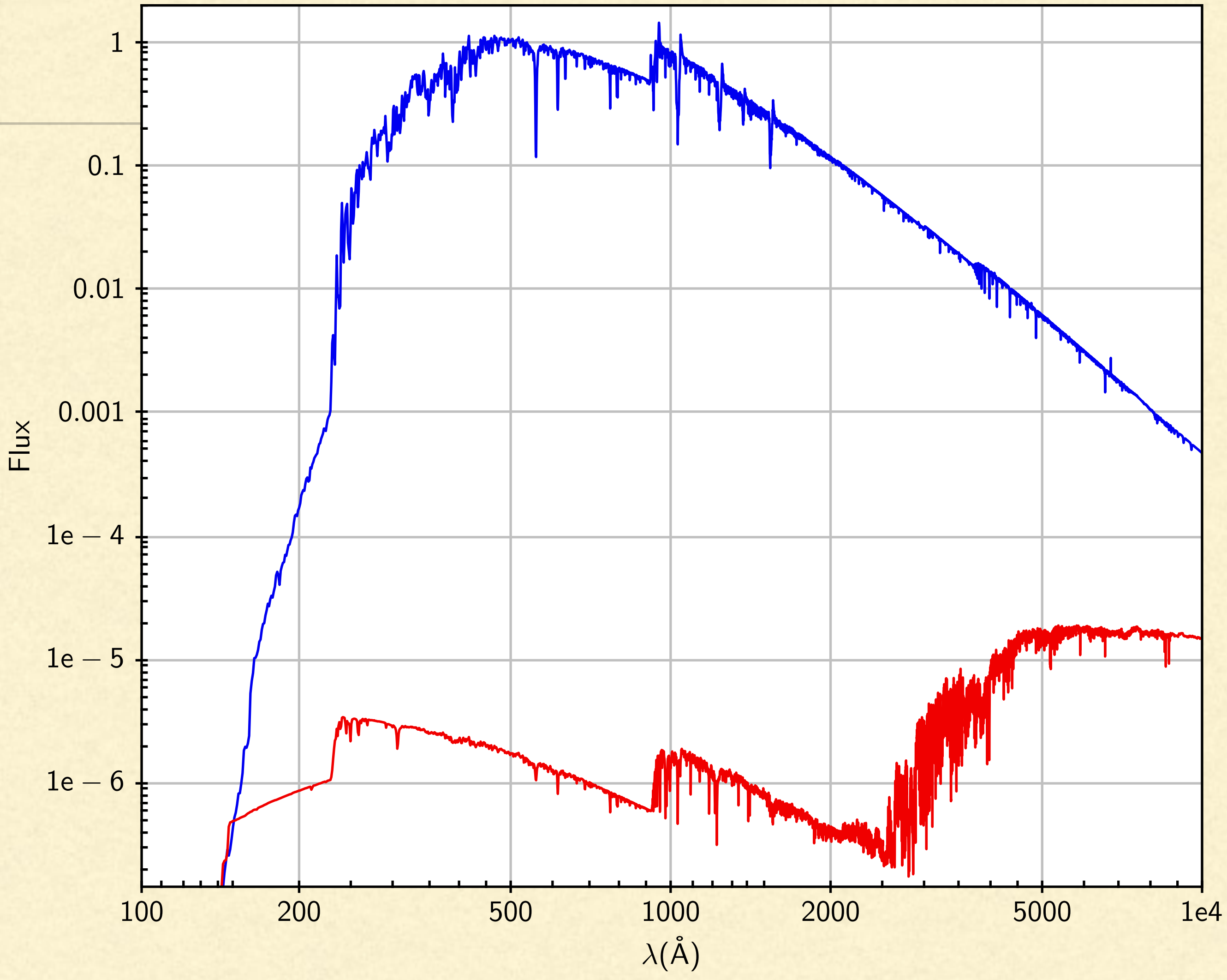

z = 0

t = 10,000 Myr

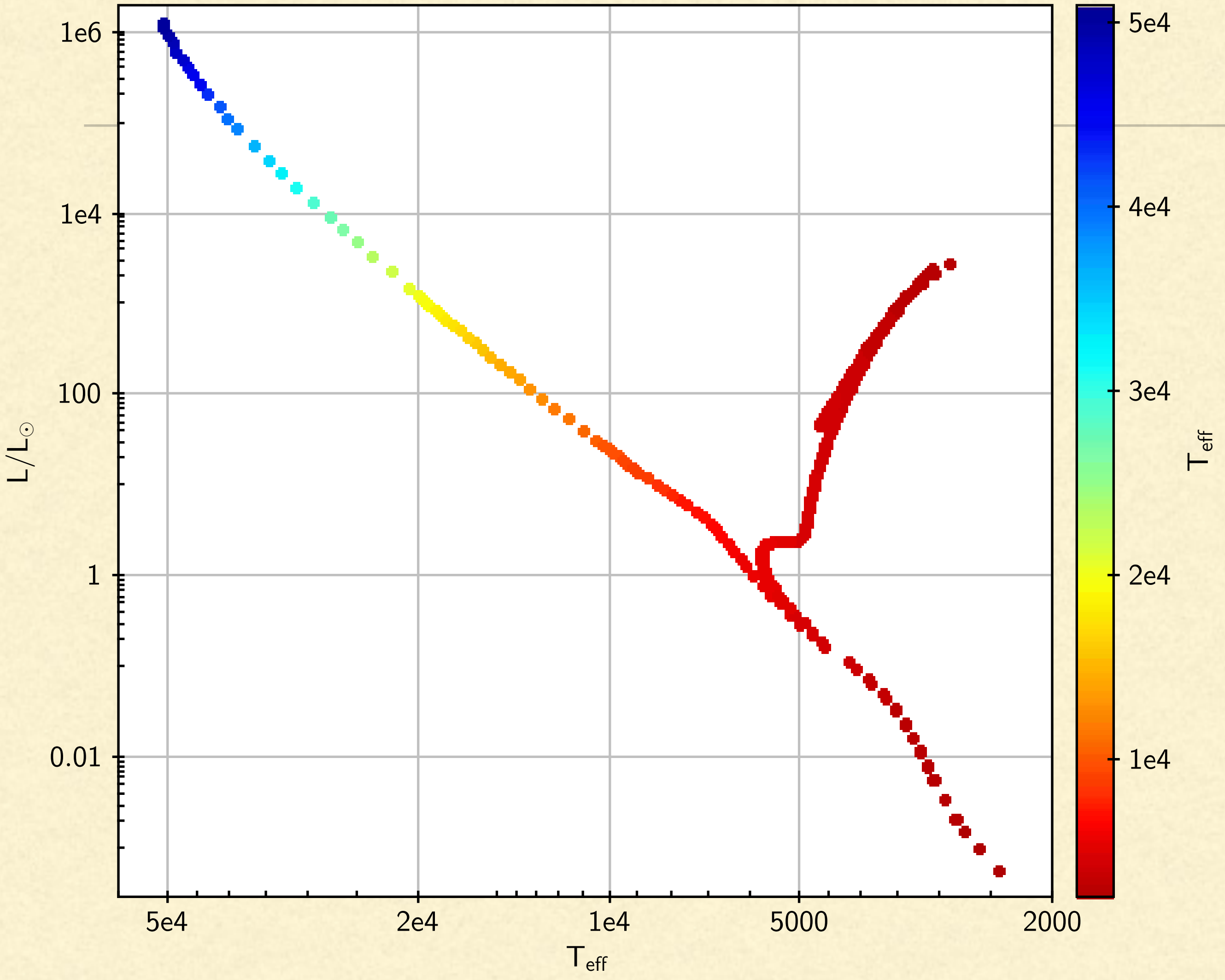

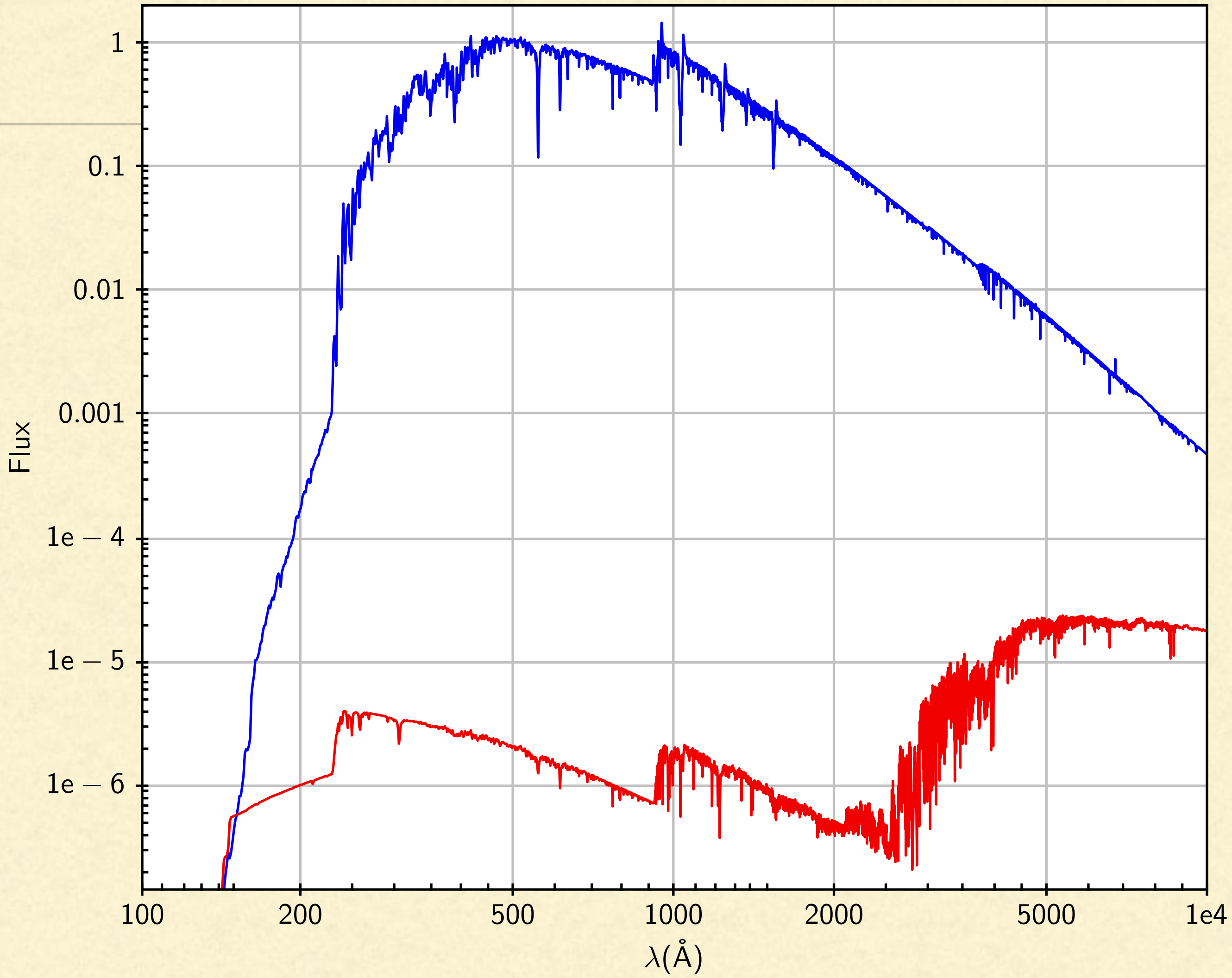

z = 0.3

t = 5,000 Myr

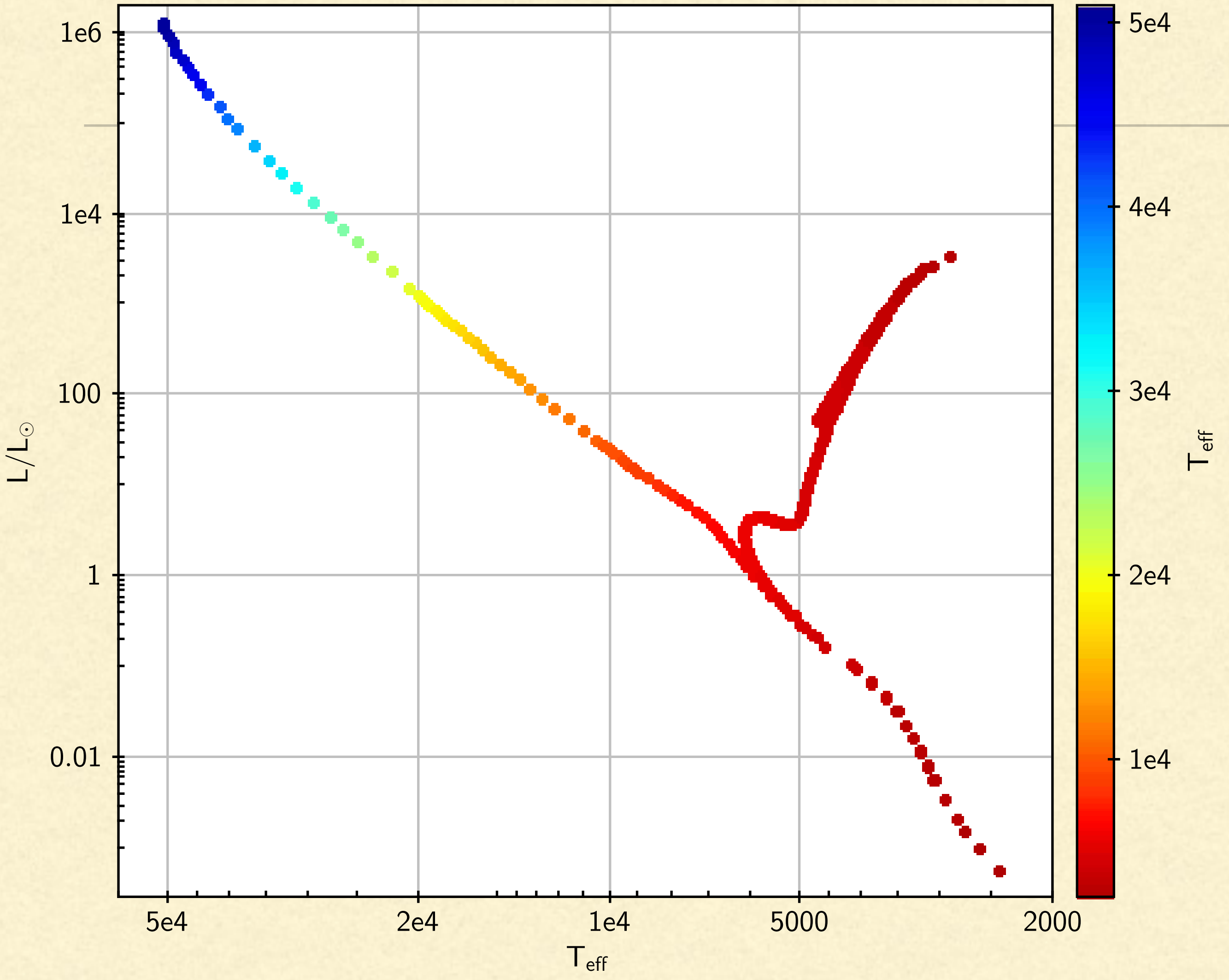

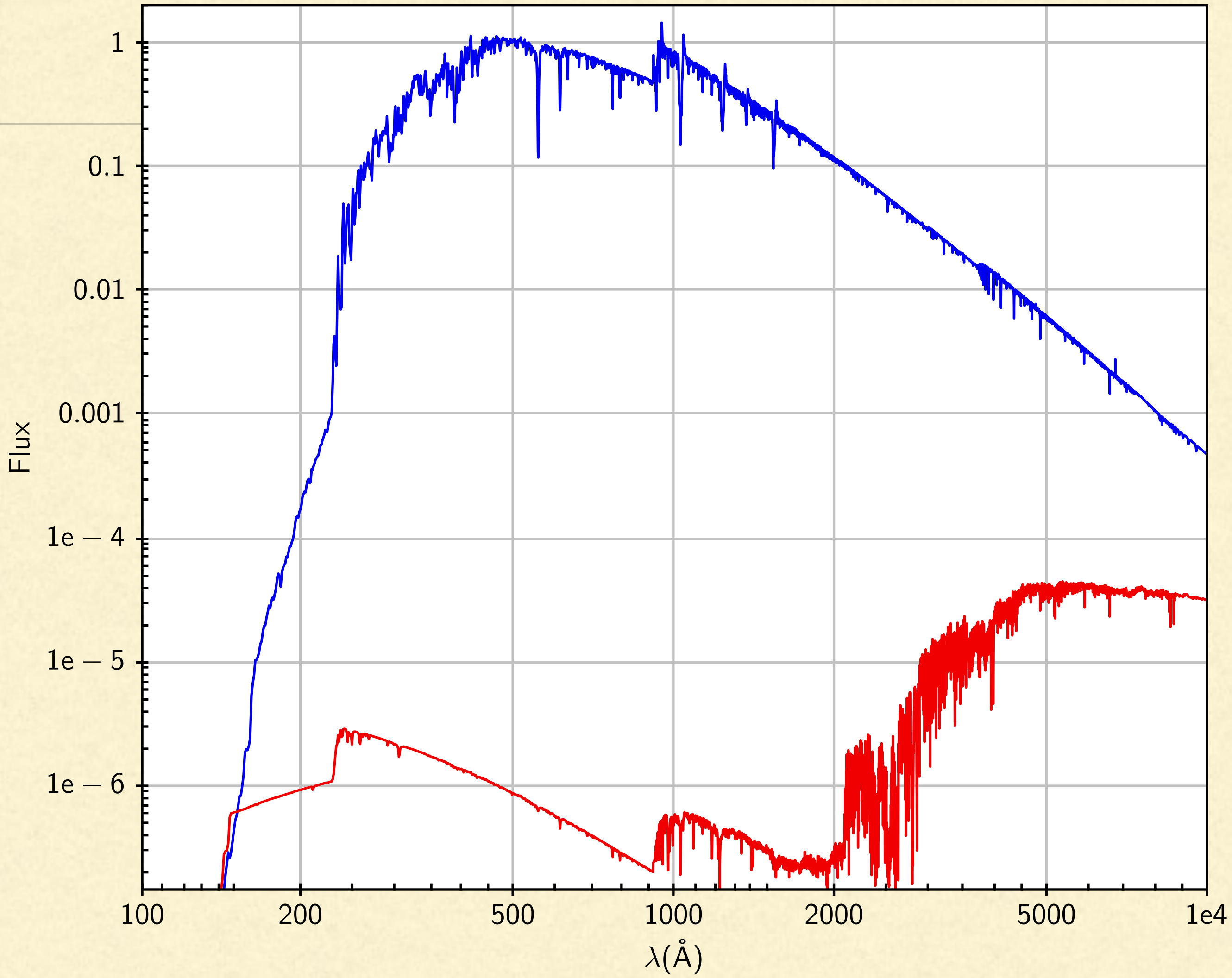

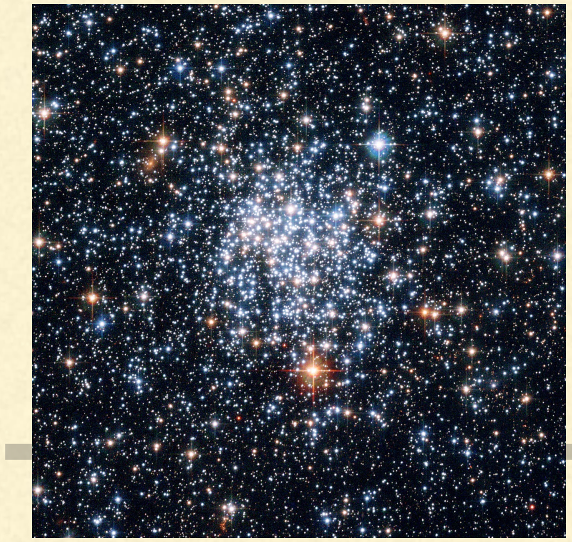

z = 1.2

t = 2,000 Myr

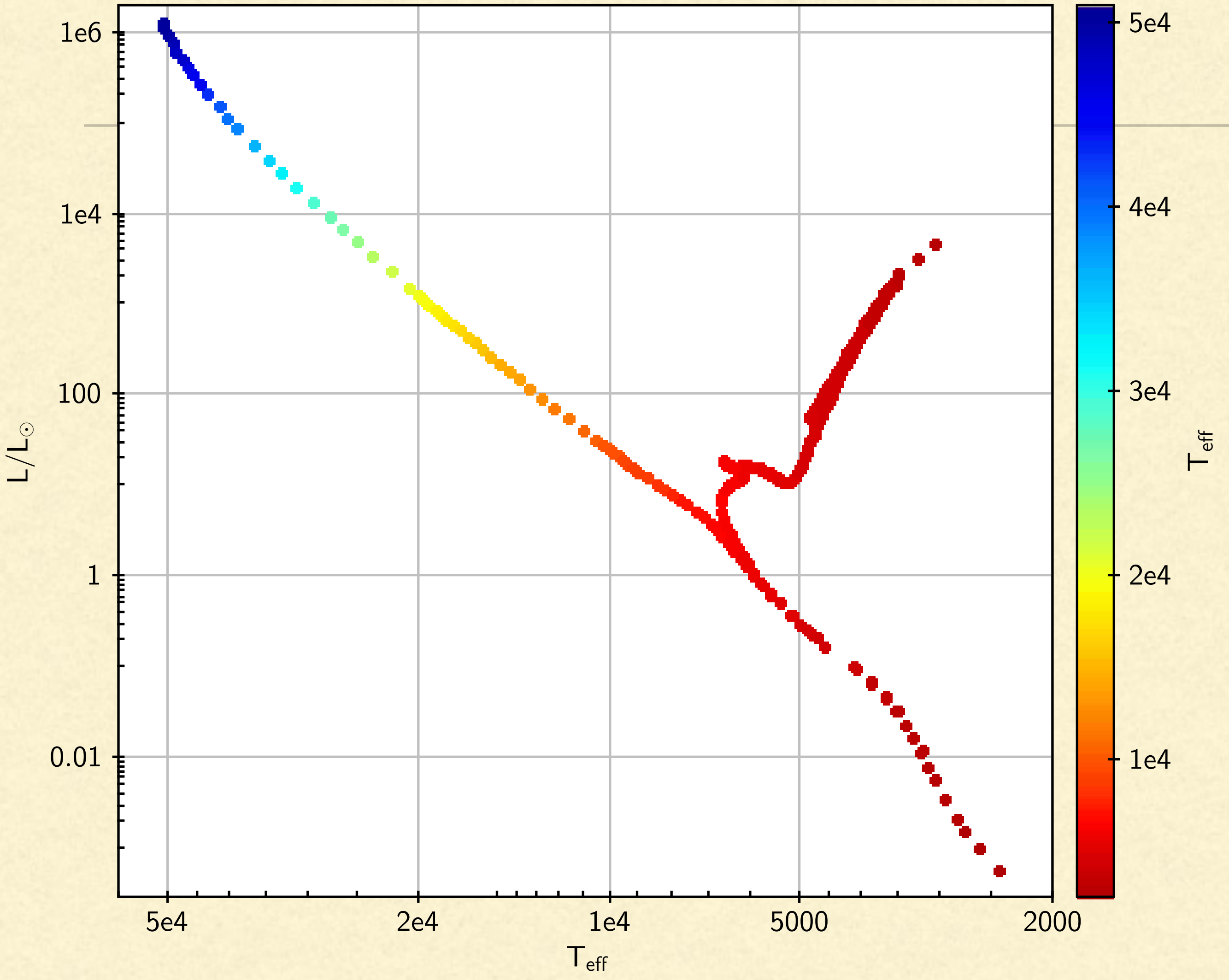

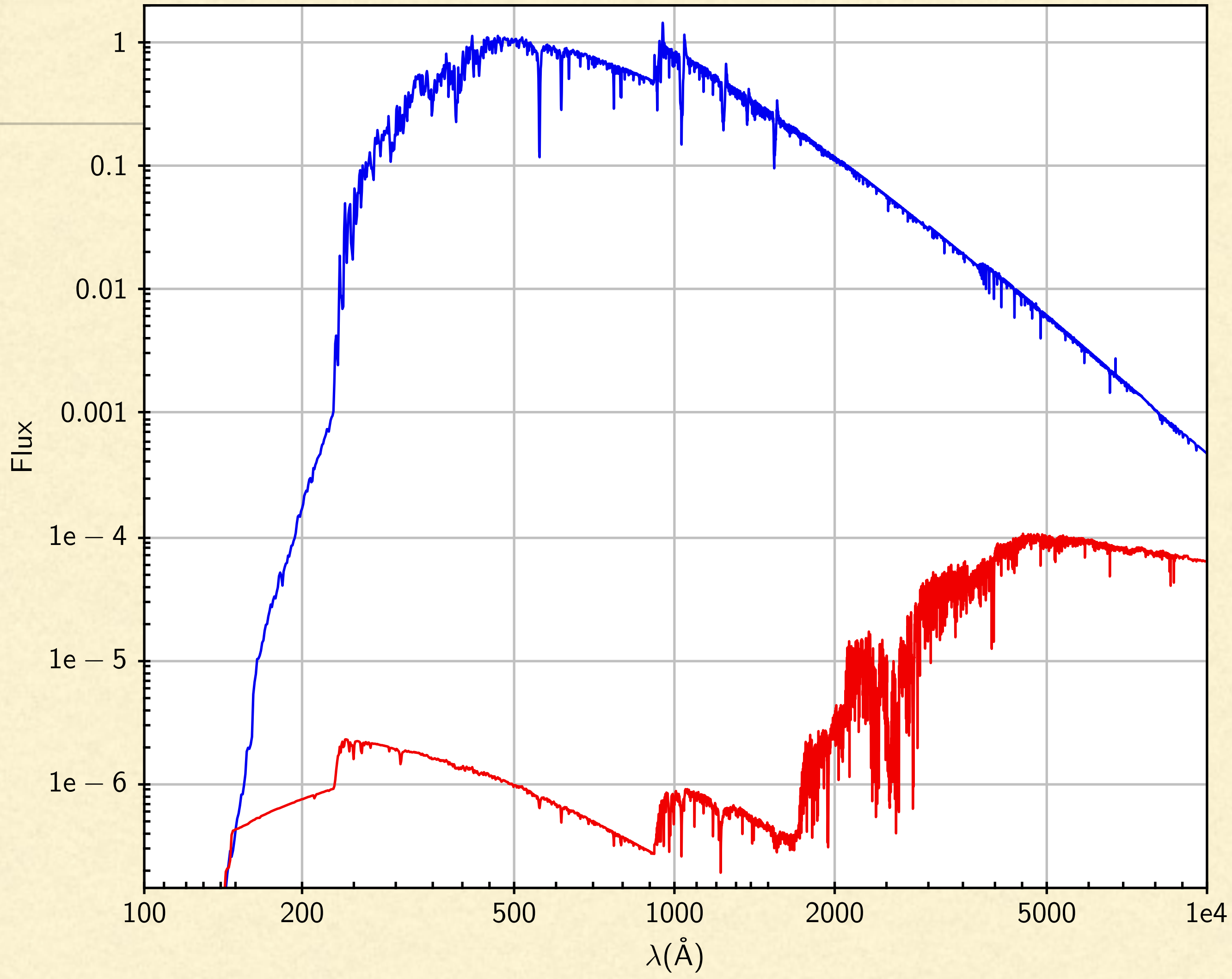

z = 3.2

t = 1,000 Myr

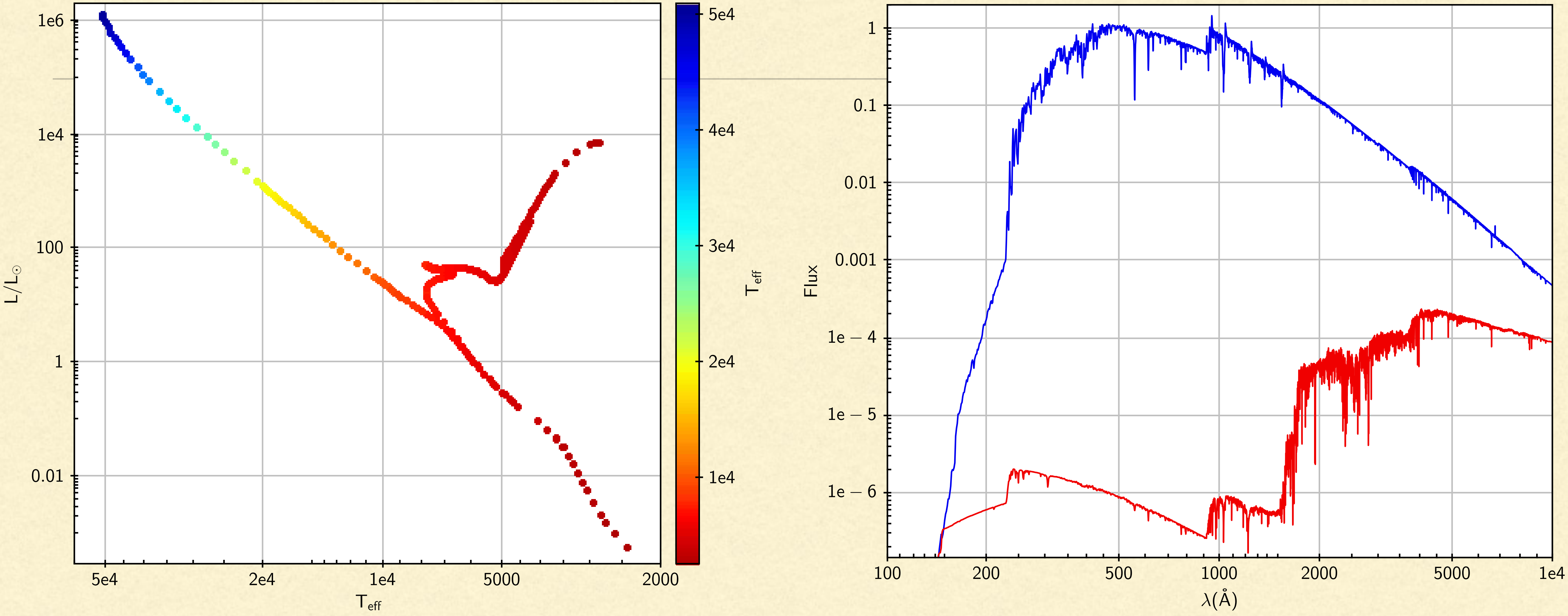

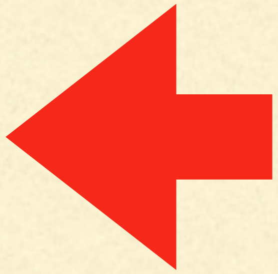

z = 5.6

t = 500 Myr

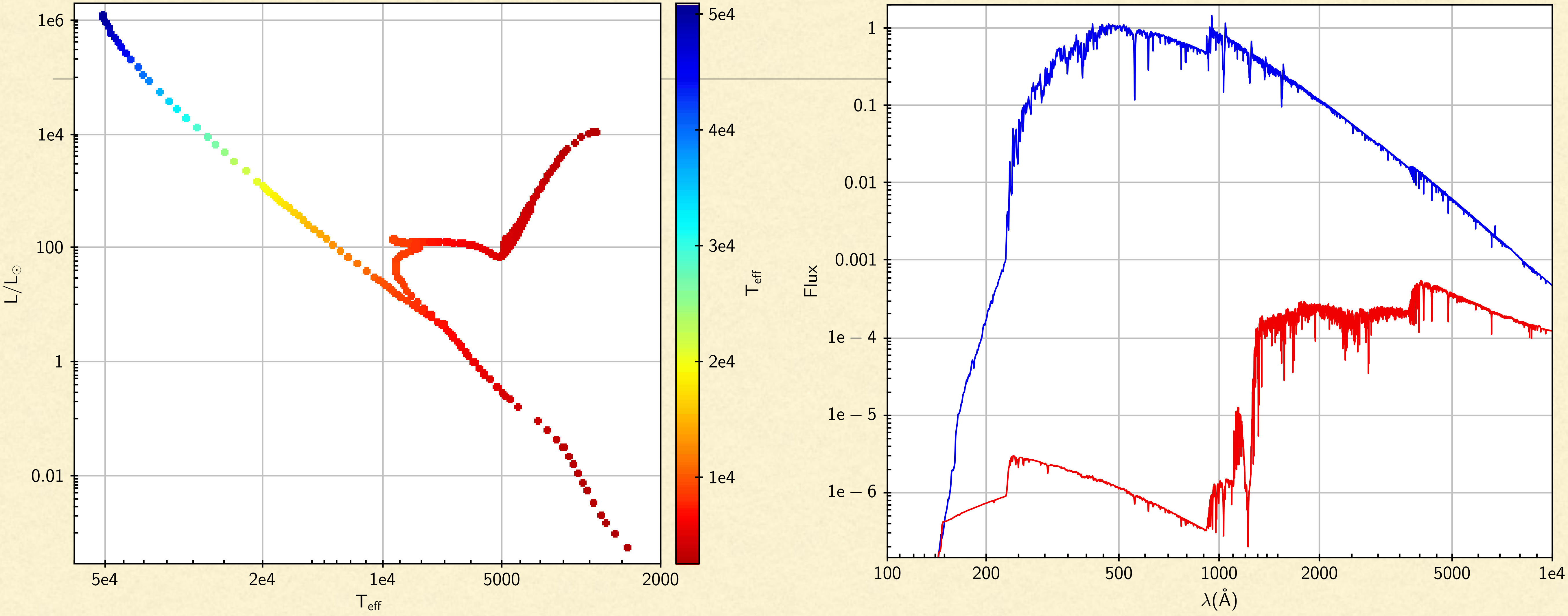
1e6
1e4
100
1
0.01
L/L$_\odot$
5e4
2e4
1e4
5000
2000
T$_{\rm eff}$
5e4
4e4
3e4
2e4
1e4
T$_{\rm eff}$
1
0.1
0.01
0.001
1e − 4
1e − 5
1e − 6
Flux
100
200
500
1000
2000
5000
1e4
λ(Å)

z = 9.5

t = 400 Myr

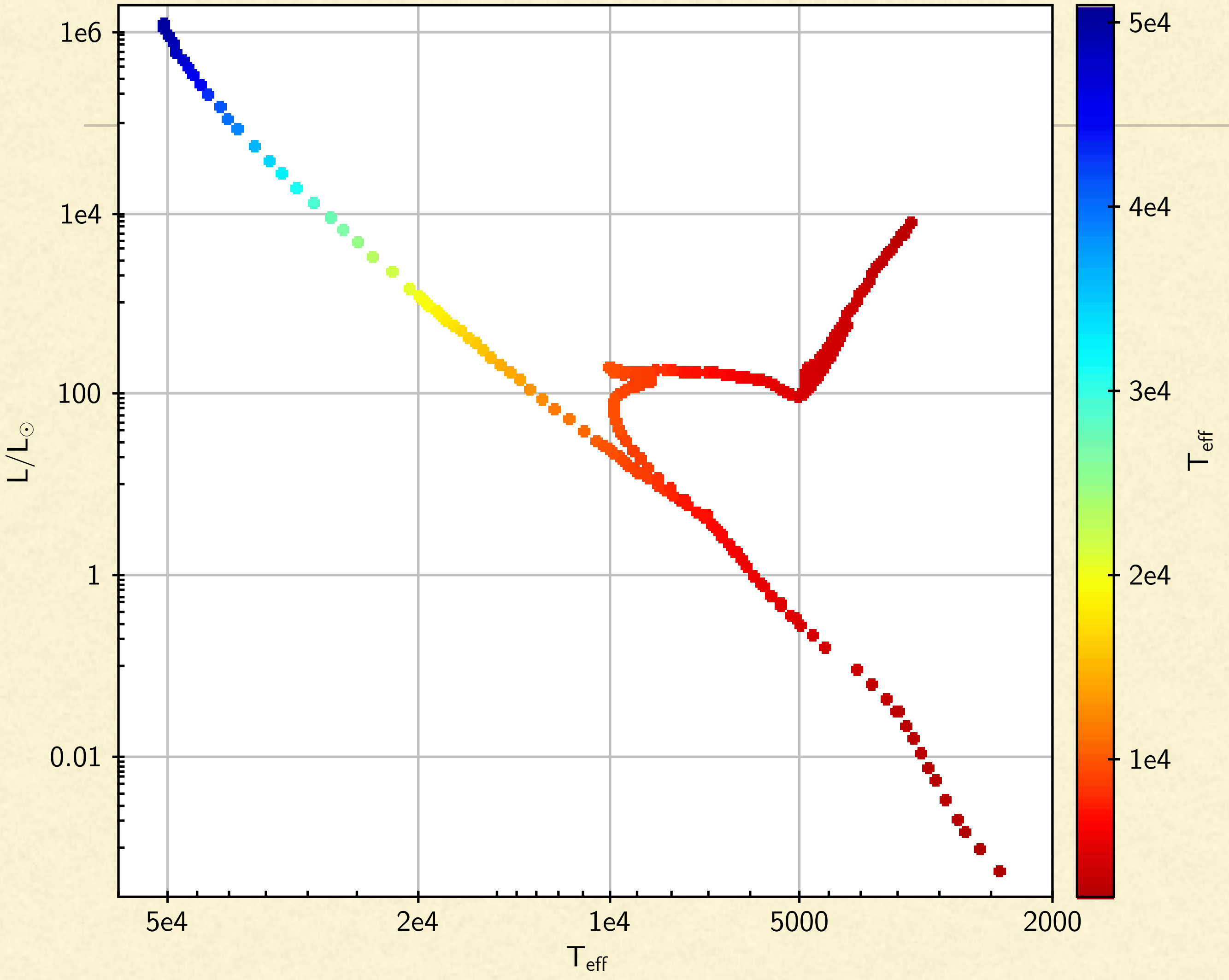

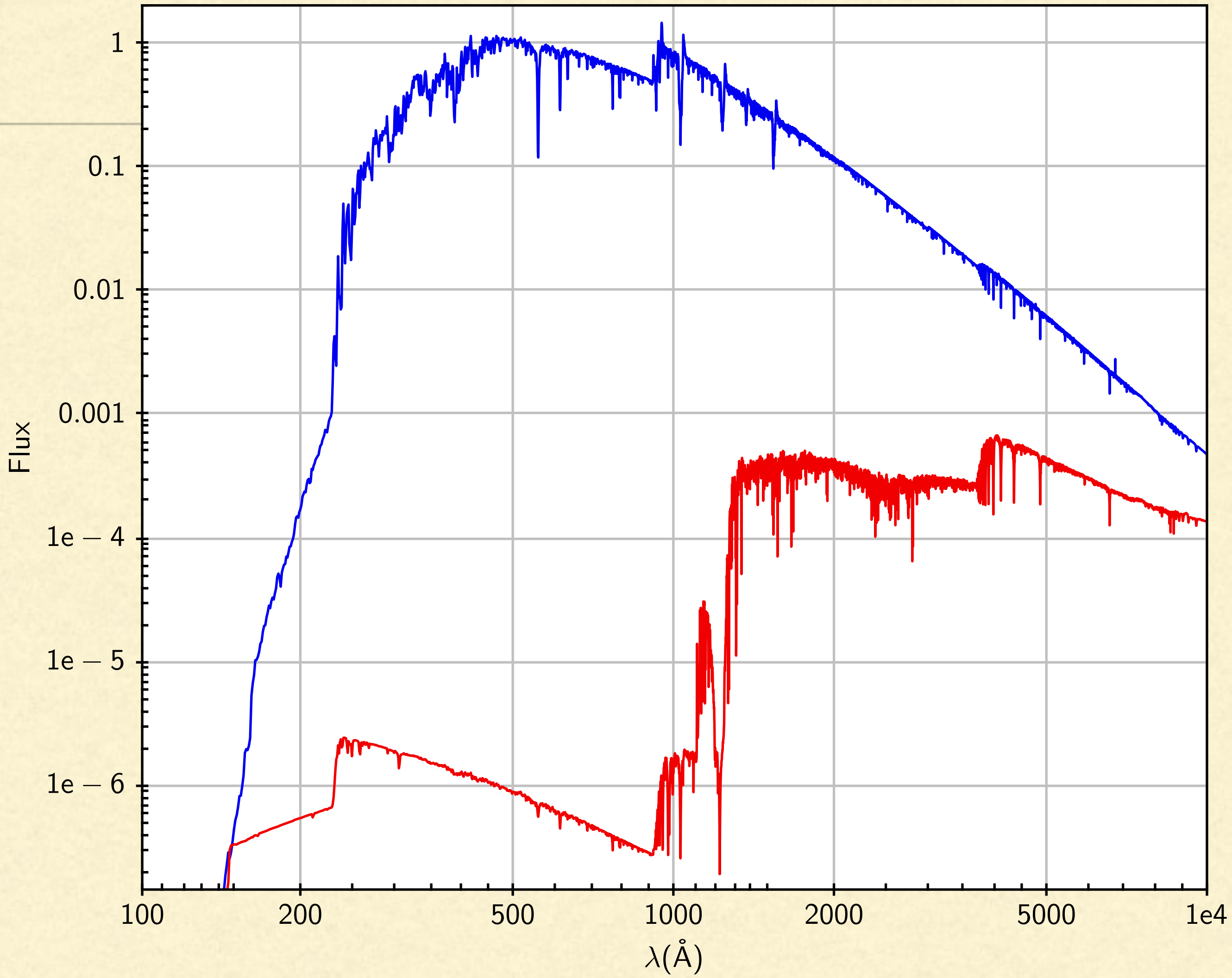

z = 11.2

t = 300 Myr

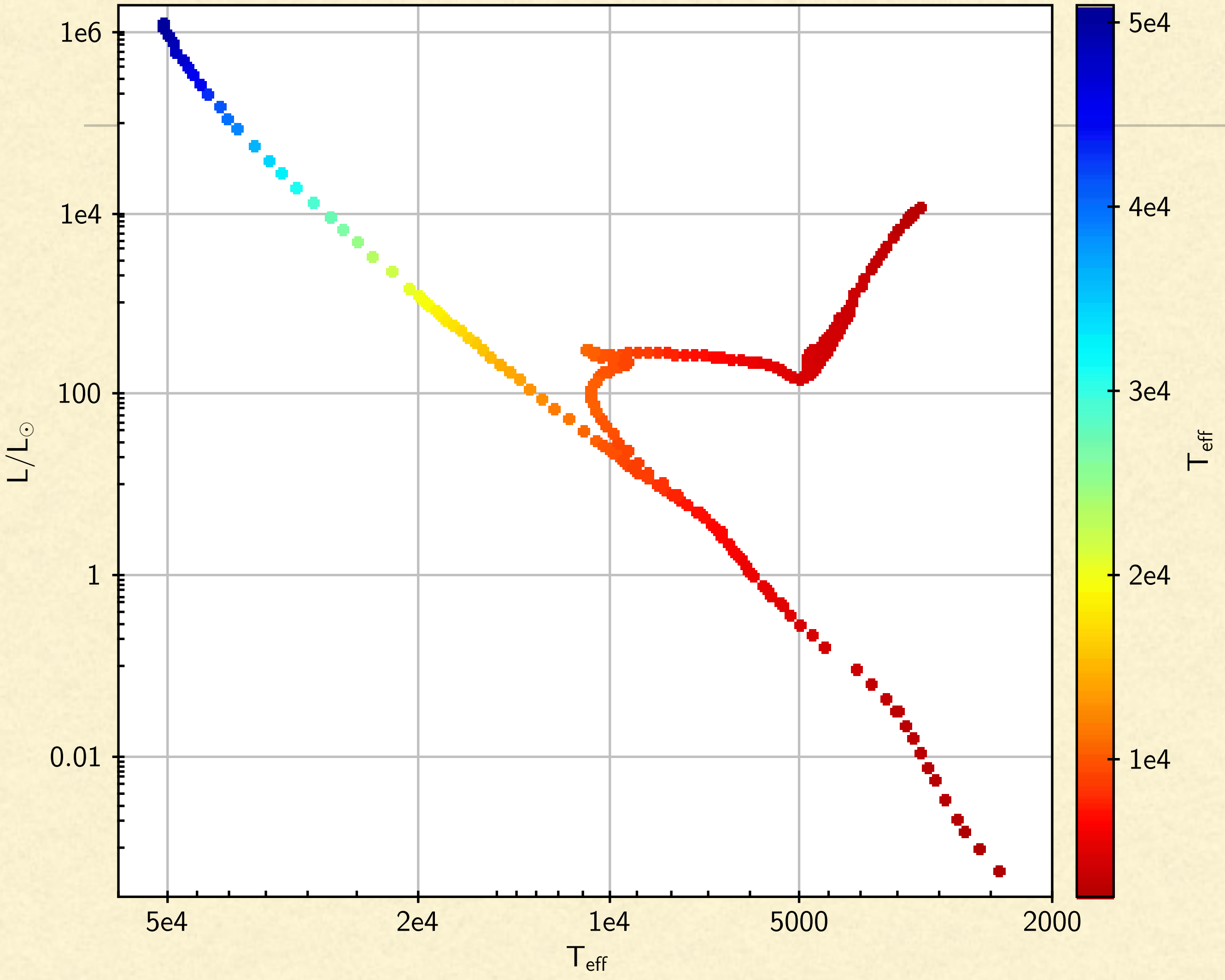

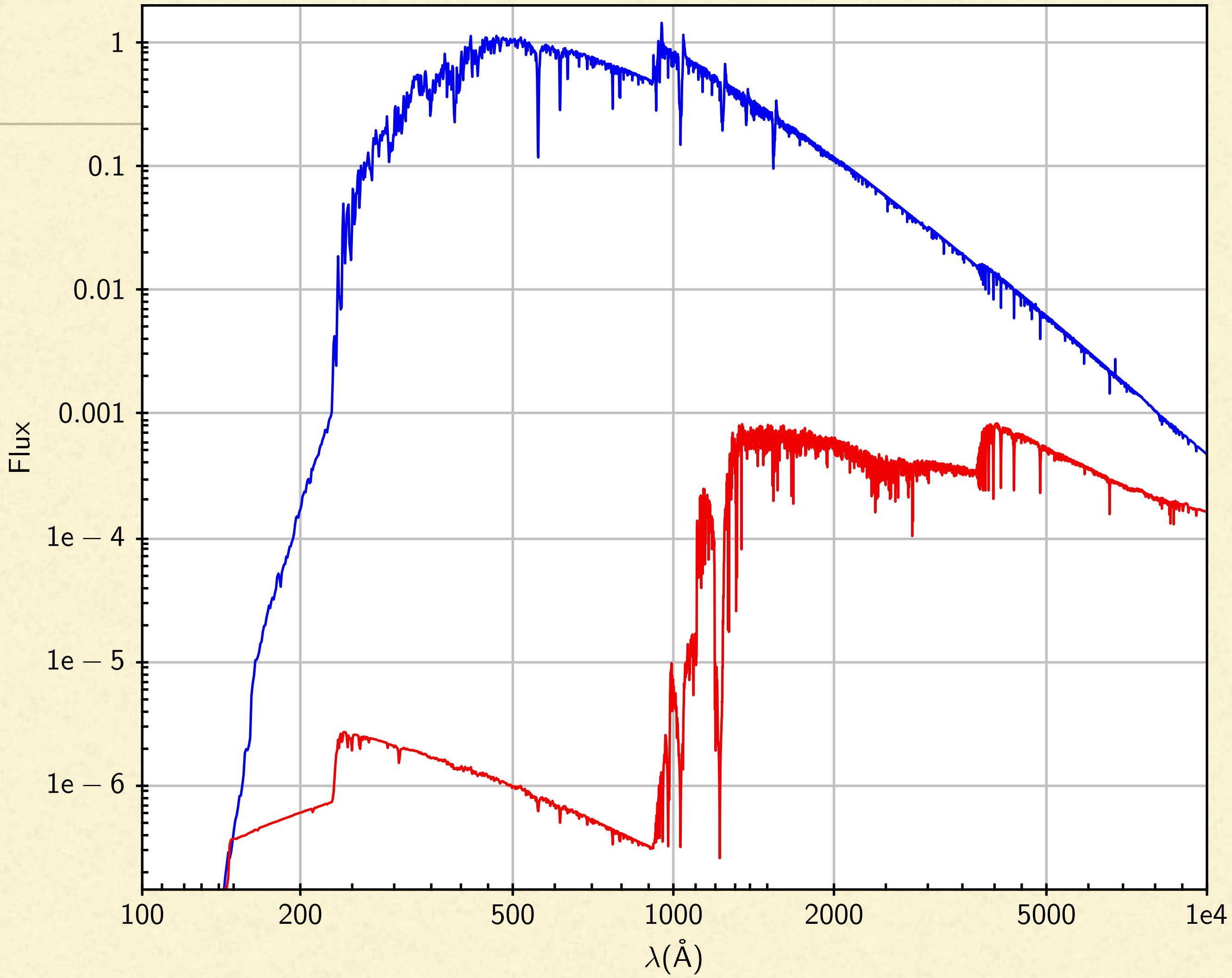

z = 13.8

t = 200 Myr

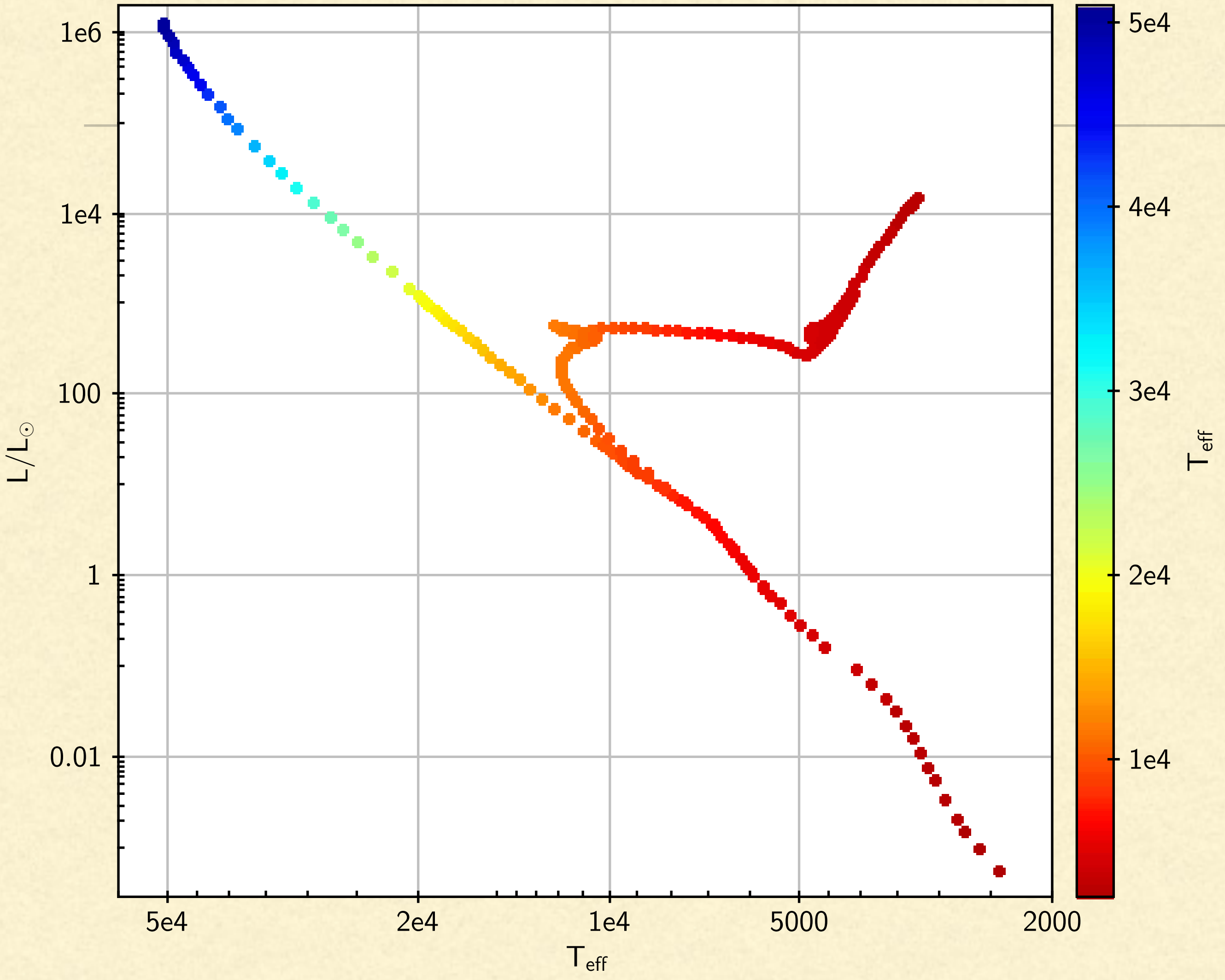

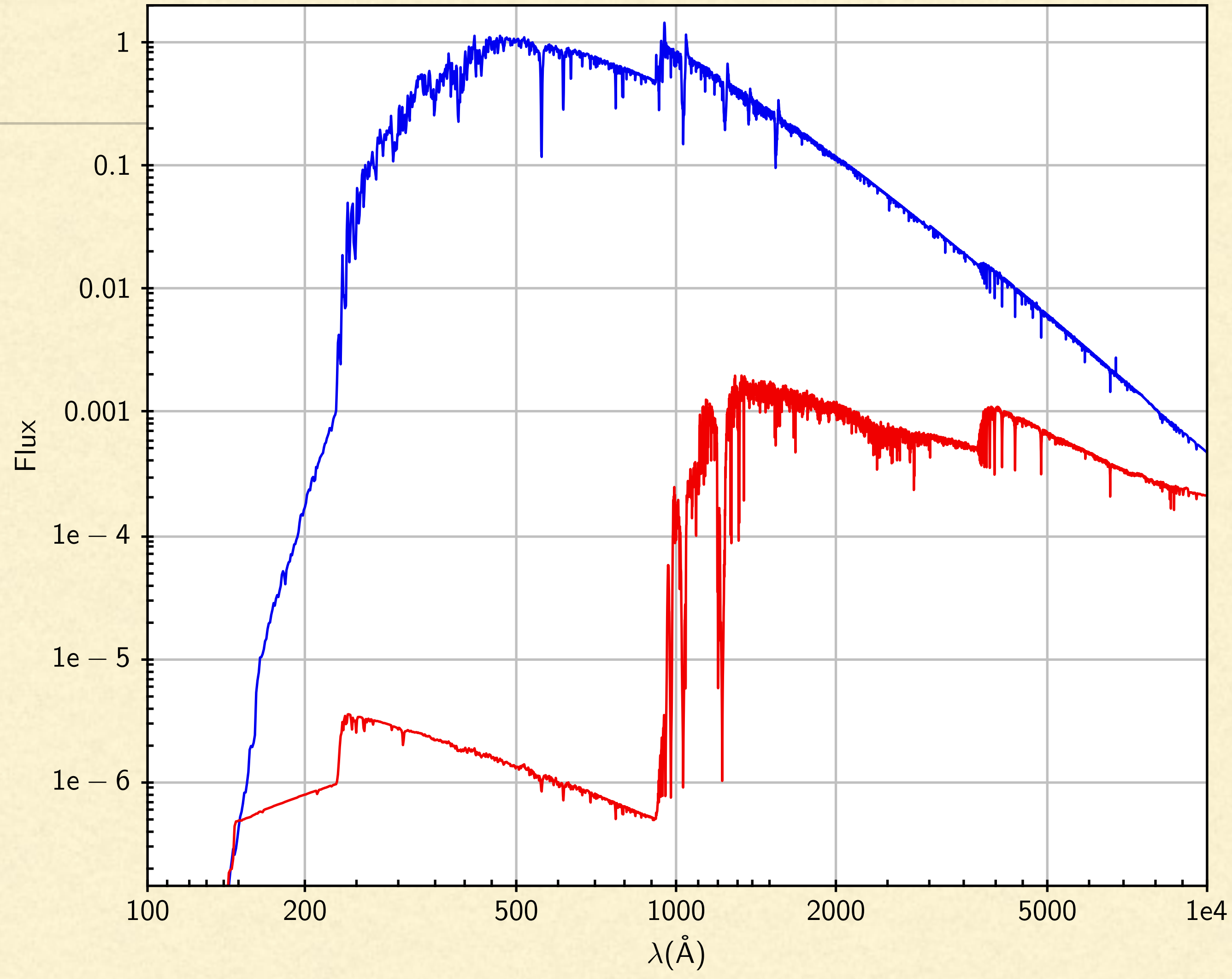

z = 18.3

t = 100 Myr

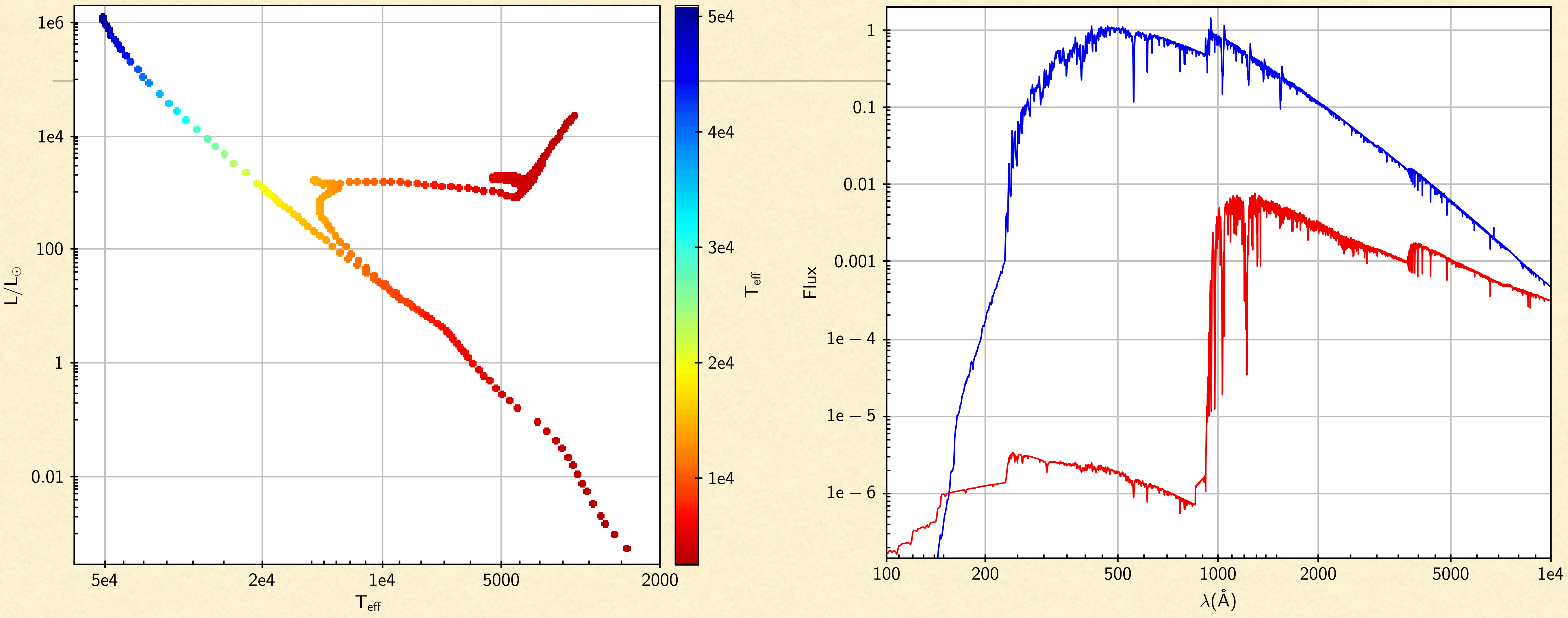
1e6
1e4
100
1
0.01
L/L$_\odot$
5e4
2e4
1e4
5000
2000
T$_{\rm eff}$
5e4
4e4
3e4
2e4
1e4
T$_{\rm eff}$
1
0.1
0.01
0.001
1e − 4
1e − 5
1e − 6
Flux
100
200
500
1000
2000
5000
1e4
λ(Å)

z = 30

t = 50 Myr

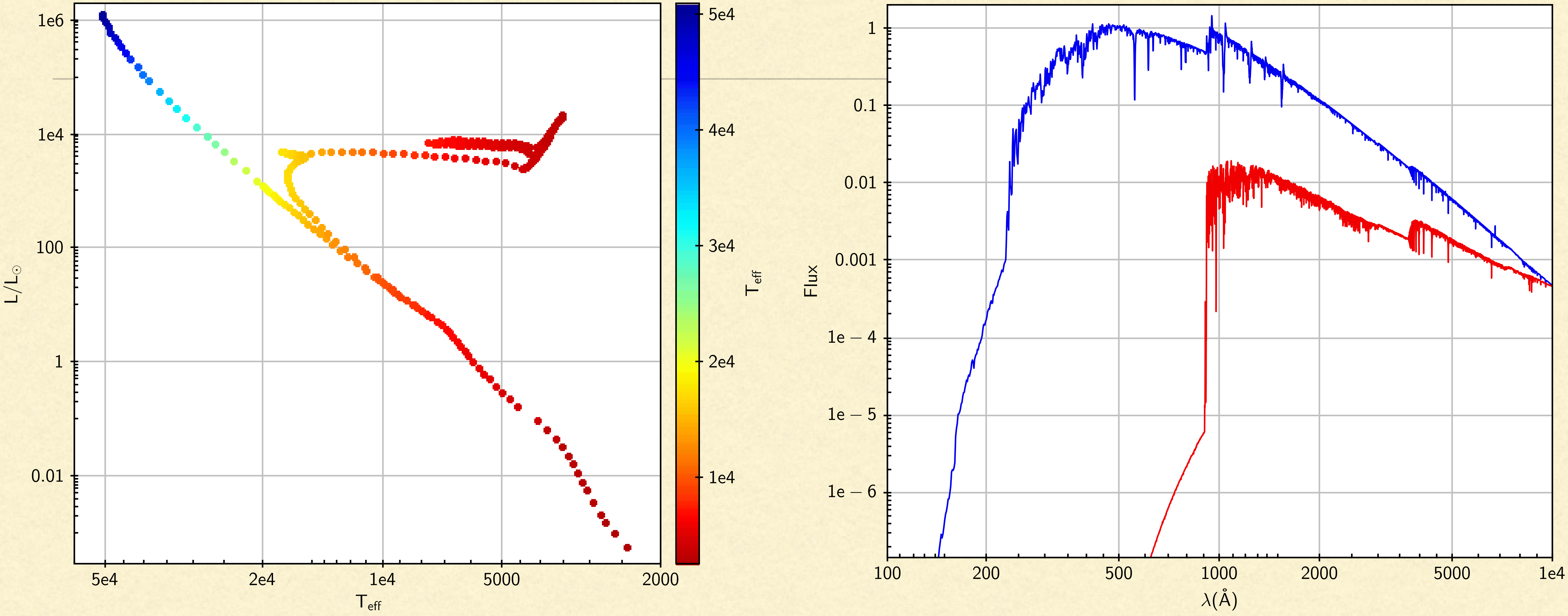
1e6
1e4
100
1
0.01
L/L$_\odot$
5e4
2e4
1e4
5000
2000
T$_{eff}$
5e4
4e4
3e4
2e4
1e4
T$_{eff}$
1
0.1
0.01
0.001
1e − 4
1e − 5
1e − 6
Flux
100
200
500
1000
2000
5000
1e4
λ(Å)

z = 48

t = 20 Myr

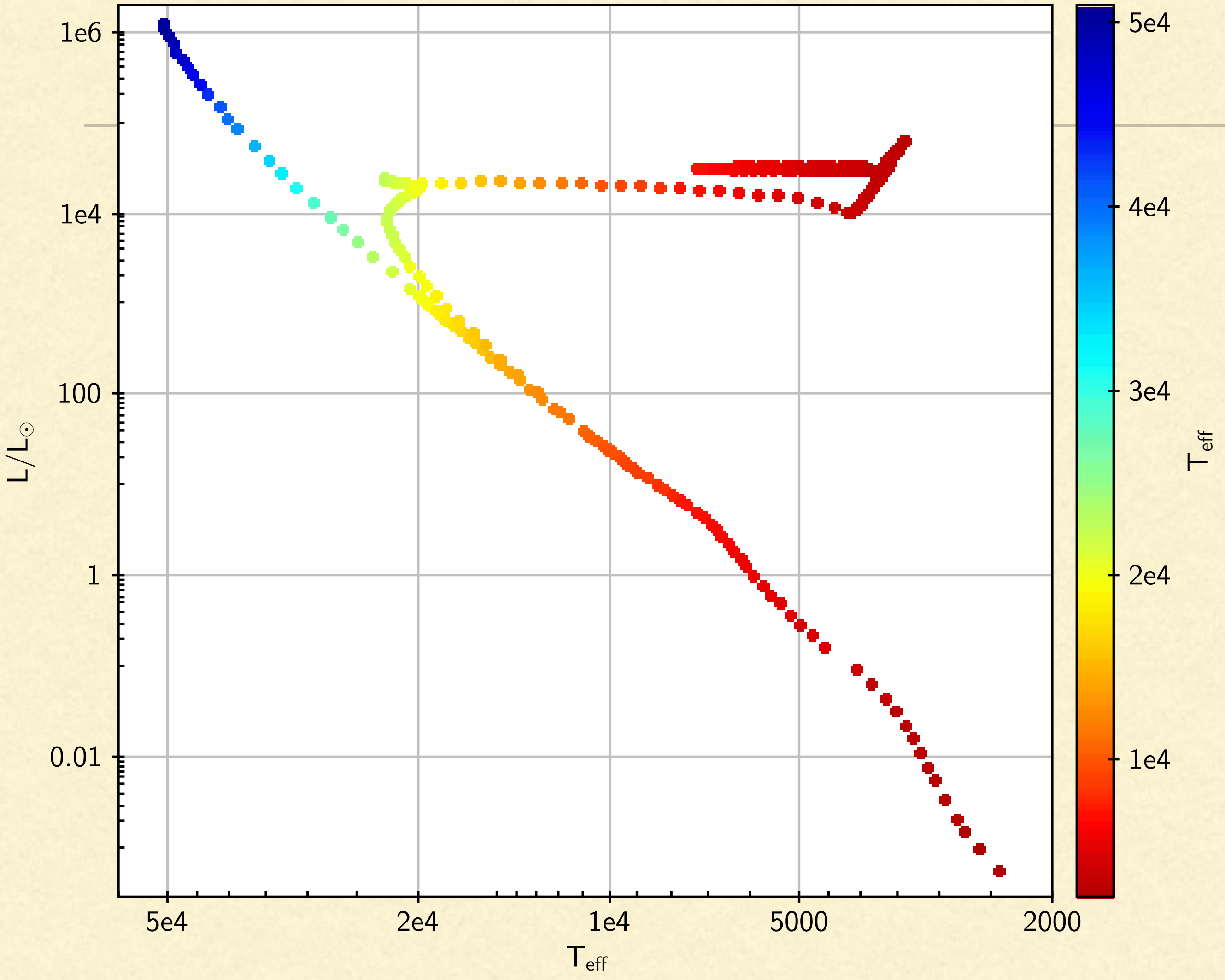

1e6
1e4
100
1
0.01
L/L$_\odot$
5e4
2e4
1e4
5000
2000
T$_{eff}$
5e4
4e4
3e4
2e4
1e4
T$_{eff}$

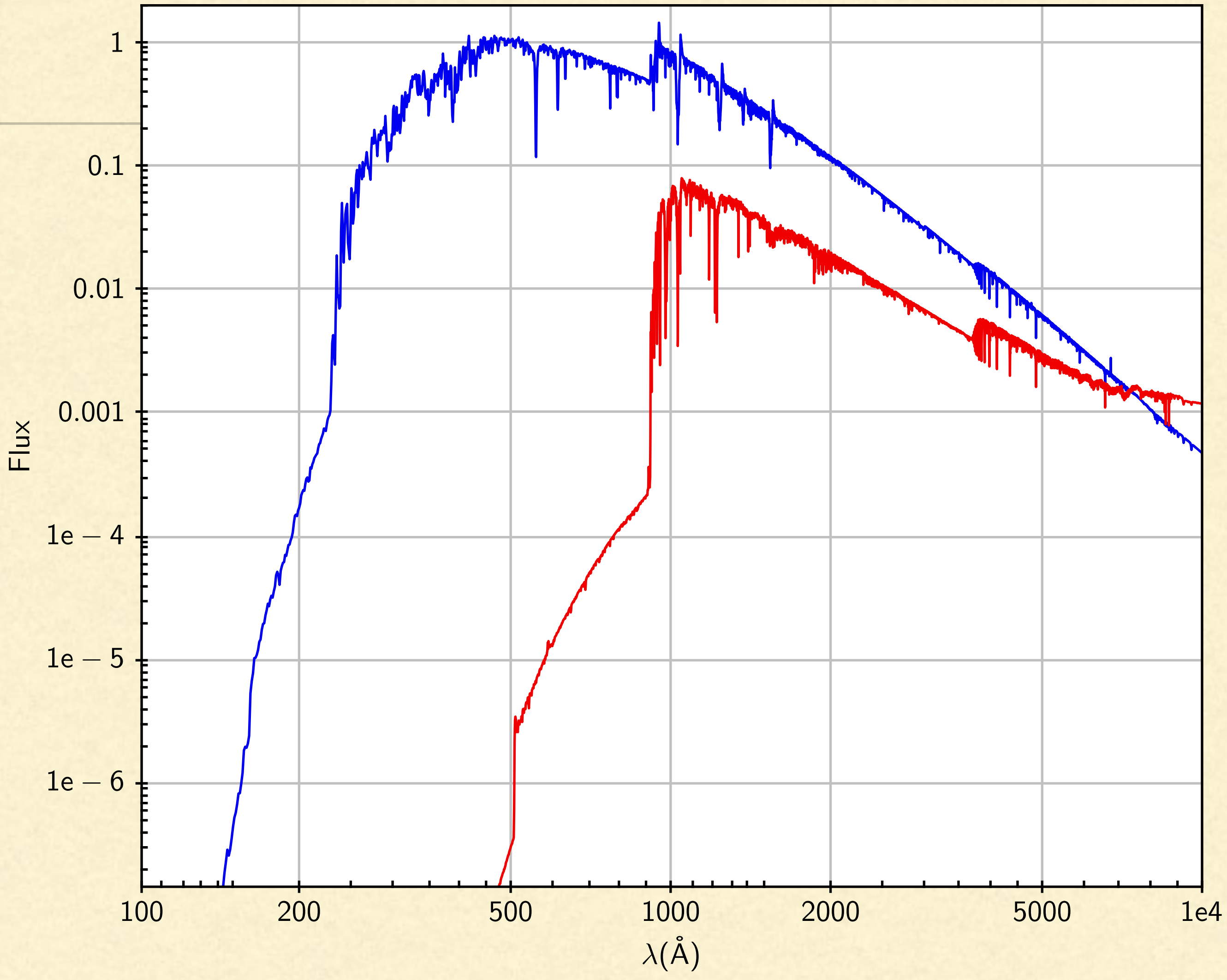

1
0.1
0.01
0.001
1e − 4
1e − 5
1e − 6
Flux
100
200
500
1000
2000
5000
1e4
λ(Å)

z = 89

t = 10 Myr

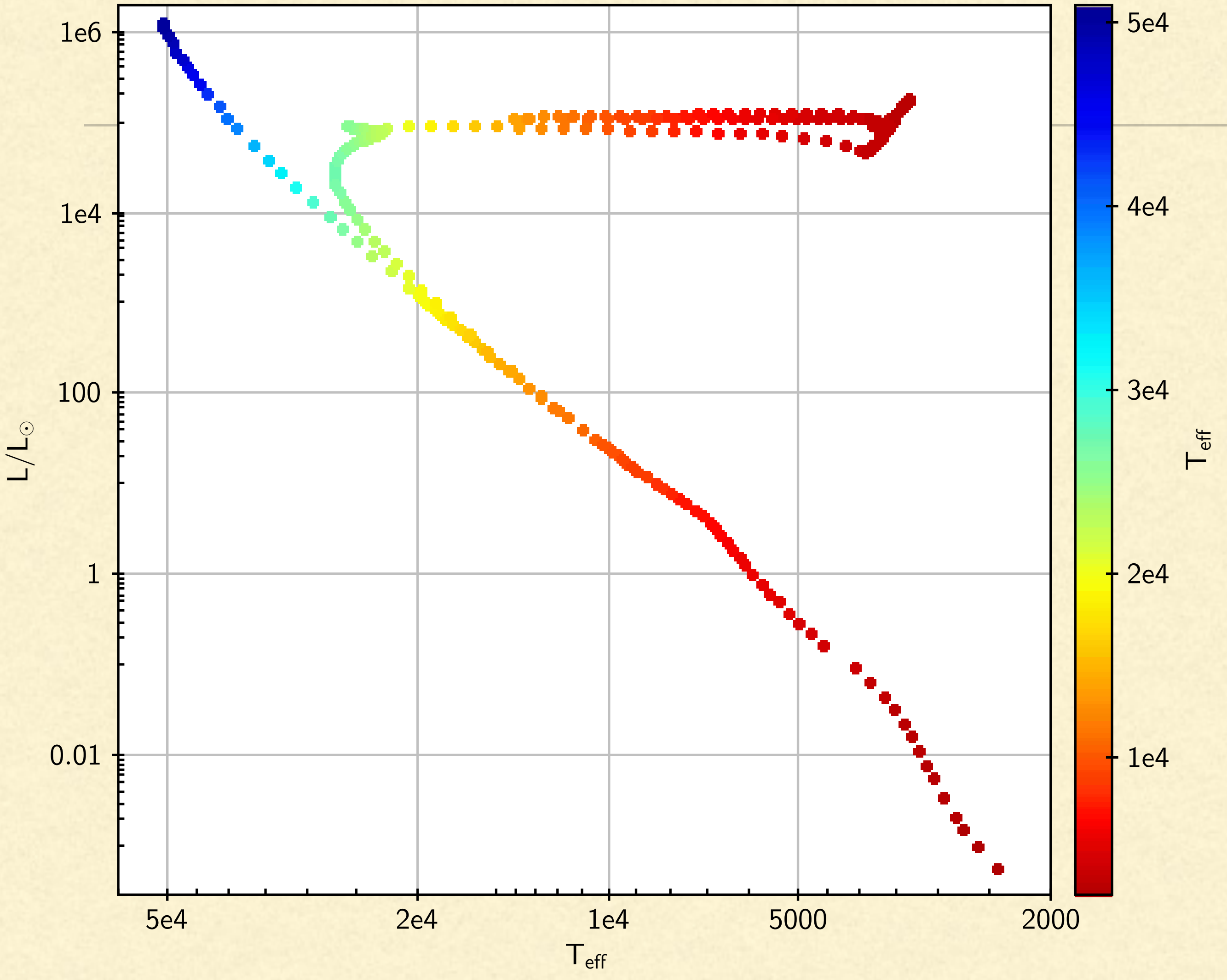
1e6
1e4
100
1
0.01
L/L$_\odot$
5e4
2e4
1e4
5000
2000
T$_{\rm eff}$
5e4
4e4
3e4
2e4
1e4
T$_{\rm eff}$

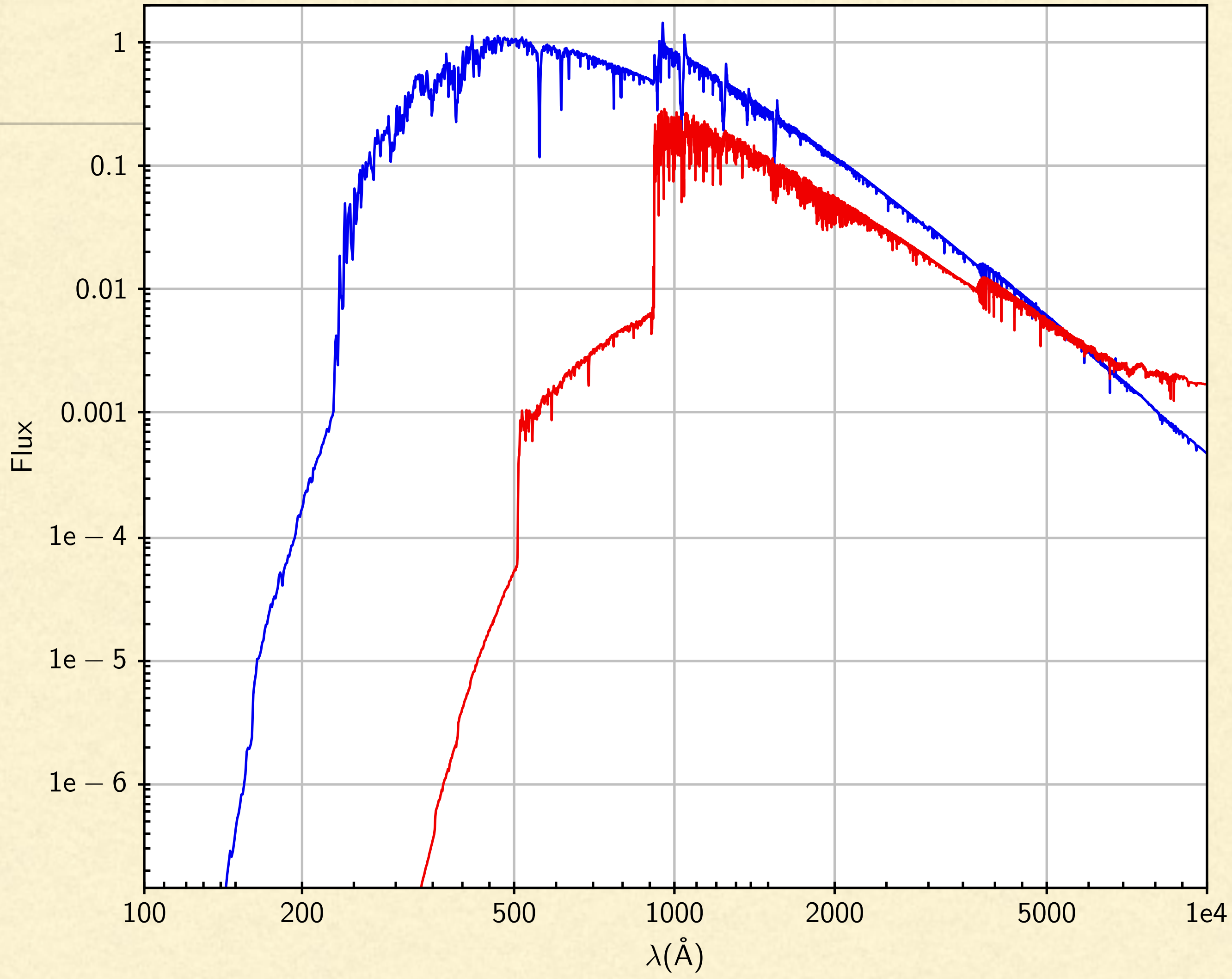
1
0.1
0.01
0.001
1e − 4
1e − 5
1e − 6
Flux
100
200
500
1000
2000
5000
1e4
λ(Å)

z = 140

t = 5 Myr

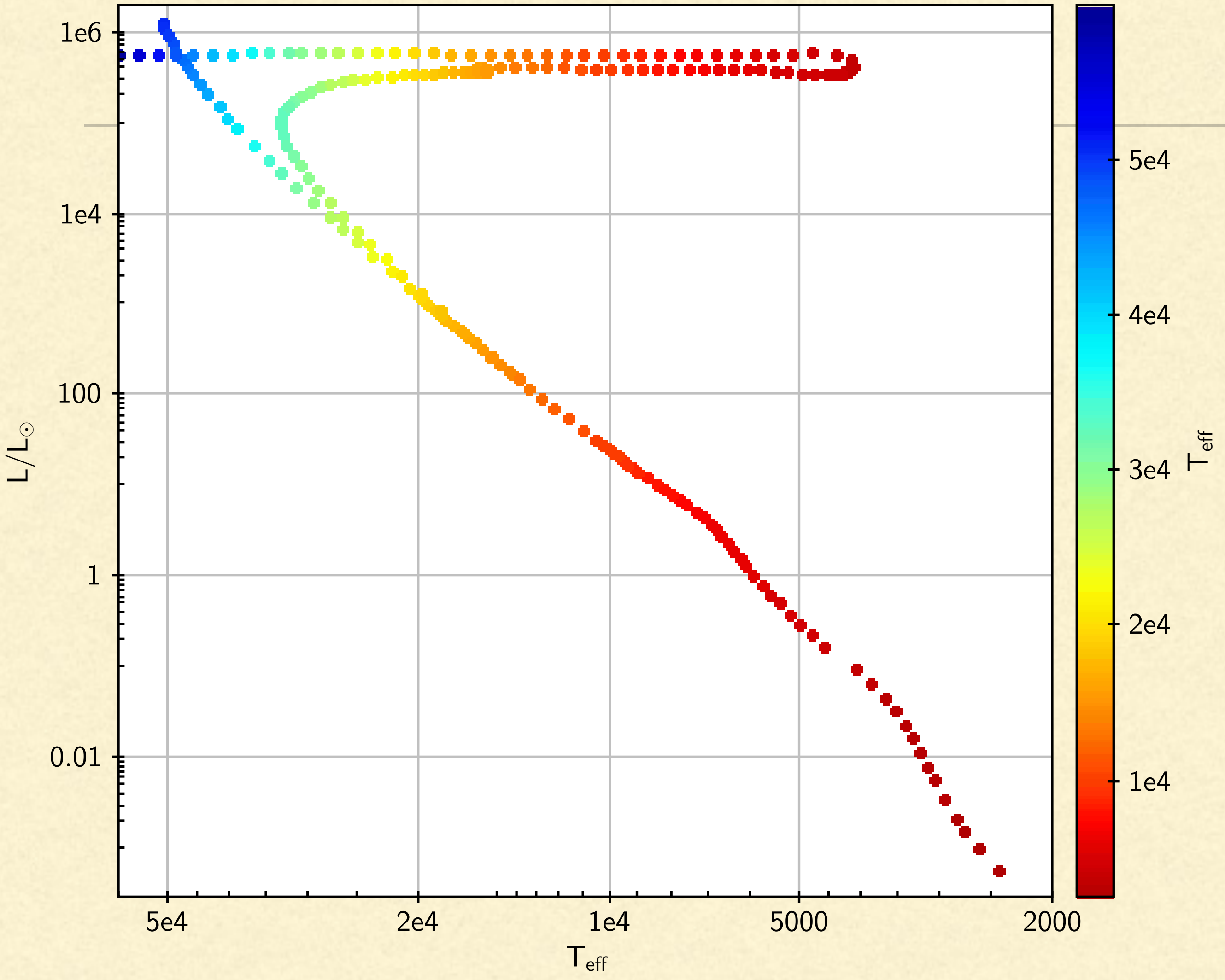
1e6
1e4
100
1
0.01
L/L$_\odot$
5e4
2e4
1e4
5000
2000
T$_{eff}$
5e4
4e4
3e4
2e4
1e4
T$_{eff}$

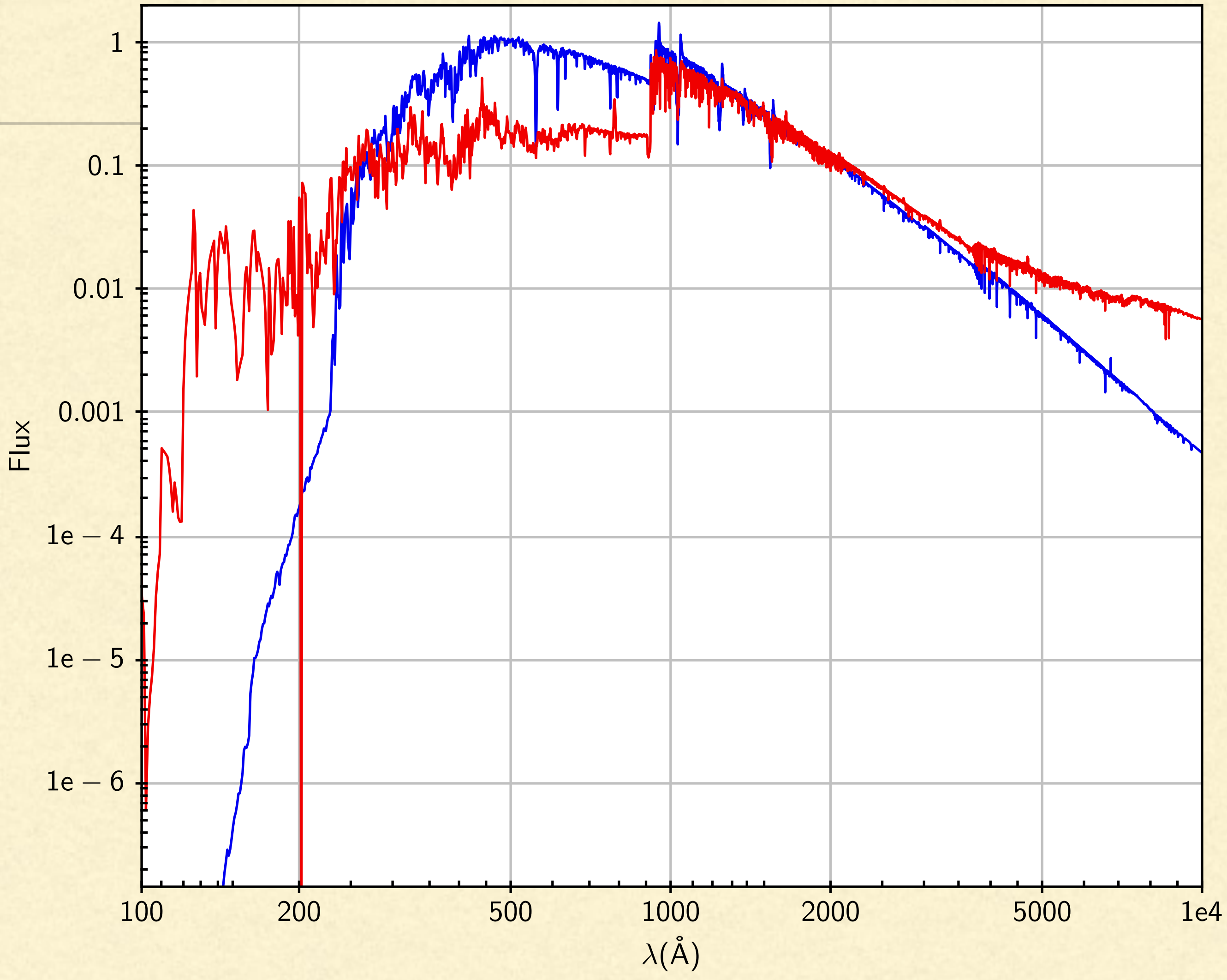
1
0.1
0.01
0.001
1e − 4
1e − 5
1e − 6
Flux
100
200
500
1000
2000
5000
1e4
λ(Å)

z

t = 2 Myr

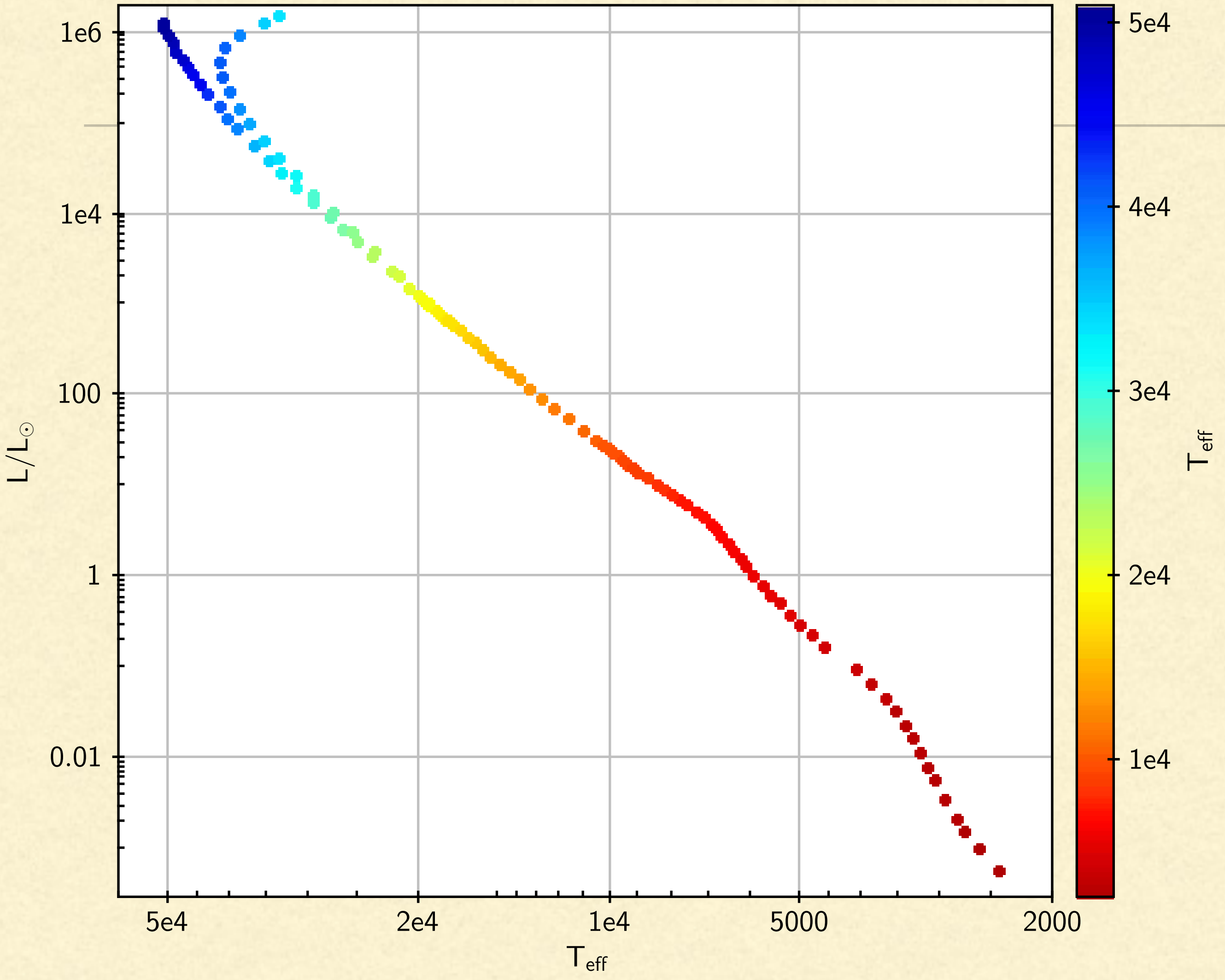
1e6
1e4
100
1
0.01
L/L$_\odot$
5e4
2e4
1e4
5000
2000
T$_{\rm eff}$
5e4
4e4
3e4
2e4
1e4
T$_{\rm eff}$

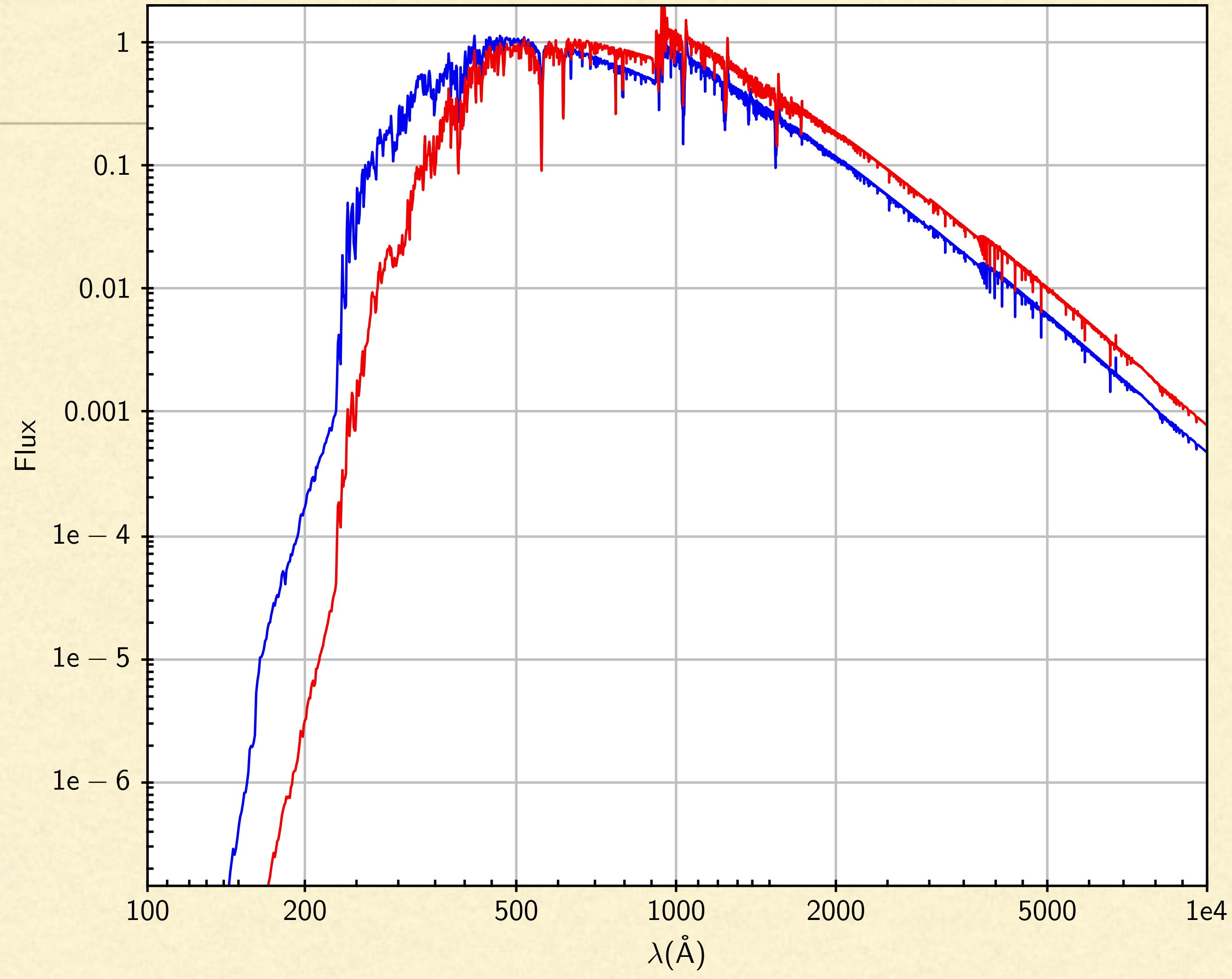
1
0.1
0.01
0.001
1e − 4
1e − 5
1e − 6
Flux
100
200
500
1000
2000
5000
1e4
λ(Å)

z

$t = 0$

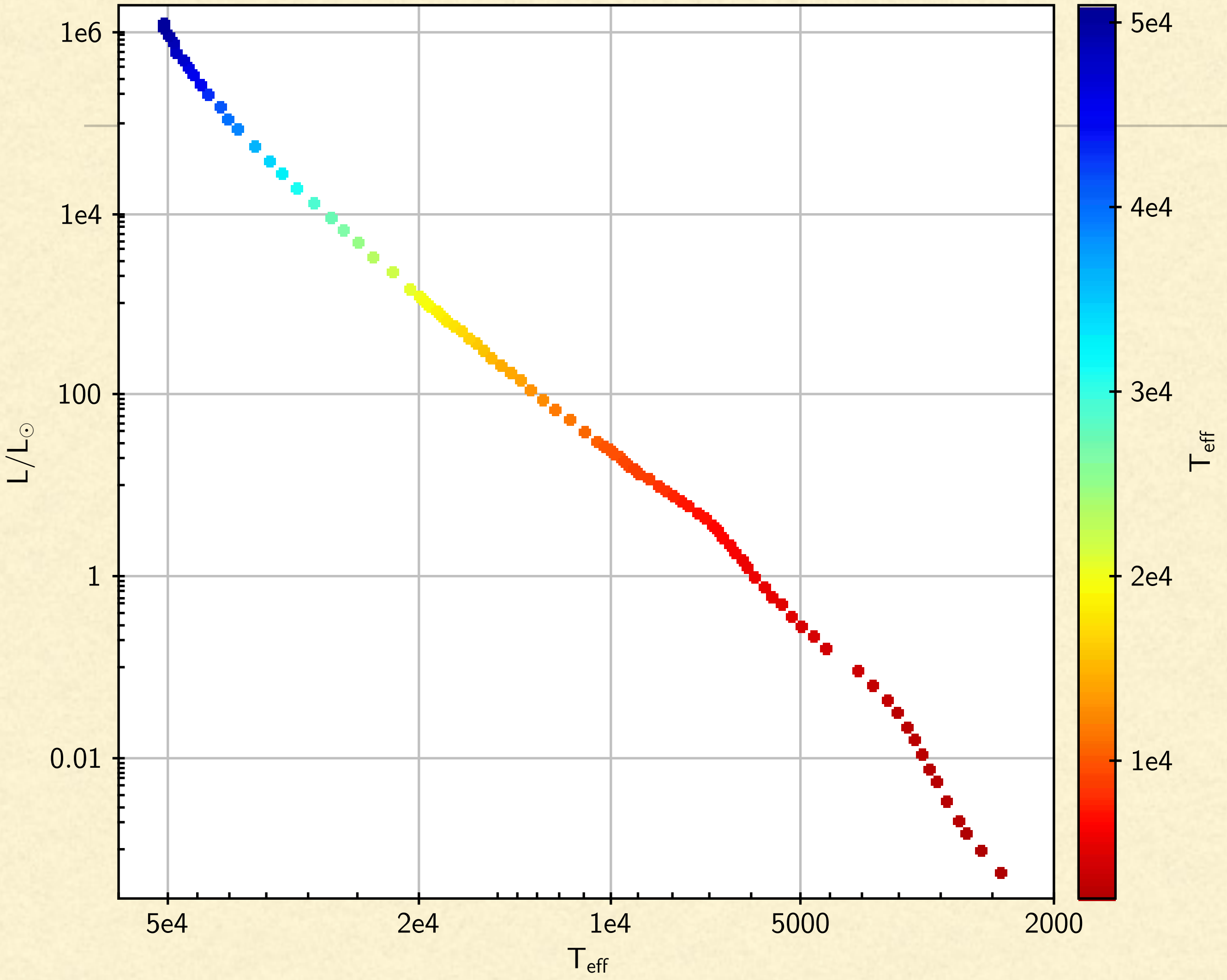
1e6
1e4
100
1
0.01
$L/L_\odot$
5e4
2e4
1e4
5000
2000
T_{eff}
5e4
4e4
3e4
2e4
1e4
T_{eff}

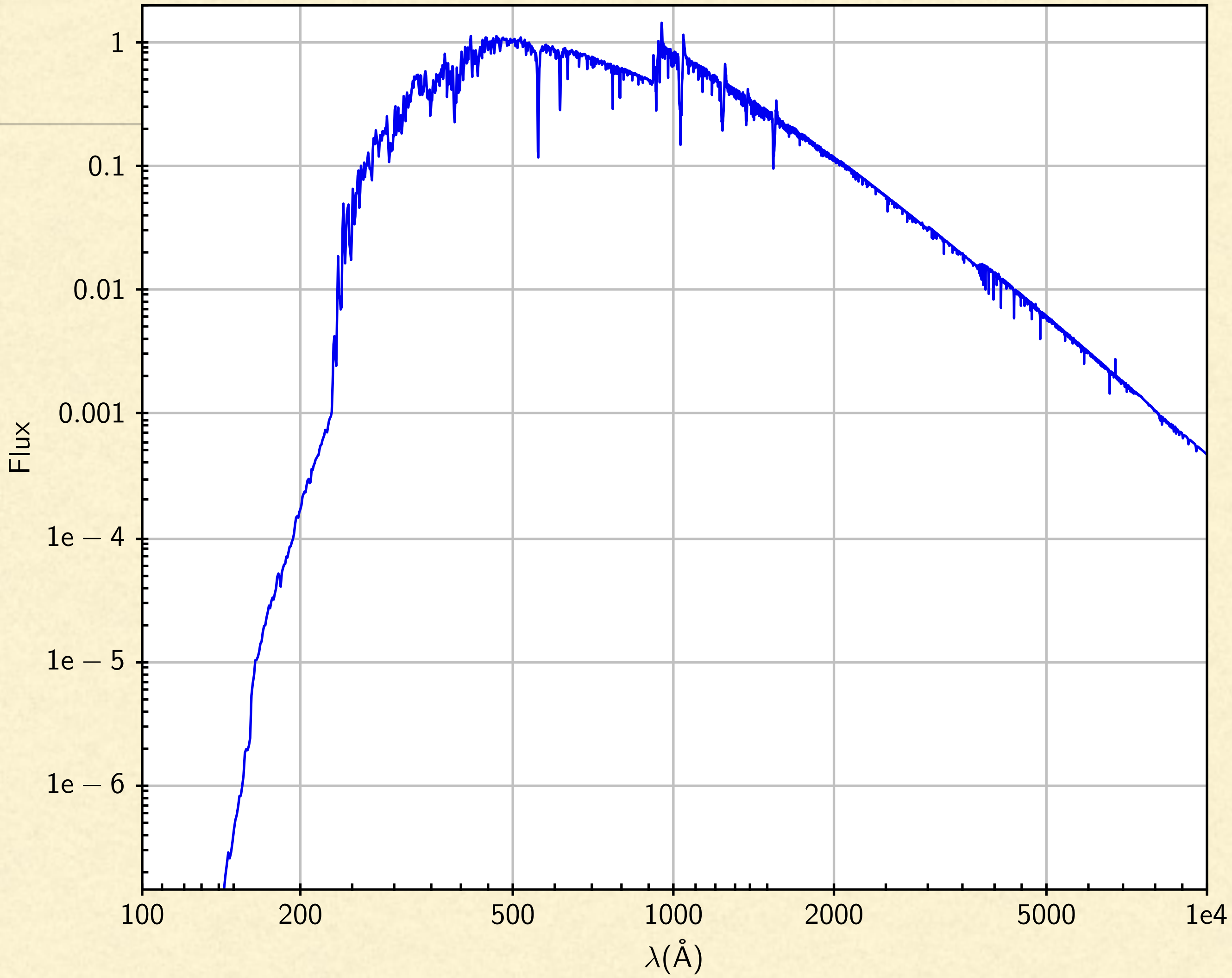
1
0.1
0.01
0.001
1e − 4
1e − 5
1e − 6
Flux
100
200
500
1000
2000
5000
1e4
λ(Å)

z

Age of the universe vs. redshift (z)

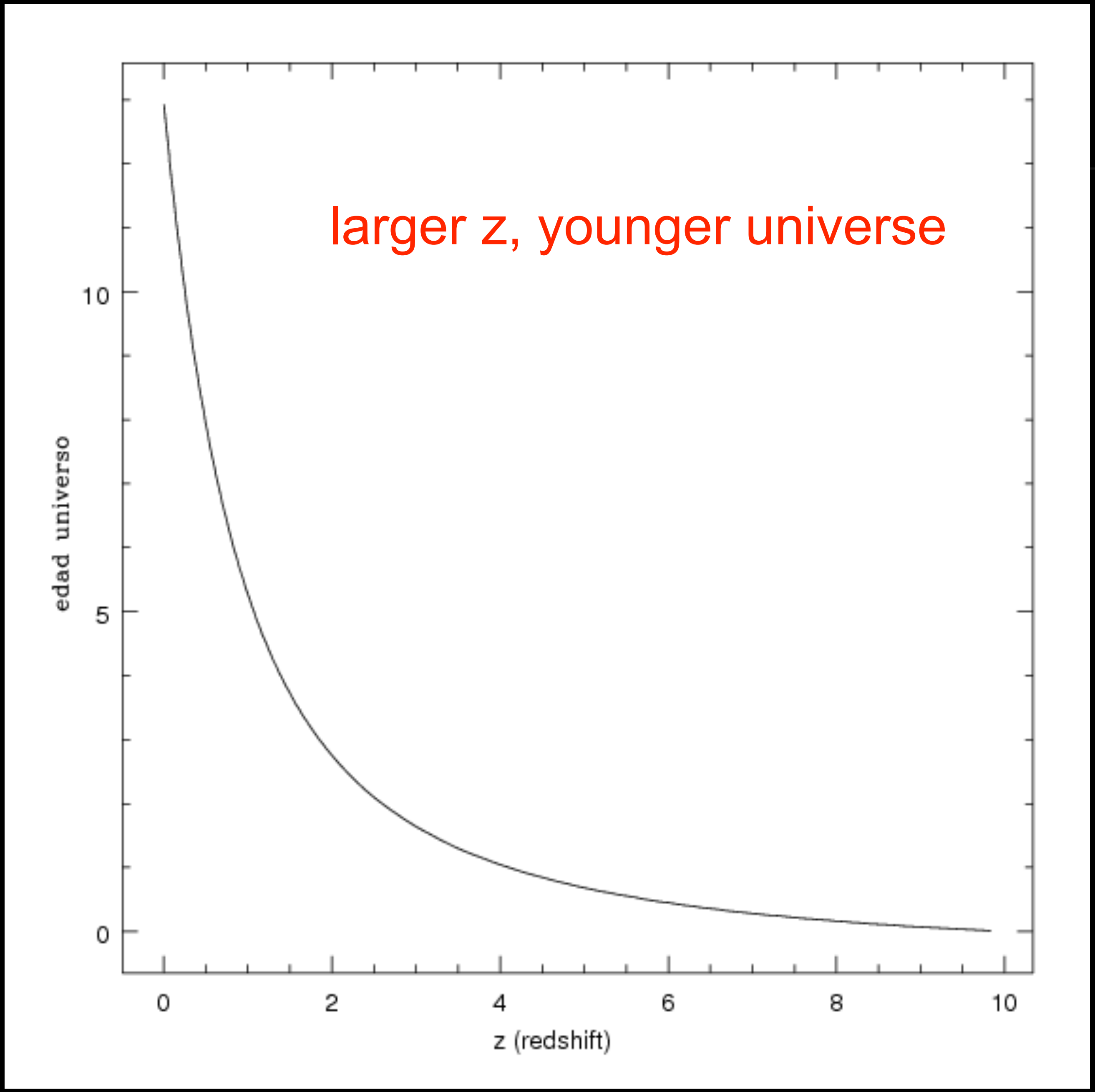

% of age at given z

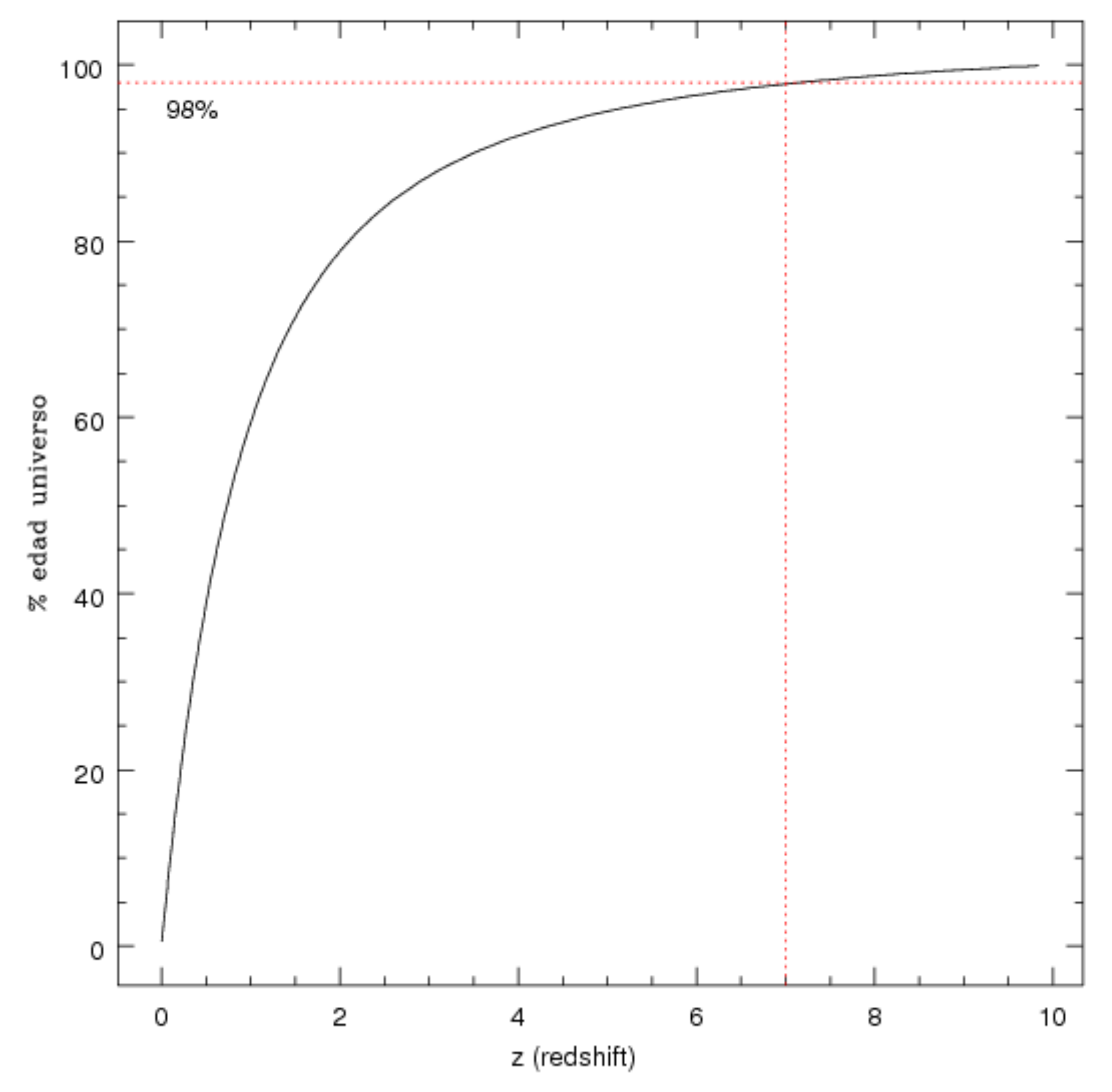

Objects at z = 7 have been there for 98% of the age of the universe

Effects of the cosmological redshift (z)

$z = 0$

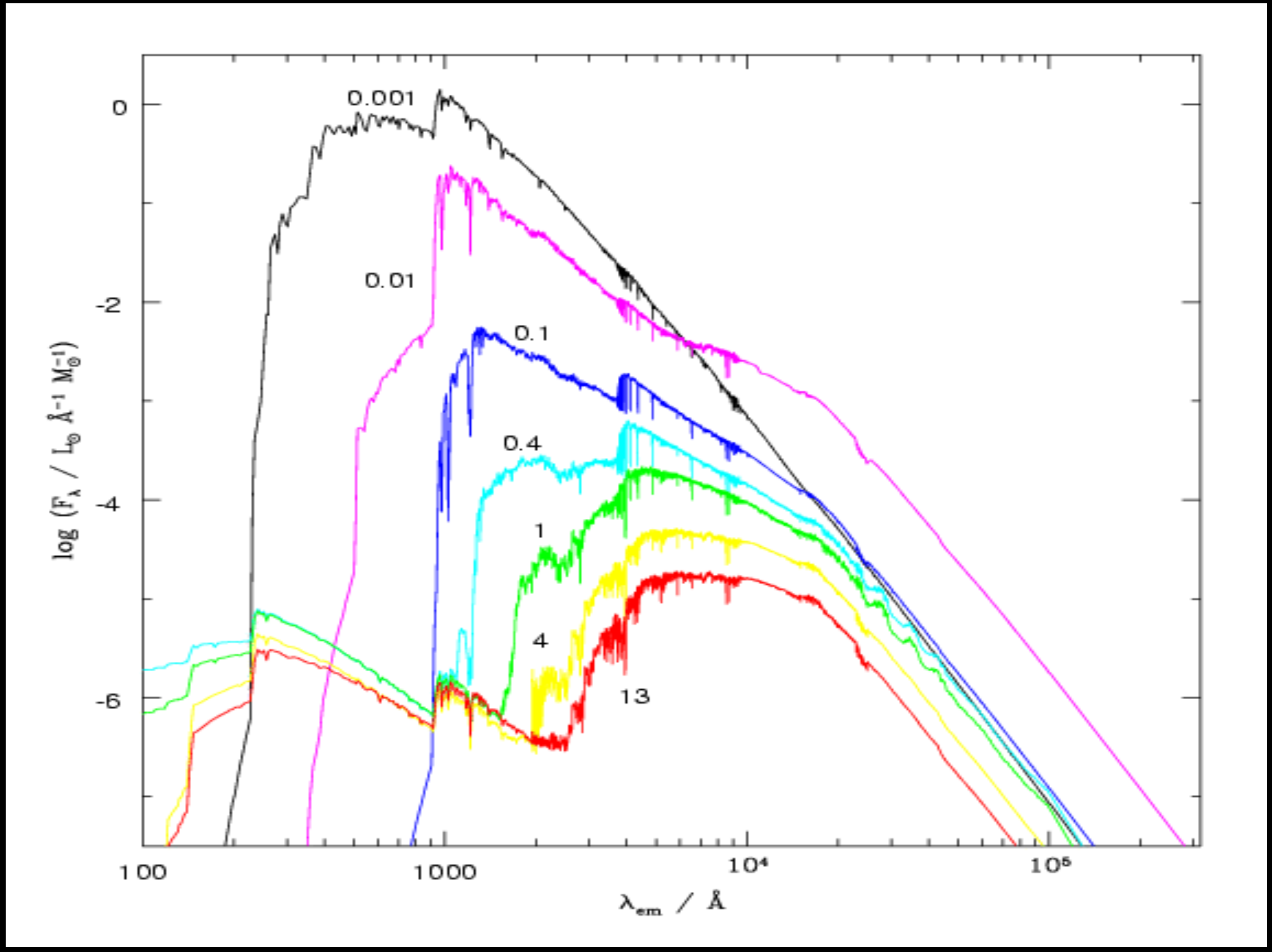

$z = z(t)$

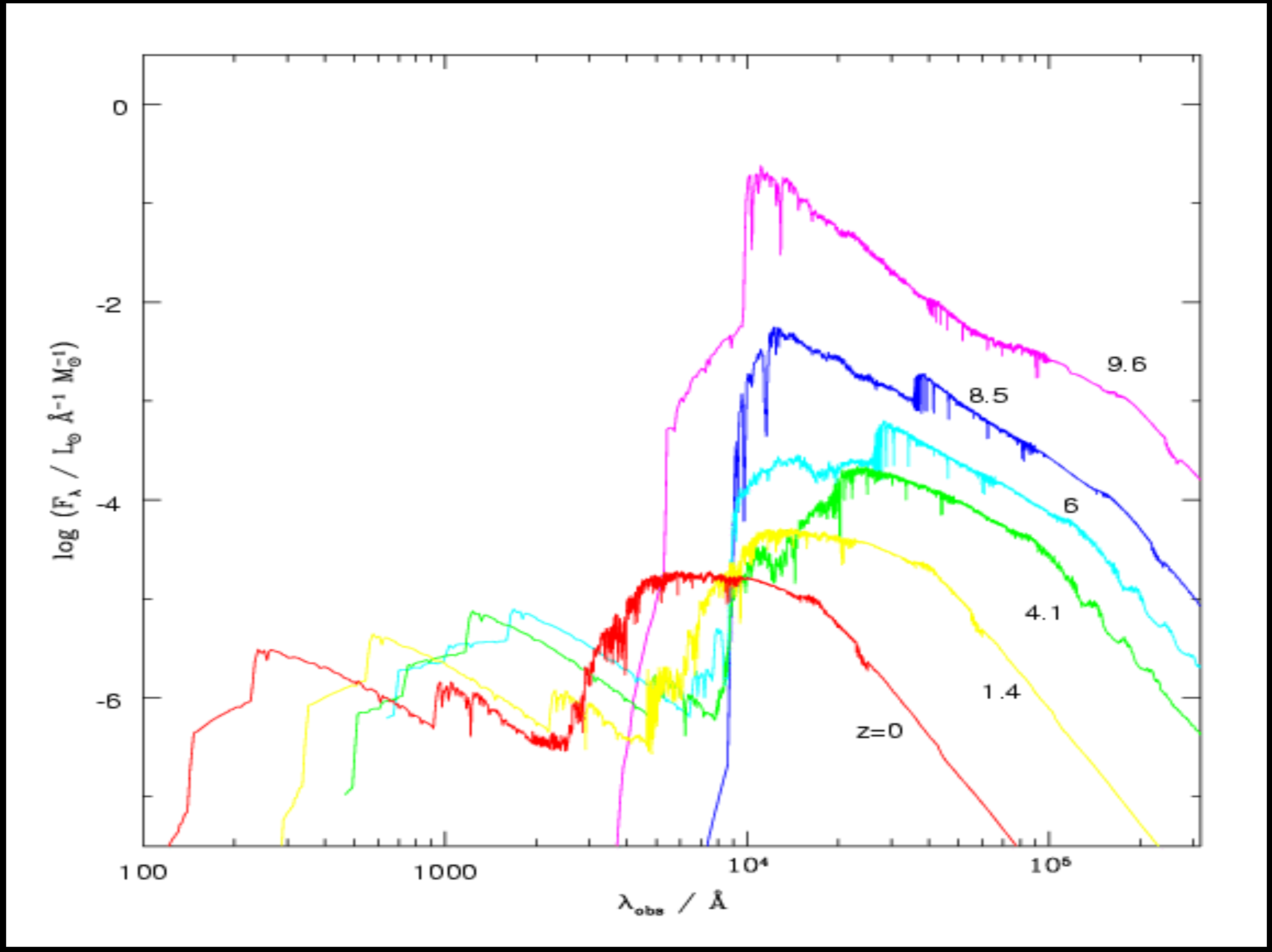

Effects of the cosmological redshift (z)

$z = 0$

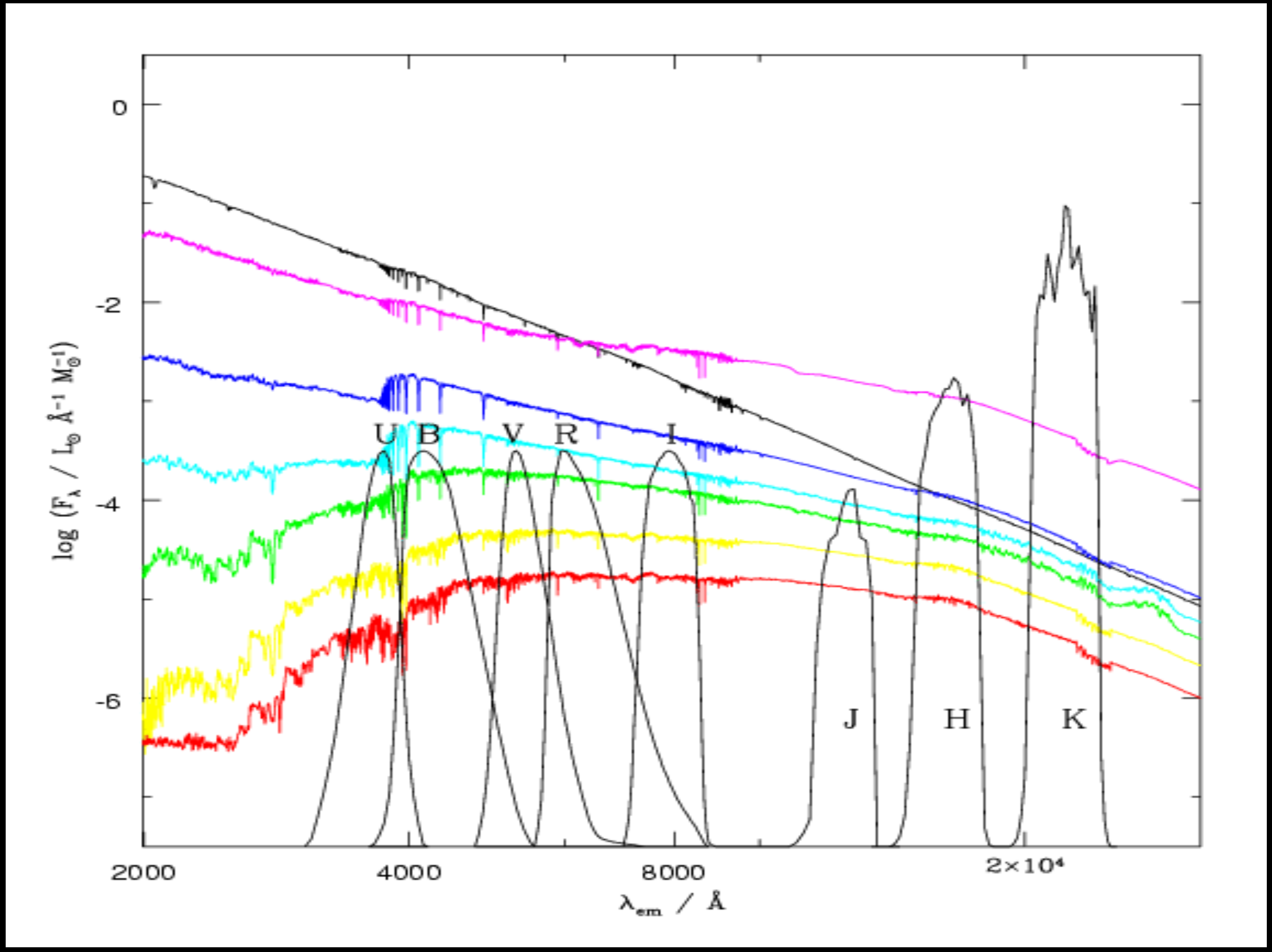

$z = z(t)$

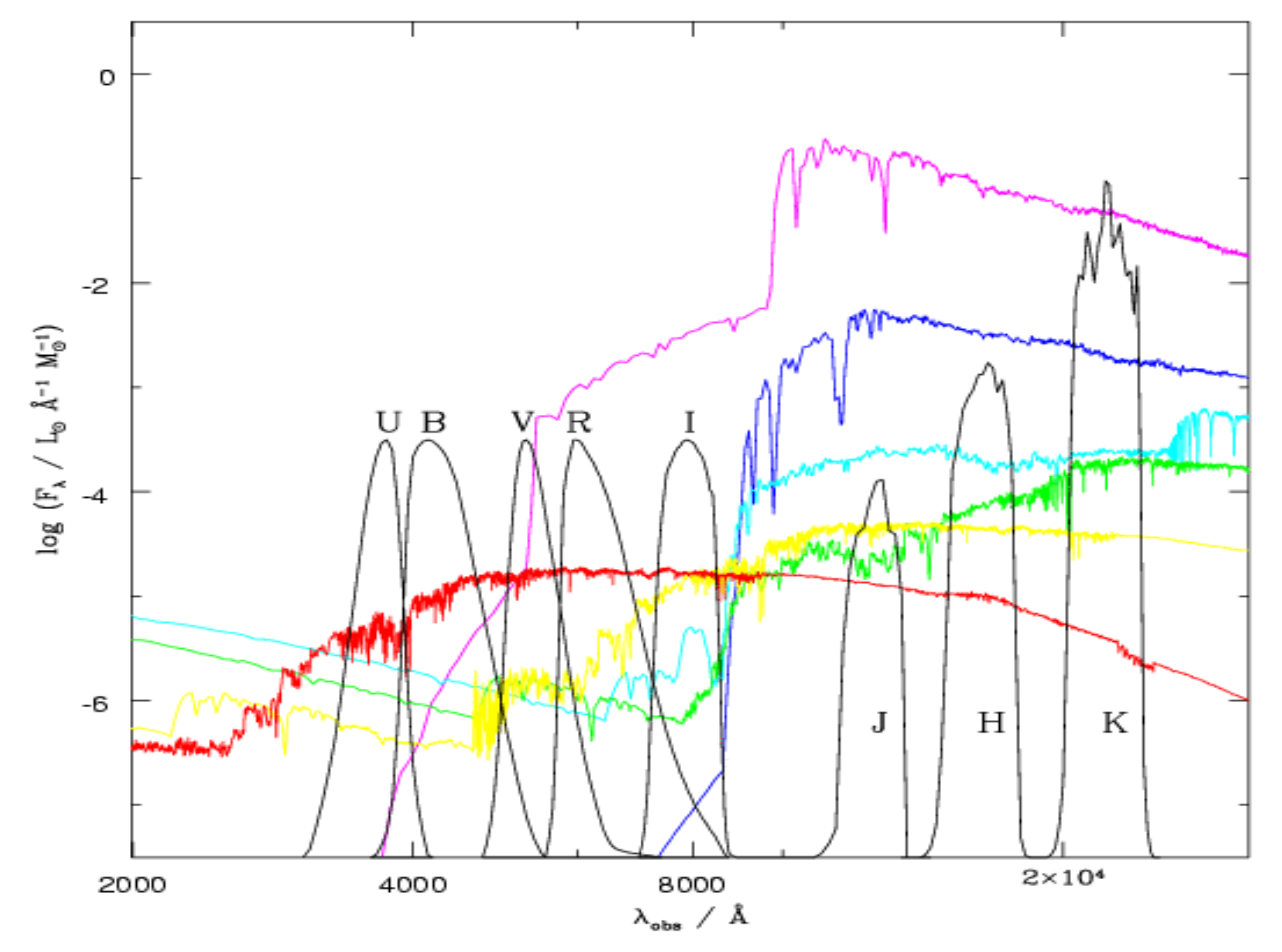

Effects of the cosmological redshift (z)

$z = 0$

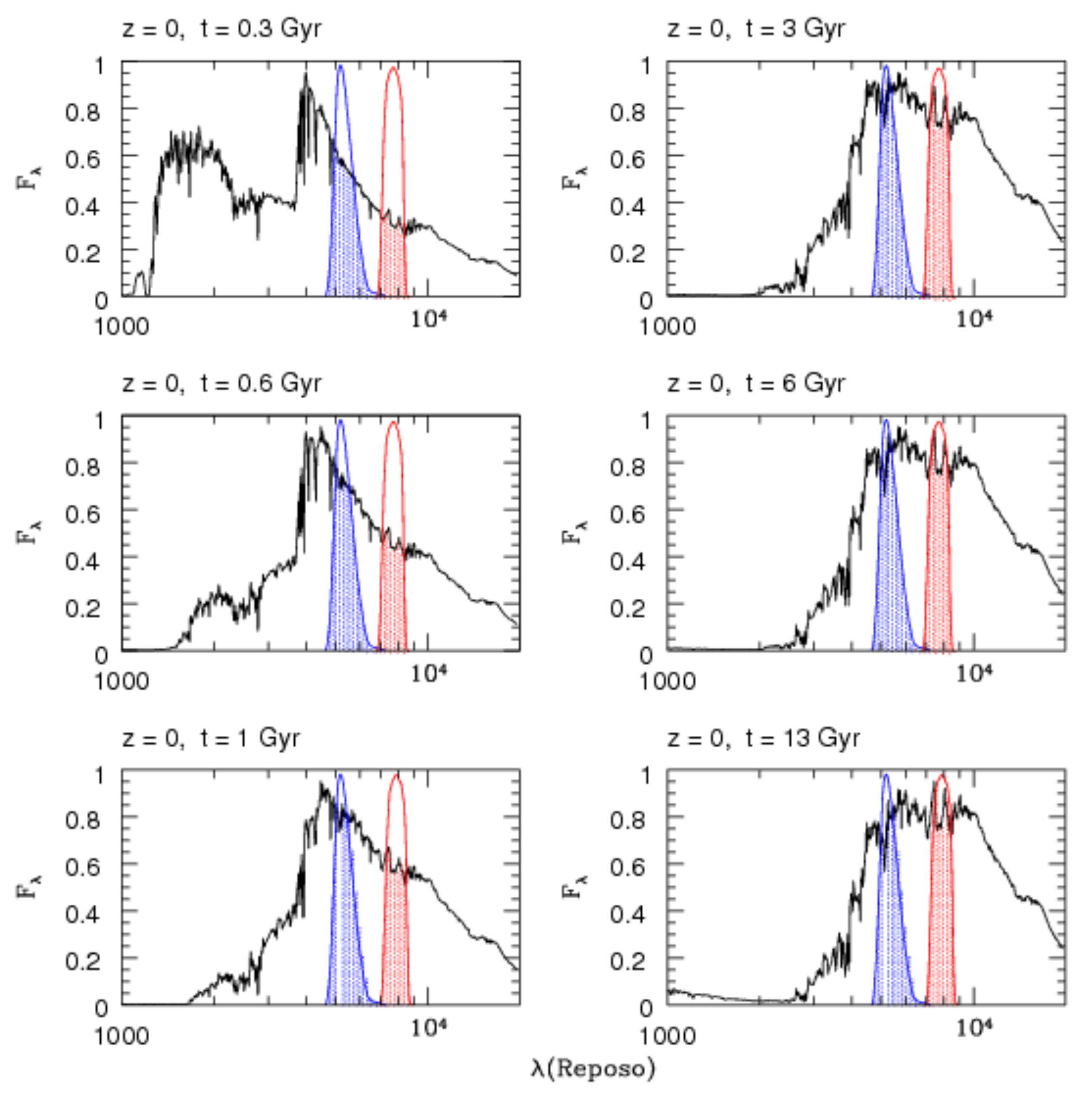

$z = z(t)$

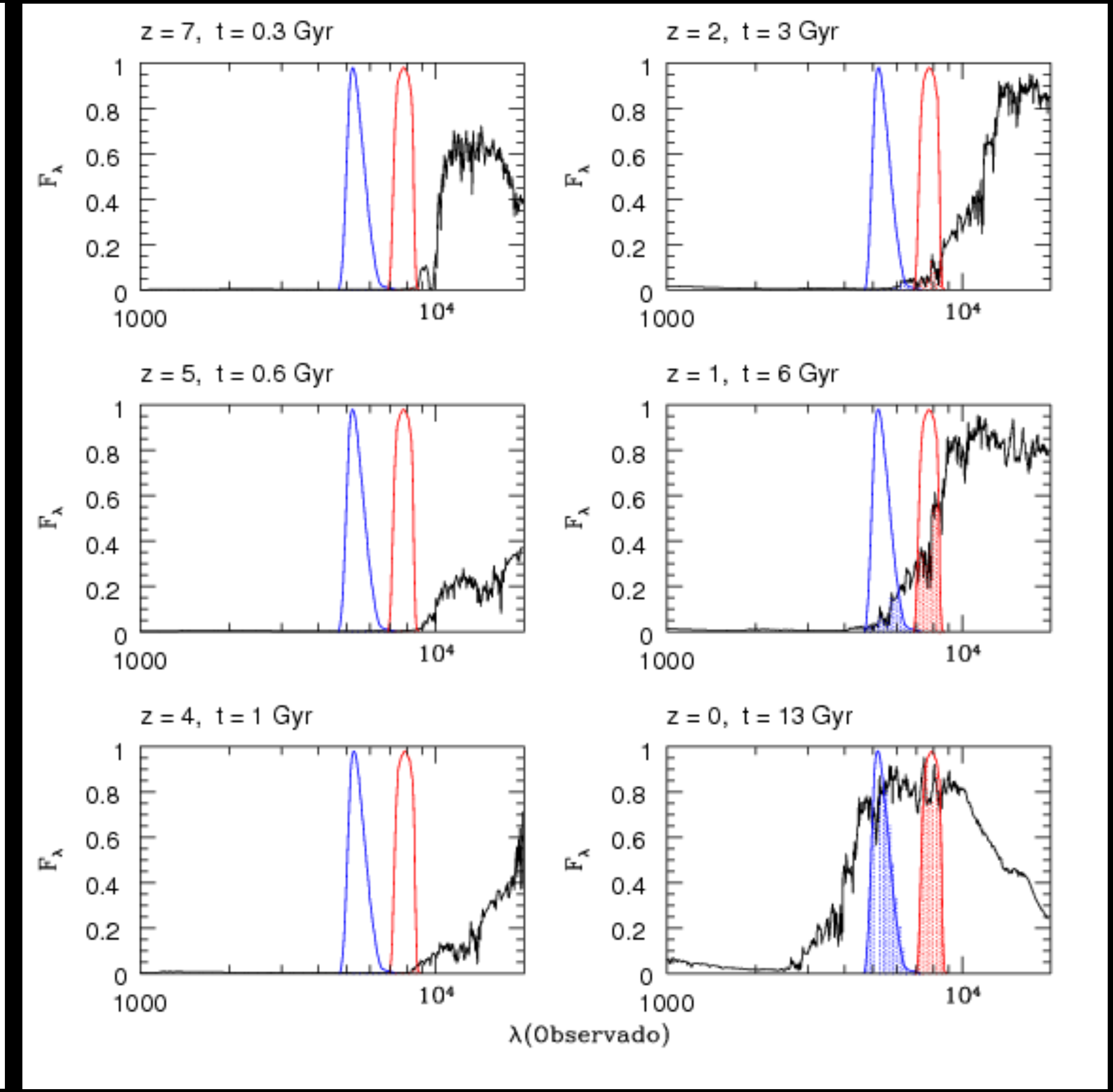

Using dropouts to discover young distant galaxies

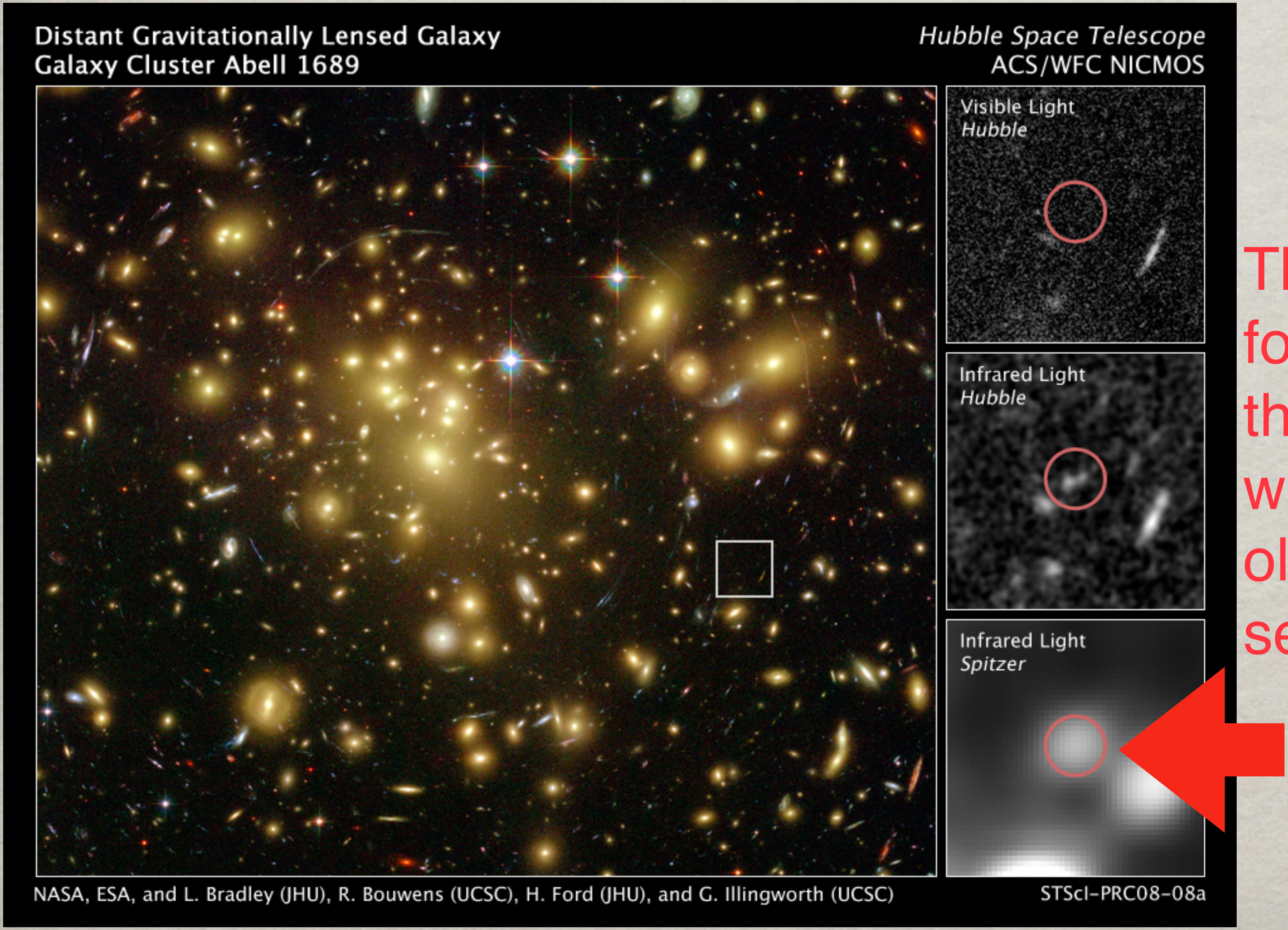

This is a galaxy formed when the universe was 700 Myr old, 13 Gyr ago, seen at z ~ 6

HUDF09: 16 galaxias a z~7 y 5 galaxias a z~8

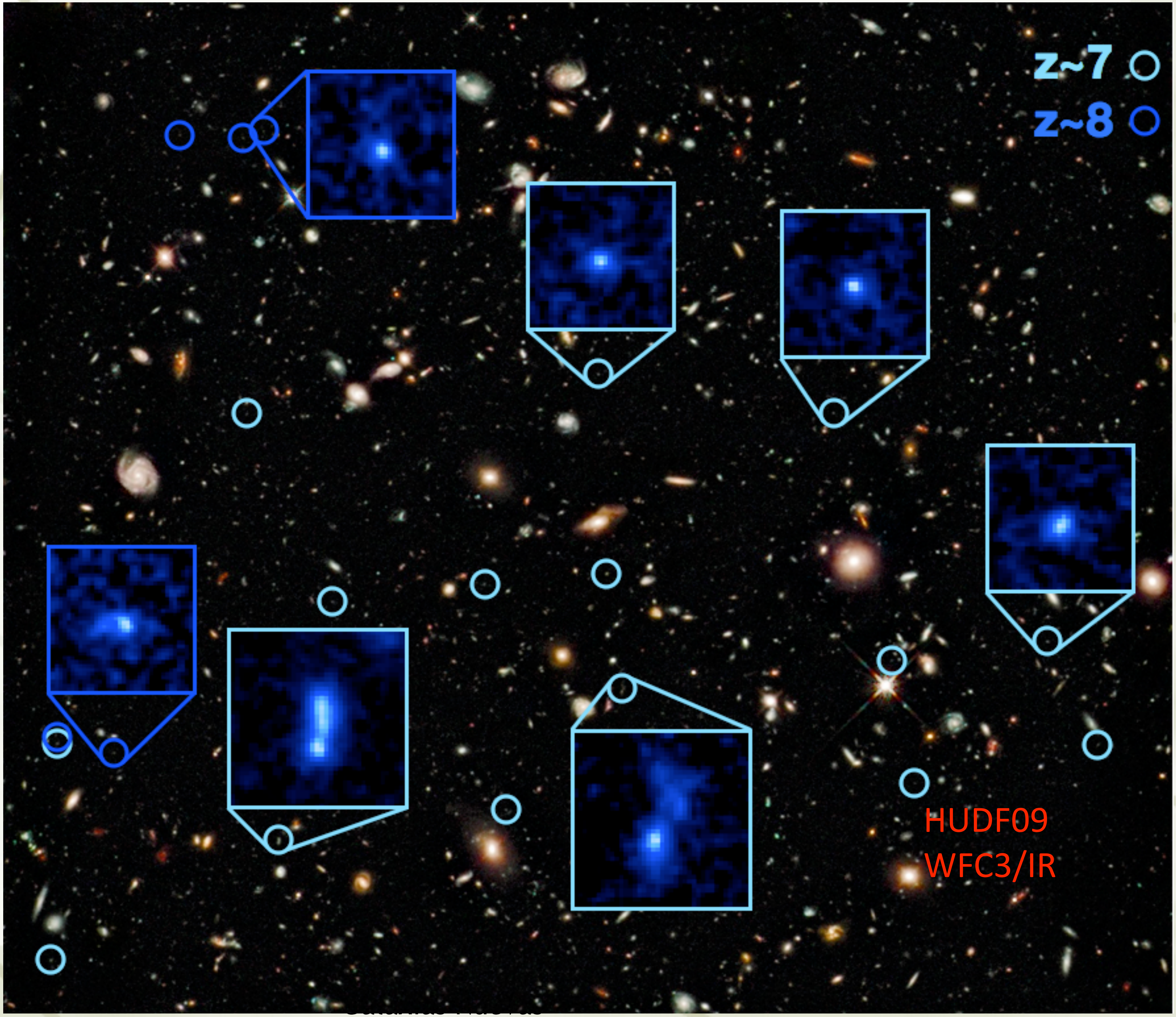

HUDF09 image
~2.2′

Boxes ~2.5”

z~8: Bouwens et al. (2010)

z~7: Oesch et al. (2010)

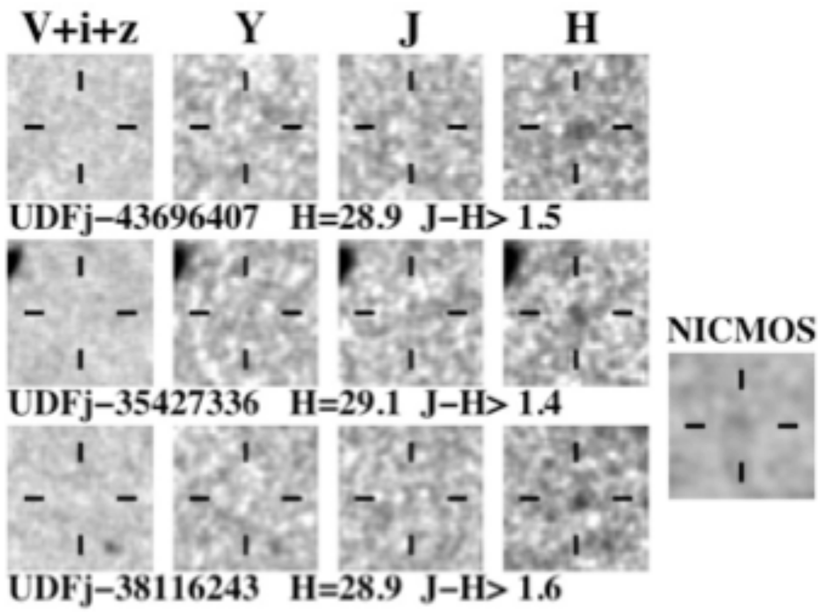

Figure 1. Optical and near-infrared images of the three z~10 J-dropout candidate galaxies from the ultra-deep HUDF optical ACS (V+i+z) data[29] and the correspondingly deep HUDF09 near-IR WFC3/IR (Y, J, H) data.[3,8] None of the candidates is detected in the deep ACS BViz observations. A stacked NICMOS image with a faint, 3σ detection is shown next to the two z~10 candidates that lie in the NICMOS data on the HUDF. Other properties of the candidates are given in Table 1 in the Supplementary Material. Each cutout is 2.4″ × 2.4″ on a side

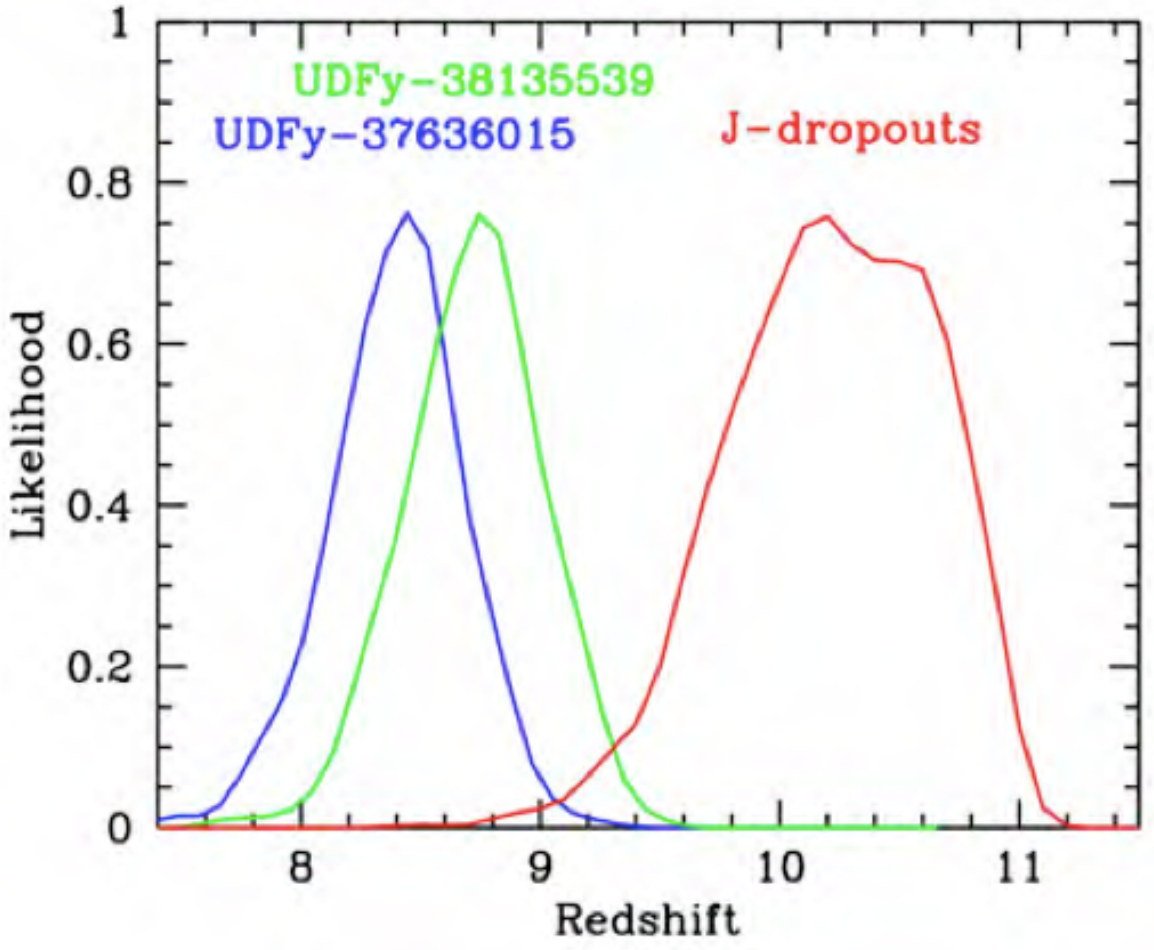

Figure 2. Predicted redshift distribution for the current z~10 J-dropout candidate sample (red line) and the two highest-redshift z~8.5 Y-dropout candidates (blue and green lines). The redshift distributions were derived (see Supplementary Info §8) by adding artificial sources to the HUDF09 WFC3/IR data and reselecting them

some individual z~8 Spitzer 3.6 µm images

Hubble and Spitzer results combine to show us that z~8 galaxies could well have been forming stars two-three hundred million years earlier (at z>10-11)

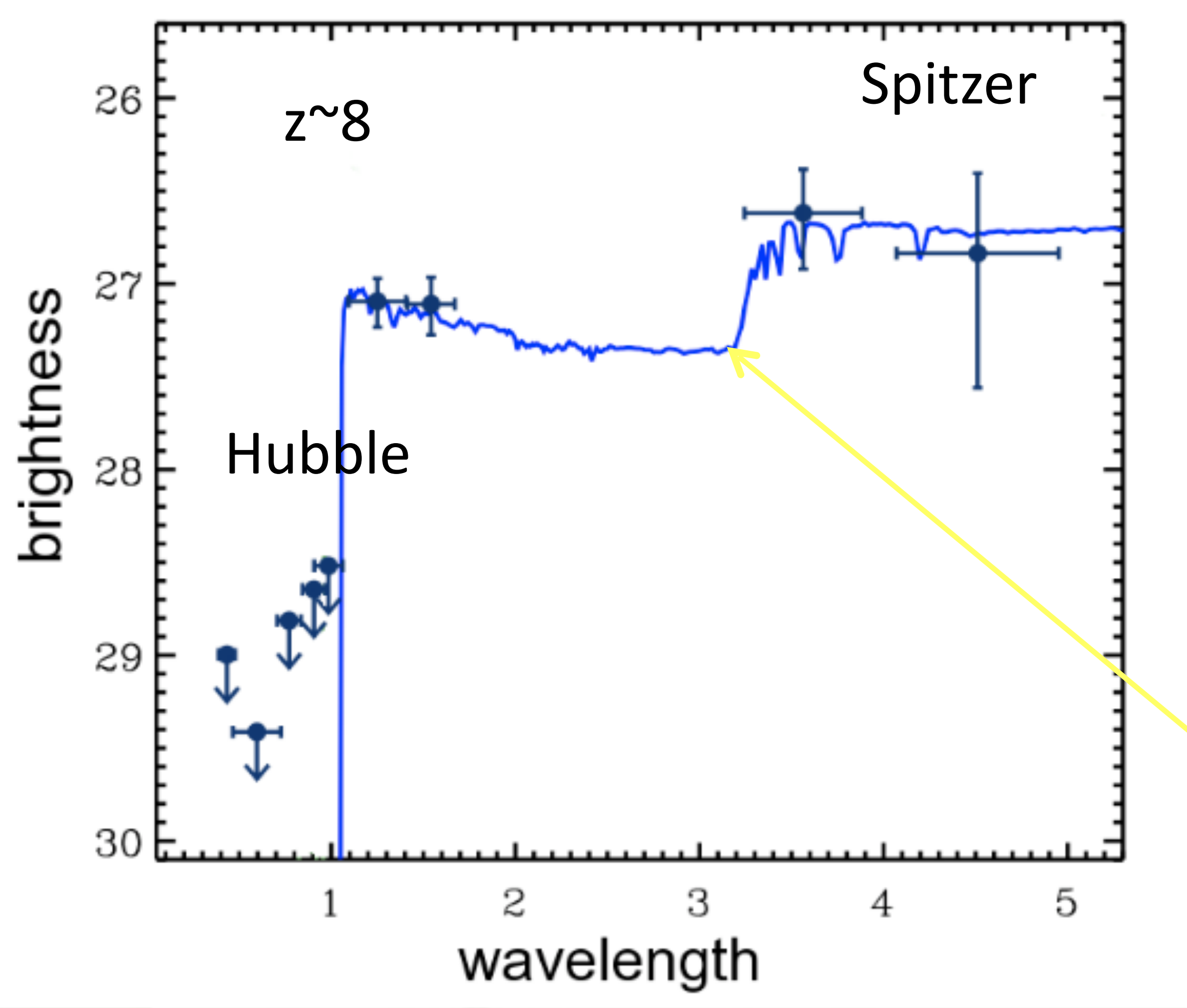

z~8 summed Spitzer images

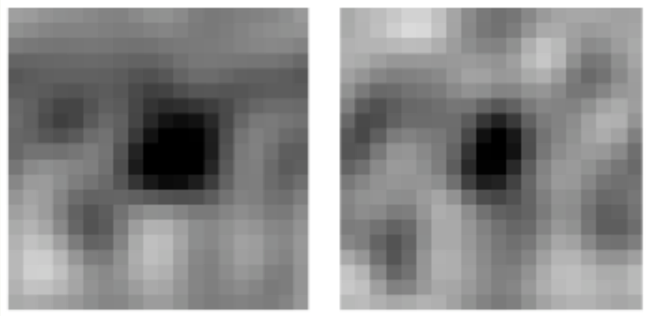

3.6 µm 4.5 µm

Labbé/Gonzalez et al

Model fit is BC03 CSF 0.2$Z_\odot$ log M = 9.3

z~7.7 and 300 Myr (SFH weighted age = t/2)